

# Neuropsychiatric Drug Biosensors in Organelles, Cells, Biofluids, & Behaving Animals

Thesis by  
Anand Kumar Muthusamy

In Partial Fulfillment of the Requirements for the  
Degree of  
Doctor of Philosophy

The logo for the California Institute of Technology (Caltech), featuring the word "Caltech" in a bold, orange, sans-serif font.

CALIFORNIA INSTITUTE OF TECHNOLOGY  
Pasadena, California

2024  
Defended October 20, 2023

© 2024

Anand Kumar Muthusamy  
ORCID: 0000-0003-1041-914X

All rights reserved



For Chinna & Papayee Muthusamy, V. N. & Annapoorna Gopalakrishnan, and  
Duraisamy & Suganthi Muthusamy

## ACKNOWLEDGEMENTS

I have had the luck of having several excellent mentors and colleagues who have shaped my life path. They have energized me on this journey, and I wholeheartedly thank them.

I am grateful to Dr. E. James Petersson for his mentorship in life and science, instruction in chemical biology, and advice in starting a career in science. My first experience at the bench was in James' lab, and his creativity and love for science were infectious. He also was incredible at picking driven lab members from whom I soaked up so much hands-on knowledge. John Warner, a graduate student in the lab at the time, taught me how to conduct research in molecular biology and brought me onto his "magic bullet" project. Later, Lee Speight, another graduate student, taught me synthetic organic chemistry and how to perform careful biophysical measurements. Along the way, I learned an incredible amount from other graduate students: Rebecca Wissner, Jacob Goldberg, Anne Wagner, Solongo Batjargal, Jerri Wang, Christopher Walters, Stella Chen, Miklos Robkis, Ohm Sungwienwong, and John Ferrie. I cherish all our time in the lab, group meetings, and hanging out around Philly.

Many professors at Penn provided pivotal mentorship as well. Ponzy Lu created an excellent biochemistry program and held us all to a high standard. His Chem022 is legendary; I still use the order of magnitude and dimensional analyses we learned there. Phil Nelson has a beautiful view of the world, and his Phys280 cemented biophysics in my toolkit. His *From Photon to Neuron* was an invaluable reference as I dove into microscopy and neuroscience later. Dave Chenoweth has an amazing eye for chemical biology. He taught an excellent advanced synthetic chemistry course which built my intuition in organic chemistry. He was an unwavering supporter — I could always rely on his advice and encouragement. Adriana Petryna was another incredible supporter and mentor in medical anthropology. She was able to convert my raw interests and energy into a concrete research direction. Thanks to her, I could cross over from science to conduct research in the Penn Humanities Forum. My friends in the Student Committee on Undergraduate Education and the Penn Bioethics Journal rounded out my personal development.

I had some more luck on my side when I happened to hear Luke Lavis talk at a symposium in Chem '73. I was nearing graduation but did not have a plan about

what to do afterward. But, after hearing about reviving the spirit of Bell Labs and the MRC for neuroscience and seeing Luke, a chemist, making tools for biologists, I was hooked. Long story short: Luke invited me to Ashburn later that summer for an interview. I am happy to say I spent two wonderful years in Luke's lab. Luke taught me synthetic chemistry, dye photophysics, and how to make excellent tools beloved by biologists. Making and sharing JaneliaFluor dyes was the ultimate gratification for us tool builders. Jonathan Grimm was an incredible mentor in synthetic chemistry and, to date, the exemplar I think about for focus and efficiency in the lab. Charles Kim broadened my view of science and the world, showing me how to talk to neuroscientists and make sense of their experiments. I broadened my horizons thanks to several interest groups in optics, Python, and virtual reality. I loved the calm, focused energy aimed at building from our imaginations that Janelia harbored. When I arrived, I knew almost no one and almost nothing about neuroscience. I left with several friends, colleagues, and an inspiration to learn more about the brain.

Henry Lester was truly the perfect mentor for me, a chemist entering neuroscience. Henry has a unique sense of biological scales across time and space that has left a deep impression on how I approach science. Having a mentor who always makes time for you and digs into the details is incredibly empowering. I will never forget joining the lab without having performed microscopy and learning it quickly from hands-on sessions with Henry. I benefited from Henry's Caltech staple, Bi150, as an intro to neuroscience, and later his new Bi163 related to psychiatric disorders. Additionally, his ability to collaborate widely has enriched me directly, with scientists joining our projects and, more broadly, by offering an exemplary approach to teamwork. The mix of fun and creative energy matched to rigor in discussions and lab meetings was what I was hungry for. He provided mentorship while giving me the freedom to lead my projects and take long shots. Thanks to Henry, I have come into my own as a scientist.

My colleagues in the Lester lab laid the groundwork. Amol Shivange and Phil Borden paved the way with their construction of the first biosensor scaffold. Aron Kamajaya took a bold shot at mutagenizing the scaffold to yield critical variants useful for ketamine and fentanyl biosensors. Aaron Nichols refined and strengthened the molecular biology techniques. Brandon Henderson provided expert guidance in several physiological measures, especially acute slices, and helpful comments on my writing. Kallol Bera, Jonathan Wang, Tanner Lakin, Zachary Blumenfeld,

Bruce Cohen, and Purnima Deshpande helped me along the way and created a collaborative and collegial environment. I had the pleasure of working with and mentoring younger lab mates, Alex Wang, Theodore Chin, Janice Jeon, and Zoe Beatty, who each stand out in their unique ways. The final chapter of this work in particular was made possible by a tremendous effort from Theo and Alex. Theo was a force of nature in performing directed evolution experiments and culturing iPSC-derived neurons. Alex brought an impressive ambition to learn molecular biology and neuroscience and helped develop our computer vision analysis from scratch. The many hours we spent troubleshooting, taking walks, and sharing meals as we grappled with the problem at hand are some of my fondest memories.

My collaborators at Caltech have enriched my experience. Matthew Rosenberg and I had a fruitful time pursuing a Chen Innovator award, where I learned behavior and computational ethology from him. All of our time at the whiteboard, in the lab, and talking science all around LA was one of the highlights of my PhD. Markus Meister and Yuki Oka provided guidance on this project and, again, helped a young chemist enter neuroscience. I thank the many members of the labs of Dennis Dougherty, Doug Rees, Wei Gao, Yuki Oka, Markus Meister, and Victoria Orphan. Haley Knox brought an excellent rigor in our experiments incorporating unnatural amino acids into biosensors. Scott Virgil was a thrill to work with as we chirally resolved methadone. Jens Kaiser and his Molecular Observatory helped start the crystallography work with the opioid biosensors. Aiden Aceves is an extremely sharp and thoughtful scientist and human and provided the earliest inklings of how to construct protein sequence/function datasets amenable to machine learning and advised on docking studies. I owe many thanks to numerous members of the Caltech community whose names are not listed here but who have made for an incredible community and greatly helped me.

Beyond Caltech, Chris Evans at UCLA provided invaluable advice on beginning the opioid library screening project. He led a neuroscience of addiction course at CSHL in 2019 that sparked my interest in physiology and behavior. At that course, I was enthralled with a series of talks, particularly by David Belin's argument for fleshing out endophenotypes of substance abuse disorders and explaining the switch from initial drug exposures to compulsive intake.

I thank my committee for their guidance in this research and my career. Viviana Gradinaru provided a superb introduction to neuroscience in her courses. She was a steadfast supporter as I picked up new skills and explored career paths. The

CLOVER Center is truly a gift to life science. Mikhail Shapiro provided guidance as a chemist entering neuroscience. Thanks to his encouragement, I learned survival surgeries and how to deploy biosensors *in vivo*. Stephen Mayo provided a wealth of career advice, and I soaked up his wisdom in protein engineering at our weekly meetings. Dennis Dougherty always set a high bar for rigor high and provided expert feedback from my very first proposition to this thesis.

Finally, my friends, family, and communities have been my foundation and inspiration. I thank all of you in Houston, Philadelphia, Ashburn, and Los Angeles who have helped make me feel at home. In particular, the community in Katy, TX, provided me with teachers and coaches who built my academic foundation. I am overwhelmed when I think about how many hours you all poured into me.

Nathan Koocher and I have a special bond because we were each other's first friends at Penn and went through science and graduate school in near lockstep. I shared every up and down along the way with him, and am much better for his support and advice. David Pankciewicz has been a tremendous friend who has always been there for me. For years, he said he would travel whenever and wherever for my defense and, indeed, he did! His passion for life and adventure has been energizing through the years. Karthik Manohar is a childhood friend and the best conversationalist I know. I always enjoyed talking about life, especially that one late night in Joshua Tree. Vivek Karun is another childhood friend whom I could always talk to. I will never forget us around the West side with our heads in the clouds and will cherish our Thanksgiving dinner during the pandemic. David Brown and Tatyana Dobрева are kindred spirits in the quest to build new institutions. They are exemplary citizens of science, creating opportunities wherever they go. Deepa Muthusamy, my sister, has been someone I could call up at any hour. We have grown closer together over the past several years, especially during the summer visits to LA and the winters in Houston.

Charlene Kim has been through it all with me in the lab. I recall all the technical problems we had to solve over the years, from cells to slices to animals, particularly through the COVID-19 pandemic. I learned that we are limited by our courage rather than external challenges; she was a bright light through those days. I also remember the carefree moments of taking a behavioral neuroscience class together and enjoying studying elephants and monkeys. Her intuition for the physicality of biological systems, especially animals, is par excellence. She has been an incredible inspiration through this process, and I cherish all her care and support.

Finally, I thank my parents, Duraisamy and Suganthi Muthusamy, for all that they have done. They have given me the gift of a blessed life and served as role models each in their own way. I am grateful for all the time we spent together as I grew up in Houston. I remember all the places we went: the park, zoo, museums, Westhollow Technology Center, camping all over Texas, and traveling all over India. I was at once under their wings and allowed to venture on my own. They brought love and balance in all things. I look back on those times as formative in shaping my ability to fearlessly explore places and ideas. I am the product of all the time and energy they poured into me—I appreciate that increasingly, year after year.

Thanks to this journey, I see the natural world with even more curiosity and a bit more clarity. I hope to keep learning from you all and keep doing you proud.

## ABSTRACT

This work develops and applies the first genetically encoded drug biosensors in newly designed cellular and behavioral assays addressing substance abuse disorders. The work develops methods in protein engineering, optical physiology, and computational ethology. A capstone study provides a general means to develop opioid biosensors and demonstrates the utility of continuous fentanyl monitoring alongside behavior. This work provides a framework to optimize CNS drug dosing for well-being assessed via ethologically relevant tasks.

### **Chapter 1: Continuous monitoring & substance use disorders**

This chapter argues for continuous, *in situ* monitoring for the life sciences, particularly in neurobiology. Opioid use disorder is an exemplary case for this work, given the correlation between pharmacokinetics and tolerance, withdrawal, and overdose. A technology map analysis shows that biosensor design is a bottleneck for continuous monitoring methods, accentuating the need for molecular engineering approaches such as protein engineering.

### **Chapter 2: iNicSnFR and “inside-out pharmacology**

This publication reports the evolution of the first genetically encoded fluorescent drug sensor, a biosensor of nicotine, iNicSnFR, and introduces the concept of sub-cellular pharmacokinetics via optical physiology. Prior biophysical studies implied nicotine engaged the nicotinic acetylcholine receptor in “inside-out” effects: chaperoning, matchmaking, and escorting within neurons. This work directly shows the requisite first step: nicotine rapidly (~seconds) equilibrates in the endoplasmic reticulum. A critical technical advance was optimizing biosensor localization within organelles and correcting for pH artifacts to enable quantitative imaging experiments. Based on these results, a dynamical simulation indicated that a single cigarette would maintain activation of the “inside-out” pathway until the next smoking session. This outcome blurs the conventional views of “acute” and “chronic” effects and explains, in part, a mechanism for instantiating nicotine dependence.

### **Chapter 3: iS-methadoneSnFR, acid trapping, and “location bias**

This publication introduces the first biosensor of an opioid, S-methadone, and reveals an acid-trapping effect in the Golgi apparatus. Methadone is clinically administered as a racemate salt, the only commercially available formulation. We developed a chiral resolution method to separate isomers and then employed protein engineering

to develop a sensitive and selective biosensor of S-methadone. Recent findings have shown that opioid receptors can signal from within endosomes and the Golgi apparatus. iS-methadoneSnFR was used to demonstrate an acid trapping effect in the Golgi apparatus where S-methadone was concentrated 3-4x compared to the extracellular concentration. This result enriches our view of “location bias” for opioid agonism and encourages similar studies for other ligands and their GPCRs.

#### **Chapter 4: A library screening approach for iDrugSnFRs**

This publication introduces a method for discovering new “biosensor x drug” hit pairs by constructing protein and drug libraries and utilizing robotic liquid handling methods. This approach extends the substrate scope for genetically encoded biosensors beyond the conventional scope attributed to naturally occurring binding protein-ligand interactions.

#### **Chapter 5: A perspective piece on cannabis vapor self-administration**

This publication reviews a new behavioral paradigm for vapor cannabis administration reported by Freels et al. 2020. A.K.M provides an original analysis considering the chemical composition of the cannabis samples and its pharmacokinetic and neurobiological consequences. This work was published as a perspective piece in the Journal of Neuroscience and has been cited by research literature developing new vapor administration systems.

#### **Chapter 6: Generating iOpioidSnFRs & discovery of a detrimental, repetitive behavioral pattern that tracks [fentanyl] waveform**

This manuscript reports a mapping between periplasmic binding protein mutations and affinity for opioid subclasses, enabling a systematic approach to protein engineering. Several iOpioidSnFRs are reported for clinically used opioids such as morphine, codeine, naloxone, tapentadol, levorphanol, and fentanyl. Application of iFentanylSnFR *in vivo* discovered a [fentanyl]-locked behavioral pattern where animals repeatedly circle and stall. The entire time course and the relative time spent circling or stalling varies by individual, demonstrating the need for individual, *in situ* measurements of both [drug] and behavior. This work introduces an ethologically relevant survival task, foraging for water in a labyrinth maze, to the field of substance use disorders. Mice treated with fentanyl displayed a similar repetitive behavior for up to ~3 h, trading off completely with successful foraging.



## PUBLISHED CONTENT AND CONTRIBUTIONS

*In reverse chronological order:*

1. **Muthusamy, A. K.**, Rosenberg, M. H., Kim, C. H., Wang, A. Z., Ebisu, H., Chin, T. M., Koranne, A., Marvin, J. S., Cohen, B. N., Looger, L. L., Oka, Y., Meister, M., & Lester, H. A. (2024). Correspondence of fentanyl brain pharmacokinetics and behavior measured via engineering opioids biosensors and computational ethology. *bioRxiv*. <https://doi.org/10.1101/2024.03.15.584894v1>.

*Reported in Chapter 6*

*A.K.M. conceived of the project, evolved the biosensors, performed biophysical characterization, performed all behavioral tests, co-wrote the machine vision pipeline reported in this work, analyzed the data, and wrote the manuscript with feedback from the authors.*

2. Nichols, A. L., Blumenfeld, Z., Luebbert, L., Knox, H. J., **Muthusamy, A. K.**, Marvin, J. S., Kim, C. H., Grant, S. N., Walton, D. P., Cohen, B. N., Hammar, R., Looger, L., Artursson, P., Dougherty, D. A., & Lester, H. A. (2023). Selective serotonin reuptake inhibitors within cells: Temporal resolution in cytoplasm, endoplasmic reticulum, and membrane. *Journal of Neuroscience*, 43(13), 2222-2241. <https://doi.org/10.1523/JNEUROSCI.1519-22.2022>

*A.K.M. designed imaging experiments and assisted in analyses.*

3. **Muthusamy, Anand K**, Lester, Henry A, Looger, Loren L, Marvin, Jonathan S. "Engineered opioid biosensors." U.S. Patent Application 17/553,725, filed June 23, 2022.

*Adapted in Chapter 1 and Appendix A*

*A.K.M. conceptualized the iOpioidSnFR class of biosensors with the co-inventors, performed experiments, and wrote the application.*

4. Beatty, Z. G., **Muthusamy, A. K.**, Unger, E. K., Dougherty, D. A., Tian, L., Looger, L. L., Shivange, A. V., Bera, K., Lester, H. A., & Nichols, A. L. (2022). Fluorescence screens for identifying central nervous system-acting drug-biosensor pairs for subcellular and supracellular pharmacokinetics. *Bio-protocol*, 12(22), e4551-e4551. <https://doi.org/10.21769/BioProtoc.4551>

*Reported in Chapter 4*

*A.K.M. performed the 2018 opioid library screen, assisted in planning the 2017 screen, advised Z.G.B. in performing the 2019 screen, and edited the manuscript.*

5. **Muthusamy, A. K.**, Kim, C. H., Virgil, S. C., Knox, H. J., Marvin, J. S., Nichols, A. L., Cohen, B. N., Dougherty, D. A., Looger, L. L., & Lester, H. A. (2022). Three mutations convert the selectivity of a protein sensor from nicotinic agonists to S-methadone for use in cells, organelles, and biofluids. *Journal of the American Chemical Society*, 144(19), 8480-8486. <https://doi.org/10.1021/jacs.2c02323>

*Reported in Chapter 3*

*A.K.M. evolved the biosensor, performed dose response and imaging experiments, analyzed all data, and wrote the manuscript.*

6. Nichols, A. L., Blumenfeld, Z., Fan, C., Luebbert, L., Blom, A. E. M., Cohen, B. N., Marvin, J. S., Borden, P. M., Kim, C. H., **Muthusamy, A. K.**, Unger, E. K., Tian, L., Looger, L. L., Dougherty, D. A., & Lester, H. A. (2022). Fluorescence activation mechanism and imaging of drug permeation with new sensors for smoking-cessation ligands. *Elife*, 11, e74648. <https://doi.org/10.7554/eLife.74648>

*A.K.M. designed imaging experiments and assisted in analyses.*

7. **Muthusamy, A. K.** (2020). Cannabis extract composition determines reinforcement in a vapor self-administration paradigm. *Journal of Neuroscience*, 40(33), 6264-6266. <https://doi.org/10.1523/JNEUROSCI.0814-20.2020>

*Reported in Chapter 5*

*A.K.M. independently researched and prepared this manuscript.*

8. Bera, K., Kamajaya, A., Shivange, A. V., **Muthusamy, A. K.**, Nichols, A. L., Borden, P. M., Grant, S., Jeon, J., Lin, E., Bishara, I., Chin, T. M., Cohen, B. N., Kim, C. H., Unger, E. K., Tian, L., Marvin, J. S., Looger, L. L., & Lester, H. A. (2019). Biosensors show the pharmacokinetics of S-ketamine in the endoplasmic reticulum. *Frontiers in Cellular Neuroscience*, 13, 499. <https://doi.org/10.3389/fncel.2019.00499>

*A.K.M. designed imaging experiments and assisted in analyses.*

9. Shivange, A. V., Borden, P. M., **Muthusamy, A. K.**<sup>\*</sup>, Nichols, A. L., Bera, K., Bao, H., Bishara, I., Jeon, J., Mulcahy, M. J., Cohen, B., O’Riordan, S. L., Kim, C., Dougherty, D. A., Chapman, E. R., Marvin, J. S., Looger, L. L., & Lester, H. A. (2019). Determining the pharmacokinetics of nicotinic drugs in the endoplasmic reticulum using biosensors. *Journal of General Physiology*, 151(6), 738-757. <https://doi.org/10.1085/jgp.201812201>

*Reported in Chapter 2*

<sup>\*</sup> *co-1st author, A.K.M. optimized biosensor transfection conditions, performed*

*imaging experiments, modified the perfusion and imaging rig to address pH artifacts, and analyzed data.*

10. **Muthusamy, A. K.**, Shivange, A. V., Nichols, A. L., Kamajaya, A., Jeon, J., Borden, P. M., Marvin, J. S., Unger, E. K., Bao, H., Chapman, E. R., Tian, L., Looger, L. L., & Lester, H. A. (2018). Microscopy using fluorescent drug biosensors for “inside-out pharmacology”. *Biophysical Journal*, 114(3), 358a.

*A.K.M. performed the imaging, wrote this abstract, and presented this work at the Biophysical Society. This abstract has been cited in the research literature and provided a foundation for Chapters 2 and 3.*

## TABLE OF CONTENTS

Acknowledgements . . . . .	iv
Abstract . . . . .	ix
Table of Contents . . . . .	xiii
List of Illustrations . . . . .	xvi
List of Tables . . . . .	xxxi
Chapter I: Introduction: Continuous Monitoring & Substance Abuse Disorder	1
1.1 Humans as Tool Makers . . . . .	1
1.2 The Uniqueness of CNS Disorders . . . . .	2
1.3 Molecular and Behavioral Features of Opioid Use Disorder . . . . .	3
1.4 The Biosensor-Transduction System Bottleneck in “Reading” Biology <i>in situ</i> . . . . .	6
1.5 iOpioidSnFRs and Their Opioids . . . . .	7
1.6 References . . . . .	10
Chapter II: iNicSnFR: Determining the Pharmacokinetics of Nicotinic drugs in the Endoplasmic Reticulum Using Biosensors . . . . .	15
2.1 Abstract . . . . .	15
2.2 Introduction . . . . .	16
2.3 Materials and Methods . . . . .	19
2.4 Results . . . . .	27
2.5 Discussion . . . . .	50
2.6 Supplemental Information . . . . .	54
2.7 Acknowledgements . . . . .	66
2.8 References . . . . .	67
Chapter III: Evolution of iS-methadoneSnFR for Subcellular Pharmacokinetics and Biofluid Measurements . . . . .	75
3.1 Abstract . . . . .	75
3.2 Introduction . . . . .	76
3.3 Lead Discovery: Methadone Isomer x Nicotinic Biosensor Library Screen . . . . .	78
3.4 Directed Evolution of iS-methadoneSnFR . . . . .	78
3.5 Biophysical Characterization of iS-methadoneSnFR . . . . .	80
3.6 Application in Mammalian Biofluids and Cells . . . . .	81
3.7 Discussion . . . . .	85
3.8 Supplemental Data . . . . .	86
3.9 Materials and Methods . . . . .	95
3.10 References . . . . .	106
Chapter IV: Fluorescence Screens for Identifying Central Nervous System–Acting Drug–Biosensor Pairs for Subcellular and Supracellular Pharmacokinetics	109
4.1 Abstract . . . . .	109

4.2	Background: CNS Drugs & Sensors . . . . .	109
4.3	2017 Screen: Psychiatric Drugs . . . . .	111
4.4	2018 Screen: Opioids . . . . .	114
4.5	2019 Screen: 5-HT <sub>3</sub> Ligands, CB <sub>1</sub> /CB <sub>2</sub> Ligands, and Neonicotinoids . . . . .	116
4.6	Notes on Generalizability of OpuBC-Based Biosensors . . . . .	118
4.7	Acknowledgments . . . . .	120
4.8	References . . . . .	120
Chapter V: Chemical and Pharmacokinetic Perspective on Freels et al., 2020: Cannabis Extract Composition Determines Reinforcement in a Vapor Self- Administration Paradigm . . . . .		
		122
5.1	Perspective on Freels et al, 2020 . . . . .	122
5.2	References . . . . .	126
Chapter VI: iOpioidSnFRs & Recording Fentanyl <i>in vivo</i> Alongside A Com- puter Vision Routine for Quantifying Behavior . . . . .		
		129
6.1	Abstract . . . . .	129
6.2	Introduction: Opioid Use Disorder, Pharmacokinetics, & Behavior Paradigms . . . . .	130
6.3	Results . . . . .	133
6.4	Discussion . . . . .	155
6.5	Acknowledgements and Funding . . . . .	158
6.6	Supplemental Figures . . . . .	159
6.7	Supplemental Tables . . . . .	169
6.8	Methods . . . . .	170
6.9	References . . . . .	188
Appendix A: Biosensor Amino Acid Sequences . . . . .		196

## LIST OF ILLUSTRATIONS

<i>Number</i>	<i>Page</i>
1.1 Figure from Williams, 2013: time scales for processes in $\mu$ -opioid receptor signaling, desensitization, and tolerance from experimental studies. Reproduced with permission. . . . .	4
1.2 Figure from Belin-Rauscent, 2016: the “spiral” of the entire addiction process with a distinct switch between drug seeking and compulsive use and relapse. Reproduced with permission. . . . .	5
2.1 Strategy of the experiments. (A) Nicotine ( $pK_a$ , 7.5–8.1) and varenicline ( $pK_a$ , 9.5–10) are weak bases. They interconvert on a millisecond time scale between protonated and deprotonated forms; these are respectively membrane impermeant and permeant. (B) The tactic of confining a genetically encoded fluorescent nicotinic drug sensor to the PM or the ER. (C) Choline, ACh, and N’MeNic exist only as charged, membrane-impermeant forms near physiological pH. . . . .	18
2.2 The genetically encoded family of biosensors for nicotinic drugs, iNicSnFRs. (A) Cartoon of the x-ray crystallographic structure of iNicSnFR1, crystallized in the presence of nicotine. The structure is available as PDB file 6EFR. The iNiCSnFR family are fusion proteins. A superfolder cpGFP (shown in green) has been inserted into the coding sequence of OpuBC, a choline/betaine PBP from <i>T. spX513</i> . The linker sequences (shown in dark blue; see Fig. 2.11) were selected for optimal $\Delta F/F$ . One poorly resolved linker residue, Pro323, is shown as a dashed backbone. The engineered OpuBC is shown in cyan, except that the backbone residues near the incompletely resolved nicotine ligand are shown in gray. The nicotine-binding site lies between the two lobes of the PBP; these move relative to each other. . . . .	30

- 2.3 The pH dependence of purified iNicSnFR3a in solution, over the range pH 5.5–9.0, at 25°C. Measurements were performed in 3× PBS, adjusted to nominal pH within 0.1 pH unit. (A–C) Measurements in a spectrofluorometer (see Materials and Methods). 100 nM protein. Fluorescence is measured in the absence of ligand and termed  $F_0$ . (A) Excitation spectra at various pH values, measured at a  $\lambda_{em}$  of 535 nm. (B) Emission spectrum at a  $\lambda_{ex}$  of 400 nm. Note that  $F_0$  depends to only a limited extent on the pH. (C) Emission spectrum at  $\lambda_{ex} = 485$  nm. Note the strong dependence on pH. . . . . 33
- 2.4 Protein levels and subcellular imaging of iNicSnFR3a\_PM and iNicSnFR3a\_ER in HeLa cells. (A) Typical immunoblots with anti-GFP immunoreactivity to lysates (1  $\mu$ g protein) from HeLa cells transfected with either iNicSnFR3a\_PM (top) or iNicSnFR3a\_ER (bottom). In each panel, the leftmost lane is the 75-kD molecular weight marker (MWM). The two middle lanes are duplicate samples of purified, diluted iNicSnFR3b (~61 kD). The two rightmost lands are duplicate samples from the transfected cells. Bands for iNicSnFR3a\_PM appear at ~68 kD (slightly below the MWM), and bands for iNicSnFR3a\_ER appear at ~61 kD (markedly below the MWM and comparable with purified biosensor), confirming the predicted size difference of 7 kD between the two constructs. . . . . 36
- 2.5 Dose–response relations for nicotine-induced  $\Delta F$  in HeLa cells. Exemplar data for iNicSnFR3a\_PM and iNicSnFR3a\_ER expressed in transfected HeLa cells. (A and C) 20-s nicotine dose application followed by 20-s wash in HBSS. The average response for three cells at each dose is overlaid in a 30-s window for the PM and ER traces in A and C, respectively. The SEM is shown as colored bands. . . . . 39

- 2.6 Nicotine in the ER of neurons. (A–D) Exemplar nicotine-induced fluorescence increases for cultured hippocampal neurons transduced with AAV2/1.sin1.iNicSnFR3b\_PM (A and B) or with AAV2.sin1.iNicSnFR3b\_ER (C and D). (A and C) 20-s nicotine pulses, followed by 20 s wash in HBSS. The average waveform for five cells at each [nicotine] is overlaid for the PM and ER traces in A and C, respectively. The SEM is shown as colored bands around each line. Dose–response relations are shown in B and D. (E and F) Human dopaminergic neurons transfected with iNicSnFR\_ER3a. (E) Typical nicotine-induced fluorescence during 20-s pulses of nicotine at the indicated concentrations. Data were subjected to a triangle filter (half-time, 1 s). (F) Full dose–response data from 20 transfected human dopaminergic neurons. Inset, start of the dose relation at [nicotine]  $\leq 5 \mu\text{M}$ . The slope of the line,  $[\Delta F/F_0]/[\text{nicotine}]$ , is  $0.087\text{M}^{-1}$ . . . . . 42
- 2.7 Micro-iontophoretic nicotine application. (A) Cultured mouse hippocampal neurons transduced with AAV\_iNicSnFR3b\_ER. A nicotine-containing micro-iontophoretic pipette was positioned  $<10 \mu\text{m}$  above the cell in ROI 1. A 10-nA outward current pulse (32-s duration) was delivered. Most cells in the area showed fluorescence increases. (B) Fluorescence traces recorded simultaneously for cells at three distances from the pipette. . . . . 43
- 2.8 Simulations of nicotine pharmacokinetics and pharmacodynamics during smoking. (A) The pharmacokinetic/pharmacodynamic model, implemented in Matlab SimBiology. Individual parameters and structures and smoking dosages are presented in Table 2.3 and in Supplemental ZIP File. (B1) Nicotine concentrations in the plasma/CSF/ER and in the “sequestered” compartment, during 40 simulated hours for the standard habit (Table 2.3 and Supplemental ZIP File). The latter compartment was termed the “peripheral compartment” by Benowitz et al. (1991), but that terminology is less preferable in discussions of the nervous system. Note the logarithmic [nicotine] scale. (B2) Effects on the two processes shown in A. Note that the standard habit nearly activates nAChR protein chaperoning (inside-out process)  $>50\%$ , but activates nAChR channel activation (outside-in process)  $<20\%$ . . . . . 45



- 2.9 Varenicline activity against purified iNicSnFR3a (A–C) and iNicSnFR3b expressed in hippocampal neurons (D–G). (A) Dose–response relations for varenicline-induced  $\Delta F/F_0$ , measured in  $3\times$  PBS, pH 7.4. Mean  $\pm$  SEM; three measurements. (B) Stopped-flow measurements at various [varenicline]. (C) Isothermal titration calorimetry. (D–G) Exemplar varenicline-induced fluorescence increases for cultured hippocampal neurons transduced with AAV2/1.syn1.iNicSnFR3b\_PM (D and E) or with AAV2/1.syn1.iNicSnFR3b\_ER (F and G). (D and F) 30-s varenicline pulses, followed by 40-s wash in HBSS. The average waveform for five cells at each [varenicline] is overlaid for the PM and ER traces in A and C, respectively. The SEM is shown as colored bands around each line. (E and G) Dose–response relations, fitted to a single-component Hill equation, including zero response at zero [varenicline]. Parameters are shown. . . . . 47
- 2.10 Simulated pharmacokinetics and pharmacodynamics during oral varenicline administration. (A) In the pharmacokinetic model for orally administered varenicline, the lungs are replaced by the digestive tract. The parameters derive from studies on humans (Faessel et al., 2006). The parameters are given in Table 2.3 and in Supplemental ZIP File. (B1) Varenicline concentrations in two compartments: the plasma/CSF/ER and the sequestered compartment. (B2) Effects on the two processes shown in A. Note that recommended treatment with varenicline almost completely activates nAChR protein chaperoning (inside-out process), but only slightly produces nAChR channel activation (outside-in process). . . . . 49
- 2.11 Sequences of PBPs and constructs described in this paper and/or studied in preliminary experiments. . . . . 56

- 2.12 Directed evolution of the iNicSnFR family. (A) A history of our progress toward the goal of  $\Delta F/F_0 > 0.3$  at 1  $\mu\text{M}$  nicotine. Initial experiments used ChoX, a choline PBP from *Sinorhizobium meliloti*. However, these constructs responded to ligands in solution with a time constant of  $\tau > 100$  s and were also poorly expressed in mammalian cells. We ceased systematic development of ChoX-based constructs. Later experiments used OpuBC from *T. spX513*, as described in the text and in Fig. 2. The reported values were measured in *Escherichia coli* cell lysates; values for key constructs were later verified with samples of the purified proteins. (B) Final stages in protein engineering of iNicSnFR constructs. For constructs denoted by black or white symbols,  $\Delta F/F_0$  at  $>1$   $\mu\text{M}$  nicotine was extrapolated from measurements on bacterial lysates as  $[\Delta F/F_{\text{max}}]/EC_{50}$ . . . . . 58
- 2.13 Photoswitching (bleaching) is noticeable at high [nicotine] with focused laser illumination. (A) Photoswitching (bleaching) increases at the highest illumination intensities and at higher [nicotine]. HeLa cells transfected with iNicSnFR3a\_PM. Imaging at 1 and 30  $\mu\text{M}$  nicotine, with 100% and 10% laser intensity (top and bottom, respectively). At 30  $\mu\text{M}$  nicotine, photoswitching reduced the steady-state  $\Delta F$  to 45 versus 71% of the peak  $\Delta F$  for 100% and 10% laser intensity, respectively. The steady-state ratio,  $\Delta F(30 \mu\text{M})$  to  $\Delta F(1 \mu\text{M})$  was 4.92 versus 11.2 for 100% and 10%, respectively, indicating that high intensities artifactually shifted the dose–response relation ([nicotine] vs.  $\Delta F$ ) to lower [nicotine]. . . . . 60
- 2.14 Responses to nicotine with iNicSnFR\_ER in SH-SY5Y cells and HEK293 cells. (A and B) iNicSnFR\_ER was transfected and imaged in SH-SY5Y (A) and HEK293 cells (B). Nicotine pulses were applied for 20 s at 40-s intervals. The nicotine concentration was stepped from 256  $\mu\text{M}$  to 250 nM and then from 250 nM to 256  $\mu\text{M}$  in 4 $\times$  concentration steps in HBSS. The mean of three cells is given as a solid black line, and the SEM is given as gray bounds. . . . . 61

- 2.15 Human iPSCs, differentiated to dopaminergic neurons, transduced with AAV\_iNicSnFR3b\_ER. This figure accompanies the video of a descending, then ascending, series of nicotine concentrations at fivefold steps between 0.2 and 125  $\mu\text{M}$ . Concentrations and washes (“0  $\mu\text{M}$ ”) are marked on the video. (A) The image shows a single frame taken at 25  $\mu\text{M}$  nicotine, indicating three cells (dim, moderate, and bright). (B) Plots of the average absolute intensity of these images (log scale), without correction for sloping baseline or conversion to  $\Delta F/F_0$ . Note that in the descending phase, the responses begin more quickly and, at the lower [nicotine], show an initial transient. This is an artifactual result when solutions in a pH-regulated reservoir are allowed to remain in gaspermeable intermediate tubing, allowing  $\text{CO}_2$  to escape and rendering the solutions slightly more basic (see Materials and methods). The second application of each solution utilizes solution that has recently moved from the larger reservoir; the transients no longer appear. . . . . 62
- 2.16 Varenicline at iNicSnFR3a expressed in HeLa cells. (A and C) Dose–response relations for varenicline-induced  $\Delta F/F_0$ . Mean  $\pm$  SEM; three measurements. (B and D) Dose–response plots for  $\Delta F/F_0$  at each response in A and C, against [varenicline]. Single-component Hill equation fit, including zero response at zero [varenicline]. Parameter values are shown. . . . . 63
- 3.1 iS-methadoneSnFR in primary culture and human biofluids. . . . . 75
- 3.2 Biosensing Scheme for iS-methadoneSnFR. (a) Crystal structure of iNicSnFR3a (PDB:7S7T) mutated in silico to iS-methadoneSnFR (mutations shown in orange spheres). All but one putative cation $\pi$  residue in iNicSnFR3a were maintained in iS-methadoneSnFR’s binding pocket (critical residues Y65, Y357, and Y460 shown as yellow spheres). (b) Biosensor mechanism: in the unbound state, GFP’s chromophore has a poor environment for fluorescence. The PBP binds S-methadone with a “Venus fly trap” conformational change, increasing the brightness of the GFP chromophore. . . . . 77

- 3.3 Improving Sensitivity and Selectivity Toward iS-methadoneSnFR. (a) Directed evolution strategy. (b) Fluorescence responses to S-methadone. iNicSnFR3a (black) has several variants (faded curves), of which one has markedly better sensitivity, owing to the N11E mutation (blue). This lead was evolved to iS-methadoneSnFR (red), which included reoptimization at position 11. Only the final biosensor had sufficient sensitivity at 1  $\mu\text{M}$  (vertical black line; the relevant maintenance concentration). (c) Shift in selectivity from iNicSnFR3a (black) to iS-methadoneSnFR (red) measured by S-slope (see text). Note the scale change at the axis break. . . . . 79
- 3.4 Selectivity and biophysical properties of iS-methadoneSnFR. (a) iS-methadoneSnFR vs endogenous neurotransmitters and choline. Responses to ACh and choline had S-slopes  $< 0.1 \mu\text{M}^{-1}$ . (b) iS-methadoneSnFR vs other clinically used opioids. The response to R-methadone was near zero at  $\sim 1 \mu\text{M}$ . Weak or no responses were observed for other drugs tested. EDDP is 2-ethylidene-1,5-dimethyl-3,3-diphenylpyrrolidine, the major metabolite of methadone. (c) Isothermal titration calorimetry of purified iS-methadoneSnFR. Thirty  $\mu\text{M}$  of the biosensor was mixed with 2  $\mu\text{L}$  injections of 300  $\mu\text{M}$  S-methadone. (d) Stopped-flow kinetic measurements with racemic methadone. . . . . 82
- 3.5 Structural Basis of S-methadone Recognition. (a) PDB:7S7T(iNicSnFR3a, varenicline bound) showing cation- $\pi$  interactions with Y65 and Y357. S-methadone was docked into 7S7T. (b) Fluorescence dose-response relations of cation- $\pi$  residue Leu mutants. (c) Aromatic side-chain screen through critical positions identified in (b) with resulting S-slope. Note the break in y-axis. . . . . 83
- 3.6 iS-methadoneSnFR dose-response relation in biofluids. 1:1 mixture of drug:biosensor in 3 $\times$  PBS pH 7.4 with either human sweat or human saliva and 1:3 mixture with mouse serum (no pH adjustment of any biofluid). . . . . 83

- 3.7 Spinning disk confocal imaging of HeLa cells transfected with (a) iS-methadoneSnFR\_PM, (b) \_ER, and (c) \_Golgi (470 nm excitation, 535 nm emission, 100× 1.4 NA objective). Scale bar = 10 μm. (d) S-slope plotted for each organelle response at 0–250 nM S-methadone. Points are average responses to a 1 min pulse of [S-methadone]. PM n = 11 cells; ER n = 10; Golgi n = 11. . . . . 84
- 3.8 Chiral resolution of racemic methadone. . . . . 86
- 3.9 Dose-response relations for previously developed biosensor variants against Rmethadone and S-methadone. Top left: nicotinic biosensors originally developed for iNicSnFR and iAChSnFRcampaigns1,11. Top right: nicotinic-null biosensors originally developed for iSKet-SnFR (ketamine biosensor) campaigns12. Table: Hill fit parameters for every biosensor-methadone enantiomer pair dose response. iNicSnFR3b displayed the greatest S-slope for both S-methadone and R-methadone while preserving dynamic range of  $\Delta F_{\max}/F_0 > 10$ . . . . 87
- 3.10 Evolution tree from iNicSnFR3a to iS-methadoneSnFR. Residue nomenclature: first and second residues before the position number are the amino acids in the OpuBC homologue from Thermoanaerobacter sp X513 and iNicSnFR3b, respectively. Functional role of the residue is noted. Each arrow and box pair represents a single residue site-saturation experiment. Red outlined boxes indicate positions that yielded only variants inferior to the parent. Blue outlined boxes indicate residues that yielded variants with modest improvements, typically 10-20% increases in S-slope. Green outlined boxes indicate mutations that yielded marked improvements accepted for additional mutagenesis rounds or, finally, for iS-methadoneSnFR. . . . 88

- 3.11 Amber suppression unnatural amino acid mutagenesis was used to incorporate the unnatural amino acid (UAA) O-methyltyrosine into positions 12 and 65 in separate constructs. (a) The dose responses for these two mutants are compared to the fully canonical sequence. Substitution at position 12 decreases dynamic range but roughly maintains  $EC_{50}$ ; however, methylation of 65Y sidechain led to a near-null mutant. (b) Mass spectrometry validation of UAA incorporation at position 12: peptide containing the UAA was identified by mass fragments. ‘b’ fragments (blue) are numbered for the fragment length starting from N-terminal end of the peptide. ‘y’ fragments (red) are numbered for the fragment length starting from the C-terminal end of the peptide. The table lists the expected and theoretical mass difference for peptide fragments containing the UAA. (c) Mass spectrometry validation of UAA incorporation at position 65 using the same method in (b). . . . . 90
- 3.12 Interactions between R- and S-methadone at iS-methadoneSnFR. Dose-response relations were measured for S-methadone in the additional presence of five R-methadone concentrations. A model of competitive inhibition with mixed alternative substrates was used to account for R-methadone and Smethadone competitive binding with partial R-methadone agonism. Consistent with the model, R-methadone right-shifted the [S-methadone] concentration-response relation but did not significantly affect the maximum response. . . . . 91
- 3.13 Kinetics of iS-methadoneSnFR’s Response. (a) 1 s stopped-flow data. Racemic methadone was mixed with purified iSmethadoneSnFR in a chamber while monitoring fluorescence. Concentrations listed are twice the final [Smethadone]. (b) The mean response for the final 10 ms of the relaxation [methadone] was fitted to the Hill equation. The  $EC_{50}$  of 8.2  $\mu\text{M}$  is ~double that of the fluorescence dose-response  $EC_{50}$  measured for Smethadone alone (Fig. 4B). . . . . 91

- 3.14 Effect of pH on the S-methadone dose-response relation. 3x PBS buffers were prepared from pH 5.0 to 7.5 in half-unit increments. Dose-response data were collected in each buffer and plotted. Hill fit parameters and computed S-slope are given in the righthand table. Like other GFP-based biosensors, the iS-methadoneSnFR response decreased at acidic pH. The S-slope remained  $> 1 \mu\text{M}^{-1}$  at pH 6.0, enabling measurements across the Golgi pH range. S-slope at pH 7.5 was 1.7x larger than that at pH 6.8 and 2.6x larger than that at pH 6.3. . . . . 92
- 3.15 Time-resolved dose-response data from imaging experiments for iS-methadoneSnFR targeted to various HeLa cellular compartments. A “stuttered step” perfusion method (1 min S-methadone on, 1 min wash, each dose applied twice) was used to minimize pH effects. Fluorescence images (40x, 1.0 NA, 470 nm excitation) were acquired at 4 Hz. Traces show mean responses (PM n = 11 cells; ER n = 10; Golgi n = 11). Data were smoothed using a 4-point moving average. SEM denoted by faint bands. . . . . 93
- 3.16 Validation in primary hippocampal neurons. (a) Spinning disc confocal imaging of a cultured mouse hippocampal neuron transduced with PHP.eB-hSyn-iS-methadoneSnFR-PM-WPRE (100x, 1.4 NA objective; 488 nm excitation, 535 nm emission. Scale bar = 10  $\mu\text{m}$ .) (b) Responses to pulses of S-methadone (2 min drug application followed by 2 min rinse). iS-methadoneSnFR detected S-methadone in neuronal cultures across the pharmacologically relevant range (50 nM to 3  $\mu\text{M}$ ). Traces are mean response  $\pm$  SEM (n = 12 neurons, SEM as gray bounds). Smethadone concentration is given above traces (in  $\mu\text{M}$ ). The final 10 s of the S-methadone response was averaged across the cells and the response to vehicle alone (HBSS) was subtracted to measure the doseresponse relation. The Hill fit parameters of the dose-response were  $F_{\text{max}}/F_0 = 1.3 \pm 0.1$ ,  $EC_{50} = 1.01 \pm 0.14 \mu\text{M}$ , and  $n_H = 0.82 \pm 0.06$ . . . . . 94
- 4.1 Graphical abstract. . . . . 110

4.2	Results map from the 2017 single concentration drug–biosensor fluorescence screen. Fluorescence response (as represented by $\Delta F/F_0$ ) for drug–biosensor pairs included in the 2017 screen. Fluorescent response shading from green ( $\Delta F/F_0 \geq 3$ ) to white ( $\Delta F/F_0 = 0$ ), in which stronger hits are represented by darker green, weaker hits by lighter green, and non-hits by white. Drug–biosensor pairs that were not screened are in black. . . . .	113
4.3	Results map from the 2018 single concentration drug–biosensor fluorescence screen. Fluorescence response (as represented by $\Delta F/F_0$ ) for drug–biosensor pairs included in the 2018 single concentration drug–biosensor fluorescence screen. Drugs are grouped by opioid category. Fluorescent response shading from green ( $\Delta F/F_0 \geq 3$ ) to white ( $\Delta F/F_0 = 0$ ), in which stronger hits are represented by darker green, weaker hits by lighter green, and non-hits by white. . . . .	115
4.4	Fluorescence response (as represented by $\Delta F/F_0$ ) for drug–biosensor pairs included in the 2019 single concentration drug–biosensor fluorescence screen. Drugs are grouped by class. Fluorescent response shading from green ( $\Delta F/F_0 \geq 3$ ) to white ( $\Delta F/F_0 = 0$ ), in which stronger hits are represented by darker green, weaker hits by lighter green, and non-hits by white. . . . .	117
6.1	A general strategy to evolve opioid biosensors from cholinergic biosensors. . . . .	132
6.2	iFentanylSnFR evolution, characterization, and application in cells and biofluids. . . . .	137
6.3	Detecting fentanyl in neurons enables real-time dosing in a freely behaving animal. . . . .	140
6.4	Recording [fentanyl] in the VTA alongside behavioral quantified by a machine vision routine. . . . .	144
6.5	The stereotyped fentanyl effect demonstrated in cumulative statistics.	146
6.6	Fentanyl effects on animals foraging for water in a labyrinth maze. . .	150



- 6.7 Evolving the two best hits for increased selectivity, yielding iTapentadolSnFR and iLevorphanolSnFR & application to a reagentless field test. (A) Principal component analysis of the cholinergic biosensor-opioid pair S-Slopes with outlier structures noted for tapentadol, levorphanol, and meptazinol. (B) A single point mutation, W436A, generates iTapentadolSnFR. Hill fit parameters for tapentadol against iTapentadolSnFR are listed. (C) Two point mutations in the 2nd shell residues, QG15T and HA455P generate iLevorphanolSnFR and shift sensitivity to acetylcholine outside the physiological range. Hill fit parameters for levorphanol against iLevorphanolSnFR are listed. (D-F) iTapentadolSnFR characterization. (D) Selectivity against other opioid drugs show no response in their pharmacologically relevant ranges. (E) Isothermal titration calorimetry: 2  $\mu\text{L}$  of 450  $\mu\text{M}$  tapentadol was injected into a cell with 45  $\mu\text{M}$  iTapentadolSnFR at 300 s intervals (raw heat, figure inset). . . . . 153
- 6.8 SI Figure 1 related to Figure 6.1: Raw data for biosensor responses plotted against each opioid ligand. A serial dilution of each opioid was prepared and mixed into a biosensor solution to achieve a final [opioid] ranging from 200  $\mu\text{M}$  to 63.3 nM with a constant [biosensor] of 100 nM. Each dose response is shown as a line graph (color legend identifies biosensor sequence). These dose responses determined the linear range for the regression for each opioid vs. biosensor. The SEM is shown as error bars (n = 3 dose responses averaged). . . . . 160

- 6.9 SI Figure 2 related to Figure 6.2 & 6.3: Raw data and additional characterization of iTapentadolSnFR, iLevorphanolSnFR, and iFentanylSnFR2.0. (A-C): 1 s stopped-flow kinetic data. 200 nM of each biosensor was mixed in equal volume to each ligand in varying concentrations as labeled. The final [opioid] in the chamber was one-half of this value. (F) 1-hour measurement of iFentanylSnFR2.0's response to 1  $\mu$ M fentanyl shows ~90% of the response immediately (~3 s) after mixing followed by a ~4 min equilibration for the remaining ~10% of the signal and then linear bleaching. (D-E): Selectivity against neurotransmitters (iFentanylSnFR2.0's response shown in the main text). (D) iTapentadolSnFR shows no response to any neurotransmitter, including acetylcholine, owing to a mutation in a critical cation- $\pi$  residue, like iFentanylSnFR2.0. (E) iLevorphanolSnFR shows diminished response to acetylcholine with S-Slope < 0.05 and ~zero response at the physiologically relevant concentrations (at ~2  $\mu$ M and below). (G-I): Selectivity against endogenous opioid peptides in fluorescent dose responses. No significant response is observed for [peptide] at the highest tested dose (200  $\mu$ M) or below for any sensor. For all dose responses: SEM shown as error bars (n = 3 dose responses averaged). . . . . 161
- 6.10 SI Figure 3 related to Figure 6.3: iFentanylSnFR2.0 Directed Evolution Tree. . . . . 162

- 6.11 SI Figure 4 related to Figure 6.4 & 6.5. (A-C) iFentanylSnFR2.0 response in primary hippocampal neurons under saturating [fentanyl]. (A) Widefield image of the neurons transduced with iFentanylSnFR2.0 (scale bar = 20 microns). 40x objective, 1.0 NA, 470 nm excitation. (B) The waveform of biosensor response during widefield fluorescence imaging. The HBSS control and then increasing [fentanyl] bath application (2 min on, 2 min washout) was applied. (C) The steady-state response after correcting for the HBSS artifact was fit with the Hill equation (parameters shown). The dynamic range observed in primary cell culture is comparable to that of the acute slice response to 1 micromolar fentanyl bath perfusion. (D-F) Individual traces from the “null” negative control experiment. iFentanylSnFR2.0 W436L (null sensor) was cloned into the same pAAV vector, packaged in AAV9, and injected into same coordinates in the VTA, replicating the protocol used for the functional sensor. Photometry recordings were conducted before and after administration (1 mg/kg fentanyl IP time noted by vertical red line). No appreciable response was observed in response to the IP. . . . . 164
- 6.12 SI Figure 5 related to Figure 6.5 & 6.6: intermediate checks on raw machine vision data. (A) X-Y position heat map (top view) of the animal’s posterior body label. Animals receiving fentanyl show a circling pattern whereas the saline cohort spends most time sitting/grooming in the corners of the arena. (B) X-Z position heat map (side view) of the second to last label on the animal’s tail (“tail\_4,” arrow in inset image of the cage). Animals receiving fentanyl show an elevated tail throughout the cage (i.e., moving around the arena displaying Straub tail). Animals receiving saline show the tail largely lies on the floor, hangs below the mesh, or is pushed up the wall when sitting in a corner. . . . . 165
- 6.13 SI Figure 6 related to Figure 6.5 & 6.6: Cross-correlations of photometry and behavioral measures. . . . . 166

- 6.14 SI Figure 7 related to Figure 6.7. \* (A) Maze with node numbering used for Figure 6.7. \* (B) Right: entropy of the maze navigation for the first  $\frac{1}{4}$  nodes visited in the maze for each animal. \* (C-E) “Intrinsic” negative control experiment—without water deprivation, animals receiving fentanyl still show repetitive navigation in the maze. Mice not deprived of water and given ad. lib. food and water in the home cage during the maze experiment. One group received saline IP and the other group received 1 mg/kg fentanyl IP. (C) Maze occupancy vs absolute time. Representative node navigation plots comparing an animal receiving saline IP (i-Sal-4 in D) vs. an animal receiving 1 mg/kg fentanyl IP (i-Fent-high-3 in E). . . . . 168

## LIST OF TABLES

<i>Number</i>	<i>Page</i>
2.1 Effect of dosing regimen variations on simulated nicotine concentrations in plasma/CSF/ER and on nAChR activation or chaperoning. Results have been averaged over 12 or 16 h. Asterisk (*) denotes 16-h average. The first row (in bold) presents our definition of a standard habit, plotted in Fig. 8. The following five rows show simulations for increasingly “denicotinized” cigarettes. The row presenting a dose of 3 mg might be appropriate for a schizophrenic’s smoking strategy (Miwa et al., 2011). . . . .	54
2.2 Structure and refinement of iNicSnFR1 crystallized with nicotine. . .	64
2.3 Parameters for nicotine and varenicline Matlab/SimBiology models. . .	65
2.4 Supplemental videos. Each video is colored using the “fire” lookup table (blue < red < white). The lookup table is constant across the field and within each video, so that cells with varying levels of iNicSnFRs begin with varying colors. The general procedure is a series of steps in concentration of a single drug (either nicotine or varenicline), separated by control solution. Field of view is 211- $\mu$ M wide. Please begin with Video 1 (nicotine). Its annotation is most complete, and it shows a “descending-increasing” series of nicotine concentrations. Figure S5 is a frame from this movie. . . . .	65
6.1 Check on DeepLabCut pose estimation quality, top view. The percent of frames with acceptable confidence for given keypoints (“Fiber” and “Mid_1”) and frames used in final analysis (“Accounted”) are given for each animal and statistics are given for each cohort. . . . .	169
6.2 Check on DeepLabCut pose estimation quality, side view. The percent of frames with acceptable confidence for the fiber, the tail position, and, final computed tail angle (“Accounted”) are given for each animal and statistics are given for each cohort. . . . .	169

*Chapter 1***INTRODUCTION: CONTINUOUS MONITORING &  
SUBSTANCE ABUSE DISORDER****1.1 Humans as Tool Makers**

Humans are toolmakers, inventing methods to extend the body and mind. There is a ~millennium of advances in body-interfacing technologies dating back to reading glasses in 1289 to present-day interactive technologies and emerging brain-computer interfaces (Ometov et al., 2021).

In the 1930s, Karl Matthens created the prototype of a spectroscopic pulse oximeter (Westhorpe & Ball, 2008). Today, wearable devices with LEDs and miniaturized optics have democratized pulse oximetry. In 1938, Isidor Rabi discovered the phenomena of nuclear magnetic resonance (NMR). In the 1940s to 50s, Felix Bloch, Edward Purcell, and others developed NMR techniques for studying materials (Cohen et al., 1995). Then, the 1970s saw the first commercially produced magnetic resonance imaging machines applied for clinical purposes. In these examples, scientists wrangle phenomena in electromagnetism and weak interactions into lab instrumentation to test physical theories. Then, another group of scientists, often physicist-turned-life scientists, adapt these tools for use in studying living matter. Eventually, a third group, typically biologists and clinicians, refine the hypotheses and perform definitive tests in biology. *Time again, we see this three-part scientific movement: discovery of physical and chemical phenomena, development of instrumentation, and advancement of biology.*

Textbook pictures of anatomy and biochemical pathways have limited explanatory power for the time dependence, emergent properties, and variance in biological systems. These limitations rear their head in the poor “predictive validity” of the tools and frameworks used to advance therapeutic candidates (Scannell et al., 2022). For example, programming cells and tissues to establish arbitrary states remains a challenge. A vexing source of variance in cell therapies is the integration into a tissue context, interaction with secretory factors, and immune tolerance (Bashor et al., 2022). There are emergent phenomena that take place in an organism that may be irreducible or only partly accounted for in a model system. We sorely lack a map of human physiology evolving over time and the tools to produce these maps.

There is still plenty of room at the bottom. Sensors and actuators provide a bridge between these basic science and engineering challenges. Sensors allow us to spy on mechanisms in real-time and provide cues to trigger actuators. Actuators are our “master hands” to control existing systems or build new ones (Feynman, 1959). The life sciences are now approaching mastery in detecting events down to the single molecule level, driven by super-resolution imaging and “next-generation sequencing” on the read-side. Frameworks like optogenetics, acoustic-sensitive materials, and logic-gated and localized chemical reactions shore up the write-side. The challenge remains in miniaturizing the read/write hardware and embedding these tools in a manner compatible with *in vivo* experiments.

## **1.2 The Uniqueness of CNS Disorders**

Multi-spatial level and continuous recordings are useful across the life sciences but most acutely needed in neurobiology. Additionally, the gap between preclinical models and human biology may be largest in phenomena related to the brain and behavior. In *The Human Illnesses*, John Allman and Peter Williamson argue that several disorders of the brain, including mental illnesses and neurodegenerative diseases, are uniquely human in their etiology and presentation (Williamson & Allman, 2011). Specifically, the dysregulation of language and emotional capabilities appears at least only intelligible to us in humans and likely uniquely in humans. Allman brings an evolutionary neurobiological perspective, highlighting the recent evolution of the brain structures implicated in these disorders and an anatomical view, pointing to the cell types like von Economo neurons restricted to animals with the richest apparent emotional lives. The authors connect a etiology involving regions such as the anterior cingulate cortex and von Economo neurons to common functional deficits across the disorders of the brain.

Researchers often rely on postmortem human brain tissue for a window into human CNS disorders. However, phenotyping is necessary at both molecular and behavioral levels, ideally in living humans. The largest study to date of its kind found a divergence in the transcriptomic profiles of living and postmortem tissue samples from individuals with Alzheimer’s disease, Parkinson’s disease, bipolar disorder, and schizophrenia (Liharska et al., 2023). At the behavioral level, there is debate around the necessity of the psychedelic effects of drugs for their antidepressant effects. A recent work found that patients receiving ketamine while under anesthesia did not experience its antidepressant effects unlike their awake counterparts people (Lii et al., 2023). These works are among emerging trends in neuroscience and psychiatry

that motivate the need for ethical, minimally invasive, longitudinal and disease-relevant measurements in humans.

The corollary to this argument is that, if we use animal models in the study of the central nervous system, we ought to design ethologically relevant paradigms. Rodents are a common preclinical model but do not naturally develop neurodegenerative diseases like Alzheimer's disease, nor do they present deficits in language or emotion that have a clear mapping to human cases (that we know of). The emerging field of "neuro AI" provides one program to address neurobiology across species: learn how the brain of a given species is adapted to its environment and goals, determine what extent the model of one species transfers to another, and discover where common structures or divergence exists (Zador et al., 2023). This and other campaigns in neuroscience now demand the measurement of events across cellular to behavioral levels. In turn, new tools for *in situ* measurement and inference methods are required.

### **1.3 Molecular and Behavioral Features of Opioid Use Disorder**

This work largely focuses on opioids use disorder (OUD) for its fundamental relationship to emotional and affective processes and the relevance to human health given the ongoing opioid epidemic. Opioids are naturally occurring, semi-synthetic, and synthetic compounds that modulate opioid receptors. Mammalian  $\mu$ -,  $\kappa$ -, and  $\delta$ - and opioid receptors transduce opioid ligand binding in defined circuits to elicit analgesia and reward (Darcq and Kieffer '18). Opioids have been consumed in one form or another for millennia; however, in the last century, potent synthetic compounds such as fentanyl have been developed that pose significant risks to human health. Synthetic opioids have driven an "opioid epidemic" of OUD and overdose death. OUD is marked by the development of tolerance that drives increasing drug consumption and the risk of uncontrolled consumption (Evans & Cahill, 2016; Williams et al., 2013). Managing OUD is complicated by incomplete knowledge of cellular tolerance mechanisms and variability in individual responses to opioids due to genetic variations, health conditions, and environmental and social factors.

Defining the pharmacokinetics (PK) of opioids at (1) the subcellular level begins to address cellular tolerance, and (2) the whole-body level provides the means to personalize opioid regimens. Subcellular PK determines drug availability for engaging receptors in various biophysical and biochemical stages (Lester et al., 2012). Opioid drugs can act as pharmacological chaperones for their receptors in the



endoplasmic reticulum (Chen & Liu-Chen, 2009; Petäjä-Repo & Lackman, 2014) and elicit G-protein coupled signaling from endosomes and Golgi apparatus (Stoeber et al., 2018). This work describes the first subcellular PK measurements of opioids using genetically encoded biosensors. Furthermore, PK in serum, interstitial fluid, or CSF quantifies the time course of a drug dose experienced by the individual. Currently, opioid PK measurements in humans are rare, infrequent, and laborious.

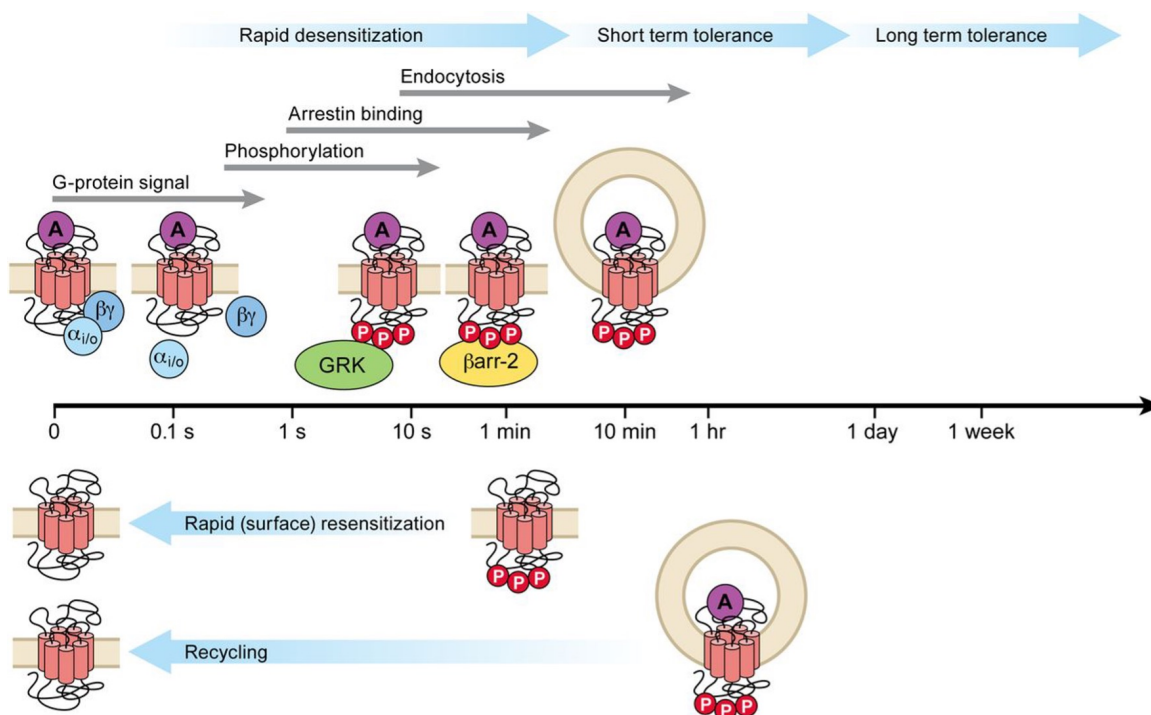


Figure 1.1: Figure from Williams, 2013: time scales for processes in  $\mu$ -opioid receptor signaling, desensitization, and tolerance from experimental studies. Reproduced with permission.

Several minimally invasive technologies exist for continuous analyte monitoring for endogenous analytes, but no suitable opioid-binding moieties exist to provide continuous opioid monitoring. One practical application is the personalization of opioid regimens to achieve the maximum effect for minimal dose. Physicians routinely employ “opioid rotations,” cycling through multiple drugs to find the ideal fit for an individual or to exploit incomplete cross-tolerance (Knotkova et al., 2009). This rotation and the polypharmacy of OUD (e.g., maintenance and relapse) demand biosensors for a variety of opioids with excellent selectivity among those drugs. This work describes the first opioid-binding moieties with sensitivity and selectivity suitable for continuous opioid monitoring.

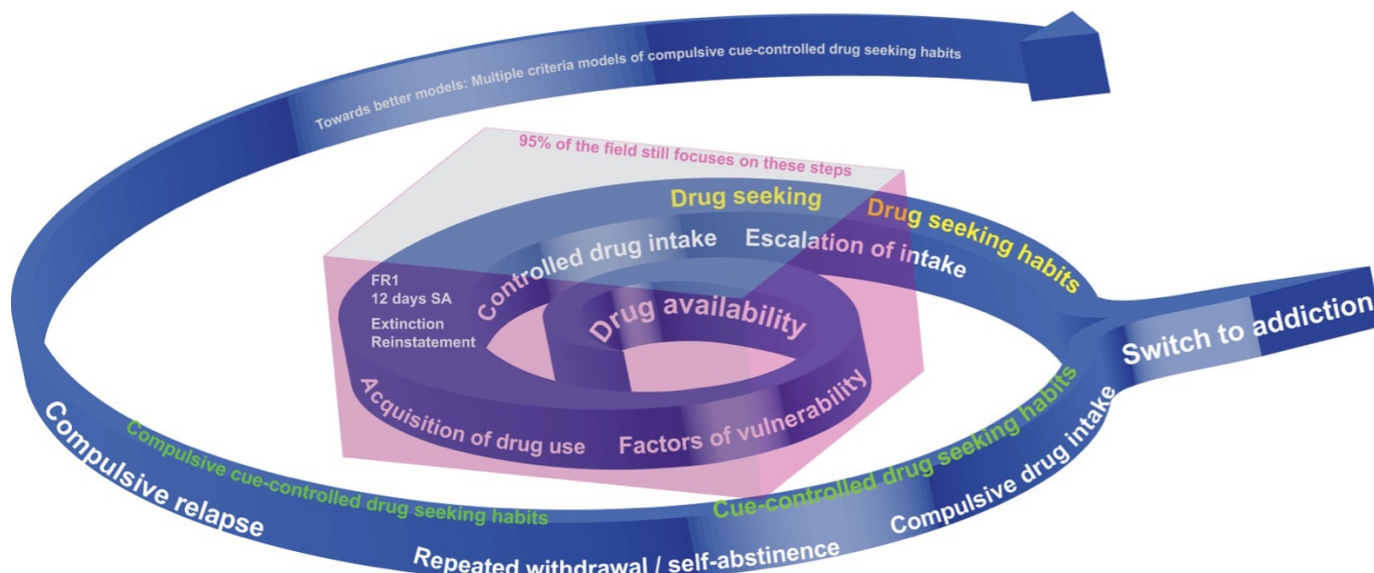


Figure 1.2: Figure from Belin-Rauscent, 2016: the “spiral” of the entire addiction process with a distinct switch between drug seeking and compulsive use and relapse. Reproduced with permission.

A touchstone for this work is the conventional picture of opioid signaling, desensitization, and tolerance (Figure 1.1). Rapid desensitization/endocytosis and resensitization/recycling occur on the ~10 s to ~few min. Notably, short-term tolerance occurs on the ~hour timescale. The view of “ligand bias” in the GPCR field argues that different ligand structures binding to the same orthosteric site can elicit different cellular consequences by biasing the receptor to interact with a particular G-protein or beta-arrestin. In this view, fentanyl has been termed a “beta-arrestin-biased ligand” (De Waal et al., 2020). How these molecular and cellular events dictate behavioral tolerance is unclear. The final chapter in this work addresses this gap by monitoring [fentanyl] in the rodent brain alongside behavior to demonstrate a repetitive behavioral pattern with no acute behavioral tolerance to the first dose of fentanyl (up to 1.0 mg/kg).

A second touchstone for this work is the visualization of the entire addiction process (Figure 1.2). David Belin’s argument is compelling: classical experiments in substance use disorder focus on controlled drug intake and do not consider the requisite events for the “switch” to addiction (Belin et al., 2016). This work presents an ethologically relevant survival task for a normative and quantitative measure of behavioral deficits. The introduction of continuous opioid measurements alongside behavior allow the experimenter to attribute particular deficits to the presence of the drug (as opposed to a withdrawal period, for example).

#### 1.4 The Biosensor-Transduction System Bottleneck in “Reading” Biology *in situ*

*This section appeared in one of A.K.M.’s propositions submitted in June 2023.*

Continuous monitoring measurements are warranted when (a) a biomarker’s concentration changes faster than the time scale needed to sample and analyze using conventional means, (b) there is an interaction between human behavior and the biomarker, or (c) a closed-loop device on a person necessitates the real-time input of [biomarker]. The four areas that exemplify the need for continuous monitoring also align with growing unmet needs in public health:

1. Metabolic health: ~min to ~hour molecular changes with relationships to appetite and exercise. Example markers: glucose, insulin, ketones, LDL/HDL cholesterol, leptin, ghrelin, and GLP-1.
2. Cardiovascular health: ~sec to ~min changes with relationships to locomotor activity and stress. Example markers: blood oxygenation, ECG, troponins, natriuretic peptides, homocysteine, and high-sensitivity C-reactive protein.
3. Hormonal health & fertility: ~hour to ~week physiological changes that underly reproductive health. Example markers: estradiol, progesterone, luteinizing hormone, follicle-stimulating hormone, cortisol, inhibin B, and prolactin.
4. Personalized drug dosing: ~hour to ~day pharmacokinetics (PK), particularly important for keeping a maintenance drug in a concentration window corresponding to the desired physiological state. Example drugs: metformin (diabetes), SSRIs/ketamine (major depressive disorder), methadone (opioid use disorder), varenicline (nicotine use disorder), various analgesics (chronic pain), levothyroxine (hypothyroidism), and various antibiotics like vancomycin that have a highly variable PK across individuals.

Generalizable, scalable, and minimally invasive continuous monitoring represents a transformative technology:

*For basic science:* Prior continuous monitoring studies typically involved a limited number of subjects and short-term cannulation in a lab. Improved scalability and resolution are needed for datasets to develop an atlas of continuous metabolomics.

*For public health:* Wearable devices offer a form factor to make diagnostics more accessible and enable off-site analysis, thereby reducing the marginal costs for healthcare. For example, Michael Snyder’s lab has developed a routine using pulse oximetry to detect pre-symptomatic COVID-19 with real-time, cloud-based analysis and personal alerts (Alavi et al., 2022; Bogu & Snyder, 2021).

*For therapeutic development:* Most R&D dollars are “lost” in phase II failures where target selection and toxicology in a wider human population become evident. Atlases of human physiology can better inform hypothesis testing in target selection and characterize sub-populations prone to adverse events.

However, the form factors of instruments limit large-scale and decentralized human studies. A handful of labs have made do with the few commoditized devices such as pulse oximeters, accelerometers, and continuous glucose monitors (CGMs) (Babu & Snyder, 2023; Hicks et al., 2023; Snyder et al., 2023); however, these measurements alone severely underdetermine physiological states. This work adopts the form factor and design choices of CGMs but generalizes its substrate scope. The fabrication of medical devices — their electronics, microfluidics, wireless communication, etc., are largely a solved problem. This work addresses the properties of ideal sensing-transduction systems that will be

- (a) sensitive within the target’s physiological concentration range,
- (b) selective against both endogenous and exogenous species,
- (c) robust in the mechanism of signal transduction,
- (d) highly multiplexable,
- (e) sufficiently responsive in terms of kinetics, and
- (f) regeneratable with minimal signal drift.

Continuous monitoring techniques accelerate the collection of *in situ* and continuous data. However, the development of these devices is bottlenecked by current biosensing and signal transduction methods (Polat et al., 2022; Smith et al., 2019; Wang et al., 2022). Nature has solved an instance of this problem using allostery in ion channels embedded in neuronal circuits (Galzi & Changeux, 1994), but these channels offer limited substrate scope and are unwieldy for the manufacturing of medical devices. Conformation-switching proteins are readily integrated into devices thanks to nanopores (Fukami-Kobayashi et al., 1999; Li et al., 2020) and offer a programmable substrate scope thanks to recent *in silico* (Praetorius et al., 2023) and directed evolution methods (Beatty et al., 2022; Muthusamy et al., 2022; Nichols et al., 2021).

## 1.5 iOpioidSnFRs and Their Opioids

Genetically encoded biosensors of endogenous ligands have been developed primarily for calcium and neurotransmitters (Marvin & Looger, 2020; Sabatini & Tian, 2020). These biosensors have been engineered to exploit a variety of fluorescent

proteins as reporters (Frommer et al., 2009). The concept of adapting nature's proteins to bind and detect non-natural substances has been established for 20+ years (Korendovych & DeGrado, 2020) along with the circular permutation strategy of modulating GFP fluorescence (Baird et al., 1999); however, advances in laboratory techniques and computational methods in protein engineering have accelerated the development of these molecules. This work begins with the application of a nicotine biosensor based on OpuBC, a naturally occurring choline-binding periplasmic binding protein, evolved to bind nicotine, another cholinergic. Evolution toward nicotinic biosensors yielded a library of biosensors for screening against new drugs. We found some mutants provided broad spectrum detection of neural drugs, representing starting hits for directed evolution. Finally, this work focused detecting a variety of clinically used opioids. We termed these biosensors, intensity-based opioid sensing fluorescent reporters, or “iOpioidSnFRs.”

iOpioidSnFRs were evolved for sufficient sensitivity to detect pharmacologically relevant [opioid] (i.e., opioid concentration). The pharmacologically relevant [opioid] range begins with the minimally effective concentration and spans the analgesic and abuse concentrations. The pharmacologically relevant range for nearly all opioids, and certainly for fentanyl, is below one micromolar. Whereas most biosensor protein evolution projects consider a single analyte, this work has developed several biosensors in parallel for several chemical structures and pharmacological classes. Most importantly, iterative single residue site-saturation mutagenesis appears to yield progressively improved biosensors in all cases tested thus far. The biosensor fitness landscape does not appear to have deep local minima so that OpuBC-cpGFP biosensors may be adapted for several opioid classes in a relatively straightforward directed evolution campaign (Chapter 6).

The four exemplar biosensors detect a set of clinically used analgesics spanning several use cases:

Fentanyl is a highly potent  $\mu$ -opioid agonist with analgesic [fentanyl] found as low as 1-10 nM in serum (FDA 2016). Fentanyl is clinically administered in formulations with varying PK: sublingual tablets, transdermal patches, and a nasal spray. Most opioid overdose deaths today in the United States involve fentanyl (Jannetto et al., 2019). Biosensors of fentanyl may enable more careful titration of fentanyl for each individual and offer a method of monitoring the risks of overdose.

S-methadone is one of the two enantiomers of methadone administered as a racemate for analgesia and opioid maintenance therapy. The pharmacokinetics of methadone

allow quantifying the time course of either R-methadone or S-methadone for therapeutic monitoring (Foster et al., 2000). Personalized monitoring may be increasingly important as prescription over telemedicine becomes more prominent. Beyond managing opioid use disorder, S-methadone has recently garnered attention as a rapidly acting antidepressant (Fogaça et al., 2019). One clinical trial is underway to test S-methadone's efficacy as an antidepressant. The PK underlying the antidepressant effect is uncharacterized, but for maintenance therapy, effective serum [methadone] appears to be in the 100s of nM to 1  $\mu$ M with nearly an order of magnitude variability across individuals (Eap et al., 2002).

Tapentadol, a  $\mu$ -opioid agonist and norepinephrine reuptake inhibitor, is the most recent FDA approval for an opioid with a novel mechanism of action (Langford et al., 2016; Singh et al., 2013). The additive nature of its two mechanisms of action allows for lower effective doses and has opened a route to less addictive opioids (Schröder et al., 2011).

Levorphanol has one of the broadest activities of any clinically used opioid, acting as an agonist of the  $\mu$ -,  $\delta$ -,  $\kappa$ -, and nociception opioid receptors, a selective serotonin/norepinephrine reuptake inhibitor, and an antagonist of NMDA and GABA receptors (Pham et al., 2015). Levorphanol's lack of cross-tolerance for  $\mu$ -OR agonism with respect to prior morphine use (Moulin et al., 1988) and its longer duration of action (~11 h half-life in humans) provide a pharmacokinetic basis for improved treatment of chronic pain (Prommer, 2007).

Most of the other opioids in this work are routinely used in clinical opioid rotation. The varied chemical properties of each of these drugs pose an interest for subcellular pharmacological studies. Furthermore, varying the formulation and regimen of a given opioid can vary its pharmacokinetics and circuit adaptations associated with degrees of maladaptive behaviors and physiological symptoms in animal models (Cahill, 2020). The varied pharmacokinetics due to genetic variation warrants personalized tailoring and tapering regimens to minimize the risks of OUD.

## 1.6 References

- Alavi, A., Bogu, G. K., Wang, M., Rangan, E. S., Brooks, A. W., Wang, Q., Higgs, E., Celli, A., Mishra, T., Metwally, A. A., et al. (2022). Real-time alerting system for covid-19 and other stress events using wearable data. *Nature Medicine*, 28(1), 175–184.
- Babu, M., & Snyder, M. P. (2023). Multi-omics profiling for health. *Molecular & Cellular Proteomics*, 22(6).
- Baird, G. S., Zacharias, D. A., & Tsien, R. Y. (1999). Circular permutation and receptor insertion within green fluorescent proteins. *Proceedings of the National Academy of Sciences*, 96(20), 11241–11246.
- Bashor, C. J., Hilton, I. B., Bandukwala, H., Smith, D. M., & Veisheh, O. (2022). Engineering the next generation of cell-based therapeutics. *Nature Reviews Drug Discovery*, 21(9), 655–675.
- Beatty, Z., Muthusamy, A., Unger, E., Dougherty, D., Tian, L., Looger, L., Shivange, A., Bera, K., Lester, H., & Nichols, A. (2022). Fluorescence screens for identifying central nervous system-acting drug-biosensor pairs for subcellular and supracellular pharmacokinetics. *BIO-PROTOCOL*, 12(22). <https://doi.org/10.21769/BioProtoc.4551>
- Belin, D., Belin-Rauscent, A., Everitt, B. J., & Dalley, J. W. (2016). In search of predictive endophenotypes in addiction: Insights from preclinical research: Vulnerability traits in addiction. *Genes, Brain and Behavior*, 15(1), 74–88. <https://doi.org/10.1111/gbb.12265>
- Bogu, G. K., & Snyder, M. P. (2021). Deep learning-based detection of covid-19 using wearables data. *MedRxiv*, 2021–01.
- Cahill, C. M. (2020). Opioid dose regimen shapes mesolimbic adaptations. *Neuropsychopharmacology*, 45(11), 1777–1778. <https://doi.org/10.1038/s41386-020-0679-y>
- Chen, Y., & Liu-Chen, L.-Y. (2009). Chaperone-like effects of cell-permeant ligands on opioid receptors. *Frontiers in Bioscience (Landmark edition)*, 14, 634.
- Cohen, J. S., Jaroszewski, J. W., Kaplan, O., Ruiz-Cabello, J., & Collier, S. W. (1995). A history of biological applications of nmr spectroscopy. *Progress in Nuclear Magnetic Resonance Spectroscopy*, 28(1), 53–85.
- De Waal, P. W., Shi, J., You, E., Wang, X., Melcher, K., Jiang, Y., Xu, H. E., & Dickson, B. M. (2020). Molecular mechanisms of fentanyl mediated  $\beta$ -arrestin biased signaling. *PLoS Computational Biology*, 16(4), e1007394.
- Eap, C. B., Buclin, T., & Baumann, P. (2002). Interindividual variability of the clinical pharmacokinetics of methadone: Implications for the treatment of opioid dependence. *Clinical Pharmacokinetics*, 41(14), 1153–1193. <https://doi.org/10.2165/00003088-200241140-00003>

- Evans, C. J., & Cahill, C. M. (2016). Neurobiology of opioid dependence in creating addiction vulnerability. *F1000Research*, 5.
- Feynman, R. P. (1959). There's plenty of room at the bottom. *Engineering and science*, 23(5).
- Fogaça, M. V., Fukumoto, K., Franklin, T., Liu, R.-J., Duman, C. H., Vitolo, O. V., & Duman, R. S. (2019). N-methyl-d-aspartate receptor antagonist d-methadone produces rapid, mTORC1-dependent antidepressant effects. *Neuropsychopharmacology*, 44(13), 2230–2238. <https://doi.org/10.1038/s41386-019-0501-x>
- Foster, D. J. R., Somogyi, A. A., Dyer, K. R., White, J. M., & Bochner, F. (2000). Steady-state pharmacokinetics of (r)- and (s)-methadone in methadone maintenance patients: Pharmacokinetics of (r)- and (s)-methadone. *British Journal of Clinical Pharmacology*, 50(5), 427–440. <https://doi.org/10.1046/j.1365-2125.2000.00272.x>
- Frommer, W. B., Davidson, M. W., & Campbell, R. E. (2009). Genetically encoded biosensors based on engineered fluorescent proteins. *Chemical Society Reviews*, 38(10), 2833–2841.
- Fukami-Kobayashi, K., Tateno, Y., & Nishikawa, K. (1999). Domain dislocation: A change of core structure in periplasmic binding proteins in their evolutionary history. *Journal of Molecular Biology*, 286(1), 279–290. <https://doi.org/10.1006/jmbi.1998.2454>
- Galzi, J.-L., & Changeux, J.-P. (1994). Neurotransmitter-gated ion channels as unconventional allosteric proteins. *Current Opinion in Structural Biology*, 4(4), 554–565. [https://doi.org/10.1016/S0959-440X\(94\)90218-6](https://doi.org/10.1016/S0959-440X(94)90218-6)
- Hicks, J. L., Boswell, M. A., Althoff, T., Crum, A. J., Ku, J. P., Landay, J. A., Moya, P. M., Murnane, E. L., Snyder, M. P., King, A. C., et al. (2023). Leveraging mobile technology for public health promotion: A multidisciplinary perspective. *Annual Review of Public Health*, 44, 131–150.
- Jannetto, P. J., Helander, A., Garg, U., Janis, G. C., Goldberger, B., & Ketha, H. (2019). The fentanyl epidemic and evolution of fentanyl analogs in the united states and the european union. *Clinical Chemistry*, 65(2), 242–253.
- Knotkova, H., Fine, P. G., & Portenoy, R. K. (2009). Opioid rotation: The science and the limitations of the equianalgesic dose table. *Journal of Pain and Symptom Management*, 38(3), 426–439.
- Korendovych, I. V., & DeGrado, W. F. (2020). De novo protein design, a retrospective. *Quarterly Reviews of Biophysics*, 53, e3.
- Langford, R. M., Knaggs, R., Farquhar-Smith, P., & Dickenson, A. H. (2016). Is tapentadol different from classical opioids? a review of the evidence. *British Journal of Pain*, 10(4), 217–221. <https://doi.org/10.1177/2049463716657363>



- Lester, H. A., Miwa, J. M., & Srinivasan, R. (2012). Psychiatric drugs bind to classical targets within early exocytotic pathways: Therapeutic effects. *Biological Psychiatry*, 72(11), 907–915.
- Li, X., Lee, K. H., Shorkey, S., Chen, J., & Chen, M. (2020). Different anomeric sugar bound states of maltose binding protein resolved by a cytolysin A nanopore tweezer. *ACS Nano*, 14(2), 1727–1737. <https://doi.org/10.1021/acsnano.9b07385>
- Liharska, L. E., Park, Y. J., Ziafat, K., Wilkins, L., Silk, H., Linares, L. M., Vornholt, E., Sullivan, B., Cohen, V., Kota, P., et al. (2023). A study of gene expression in the living human brain. *medRxiv*, 2023–04.
- Lii, T. R., Smith, A. E., Flohr, J. R., Okada, R. L., Nyongesa, C. A., Cianfichi, L. J., Hack, L. M., Schatzberg, A. F., & Heifets, B. D. (2023). Randomized trial of ketamine masked by surgical anesthesia in depressed patients. *medRxiv*, 2023–04.
- Marvin, J. S., & Looger, L. (2020, June). Genetically encoded biosensors [US Patent 10,684,282].
- Moulin, D. E., Ling, G. S., & Pasternak, G. W. (1988). Unidirectional analgesic cross-tolerance between morphine and levorphanol in the rat. *Pain*, 33(2), 233–239. [https://doi.org/10.1016/0304-3959\(88\)90095-4](https://doi.org/10.1016/0304-3959(88)90095-4)
- Muthusamy, A. K., Kim, C. H., Virgil, S. C., Knox, H. J., Marvin, J. S., Nichols, A. L., Cohen, B. N., Dougherty, D. A., Looger, L. L., & Lester, H. A. (2022). Three mutations convert the selectivity of a protein sensor from nicotinic agonists to S-methadone for use in cells, organelles, and biofluids. *Journal of the American Chemical Society*, 144(19), 8480–8486. <https://doi.org/10.1021/jacs.2c02323>
- Nichols, A. L., Blumenfeld, Z., Fan, C., Luebbert, L., Blom, A. E. M., Cohen, B. N., Marvin, J. S., Borden, P. M., Kim, C. H., Muthusamy, A. K., Shivange, A. V., Knox, H. J., Campello, H. R., Wang, J. H., Dougherty, D. A., Looger, L. L., Gallagher, T., Rees, D. C., & Lester, H. A. (2021, October 4). *Fluorescence activation mechanism and imaging of drug permeation with new sensors for smoking-cessation ligands* (preprint). *Pharmacology and Toxicology*. <https://doi.org/10.1101/2021.10.04.463082>
- Ometov, A., Shubina, V., Klus, L., Skibińska, J., Saafi, S., Pascacio, P., Fluoratoru, L., Gaibor, D. Q., Chukhno, N., Chukhno, O., et al. (2021). A survey on wearable technology: History, state-of-the-art and current challenges. *Computer Networks*, 193, 108074.
- Petäjä-Repo, U. E., & Lackman, J. J. (2014). Targeting opioid receptors with pharmacological chaperones. *Pharmacological Research*, 83, 52–62. <https://doi.org/10.1016/j.phrs.2013.12.001>

- Pham, T. C., Fudin, J., & Raffa, R. B. (2015). Is levorphanol a better option than methadone? *Pain Medicine*, *16*(9), 1673–1679. <https://doi.org/10.1111/pme.12795>
- Polat, E. O., Cetin, M. M., Tabak, A. F., Bilget Güven, E., Uysal, B. Ö., Arsan, T., Kabbani, A., Hamed, H., & Gül, S. B. (2022). Transducer technologies for biosensors and their wearable applications. *Biosensors*, *12*(6), 385.
- Praetorius, F., Leung, P. J. Y., Tessmer, M. H., Broerman, A., Demakis, C., Dishman, A. F., Pillai, A., Idris, A., Juergens, D., Dauparas, J., Li, X., Levine, P. M., Lamb, M., Ballard, R. K., Gerben, S. R., Nguyen, H., Kang, A., Sankaran, B., Bera, A. K., . . . Baker, D. (2023, January). *Design of stimulus-responsive two-state hinge proteins* (preprint). Biophysics. <https://doi.org/10.1101/2023.01.27.525968>
- Prommer, E. (2007). Levorphanol: The forgotten opioid. *Supportive Care in Cancer*, *15*(3), 259–264. <https://doi.org/10.1007/s00520-006-0146-2>
- Sabatini, B. L., & Tian, L. (2020). Imaging neurotransmitter and neuromodulator dynamics in vivo with genetically encoded indicators. *Neuron*, *108*(1), 17–32.
- Scannell, J. W., Bosley, J., Hickman, J. A., Dawson, G. R., Truebel, H., Ferreira, G. S., Richards, D., & Treherne, J. M. (2022). Predictive validity in drug discovery: What it is, why it matters and how to improve it. *Nature Reviews Drug Discovery*, *21*(12), 915–931.
- Schröder, W., Tzschentke, T. M., Terlinden, R., De Vry, J., Jahnel, U., Christoph, T., & Tallarida, R. J. (2011). Synergistic interaction between the two mechanisms of action of tapentadol in analgesia. *Journal of Pharmacology and Experimental Therapeutics*, *337*(1), 312–320. <https://doi.org/10.1124/jpet.110.175042>
- Singh, D., Nag, K., Shetti, A., & Krishnaveni, N. (2013). Tapentadol hydrochloride: A novel analgesic. *Saudi Journal of Anaesthesia*, *7*(3), 322. <https://doi.org/10.4103/1658-354X.115319>
- Smith, L. C., Bremer, P. T., Hwang, C. S., Zhou, B., Ellis, B., Hixon, M. S., & Janda, K. D. (2019). Monoclonal antibodies for combating synthetic opioid intoxication. *Journal of the American Chemical Society*, *141*(26), 10489–10503. <https://doi.org/10.1021/jacs.9b04872>
- Snyder, M., McLaughlin, T., Zahedani, A., Palmisano, S., Saberi, M., Woodward, M., Joselevitz, R., Ruan, J., Romasko, H., Agarwal, S., et al. (2023). Machine learning-based digital health application integrating wearable data and behavioral patterns improves metabolic health.
- Stoeber, M., é, D., Lobingier, B. T., Laeremans, T., Steyaert, J., Schiller, P. W., Manglik, A., & von Zastrow, M. (2018). A genetically encoded biosensor reveals location bias of opioid drug action. *Neuron*, *98*(5), 963–976.

- Wang, M., Yang, Y., Min, J., Song, Y., Tu, J., Mukasa, D., Ye, C., Xu, C., Heflin, N., McCune, J. S., Hsiai, T. K., Li, Z., & Gao, W. (2022). A wearable electrochemical biosensor for the monitoring of metabolites and nutrients. *Nature Biomedical Engineering*, *6*(11), 1225–1235. <https://doi.org/10.1038/s41551-022-00916-z>
- Westhorpe, R., & Ball, C. (2008). The pulse oximeter. *Anaesthesia and Intensive Care*, *36*(6), 767–767.
- Williams, J. T., Ingram, S. L., Henderson, G., Chavkin, C., von Zastrow, M., Schulz, S., Koch, T., Evans, C. J., & Christie, M. J. (2013). Regulation of  $\mu$ -opioid receptors: Desensitization, phosphorylation, internalization, and tolerance. *Pharmacological Reviews*, *65*(1), 223–254.
- Williamson, P., & Allman, J. M. (2011). *The human illnesses: Neuropsychiatric disorders and the nature of the human brain*. Oxford University Press.
- Zador, A., Escola, S., Richards, B., Ölveczky, B., Bengio, Y., Boahen, K., Botvinick, M., Chklovskii, D., Churchland, A., Clopath, C., et al. (2023). Catalyzing next-generation artificial intelligence through neuroai. *Nature Communications*, *14*(1), 1597.

*Chapter 2***iNicSnFR: Determining the Pharmacokinetics of Nicotinic drugs in the Endoplasmic Reticulum Using Biosensors**

Shivange, A. V., Borden, P. M., **Muthusamy, A. K.\***, Nichols, A. L., Bera, K., Bao, H., Bishara, I., Jeon, J., Mulcahy, M. J., Cohen, B., O’Riordan, S. L., Kim, C., Dougherty, D. A., Chapman, E. R., Marvin, J. S., Looger, L. L., & Lester, H. A. (2019). Determining the pharmacokinetics of nicotinic drugs in the endoplasmic reticulum using biosensors. *Journal of General Physiology*, 151(6), 738-757. <https://doi.org/10.1085/jgp.201812201>

\**co-1st author*

**2.1 Abstract**

Nicotine dependence is thought to arise in part because nicotine permeates into the endoplasmic reticulum (ER), where it binds to nicotinic receptors (nAChRs) and begins an “inside-out” pathway that leads to up-regulation of nAChRs on the plasma membrane. However, the dynamics of nicotine entry into the ER are unquantified. Here, we develop a family of genetically encoded fluorescent biosensors for nicotine, termed iNicSnFRs. The iNicSnFRs are fusions between two proteins: a circularly permuted GFP and a periplasmic choline-/betaine-binding protein engineered to bind nicotine. The biosensors iNicSnFR3a and iNicSnFR3b respond to nicotine by increasing fluorescence at  $[\text{nicotine}] < 1 \mu\text{M}$ , the concentration in the plasma and cerebrospinal fluid of a smoker. We target iNicSnFR3 biosensors either to the plasma membrane or to the ER and measure nicotine kinetics in HeLa, SH-SY5Y, N2a, and HEK293 cell lines, as well as mouse hippocampal neurons and human stem cell–derived dopaminergic neurons. In all cell types, we find that nicotine equilibrates in the ER within 10 s (possibly within 1 s) of extracellular application and leaves as rapidly after removal from the extracellular solution. The  $[\text{nicotine}]$  in the ER is within twofold of the extracellular value. We use these data to run combined pharmacokinetic and pharmacodynamic simulations of human smoking. In the ER, the inside-out pathway begins when nicotine becomes a stabilizing pharmacological chaperone for some nAChR subtypes, even at concentrations as low as  $\sim 10 \text{ nM}$ . Such concentrations would persist during the 12 h of a typical smoker’s day, continually activating the inside-out pathway by  $> 75\%$ . Reducing nicotine intake by 10-

fold decreases activation to ~20%. iNicSnFR3a and iNicSnFR3b also sense the smoking cessation drug varenicline, revealing that varenicline also permeates into the ER within seconds. Our iNicSnFRs enable optical subcellular pharmacokinetics for nicotine and varenicline during an early event in the inside-out pathway.

## 2.2 Introduction

Existing data show that nicotine evokes two processes at neuronal nicotinic acetylcholine (ACh) receptors (nAChRs). Historically, the best-characterized process is activation of nAChRs on the plasma membrane (PM). If one considers events at the scale of a neuron, activation of nAChRs at the PM may be termed the “outside-in” pathway. Like activation by the endogenous neurotransmitter ACh, activation by exogenous nicotine via the outside-in activation pathway involves an influx of Na<sup>+</sup> and Ca<sup>2+</sup> ions, depolarization and therefore increased frequency of neuronal action potentials. The outside-in pathway, and perhaps the subsequent desensitization of nAChRs, leads to the acute effects after nicotine enters the airways either from tobacco combustion (smoking) or from an electronic nicotine delivery system (ENDS; “vaping”). These acute effects, beginning within < 1 min after inhalation and lasting for dozens of minutes include a sense of well-being, a cognitive boost, appetite suppression, increased tolerance of stressful stimuli, and suppression of withdrawal (Miwa et al., 2011; Naudé et al., 2015; Nees, 2015; Picciotto et al., 2015).

Since approximately 2005, evidence has been accumulating for a second process. We term this the “inside-out” pathway, because it begins when nicotine permeates into the ER. In the ER, nicotine binds to nascent nAChRs and becomes a stabilizing pharmacological chaperone for  $\alpha 4$ - and  $\beta 2$ -subunit-containing ( $\alpha 4\beta 2^*$ ) nAChRs, increasing their exit from the ER (Fig. 2.1 A) (Kuryatov et al., 2005; Lester et al., 2009; Sallette et al., 2005). The inside-out pathway leads to up-regulation of nAChRs on the PM. The inside-out pathway results, jointly, from three properties (Fig. 2.1 A). (1) Like ACh, nicotine activates nAChRs (a pharmacological property). (2) In contrast to ACh, nicotine has a neutral, membrane-permeant form (a pharmacokinetic property). (3) In contrast to hydrolysis of ACh within < 1 ms by ACh esterase, catabolic oxidation of nicotine proceeds on a time scale of ~30 min, primarily by cytochrome P450 (another pharmacokinetic property) (Henderson & Lester, 2015; Tanner et al., 2015).

The research community has not yet reported decisive tests for the relative importance of the inside-out and outside-in pathways in nicotine dependence. Several

laboratories are testing the hypothesis that the selective up-regulation of specific nAChR subtypes via the inside-out pathway is necessary and sufficient for some early events (days to weeks) of nicotine dependence (Govind et al., 2009; Henderson & Lester, 2015). Nicotine-induced up-regulation of nAChRs via chaperoning is post-translational, involving neither gene activation nor mRNA stability of nAChR subunits (Henderson & Lester, 2015).

A satisfactory comparison of the outside-in and inside-out pathways during smoking/vaping has been hampered by lack of information about the pharmacokinetics of nicotine at the subcellular scale: How long does it take nicotine to permeate into the ER, and what is its concentration there (Hussmann et al., 2012; Lester et al., 2009; Rollema et al., 2007)? Previous data show that, when nicotine is applied for more than several hours, it up-regulates nAChRs. This up-regulation has an EC<sub>50</sub> of ~30 nM (Kuryatov et al., 2005). It has not been known (1) whether nicotine concentration in the ER reaches the EC<sub>50</sub> for up-regulation; (2) if so, how quickly; and (3) how quickly nicotine leaves the ER.

To approach these questions quantitatively, we have developed a series of genetically encoded intensity-based nicotine-sensing fluorescent reporters (iNicSnFRs). These biosensors comprise a fusion between a bacterial periplasmic-binding protein (PBP) moiety (276 amino acids), a circularly permuted GFP (cpGFP) moiety (244 amino acids), joining regions (“linkers”), and epitope tags. The development of the glutamate biosensor iGluSnFR (Marvin, Borghuis, Tian, Cichon, Harnett, Akerboom, Gordus, Renninger, Chen, Bargmann, et al., 2013b) has provided a model for this study. We report on use of a novel PBP moiety and on mutations that allow the PBP moiety of the biosensor to bind nicotine. We have directed these iNicSnFRs either to the PM (at the start of the outside-in pathway) or to the lumen of the ER (at the start of the inside-out pathway; Fig. 2.1 B). We have also verified the compartmentalization of the iNicSnFRs by showing that the fluorescence response to nicotine contrasts with responses to membrane-impermeant quaternary amines (Fig. 2.1 C).

Smoking cessation has become desirable for individual health and for public health (London, 2016). Varenicline (shown in Fig. 2.1 A), a partial agonist for  $\alpha 4\beta 2$  nAChRs and full agonist for  $\alpha 7$  nAChRs, is now the most effective synthetic drug for smoking cessation. Nonetheless, varenicline therapy succeeds in only a minority of people who aspire to quit smoking (Fagerström & Hughes, 2008). Varenicline also permeates modestly well into the central nervous system (Rollema et al., 2007). Varenicline has a half-life of ~24 h in human plasma (Faessel et al., 2006) and presumably in hu-

man brain. Exposure to varenicline also up-regulates  $\alpha 4\beta 2$  nAChRs (Govind et al., 2017; Marks et al., 2015; Turner et al., 2011), an indication that it too participates in the inside-out pathway. We therefore sought to determine whether varenicline also enters the ER and, if so, how much and how quickly. Serendipitously, an iNicSnFR also binds to and senses varenicline, and we suggest how varenicline's entry into the ER may limit its therapeutic actions.

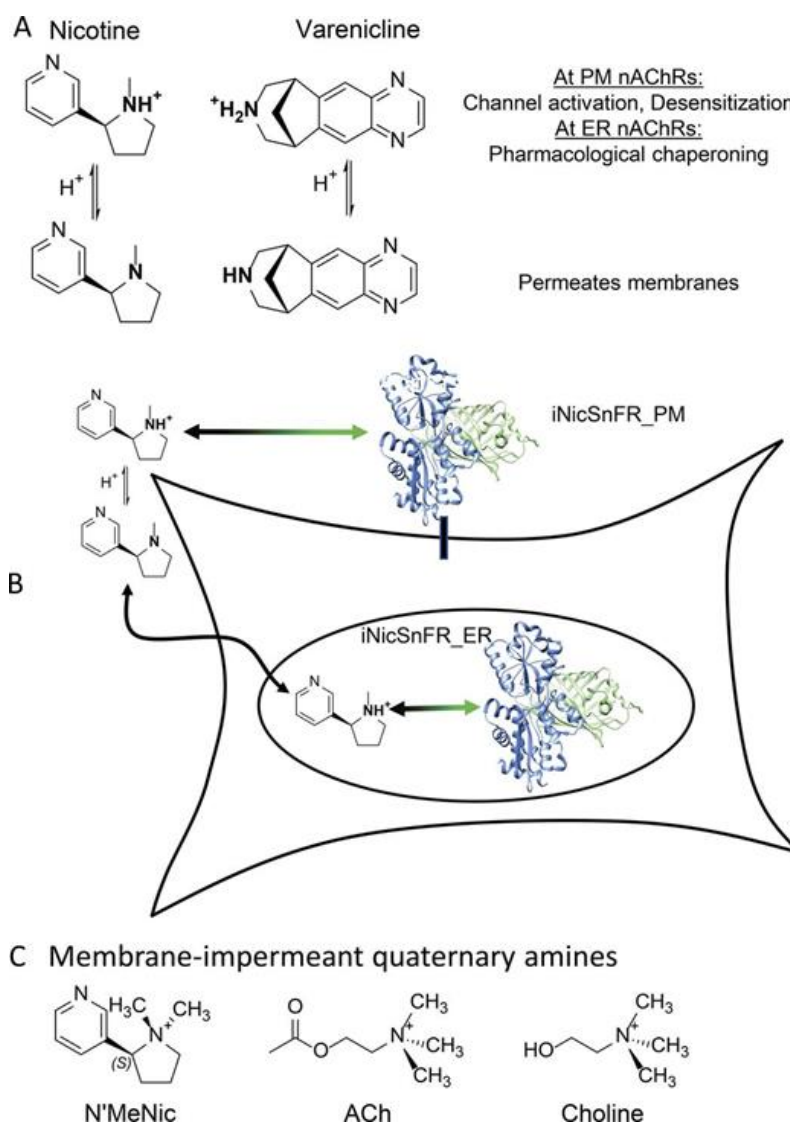


Figure 2.1: Strategy of the experiments. (A) Nicotine ( $pK_a$ , 7.5–8.1) and varenicline ( $pK_a$ , 9.5–10) are weak bases. They interconvert on a millisecond time scale between protonated and deprotonated forms; these are respectively membrane impermeant and permeant. (B) The tactic of confining a genetically encoded fluorescent nicotinic drug sensor to the PM or the ER. (C) Choline, ACh, and N'MeNic exist only as charged, membrane-impermeant forms near physiological pH.

## 2.3 Materials and Methods

### Directed evolution of iNicSnFR proteins using bacterial-expressed protein assays

The Results section, below, begins by describing the overall strategy in constructing the iNicSnFRs. Class F PBPs consist of two domains that move relative to each other when the ligand binds at the interdomain interface (Berntsson et al., 2010). Previous biosensor constructs have placed a cpGFP molecule within the PBP. We constructed and measured ~12,000 mutants iteratively, using fluorescence measurements as described below. We incorporated four additional linker1 residues before the N terminus of the “superfolder” cpGFP gene (Marvin et al., 2018; Pédelacq et al., 2006) and four additional linker-2 residues after the C terminus of the superfolder cpGFP, because this cpGFP variant functions well in the ER (Aronson et al., 2011). We inserted linker1-cpGFP-linker2 at candidate positions within OpuBC sequence at positions near the interdomain interface of the PBP, based on previous structural data cited in Results for choline- and betaine-binding class F PBPs. We optimized linker1 and linker2 with site-saturated mutagenesis (SSM).

The ligand-binding site (originally for choline and/or betaine) lies at the interdomain interface of the PBP. To optimize the ligand site for nicotine, we performed SSM on several residues near the possible cation- $\pi$  residues (first-shell residues that lie within 7 Å of the ligand binding pocket; Fig. 2.11), as well as on “second-shell” residues (residues that showed intraprotein interactions with the first-shell residues). Mutagenesis was performed by slight modifications to the Quikchange mutagenesis protocol (Agilent). Each round of SSM used NN(C/G) oligonucleotides that provided > 96% residue coverage for a collection of 188 randomly chosen clones.

One design goal was a 30% increase in fluorescence ( $\Delta F/F_0 = 0.3$ ) at [nicotine] = 1  $\mu\text{M}$ , a concentration thought to lie in the range of the peak [nicotine] in the plasma and brain of a smoker (Benowitz et al., 1991; Rollema et al., 2010). In preliminary characterization, lysates were tested with excitation at 485 nm and emission at 535 nm. Automated 96-well fluorescence plate readers were used to measure resting and nicotine-induced fluorescence ( $F_0$  and  $\Delta F$ , respectively; Tecan M1000, equipped with monocomators; and Tecan Spark M10, equipped with filters). The beneficial substitutions identified were combined with side-directed mutagenesis (SDM), and the “best” combination in each round of evolution was used as a template for the next round of SSM (Fig. 2.12).



We conducted one or more rounds of SSM experiments at each of the 25 codons shown in Fig. 2.11. In sum, these experiments improved the  $\Delta F/F_0$  at 1  $\mu\text{M}$  nicotine by a factor of 105 (Fig. 2.12). In early experiments on weakly responding constructs, we measured responses to much higher concentrations (up to 10 mM). We extrapolated to responses at 1  $\mu\text{M}$  nicotine, based on the  $EC_{50}$ , on the maximal  $\Delta F$  ( $\Delta F_{\text{max}}$ ) and the observed Hill coefficient of  $\sim 1$ . We used automated liquid-handling devices at several stages of mutagenesis and quantification.

### Measurements on purified iNicSnFRs

Biosensors selected for further study were purified with the His<sub>6</sub> sequence (Fig. 2.11). Proteins were purified by Ni-NTA affinity chromatography as described (Marvin, Borghuis, Tian, Cichon, Harnett, Akerboom, Gordus, Renninger, Chen, Bargmann, et al., 2013b), using PBS, pH 7.4, and elution in an imidazole gradient (10–200 mM). Proteins were concentrated by centrifugation through a 10- or 30-kD cutoff column and by dialysis against PBS. The dialyzed protein was quantified, and 50 or (preferably) 100 nM was used in dose–response studies to characterize responses to various ligands.

We conducted isothermal titration calorimetry experiments with a Malvern Microcal ITC200 instrument. Purified iNicSnFR3a (100  $\mu\text{M}$ ) was titrated with 1 mM nicotine in PBS at 25 °C. Analyses used the Origin software bundled with that instrument.

Proteins purified by size-exclusion chromatography were subjected to high-throughput crystallization trials in the presence of nicotine. Crystals were grown with hanging drop vapor diffusion at room temperature. Promising crystals of iNicSnFR1 were obtained with 15 mg/ml protein, 6 mM nicotine, 50 mM MgCl<sub>2</sub>, 10 mM HEPES, pH 7.5, and 30% vol/vol polyethylene glycol monomethyl ether 550. The diffraction datasets were collected at Stanford Synchrotron Radiation Laboratory. The data were reduced using Mosflm (Powell et al., 2017) and Scala (Evans, 2011). The structure was solved using the CCP4 software suite (Evans, 2011) to carry out molecular replacement using a solved unliganded, open structure of an earlier version of iACh-SnFR construct (Borden et al., 2020). The structure was iteratively rebuilt using Coot (Emsley et al., 2010) and refined using PHENIX. The maximum resolution was 2.4 Å. After refinement (Table 2.2), the electron density for the ligand was incompletely resolved; therefore the molecular docking program SwissDock was used to study protein–ligand interactions (Fig. 2.2 B) and to design further SSM libraries. After we obtained the modeled-liganded, partially closed structure of Fig.

2.2 B, we concentrated on mutating the residues noted; this structural information accelerated progress toward the criterion responses of  $\Delta F/F_0 = 0.3$  at  $[\text{nicotine}] = 1 \mu\text{M}$ .

Spectrally resolved fluorescence measurements of pH dependence (Fig. 2.3, A–C) were conducted with an ISS (Champaign) K2 fluorometer running under MS-DOS. Excitation and emission bandwidths were 2 nm. Data were exported as ASCII files. Dose–response relations for ligands were conducted with the M1000 (Fig. 2.2 C) or Spark 10M (Fig. 2.3, D–H; and Fig. 2.9 A) plate reader. For excitation wavelength ( $\lambda_{\text{ex}}$ ) of 400 nm, an ideal emission filter would have been centered at  $\sim 500$  nm; but none was available, so we measured the  $\sim 2$ -fold lower emission with a filter centered at an emission wavelength ( $\lambda_{\text{em}}$ ) of 535 nm.

Stopped-flow experiments were conducted on an Applied Photophysics SX-18MV instrument at 25 °C. Equal volumes of iNicSnFR3a solution (100 nM) and ligand solution in PBS were mixed, yielding the final nicotine and varenicline concentrations given in Fig. 2.2 D and Fig. 2.9 B, respectively. The samples were excited at 470 nm via a monochromator (9.3 nm slit width), and the emission was collected at 520 nm using a 10-nm band-pass filter. Waveforms were fitted to single exponential waveforms, using Applied Photophysics software.

### **Expression in mammalian cells**

We constructed two variants of the iNicSnFR biosensors for expression in mammalian cells. The constructs were cloned into vectors designed for expression either on the PM (iNicSnFR\_PM) or in the ER (iNicSnFR\_ER). For iNicSnFR3a\_PM and iNicSnFR3b\_PM, we cloned the bacterial constructs into pCMV(MinDis), a variant of pDisplay (Invitrogen) lacking the hemagglutinin tag (Marvin et al., 2013). To generate iNicSnFR3a\_ER and iNicSnFR3b\_ER, we replaced the 14 C-terminal amino acids (QVDEQKLISEEDLN, including the Myc tag; Fig. 2.11, final line) with an ER-retention motif, QTAEKDEL.

We conducted cDNA transfection experiments on iNicSnFR3a\_PM and iNicSnFR3a\_ER expressed in HeLa cells, in SH-SY5Y cell, in HEK293 cells, and in N2a cells. All cell lines were purchased from ATCC and cultured according to ATCC protocols. Chemical transfection was achieved by combining 0.5 or 1  $\mu\text{g}$  of plasmid with 1  $\mu\text{l}$  of Lipofectamine 2000 (1 mg/ml; Invitrogen) in 500  $\mu\text{l}$  OptiMEM (Gibco), incubating at room temperature for 30 min, and adding to dishes with fresh OptiMEM. Cells were incubated in the transfection medium for 24 h and then in

growth media for ~24 h before imaging.

For experiments on cultured mouse hippocampal neurons, an effective expression procedure used adeno-associated viral (AAV2) constructs. As stated in Results, iNicSnFR3a and iNicSnFR3b gave identical  $\Delta F$  in solution experiments and in transfection experiments. After we obtained preliminary data with AAV2/1 constructs for iNicSnFR3b with a synapsin promoter (in this paper, usually abbreviated AAV2\_iNicSnFR3b\_PM and AAV2\_iNicSnFR3b\_ER); we therefore judged that it was an unnecessary expense to generate the analogous iNicSnFR3a AAV constructs. The cells were grown on circular coverslips (1 cm diameter) glued to the bottom of 35-mm culture dishes (MatTek).

### **GFP immunoblot quantitation of biosensor levels**

Transfected HeLa cells were lysed using 50 mM NaCl, 50 mM NaH<sub>2</sub>PO<sub>4</sub>, 2 mM EDTA, 2 mM EGTA, and 2% Triton X-100, pH 7.4 with 40 strokes of a disposable polypropylene pestle and incubated for 3 h at 4°C with agitation to solubilize membrane-bound proteins. The membrane fraction was pelleted via centrifugation (21,130 g for 10 min at 4°C) and the supernatant was isolated. Isolated proteins were incubated at 95°C for 5 min in 1× Laemmli sample buffer and 355 nM  $\beta$ -mercaptoethanol (BioRad). The pH of each sample was adjusted with 1 M Tris base and then alkylated using 100 mM iodoacetamide at 20–25°C for 1 h in the dark. Proteins were separated by SDS-PAGE using a 6–18% bis-Tris gel and transferred to Immun-Blot low fluorescence polyvinylidene fluoride membranes (BioRad). Membranes were blocked using Odyssey Tris-buffered saline (TBS; Li-Cor) for 1 h at room temperature and then incubated with mouse anti-GFP antibodies (2955S; Cell Signaling), diluted 1:1,000 in Odyssey TBS-blocking buffer, supplemented with 0.1% Tween-20 (“antibody buffer”) overnight at 4°C. After washing, the membrane was incubated with anti-mouse secondary antibodies (925-32212; Li-Cor) diluted 1:10,000 in antibody buffer. The blot was washed and visualized using an Odyssey scanner (Li-Cor). Anti-glyceraldehyde-3-phosphate dehydrogenase (GAPDH) antibodies (1:1,000 in antibody buffer; Ab9483; Abcam) were used as a loading control. GAPDH immunoreactivity was visualized with anti-goat secondary antibodies (1:10,000; 926-68074; Li-Cor). Anti-GAPDH primary and secondary antibodies were added concurrently with anti-GFP primary and secondary antibodies. To quantify biosensor levels, a standard curve of purified soluble iNicSnFR3b protein (0.23, 1.15, and 5.76 ng protein, in duplicate) was used in each blot. Data were analyzed using Odyssey application software (version 3.0; Li-Cor).

### **Preparation and transduction of hippocampal neurons**

A pregnant mouse was euthanized at embryonic day 16. The pups were removed from the uterine sac and decapitated before dissection. The hippocampi from several pups were combined and digested in 50 units of papain for 15 min. After DNase treatment, cells were triturated in Hanks balanced salt solution (HBSS; ThermoFisher; GIBCO) with 5% equine serum and spun down through a 4% BSA solution. The pellet was resuspended in plating medium, and the cells were plated onto glass bottom 35-mm imaging dishes (MatTek) coated with poly-d-lysine, poly-l-ornithine, and laminin. After 1 h, the cells were flooded with 3 mL of culture medium, and half of the culture medium was changed every 3 d. At 3 d *in vitro*, the cells were infected with AAV2\_iNicSnFR3b\_PM or AAV2\_iNicSnFR3b\_ER at a multiplicity of infection of 100,000 or 50,000, respectively.

### **Expression in dopaminergic neurons differentiated from human induced pluripotent stem cells (iPSCs)**

Fujifilm CDI (formerly named Cellular Dynamics International; CDI) furnished iCell DopaNeurons. These are human dopaminergic neurons differentiated from iPSCs. The supplier has measured that 89% of the cells are positive for tyrosine hydroxylase (TH) by fluorescence-activated cell sorting. The iCell DopaNeurons were maintained in 95% BrainPhys Neuronal medium (StemCell Technologies), 2% iCell Neural Supplement B (CDI), 1% iCell Nervous System Supplement (CDI), 0.1% of 1 mg/ml laminin (Sigma), and 1% N-2 Supplement 100× (ThermoFisher) and supplemented with penicillin and streptomycin. iCell DopaNeurons were maintained on dishes for 17–24 d before imaging. Glass bottoms of the 35-mm imaging dishes (MatTek) were coated with ~0.07% poly(ethyleneimine) solution and incubated at 37°C for 1 h. Dishes were rinsed with PBS, then rinsed with water and air dried overnight. Glass bottoms were then coated with 80 µg/ml laminin solution for 30 min at 37°C before cells were plated. We confirmed that ≥ 40% of the cells stained for TH by immunocytochemistry using a previously described assay (Srinivasan et al., 2016).

iCell DopaNeurons were transfected after either 13 or 21 d in culture using the Viafect kit (E4981; Promega) at 4:1 transfection reagent (µl) to DNA (µg) ratio. The transfection mixture was prepared in 100 µl OptiMEM (ThermoFisher), containing 4 µL of Viafect transfection reagent and 1 µg of either iNicSnFr3a\_ER or iNicSnFr3b\_PM cDNA. The mixture was incubated for 10–15 min and then added directly to fresh maintenance medium in the culture dish. Transfection medium was

removed after 24 h, and cells were incubated for 48–72 h further before imaging.

iCell DopaNeurons were transduced with AAV2\_iNicSnFr3b\_ER virus particles after 7 d in culture. 1  $\mu$ l of the stock ( $2 \times 10^{12}$  genome copies/ml) was mixed with 100  $\mu$ l of maintenance medium, and then the mixture was added to 2 ml of maintenance medium in the culture dish. Cells were studied after 24 d in culture.

### **Time-resolved fluorescence measurements in live mammalian cells**

Experiments have been conducted at room temperature with four inverted microscope systems; each produced useful fluorescence increases when nicotine or varenicline was perfused into the chamber. Early experiments used a Zeiss 510 spectrally resolved laser-scanning confocal microscope, previously used for other biosensors that use cpGFP moieties. This group includes the GCaMP sensors and iGluSnFR (Marvin, Borghuis, Tian, Cichon, Harnett, Akerboom, Gordus, Renninger, Chen, Bargmann, et al., 2013a). We find that signals with the iNicSnFR constructs have brightness and dynamic range similar to those of the previous cpGFP-based biosensors.

Most datasets were taken on an Olympus IX-81 microscope, in wide-field epifluorescence mode. Images were acquired at 3–4 fps with a back-illuminated EM charge-coupled device camera (iXon DU-897; Andor Technology) (Pantoja et al., 2009), controlled by Andor IQ2 software. Initial experiments used excitation by the 488-nm line of an argon laser (IMA101040ALS; Melles Griot) (Richards et al., 2011); however, this produced speckles and also excessive bleaching when the iNicSnFR was activated by ligands (Fig. S3). Therefore, we installed a considerably weaker incoherent light source: a light-emitting diode (LED). Although a peak at  $\sim$ 485 nm would have been optimal, the closest available LED had peak emission at 470 nm (LZ1-10DB00; LED Engin). We used a 40-nm band-pass filter, centered at 470 nm (ET 470/40X; Chroma Technology), at currents of 40–800 mA. The epifluorescence cube was previously described (Srinivasan et al., 2011). We obtained useful signals with 20 $\times$  (numerical aperture [NA] 0.4), 40 $\times$  (NA 1.0; oil), 63 $\times$ , and 100 $\times$  (NA 1.45) lenses. The 40 $\times$  lens proved most convenient for imaging several adjacent cells and was relatively insensitive to modest drift of the focus. For HeLa cells, the PM-directed constructs were measured with a region of interest (ROI) that included only the cell periphery.

Solutions were delivered from elevated reservoirs by gravity flow, through solenoid valves (Automate Scientific), then through tubing fed into a manifold at a rate of 1–2

mL/min. Experiments were performed with HBSS buffer, except that iPSC-derived neurons were studied in PBS plus d-glucose (5.56 mM), MgCl<sub>2</sub> (0.49 mM), MgSO<sub>4</sub> (0.4 mM), KCl (5.33 mM), and CaCl<sub>2</sub> (1.26 mM). The most robust datasets were taken with gas-impermeable fluorinated ethylene propylene-lined Versilon tubing. This minimized loss of CO<sub>2</sub>, which in turn would produce transient pH increases that artifactually increased biosensor fluorescence in the absence of ligand (Fig. 2.15). Culture dishes were placed on a Warner Instruments SA-TS100 adapter that supported a DH-40i perfusion ring. With this arrangement, the stainless steel tubes for the inlet and aspiration were separated by 5 mm. Videos of dye solutions showed that local solution changes proceeded with a time constant of <1 s (California Institute of Technology “Katz” station). As usual in fluorescence imaging experiments, we excluded data from the brightest cells, because these may have fluorescent impurities or aggregates that produce a rapidly bleaching baseline (an example is the black trace in Fig. 2.15). Data analysis procedures included subtraction of blank (extracellular) areas and corrections for baseline drifts.

Experiments with micro-iontophoretic nicotine application (Fig. 2.7) used the following optical and electrophysiological instruments. A Nikon Diaphot 300 wide-field microscope was equipped with an Hg arc lamp (100 W), a 40x (NA 0.33) objective lens, and a fluorescein/GFP epifluorescence cube. Images were acquired with a Hamamatsu Orca 03G camera, controlled by Hamamatsu software. Iontophoretic pipettes were filled with 1 M nicotine HCl, had resistance of ~50 MΩ and were mounted on a micromanipulator. Current was supplied by an Axon Instruments Geneclamp 500, commanded by Axon Instruments pCLAMP software (California Institute of Technology “Erlanger” station).

### **Structured illumination microscopy and confocal fluorescence images**

Cells were cotransfected with cDNA for DsRed2-ER (Srinivasan et al., 2012) and with iNicSnFR3a\_ER or iNicSnFR3a\_PM (0.5 μg of each construct combined with 1 μL of Lipofectamine 2000 was added to the cells in OptiMEM and incubated for 24 h, followed by incubation in growth media for ~24 h). The image in Fig. 2.4 C1 was acquired as Z stacks with a Zeiss ELYRA S.1 microscope, equipped with a 63× NA 1.4 objective lens. GFP illumination was at 488 nm, observed through a 495–550 nm band-pass + 750 nm long-pass filter. DsRed2-ER was illuminated at 561 nm and observed through a 570–620 band-pass + 750 long-pass filter. The structured illumination grating was rotated five times and processed using Zeiss ZEN software to produce the final image.

The image in Fig. 2.4 C2 was acquired with a Zeiss LSM 710 laser-scanning confocal microscope, equipped with a 63x NA 1.4 objective lens. Neither microscope has a perfusion system; solutions were changed with a pipette. Nicotine (15  $\mu$ M nicotine in HBSS) was used to wash and replace the growth medium in the dishes before imaging.

### **Reagents**

(—)–Nicotine salts or free base (>98% purity) were obtained from several suppliers, with no detectable difference in properties. Samples of N'-methylnicotinium (N'MeNic; Fig. 2.1 C) were obtained from two sources, with no detectable difference in properties. A sample was synthesized by M.R. Post (California Institute of Technology), as described (Post et al., 2017), and purified by P.S. Lee (Janelia Research Campus). Other samples were purchased from Toronto Research ((S)-1'-methylnicotinium Iodide; M323280), and purity was verified by NMR by D.P. Walton (California Institute of Technology).

### **Pharmacokinetic and pharmacodynamic simulations**

Simulations of nicotine and varenicline in human subjects were constructed and run in Matlab (2017a and later releases) using the SimBiology App. The detailed parameters of the simulation are given in Table 2.3. The code is available in SimBiology format (.sbproj, which presents the formatting of the diagrams in Fig. 2.8 A and Fig. 2.10 A, and in Systems Biology Markup Language [.xml]. See the ZIP file contained in the Supplemental material).

### **Data analysis software**

Image video files, spectral data, and dose–response data were analyzed further and presented with general purpose software. These programs include ImageJ, Excel (Microsoft), and Origin (OriginLab).

### **Online supplemental material**

Online supplementary information includes text information that amine-containing buffers produce anomalous results and that acidic vesicles are candidates for the “sequestered compartment”; Table 2.2 shows steps in structure and refinement of iNicSnFR1 crystallized with nicotine; Table 2.3 shows parameters for nicotine and varenicline Matlab/SimBiology models; Fig. 2.3 shows sequences of PBP and constructs described in this paper and/or studied in preliminary experiments; Fig. 2.4 shows directed evolution of the iNicSnFR family; Fig. 2.13 shows photoswitching

noticeable at high [nicotine] with focused laser illumination; Fig. 2.14 shows responses to nicotine with iNicSnFR\_ER in SH-SY5Y cells and HEK293 cells; Fig. 2.15 shows human iPSCs, differentiated to dopaminergic neurons, transduced with AAV\_iNicSnFR3b\_ER; and Fig. 2.16 shows varenicline at iNicSnFR3a expressed in HeLa cells. Additional online supplementary information includes a ZIP file containing Matlab SimBiology models for nicotine and varenicline in .sproj and Systems Biology Markup Language (.xml) format. Additional online supplementary files include a guide to the online videos, of which there are nine.

## 2.4 Results

### Development and characterization of iNicSnFRs

We identified and optimized iNicSnFRs in parallel with the research program that produced the genetically encoded ACh biosensor molecule, iAChSnFR (Borden et al., 2020). We had two goals for the optimized iNicSnFRs. (1) We sought  $\geq 30\%$  increase in fluorescence ( $\Delta F/F_0 \geq 0.3$ ) at [nicotine] = 1  $\mu\text{M}$ , a concentration thought to lie at the upper end of the range of the peak [nicotine] in the plasma and brain of a smoker. (2) We sought to achieve this response with a time constant  $< 1$  s.

Many bacterial and archaeal species use the quaternary amines choline, glycine betaine, and proline betaine as osmolytes or energy sources. PBPs (also called substrate-binding proteins; SBPs) from some of these species bind these ligands, then present the ligands to transporters in the inner membrane. Structural studies of ligands bound to PBPs show a feature first noted by (Schiefner et al., 2004): a “box” of four aromatic side chains that participate in cation- $\pi$  interaction(s) with the quaternary amine. This feature was previously noted for nAChRs (Brejc et al., 2001; Morales-Perez et al., 2016; Zhong et al., 1998). Furthermore, a cation- $\pi$  box participates prominently in binding to other Cys-loop and G protein-coupled receptors (GPCRs) for other primary and secondary amine ligands including serotonin, GABA, glycine, and many drugs that mimic those transmitters (Van Arnam et al., 2013). We hypothesized that choline- and/or betaine-binding PBPs could be mutated by experimenters to bind ACh, nicotine, and perhaps other alkaloid (nitrogen containing, weakly basic) drugs. PBPs undergo substantial, well-characterized ligand-induced conformational changes upon binding their target ligand. In SnFRs, cpGFP is inserted into a PBP in such a way that this conformational change is allosterically transduced into rearrangements of the chromophore environment, leading to changes in fluorescence intensity, lifetime, etc. (Marvin, Borghuis, Tian, Cichon, Harnett, Akerboom, Gordus, Renninger, Chen, Bargmann, et al., 2013b).



We reasoned that this strategy would work similarly well with PBPs mutated to bind exogenous molecules, so as to enable families of genetically encoded fluorescent biosensors for drugs (iDrugSnFRs).

In preliminary experiments, we synthesized the genes and expressed in bacterial PBPs of structural Class F (Berntsson et al., 2010), thought to bind choline and/or betaine. Studies included ChoX from *Sinorhizobium meliloti* (Oswald et al., 2008), ProX from *Archaeoglobus fulgidus* (Schiefner et al., 2004), OpuAC from *Lactococcus lactis* (Wolters et al., 2010), OpuCC from *Bacillus subtilis* (Du et al., 2011), and OpuBC from *Bacillus subtilis* (Pittelkow et al., 2011). An OpuBC homologue (possibly a ProX homologue) from the hyperthermophilic bacterial species *Thermoaerobacter sp X513* appears in genomic databases, but was not previously characterized. We first performed isothermal titration calorimetry to detect any binding with the purified proteins. This paper presents experiments with the most promising PBP, the *T. sp X513* OpuBC homologue; we found that betaine, choline, and ACh bind to this protein. We coupled it to cpGFP and optimized its sensitivity to nicotine, as described in Materials and methods and in Fig. 2.1 and Fig. 2.12.

We obtained an x-ray crystallographic structure of an early iNicSnFR, termed iNicSnFR1, in the presence of nicotine at 2.4 Å resolution (Fig. 2.2 A and Table 2.1, deposited as PDB file 6EFR). This construct has an apparent nicotine EC<sub>50</sub> of 250 μM. This is, to date, the only iNicSnFR structure we have obtained in a liganded, closed (or partially closed) conformation. The structure, in common with several other OpuBC-related structures discussed above, reveals the ligand at the interface between two domains of the PBP moiety. Four aromatic side chains, contributed by both lobes, surround the pyrrolidine nitrogen. This resembles the “aromatic box” found in many PBPs that bind quaternary amines, as well as in nAChRs. We also obtained x-ray crystallographic structures of several other constructs in the iNicSnFR series; but in these, the upper domain of the PBP was flexed away from its position in Fig. 2.2 A, and there was no ligand present. Fig. 2.2 B presents our model of the ligand–protein interaction site of iNicSnFR3a and iNicSnFR3b.

During the development of iAChSnFR, for additional assurance that the ligand binds approximately as predicted in Fig. 2.2 B, we mutated several of the putative cation- $\pi$  residues annotated as  $\alpha$  through  $\eta$  noted in Fig. 2.11. The most dramatic elimination of sensitivity occurred at the  $\gamma$  aromatic residue, with the Y357A mutation. In Fig. 2.5 E, presented below, we show that incorporating the equivalent mutation into an iNicSnFR also eliminates nicotine sensitivity.

We used excitation near the absorption peak at 485 nm, and we made emission measurements at wavelengths >510 nm. Fig. 2.2 C shows dose–response relations for  $\Delta F$  induced at iNicSnFR3a by three nicotinic agonists: nicotine, ACh, choline, and cotinine. The  $EC_{50}$  for choline is more than fourfold greater than for nicotine, showing a greater-than-desired sensitivity, but higher than the usual value for choline in brain ( $\sim 10 \mu\text{M}$ ) (Klein et al., 1992). The near-zero  $\Delta F$  values for cotinine are too small for systematic study. The iNicSnFR3a and iNicSnFR3b proteins differ by one amino acid substitution at codon 11 (Asn vs. Glu, respectively; Fig. 2.11) and have no detectable photophysical differences.

The stopped-flow data (Fig. 2.2 D) show that the fluorescence increase reached steady-state with time constants extrapolating to a value of  $k_{\text{off-ext}} = 2.0 \text{ s}^{-1}$  at the lowest [nicotine]. This satisfied the criterion that the kinetics should be substantially complete within 1 s. In other experiments that diluted premixed solutions of 200 nM iNicSnFR3a plus nicotine into PBS, we measured modestly higher values of  $k_{\text{off-dil}} = 3.3 \pm 0.3 \text{ s}^{-1}$ . However, we consider  $k_{\text{off-dil}}$  measurements less satisfactory because the resulting iNicSnFR3a concentrations were just 8 nM, producing small and noisy signals. The isothermal titration calorimetry data (Fig. 2.2 E) also show that nicotine binds to iNicSnFR3a ( $K_d = 10 \pm 2.5 \mu\text{M}$ ). Thus, all the available data indicate a non-cooperative interaction between iNicSnFR3a and nicotine, with a  $K_d$  between 10 and 30  $\mu\text{M}$ , that is complete within  $\sim 1 \text{ s}$ .

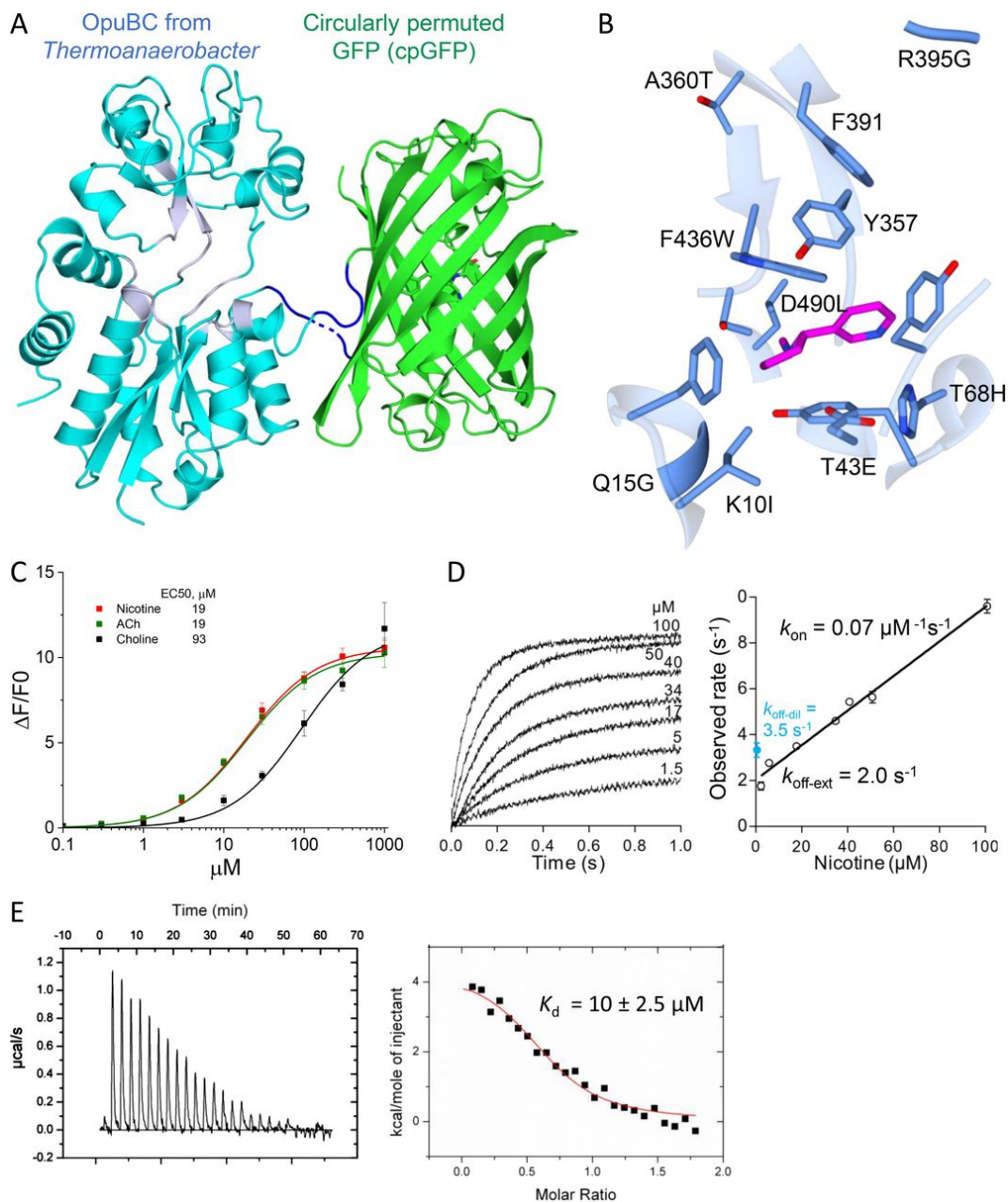


Figure 2.2: The genetically encoded family of biosensors for nicotinic drugs, iNicSnFRs. (A) Cartoon of the x-ray crystallographic structure of iNicSnFR1, crystallized in the presence of nicotine. The structure is available as PDB file 6EFR. The iNicSnFR family are fusion proteins. A superfolder cpGFP (shown in green) has been inserted into the coding sequence of OpuBC, a choline/betaine PBP from *T. spX513*. The linker sequences (shown in dark blue; see Fig. 2.11) were selected for optimal  $\Delta F/F$ . One poorly resolved linker residue, Pro323, is shown as a dashed backbone. The engineered OpuBC is shown in cyan, except that the backbone residues near the incompletely resolved nicotine ligand are shown in gray. The nicotine-binding site lies between the two lobes of the PBP; these move relative to each other.

(B) To generate later iNicSnFRs, the binding site of OpuBC was further engineered by mutagenesis for acceptable sensitivity to nicotine. ~12,000 mutants were screened during the design of iNicSnFR3a and iNicSnFR3b. The image shows redesign of the nicotine-binding site of iNicSnFR1, naming the additional mutations present in iNicSnFR3a and iNicSnFR3b. Portions of the cartoon shown in gray are identical to the gray regions of OpuBC in A. The  $\alpha$ -carbon atoms remain at the positions in the x-ray crystallographic data (PDB file 6EFR), and the conformers of the mutated side chains were selected based on the best-fit rotamer using University of California, San Francisco (San Francisco, CA) Chimera software. The pyrrolidine group of nicotine is at left, seen edge-on; the pyridine group is at right, seen from an acute angle. Also shown is Y357, which remains wild type in all iAChSnFR and iNicSnFR constructs (Fig. 2.11). The Y357A mutation renders all iNicSnFR and iAChSnFR constructs insensitive to the ligand. Also shown is F391, which remains unchanged in all iNicSnFR and iAChSnFR constructs, but differs from the glutamate in OpuBC. (C) Dose–response relations for purified iNicSnFR3a. Data were fitted to a single Hill equation with an assumed Hill coefficient of 1. Data are mean  $\pm$  SEM ( $n \leq 3$ ). (D) Stopped-flow analysis. The rate constant for fluorescence decay,  $k_{\text{off}}$ , was measured most consistently by extrapolation of the  $k_{\text{on}}$  value to zero [nicotine] ( $k_{\text{off-ext}}$ ). The ratio,  $k_{\text{off-ext}}/k_{\text{on}}$ , gives an equilibrium-binding constant  $K_d = 29 \mu\text{M}$ . The blue symbols and label show measurements of  $k_{\text{off}}$  in experiments that diluted an iNicSnFR3a-nicotine solution by 25-fold to [nicotine] values  $< 1 \mu\text{M}$  ( $k_{\text{off-dil}}$ ). (E) Isothermal titration calorimetry for nicotine. The data yield an equilibrium-binding constant  $K_d = 10 \pm 2.5 \mu\text{M}$ , and a stoichiometry of  $0.65 \pm 0.03$  moles of nicotine per mole of protein.

#### *pH dependence of an iNicSnFR*

We based additional photophysical studies on previous data with the GCaMP family. In the inactive conformation of cpGFP, the fluorophore has a  $\text{pK}_a$  of 8–9. At neutral pH, the fluorophore is almost fully protonated, decreasing the absorption in the band centered at  $\lambda_{\text{ex}} \sim 485 \text{ nm}$  (Barnett et al., 2017). In the active form, the  $\text{pK}_a$  is  $\sim 7$ , so that some of the fluorophore molecules are deprotonated. This allows absorption and fluorescence (Barnett et al., 2017). Our pH studies have the additional feature that nicotine itself is a weak base (Fig. 2.1, A and B), as are varenicline and many other neural drugs. One expects both the pH dependence of the biosensor, and that of the ligand, to affect measurements with iNicSnFRs.

We investigated the pH dependence of both ligand-independent and ligand-induced fluorescence ( $F_0$  and  $\Delta F$ , respectively, Fig. 2.3). Throughout the pH range from 5.5 to 9.0, excitation at  $\lambda_{\text{ex}} = 400$  nm produces detectable  $F_0$  at an  $\lambda_{\text{em}}$  of 535 nm, and this is nearly independent of pH (Fig. 2.3, A and B). This agrees with previous data on cpGFP-based biosensors (Barnett et al., 2017). The  $F_0$  values for  $\lambda_{\text{ex}} = 485$  nm show the expected, contrasting strong pH dependence (Barnett et al., 2017):  $F_0$  is approximately inversely proportional to  $[\text{H}^+]$  (Fig. 2.3 C).

We determined the  $\Delta F$  dose–response relations of iNicSnFR3a using excitation at  $\lambda_{\text{ex}} =$  either 400 or 485 nm. At basic pH, we found the most reliable signals at  $\lambda_{\text{ex}} = 485$  nm, where nicotine induces increased fluorescence ( $\Delta F > 0$ ; Fig. 2.3 E). The  $\Delta F_{\text{max}}$  decreases with increasing pH. Thus,  $\Delta F_{\text{max}}/F_0$  at pH 7.5 is 14.5; but at pH 9.0,  $\Delta F_{\text{max}}/F_0$  is only 3.5. This analysis is summarized by plotting both  $F_0$  and  $F_0 + \Delta F_{\text{max}}$  in the measured range (Fig. 2.3 G). The pH dependence of the  $F_0$  measurements is consistent with those measured more precisely in a spectrofluorometer (Fig. 2.3 C). The pH dependence of the fully saturated biosensor ( $F_0 + \Delta F_{\text{max}}$ ) resembles that for the fully saturated GCaMP sensors (Barnett et al., 2017), reaching a plateau under basic conditions; however, the apparent  $\text{pK}_a$  of iNicSnFR3a may be shifted to the right by  $\sim 0.5$  pH units from that for GCaMP6m (Barnett et al., 2017).

At acidic conditions for  $\lambda_{\text{ex}} = 485$  nm, nicotine evokes little or no  $\Delta F$ ; we therefore excited at  $\lambda_{\text{ex}} = 400$  nm and measured the nicotine-induced fluorescence decrease ( $\Delta F < 0$ ; Fig. 2.3 H). At pH = 7.5 and 8.0, where the two measurement modes both have adequate signals, the two modes yield good agreement in  $\text{EC}_{50}$  values (Fig. 2.3 I), consistent with the idea that the two modes are measuring the same nicotine-iNicSnFR binding. Nicotine exhibits a  $\sim 20$ -fold decrease in  $\text{EC}_{50}$  as the pH is increased from 6.0 to 9.0 (Fig. 2.3 I). Both this pH dependence of the response to nicotine and the large pH dependence of  $F_0$  are complicating factors in our live-cell experiments.

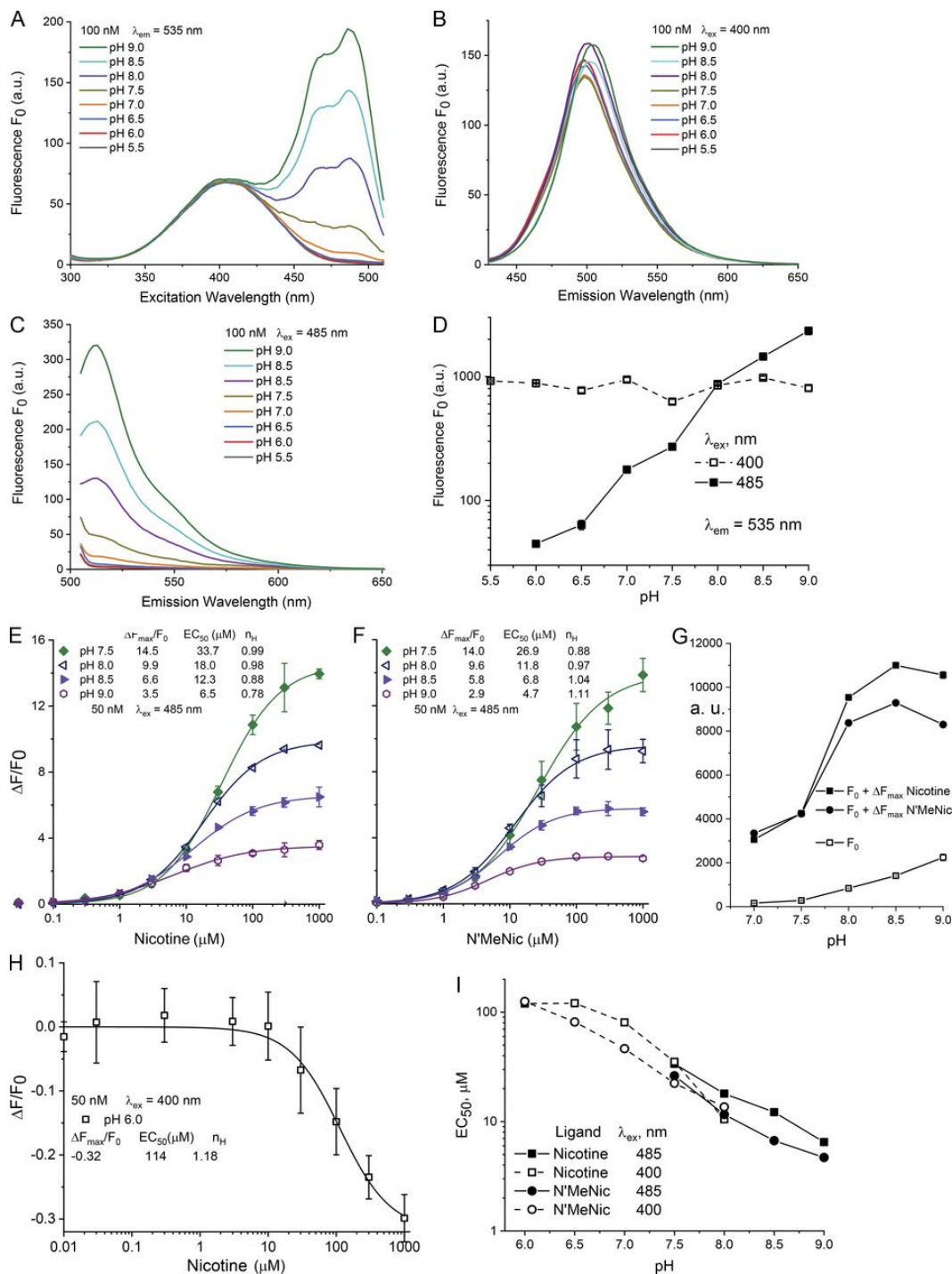


Figure 2.3: The pH dependence of purified iNicSnFR3a in solution, over the range pH 5.5–9.0, at 25°C. Measurements were performed in 3× PBS, adjusted to nominal pH within 0.1 pH unit. (A–C) Measurements in a spectrofluorometer (see Materials and Methods). 100 nM protein. Fluorescence is measured in the absence of ligand and termed  $F_0$ . (A) Excitation spectra at various pH values, measured at a  $\lambda_{em}$  of 535 nm. (B) Emission spectrum at a  $\lambda_{ex}$  of 400 nm. Note that  $F_0$  depends to only a limited extent on the pH. (C) Emission spectrum at  $\lambda_{ex} = 485$  nm. Note the strong dependence on pH.

(D–H) Measurements in a 96-well plate reader, bandwidth 20 nm for excitation and 25 nm for emission; 50 nM protein, 25°C. (D) Data analogous to those of B and C. pH dependence of  $F_0$ , with  $\lambda_{\text{ex}} = 400$  nm (open symbols) or 485 nm (closed symbols). Arbitrary units on the y axis (log scale; 30–3,000 arbitrary units; a.u.) differ from those taken with the instrument of A–C. Values for SEM are smaller than the size of the symbols. (E and F) Fluorescence dose–response relations for nicotine (E) and for N’MeNic (F). Excitation at 485 nm, at varying pH between 7.5 and 9.0. The data have been fitted to a single Hill equation, with parameters given in the legend. Error bars give SEM. Uncertainties for the  $\Delta F_{\text{max}}/F_0$  and  $EC_{50}$  values are <10%, and for the Hill coefficient ( $n_H$ ) value are <0.2. (G) Summary of E and F to show both the unliganded fluoresce ( $F_0$ ) and maximal fluoresce ( $F_0 + \Delta F_{\text{max}}$ ) in the pH range measured. (H) Exemplar dose–response relations from excitation at 400 nm, at pH 6.0. As expected (Barnett et al., 2017), nicotine produces a decrease in fluorescence intensity at 535 nm. The data have been fitted to a single Hill equation, with parameters given in the legend. Error bars give SEM. (I) Comparison of  $EC_{50}$  values for nicotine (squares) versus N’MeNic (circles). Data from experiments like those in B and C. Excitation at 400 and 485 nm are given by the open and closed symbols, respectively. Data were included if they were well fitted by a Hill coefficient between 0.75 and 1.2, if the observed  $\Delta F$  at 1,000  $\mu\text{M}$  ligand reached >85% of the fitted  $\Delta F_{\text{max}}$ , and if the curve-fitting algorithm provided error bounds of  $EC_{50} < 10\%$ .

#### *A special environment in the iNicSnFR3-binding site*

The nicotine derivative N’MeNic (Fig. 2.1 C) has a quaternary ammonium moiety at the pyrrolidine (N’) nitrogen. Like nAChRs (Beene et al., 2002; Post et al., 2017), iNicSnFR3 responds robustly to N’MeNic. Comparing N’MeNic-induced with nicotine-induced  $\Delta F$  over a pH range is expected to reveal further mechanistic details about the ligand–protein interaction, independent of the pH dependence of other regions and/or transitions of the biosensor protein. We consider that systematic errors render the data most reliable for  $\lambda_{\text{ex}} = 400$  nm at  $\text{pH} \leq 7.5$ , and for  $\lambda_{\text{ex}} = 485$  nm at  $\text{pH} \geq 7.5$ . Fig. 2.3 E–G show that iNiCSnFR3a responds similarly to nicotine and to N’MeNic, with respect both to  $EC_{50}$  and to  $\Delta F_{\text{max}}/F_0$ , at basic pH. Fig. 2.3 G shows that the fully liganded state has a similar pH dependence whether the ligand is nicotine or N’MeNic. We found a similar trend under acidic conditions. Fig. 2.3 I shows that, over almost the entire measurable range from pH 6.0 to 9.0, the  $EC_{50}$  value for nicotine is 1.25- to 2-fold higher than that for N’MeNic. The

modestly higher sensitivity to N' MeNic is not surprising, considering that the natural ligand of OpuBC is either choline or betaine, both quaternary compounds. Many nicotine-binding sites, such as those in AChBP and nicotinic receptors, tolerate the differences in charge density among protonated secondary amines (such as cytosine and varenicline), protonated tertiary amines (such as nicotine and ABT-418), and quaternary amines (such as choline and N' MeNic) (Daly, 2005; Van Arnam & Dougherty, 2014).

How do we explain that the  $EC_{50}$  for nicotine remains a small multiple of the N' MeNic  $EC_{50}$  over nearly the entire measurable pH range, even though the concentration of protonated nicotine in free solution decreases for pH values above its  $pK_a$  (7.5–8)? In a straightforward explanation, the binding site of iNicSnFR3, probably including a cation- $\pi$  box, stabilizes diffuse positive charges such as those in quaternary amines and in protonated tertiary amines. Previous pH dependence studies of nAChRs show this phenomenon (Petersson et al., 2002). Regardless of the underlying mechanism, the data suggest that the pH dependence of the cpGFP moiety exerts a stronger effect than the pH dependence of the weakly basic ligand, nicotine.

### **Studies with nicotine in live cells**

#### *iNicSnFR3a\_PM and iNiCSnFR3a\_ER in HeLa cells*

We conducted many of our optical and biochemical experiments in HeLa cells, which have a relatively large, flat appearance and prominent ER. Fig. 2.4 (A and B) shows protein expression of iNicSnFR3a\_PM and iNiCSnFR3a\_ER after transfection in HeLa cells. We performed immunoblotting using an anti-GFP antibody. Observed GFP immunoreactivity for proteins from iNicSnFR3a\_PM- and iNiCSnFR3a\_ER-transfected cells appears near the predicted values of ~68 and ~61 kD, respectively. Importantly, immunoblots demonstrated that the PM targeted biosensor is larger than the ER targeted biosensor, accounted for by the addition of the PM targeting sequence. We found no other bands with GFP immunoreactivity. In experiments conducted at 7–23 h post-transfection, we found that iNicSnFR3a\_PM produced lower levels of protein than iNicSnFR3a\_ER ( $22 \pm 6$  nM/mg protein compared with  $43 \pm 14$  nM/mg protein, respectively). This expression level difference was not significant when we averaged absolute protein levels across the entire dataset (Fig. 2.4 B1), but was consistent and significant when assessed within each paired (same day) set of transfections (Fig. 2.4 B2). No detectable dependence on the time since transfection was observed.



We also imaged the transfected cells with higher-resolution fluorescence microscopy (Fig. 2.4 C). We co-transfected some of these samples with DsRed2-ER to assess localization with the ER. As expected from the included targeted sequences, the iNicSnFR3a\_ER construct showed the expected ER structures typical of HeLa cells, and also colocalized well with DsRed2-ER (Fig. 2.4 C1). The iNicSnFR3a\_PM fluorescence was most intense at the periphery of the cell, as expected for a PM protein (Fig. 2.4 C2).

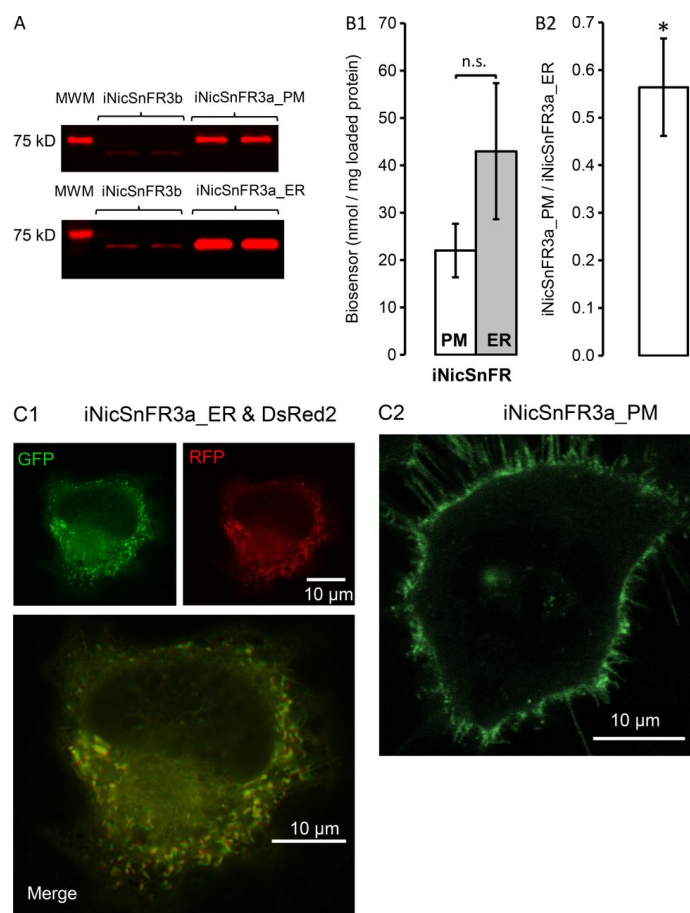


Figure 2.4: Protein levels and subcellular imaging of iNicSnFR3a\_PM and iNicSnFR3a\_ER in HeLa cells. (A) Typical immunoblots with anti-GFP immunoreactivity to lysates (1  $\mu$ g protein) from HeLa cells transfected with either iNicSnFR3a\_PM (top) or iNicSnFR3a\_ER (bottom). In each panel, the leftmost lane is the 75-kD molecular weight marker (MWM). The two middle lanes are duplicate samples of purified, diluted iNicSnFR3b (~61 kD). The two rightmost lands are duplicate samples from the transfected cells. Bands for iNicSnFR3a\_PM appear at ~68 kD (slightly below the MWM), and bands for iNicSnFR3a\_ER appear at ~61 kD (markedly below the MWM and comparable with purified biosensor), confirming the predicted size difference of 7 kD between the two constructs.

(B1) Absolute quantitation of iNicSnFR3a expression, based on GFP immunoblots, from five paired transfections, analyzed 7–23 h after transfection. Data are mean  $\pm$  SEM (two duplicate lanes loaded with 1  $\mu$ g protein per blot; one blot per transfection). Significance was determined using an unpaired Student's t test. \*,  $p \leq 0.05$ ; n.s., not significant. (B2) Ratio of iNicSnFR3a\_PM to iNicSnFR3a\_ER levels, within each set of transfections. The ratio varied from 0.40 to 0.95 with an average of  $0.56 \pm 0.10$ . The bar gives SEM. (C) Typical fluorescence microscopy images from cells co-transfected with iNicSnFR3a and with DsRed2-ER (red channel) and exposed to nicotine (15  $\mu$ M). (C1) iNicSnFR3a\_ER (green channel) and DsRed2-ER (red channel) and merged image. Structured illumination microscopy. (C2) iNicSnFR3a\_PM (only the green channel is shown). Confocal microscopy.

Fig. 2.5 presents a typical time-resolved fluorescence experiment,  $\sim$ 24 h after transfection. For reasons reported in Section 1 above, the time-resolved imaging experiments were performed with illumination near the 485 nm absorption peak (see Materials and methods). Images were gathered at 4 Hz while cells were exposed to 20-s pulses of nicotine at 40-s intervals at fourfold concentration increments between 0.25 and 256  $\mu$ M. Nicotine-induced fluorescence increases are well resolved, even at 0.25  $\mu$ M. We note good reproducibility among cells: the coefficient of variation of  $\Delta F/F_0 < 10\%$  within an experiment. Within a few seconds after the nicotine pulse begins in the extracellular solution, nicotine-induced fluorescence reaches an approximate plateau and changes by  $<10\%$  over the next 20 s (the small increase in Fig. 2.5 was observed in only some experiments). Within a few seconds after [nicotine] is stepped to zero in the external solution,  $\Delta F$  returns to zero. The temporal resolution of these experiments is limited by the speed of the solution change; we detected no difference between the iNicSnFR3a\_PM and iNicSnFR3a\_ER waveforms.

Fig. 2.5 exemplifies an idiosyncrasy of the HeLa cell nicotine-induced fluorescence increases. The dose–response relation at the higher [nicotine] shows less saturation than expected from experiments on purified iNicSnFR3a (Fig. 2.2 C and Fig. 2.3 E). We devoted little attention to this phenomenon, because [nicotine] never exceeds 10  $\mu$ M during smoking or vaping.

#### *iNicSnFR3\_ER detects only membrane-permeant molecules*

A key goal for our experiments is to distinguish ER nicotine ligands from extracellular molecules. Therefore we compared responses to nicotine itself versus two quaternary amines, thought to be membrane-impermeant molecules: N'MeNic and ACh (Fig. 2.5 E). In cells transfected with iNicSnFR3a\_PM, we found comparable

fluorescence increases among the three ligands. In contrast, for cells transfected with iNicSnFR3a\_ER, only nicotine evoked fluorescence increases. In solution, iNicSnFR3a has comparable  $\Delta F$  to nicotine, N'MeNic, and ACh (Fig. 2.2 C and Fig. 2.3, E and F). Therefore it may be concluded that iNicSnFR3a\_ER samples only intracellular molecules. Given the predominant ER localization of iNicSnFR3a\_ER (Fig. 2.4 C1), it may be concluded that this biosensor measures primarily ligands in the ER. We provide, in the section “Studies with varenicline *in vitro* and in live cells” of this paper, evidence that iNicSnFR3a\_ER responds strongly to varenicline, an additional membrane-permeant ligand.

The data of Fig. 2.5, by themselves, cannot rule out the possibility that iNicSnFR3a\_PM samples some intracellular nicotine. We argue against this possibility by noting the images of Fig. 2.4 C2, showing that iNicSnFR3a\_PM fluorescence occurs only on the periphery of the cell. To investigate further, we conducted nicotine exposure experiments on iNicSnFR3a\_PM with a 100 $\times$  objective lens, and we chose ROIs including only the periphery. We found that  $\Delta F/F_0$  measurements had comparable values to those of ROIs that include the entire cell (data not shown). One objection to these “periphery-only” experiments is that some iNicSnFR3a\_PM might remain within endosomes that cannot be distinguished from the PM by light microscopy, as found for some transporters (Chiu et al., 2002; Moss et al., 2009). However such compartments have luminal pH values  $\sim 5.5$ , and intraluminal cpGFP would fail to fluoresce. In summary, there is good evidence that iNicSnFR3a\_PM and iNicSnFR3a\_ER measure the nicotine concentration in the extracellular solution and in the ER, respectively.

Transfection of iNicSnFR3a\_PM and iNicSnFR3a\_ER into two other human clonal cell types, SH-SY5Y (Fig. 2.14 4A) and HEK293 (Fig. 2.14 B) produced similar  $\Delta F$  values in response to nicotine perfusion. We also obtained preliminary data in the only mouse cell line tested, N2a (data not shown).

We also tested whether eliminating a crucial cation- $\pi$  interaction, at the  $\gamma$  amino acid (Fig. 2.11), eliminates nicotine-induced  $\Delta F$ . In experiments on purified iAChSnFR, we found that the F357A mutation abolished sensitivity to ACh. In the present experiments, the equivalent mutation, iNiSnFR3a\_Y357A\_PM, was constructed and tested in HeLa cells. We found no detectable nicotine-induced  $\Delta F$  at concentrations  $\leq 300 \mu\text{M}$  (Fig. 2.5 F). This observation also provides assurance that the nicotine-induced  $\Delta F$  has little or no nonselective component.

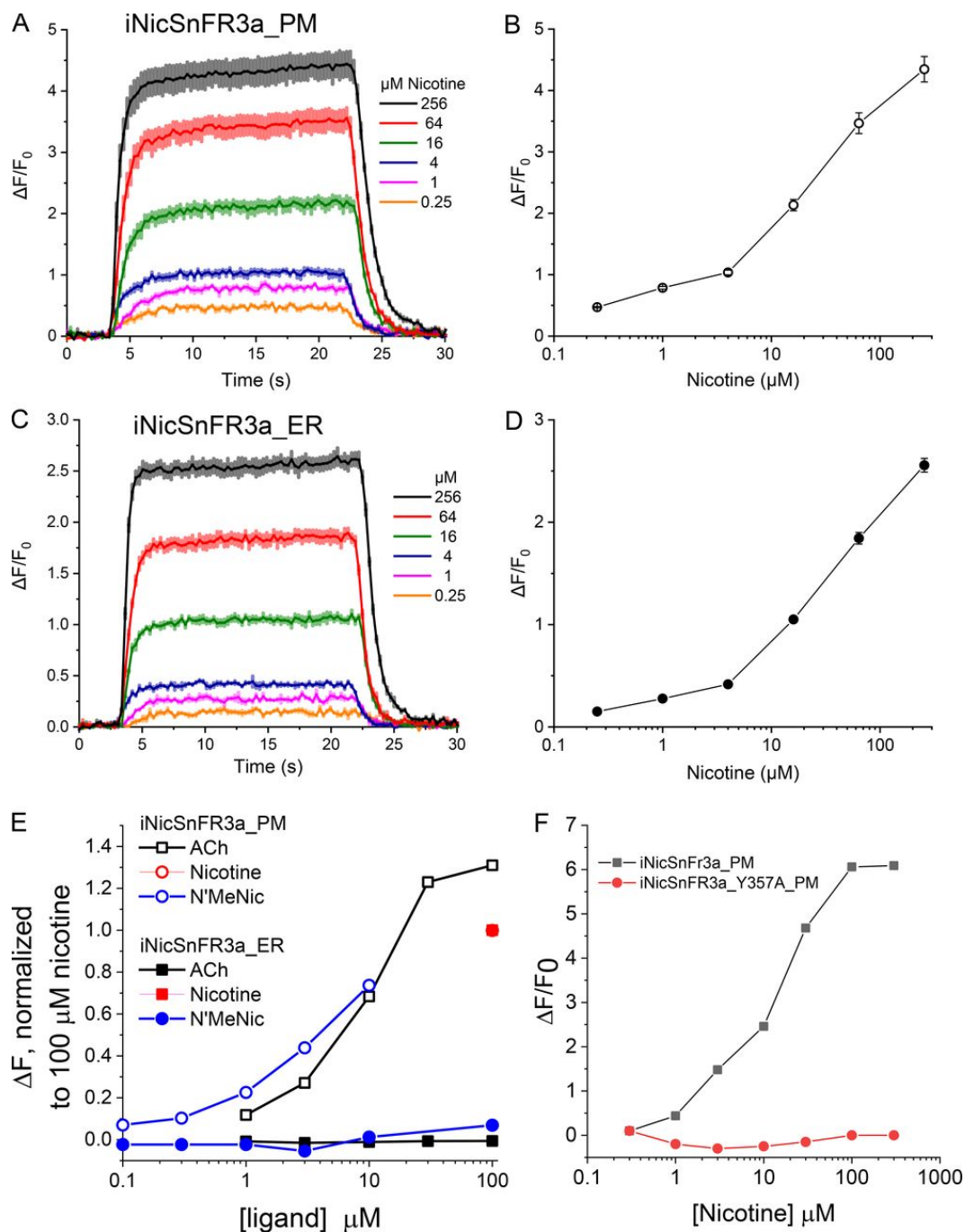


Figure 2.5: Dose–response relations for nicotine-induced  $\Delta F$  in HeLa cells. Exemplar data for iNicSnFR3a\_PM and iNicSnFR3a\_ER expressed in transfected HeLa cells. (A and C) 20-s nicotine dose application followed by 20-s wash in HBSS. The average response for three cells at each dose is overlaid in a 30-s window for the PM and ER traces in A and C, respectively. The SEM is shown as colored bands.

(B and D) The averaged  $\Delta F/F_0$  at each response in A and C, respectively, is plotted against the logarithmic concentration scale with SEM given as error bars. (E) Comparisons among nicotine itself, N' MeNic, and ACh; experiments in transfected HeLa cells. The iNicSnFR3a\_PM responses to ACh and to N' MeNic were normalized to NicSnFR3a\_PM responses for nicotine (100  $\mu$ M). The iNicSnFR3b\_ER responses to ACh and to N' MeNic were normalized to iNicSnFR3b\_ER responses for nicotine (100  $\mu$ M). Note that iNicSnFR3a\_PM responds robustly to all three ligands, but only iNicSnFR3b\_ER responds robustly only to nicotine, the only permeant molecule among the three tested. (F) Mutating a probable cation- $\pi$  interacting residue, Tyr357, eliminates nicotine-induced  $\Delta F$ . Exemplar data from cells transfected in parallel and tested on the same day.

#### *Nicotine enters the ER of neurons*

Fig. 2.6 analyzes fluorescence induced by nicotine at two variants of iNicSnFR3 expressed in neurons. An AAV2 construct yielded basal fluorescence in >50% of cultured mouse hippocampal neurons, and each fluorescent cell also showed responses to nicotine within a few seconds after an increase or decrease of extracellular nicotine. Interestingly, neurons yield roughly the same  $\Delta F/F_0$  values for iNicSnFR3b\_PM and iNicSnFR3b\_ER. A similar pattern of roughly equal nicotine-induced  $\Delta F/F_0$  in neurons was observed for cDNA transfection, with iNicSnFR3a\_PM and iNicSnFR3a\_ER. As usual for neuronal cultures, cDNA transfection led to sparser expression (<10% of cells) than viral transduction.

Dopaminergic neurons of the reward pathway located in the ventral tegmental area play a role(s) in nicotine addiction (Subramaniam & Dani, 2015). Studies also suggest that nicotine protects dopaminergic neurons of the substantia nigra pars compacta during the initial stages of Parkinson's disease, via an inside-out pathway (Henderson et al., 2016; Srinivasan et al., 2014, 2016). Therefore, we assessed the entry of nicotine into the ER of human dopaminergic neurons differentiated from iPSCs.

It is not yet routinely possible to specifically induce either ventral tegmental area-like or substantia nigra pars compacta-like dopaminergic neurons from iPSCs; therefore, we recorded fluorescence from all neurons expressing iNicSnFR3a\_ER (Fig. 2.6, E and F). The fluorescence reaches steady-state within a few seconds after nicotine appears near the cells and decays to  $F_0$  within a few seconds after removal. The  $\Delta F/F_0$  values reach a maximum of 3–4, and the [nicotine] giving half- $\Delta F_{\max}/F_0$  is on the order of 20  $\mu$ M.

We also found that viral transduction with AAV2-iNicSnFR3b\_ER proceeded efficiently in the induced iPSC cultures (Fig. 2.15). >90% of the neurons were fluorescent, and all of these gave detectable increases in the presence of nicotine. The responses resembled those for transfected dopaminergic neurons but had lower  $\Delta F/F_0$ , rarely exceeding 2. In two cells, we found that  $\Delta F$  induced by N'MeNic (100  $\mu\text{M}$ ) was <0.2 times as large as  $\Delta F$  induced by 1  $\mu\text{M}$  nicotine. This confirms that iNicSnFR3b\_ER senses only intracellular nicotine, as found for expression in HeLa cells (Fig. 2.5).

*[Nicotine] in the ER approximately equals [nicotine] at the PM*

To assess the relationship between [nicotine] in the ER versus [nicotine] applied in the extracellular solution, we compared the increase of  $\Delta F/F_0$  versus applied [nicotine], as measured by the \_ER and \_PM constructs. Two cell types (HeLa and hippocampal neurons) provided complete datasets with both \_ER and \_PM constructs (presented in Fig. 2.5 and Fig. 2.6, A–D). For this analysis, we accepted data for applied [nicotine]  $\leq 5 \mu\text{M}$ , because this concentration range is most pharmacologically relevant, well below the  $EC_{50}$ , and least subject to pH perturbation in the ER. The appropriate metric is defined as  $[\Delta F/F_0]/[\text{nicotine}]$  and has the units  $\mu\text{M}^{-1}$ . For measurements with the \_ER constructs and for the \_PM constructs, the metric is  $0.075 \pm 0.019 \mu\text{M}^{-1}$  and  $0.063 \pm 0.13 \mu\text{M}^{-1}$ , respectively (mean  $\pm$  SEM,  $n = 8$  cells in each case; Fig. 2.6 F inset, gives an exemplar plot). This similarity shows that [nicotine] in the ER is approximately equal to [nicotine] applied in the external solution. Less complete data show a similar pattern in other cell types: SH-SY5Y (Fig. 2.14 A), HEK293 (Fig. 2.14 B), and human dopaminergic neurons differentiated from iPSCs (Fig. 2.6, E and F; and Fig. 2.15).

For purposes of the simulations described in a later section, we assumed that [nicotine] is equal in the ER and in the extracellular solution. We interpret “approximately equal” as a difference of less-than twofold. The uncertainty arises primarily because of differences between the pH of the ER and extracellular solution. In most estimates, this difference is <0.2 pH units (Casey et al., 2010), but has not been measured for the cell types we investigated. As noted, it is unlikely that nicotine and varenicline at the sub- $\mu\text{M}$  concentrations of most interest perturb the pH of the ER. Such perturbation (for instance, by mitochondrial uncouplers) (Mitchell, 2011) requires that both the uncharged and charged form of the drug can permeate through membranes, either passively or via transporters(s). All previous studies on nicotine conclude that only the uncharged form is membrane-permeant (Lester et al., 2009).

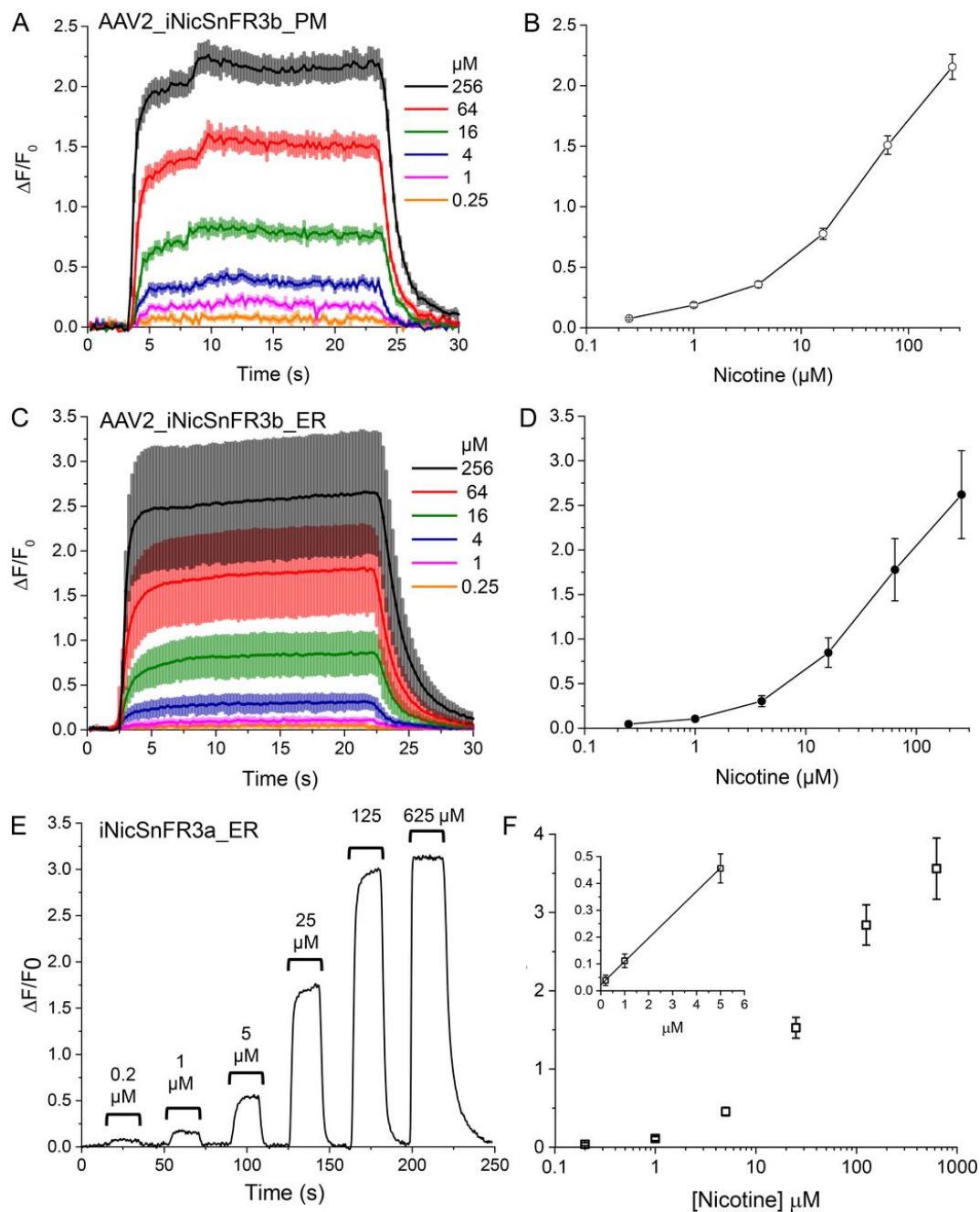


Figure 2.6: Nicotine in the ER of neurons. (A–D) Exemplar nicotine-induced fluorescence increases for cultured hippocampal neurons transduced with AAV2/1.sin1.iNicSnFR3b\_PM (A and B) or with AAV2.sin1.iNicSnFR3b\_ER (C and D). (A and C) 20-s nicotine pulses, followed by 20 s wash in HBSS. The average waveform for five cells at each [nicotine] is overlaid for the PM and ER traces in A and C, respectively. The SEM is shown as colored bands around each line. Dose–response relations are shown in B and D. (E and F) Human dopaminergic neurons transfected with iNicSnFR\_ER3a. (E) Typical nicotine-induced fluorescence during 20-s pulses of nicotine at the indicated concentrations. Data were subjected to a triangle filter (half-time, 1 s). (F) Full dose–response data from 20 transfected human dopaminergic neurons. Inset, start of the dose relation at [nicotine]  $\leq 5 \mu\text{M}$ . The slope of the line,  $[\Delta F/F_0]/[\text{nicotine}]$ , is  $0.087\text{M}^{-1}$ .

*Micro-iontophoresis of nicotine: membrane permeation does not slow fluorescence increases*

Results presented above show that a “jump” of [nicotine] in the external solution results in  $\Delta F$  in the ER. We asked whether the kinetics of  $\Delta F$  reveal any delay due to diffusion of nicotine across either the PM or the ER membrane. To decide this point, we obtained more rapid application of nicotine without complications from solution changes or pH changes. We delivered nicotine from micro-iontophoretic pipettes (Del Castillo & Katz, 1955). The data (Fig. 2.7) show that, for a cell within 10  $\mu\text{m}$  of the pipette tip, iNicSnFR3b\_ER produces fluorescence increases within <1 s, approximately equal to the response time of the iNicSnFR itself (Fig. 2.2 D). This result shows that the PM and the ER membrane do not present a detectable diffusion barrier on this time scale. For more distant cells, the fluorescence increase is slower and smaller. For instance, the cell in ROI 3,  $\sim 150 \mu\text{m}$  from the tip of the micro-iontophoretic pipette, responded completely on a time scale of  $\sim 10$  s. This is consistent with a diffusion constant on the order of  $1 \mu\text{m}^2/\text{ms}$ .

It is not possible to quantify the [nicotine] ejected from the tip of an iontophoretic pipette. We conducted dose–response studies by varying the iontophoretic current between 10 nA (as shown in Fig. 2.7) and 100 nA. As the current was increased, the  $\Delta F/F_0$  for the cell in ROI 1 did not increase; the response in the cell of ROI 2 increased modestly and became faster, to equal the value in ROI 1. The cell in ROI 3 increased more gradually, eventually reaching  $\Delta F/F_0 \sim 0.3$  at an ejection current of 100 nA.

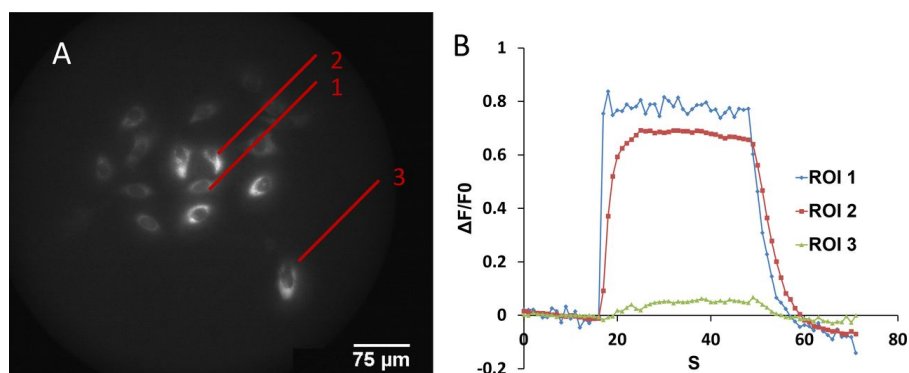


Figure 2.7: Micro-iontophoretic nicotine application. (A) Cultured mouse hippocampal neurons transduced with AAV\_iNicSnFR3b\_ER. A nicotine-containing micro-iontophoretic pipette was positioned  $<10 \mu\text{m}$  above the cell in ROI 1. A 10-nA outward current pulse (32-s duration) was delivered. Most cells in the area showed fluorescence increases. (B) Fluorescence traces recorded simultaneously for cells at three distances from the pipette.



*Simulations of the outside-in and inside-out pathways during smoking*

Our data generate two insights important for understanding the inside-out pathway. First, the genetically encoded nicotine biosensors targeted to the ER reveal that nicotine appears in the ER within  $\leq 10$  s after it appears in the extracellular solution. The delay may be as small as 1 s, but this distinction has no importance for the simulations in this section. Second, after this delay, the [nicotine] in the ER differs by less than twofold from [nicotine] in the extracellular solution.

The most complete data on pharmacological chaperoning have used extracellular nicotine, applied for several hours (Kuryatov et al., 2005). Therefore, a major question arising from previous data were whether nicotine enters the ER quickly enough to serve as a pharmacological chaperone. The answer, based on our present data, is clearly, “yes.” It is reassuring, but not crucial, to know that [nicotine] in the ER is rather close to that outside the cell, so that the highest-affinity states of nicotine-nAChR binding, which leads to pharmacological chaperoning, need not differ drastically from events at the PM.

A question of particular interest now arises about the exit of nicotine from the ER. When nicotine is removed from the extracellular solution, nicotine leaves the ER, again within 10 s. If [nicotine] in the ER drops below the  $EC_{50}$  for pharmacological chaperoning during the interval between cigarettes, then the inside-out pathway cannot readily account for nicotine dependence. We term this point the “rapid exit” problem.

The rapid exit problem may be addressed by existing data on the pharmacokinetics of nicotine during smoking. After a person receives a bolus of nicotine from a cigarette or an ENDS, [nicotine] in the body decreases with two exponential terms. During the slower phase, measurable nicotine endures in the plasma for several hours (Benowitz et al., 1991). We simulated fractional activation of the inside-out and outside-in pathways using the available data from the literature (Benowitz et al., 1991; Kuryatov et al., 2005; Rollema et al., 2007). We assume a common pattern of smoking: one cigarette, yielding 1 mg of ingested nicotine, each hour, for 12 h during each day (Table 2.1). The detailed parameters of the simulation are given in Table 2.3.

The simulations show how plasma/cerebrospinal fluid (CSF)/ER nicotine concentration varies on the time scale of minutes to hours (Fig. 2.8 B1). Clearly, [nicotine] in the ER remains greater than the  $EC_{50}$  for pharmacological chaperoning during the

entire 1-h interval between cigarettes. The inside-out pathway remains substantially activated continually during the 12–16 smoking-period hours of our simulations (Fig. 2.8 B2).

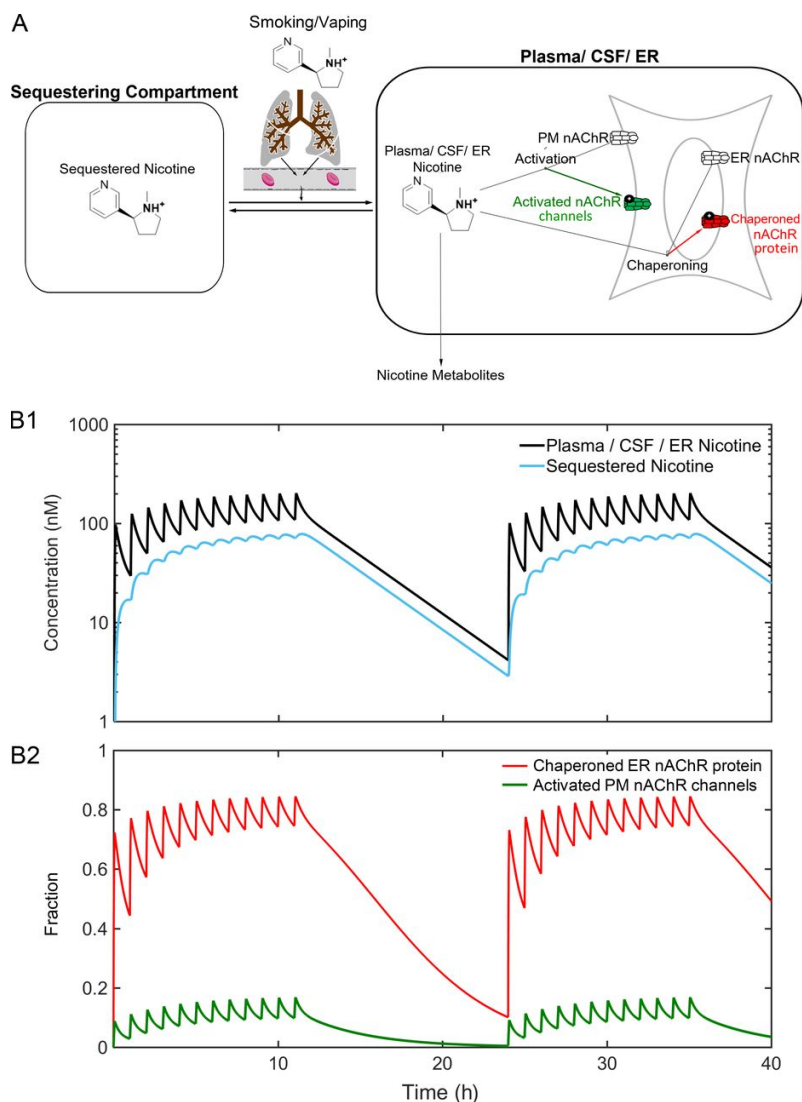


Figure 2.8: Simulations of nicotine pharmacokinetics and pharmacodynamics during smoking. (A) The pharmacokinetic/pharmacodynamic model, implemented in Matlab SimBiology. Individual parameters and structures and smoking dosages are presented in Table 2.3 and in Supplemental ZIP File. (B1) Nicotine concentrations in the plasma/CSF/ER and in the “sequestered” compartment, during 40 simulated hours for the standard habit (Table 2.3 and Supplemental ZIP File). The latter compartment was termed the “peripheral compartment” by Benowitz et al. (1991), but that terminology is less preferable in discussions of the nervous system. Note the logarithmic [nicotine] scale. (B2) Effects on the two processes shown in A. Note that the standard habit nearly activates nAChR protein chaperoning (inside-out process) >50%, but activates nAChR channel activation (outside-in process) <20%.

### Studies with varenicline *in vitro* and in live cells

In addition to detecting nicotine, the biosensors iNicSnFR3a and iNicSnFR3b also detect varenicline (Fig. 2.9 and Fig. 2.16). In fluorescence data, purified iNicSnFR3a displays a varenicline  $EC_{50}$  approximately sixfold less than for nicotine. The maximal response,  $\Delta F_{\max}/F_0$ , is at least equal to that for nicotine (Fig. 2.9 A). Note that the fitted Hill coefficient is significantly less than unity, as also noted for the live-cell imaging described below.

Biochemical characterization also indicates that varenicline binds more strongly than nicotine to iNicSnFR. The stopped-flow kinetics (Fig. 2.9 B) reveal smaller pseudo-first-order forward and reverse rate constants ( $k_{\text{on}}$  and  $k_{\text{off}}$ , respectively) than for nicotine (Fig. 2.2 D), as well as an inferred equilibrium binding constant  $K_d$ , approximately threefold less than for nicotine (compare with Fig. 2.2 D). The isothermal titration calorimetry data for the varenicline–iNicSnFR3a interaction (Fig. 2.9 C) also reveal a several-fold lower  $K_d$  (3.5  $\mu\text{M}$ ) than for nicotine.

#### *Varenicline enters the ER*

Live-cell imaging shows robust dose-dependent, varenicline-induced fluorescence increases, both in HeLa cells and in neurons, both at the PM and in the ER (Fig. 2.9 and Fig. 2.16). The pharmacologically relevant varenicline concentrations are  $<1 \mu\text{M}$ , a range that yields varenicline-induced  $\Delta F$ . Unlike the data for nicotine, the varenicline dose–response data for both HeLa cells and neurons do approach saturation, allowing the conclusion that the dose–response relations show an  $EC_{50}$  of 1–4  $\mu\text{M}$ . This agrees well with the data on purified biosensor protein.

Especially in neurons, the growth and decay phases of the ER varenicline-induced fluorescence (Fig. 2.9 F and Fig. 2.16 C) are clearly slower than either the nicotine responses presented earlier or the varenicline responses on the PM (Fig. 2.9 D and Fig. 2.16 A). The relatively slow ER varenicline responses occur even for the smallest measured [varenicline] ( $\leq 1 \mu\text{M}$ ), which are unlikely to perturb organellar pH. The slower ER entry and exit for varenicline than for nicotine are consistent with the lower  $\log D_{7.4}$  (-1.27 vs. -0.04) (Mannhold et al., 2012), as though the ER entry/exit of varenicline is rate-limited by membrane permeability.

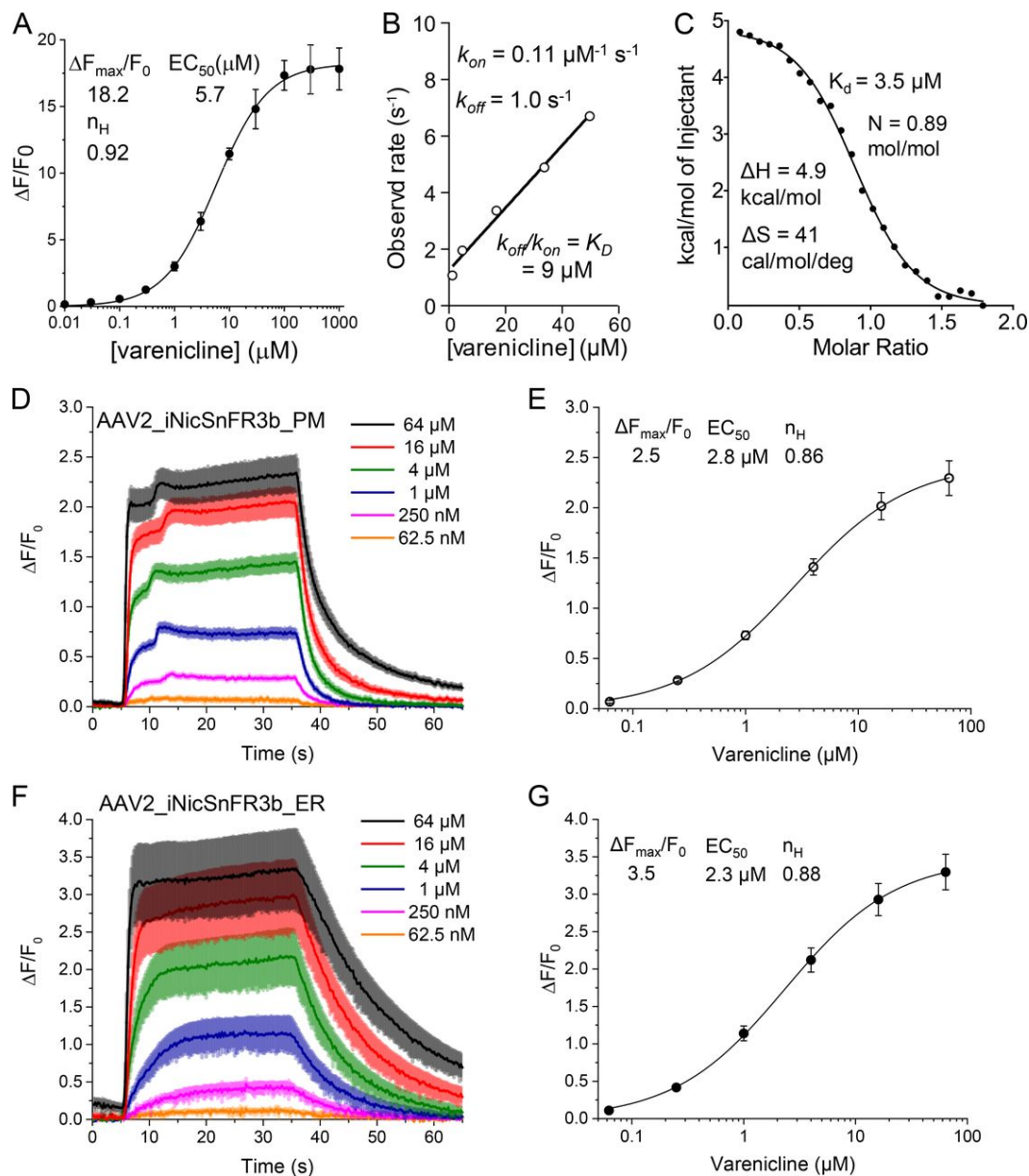


Figure 2.9: Varenicline activity against purified iNicSnFR3a (A–C) and iNicSnFR3b expressed in hippocampal neurons (D–G). (A) Dose–response relations for varenicline-induced  $\Delta F/F_0$ , measured in  $3\times$  PBS, pH 7.4. Mean  $\pm$  SEM; three measurements. (B) Stopped-flow measurements at various [varenicline]. (C) Isothermal titration calorimetry. (D–G) Exemplar varenicline-induced fluorescence increases for cultured hippocampal neurons transduced with AAV2/1.syn1.iNicSnFR3b\_PM (D and E) or with AAV2/1.syn1.iNicSnFR3b\_ER (F and G). (D and F) 30-s varenicline pulses, followed by 40-s wash in HBSS. The average waveform for five cells at each [varenicline] is overlaid for the PM and ER traces in A and C, respectively. The SEM is shown as colored bands around each line. (E and G) Dose–response relations, fitted to a single-component Hill equation, including zero response at zero [varenicline]. Parameters are shown.

*Pharmacokinetic and pharmacodynamic simulations of varenicline*

The data show that varenicline does enter the ER within < 30 s after appearing near cells and that varenicline then leaves the ER within at most 60 s after leaving the external solution, at the clinically relevant sub- $\mu$ M concentrations. These data are adequate to add a subcellular dimension to pharmacokinetic simulations for orally administered varenicline. We used a model appropriate to twice-daily oral administration and with parameters that account for the very different absorption and metabolism of varenicline (Fig. 2.10) versus nicotine (Fig. 2.8 and Table 2.3). The simulations show that the usual doses of varenicline only slightly activate the outside-in pathway of nAChR activation. In contrast, varenicline activates the inside-out pathway of pharmacological chaperoning by >50% after the second dose of varenicline and by >70% after the fifth dose.

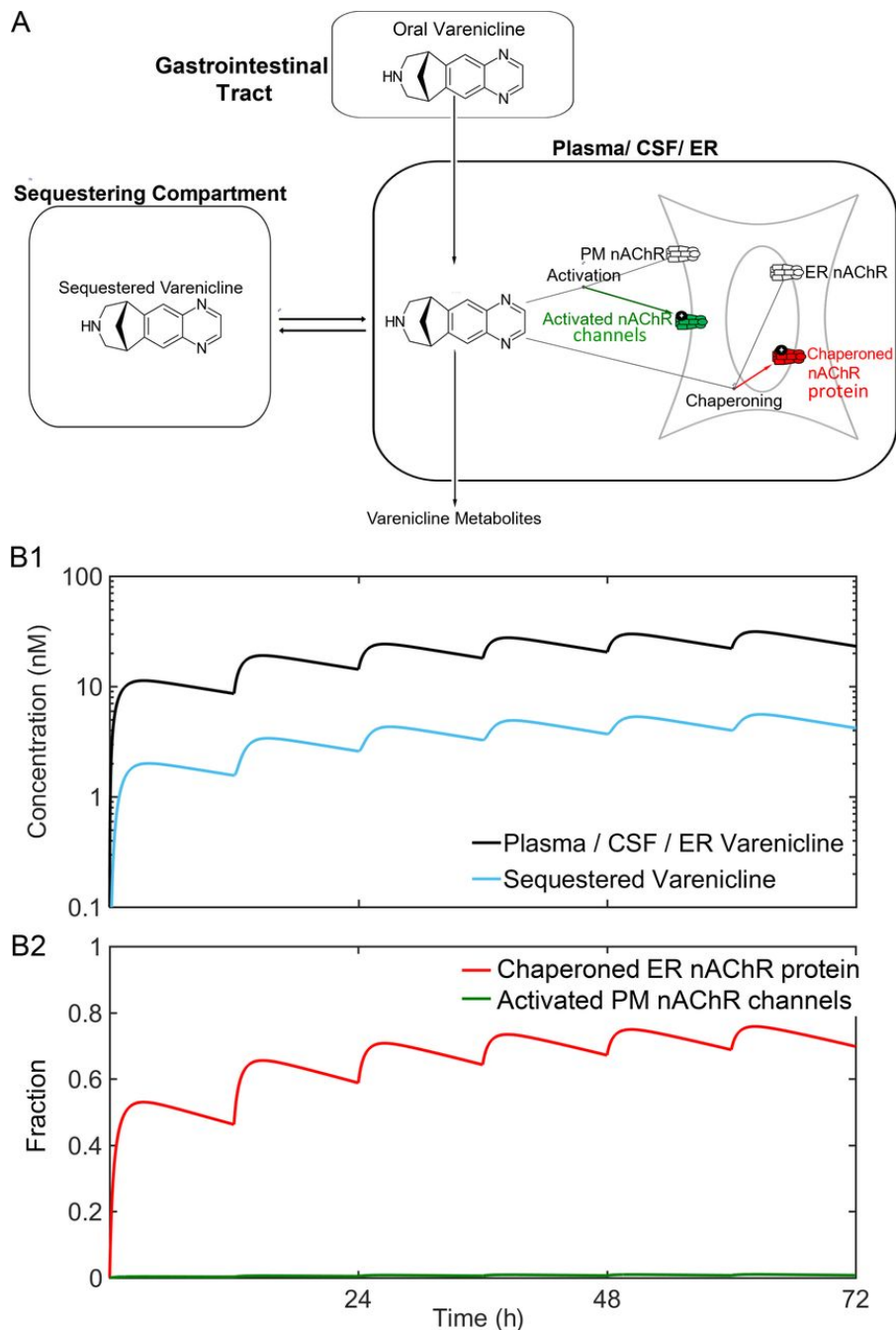


Figure 2.10: Simulated pharmacokinetics and pharmacodynamics during oral varenicline administration. (A) In the pharmacokinetic model for orally administered varenicline, the lungs are replaced by the digestive tract. The parameters derive from studies on humans (Faessel et al., 2006). The parameters are given in Table 2.3 and in Supplemental ZIP File. (B1) Varenicline concentrations in two compartments: the plasma/CSF/ER and the sequestered compartment. (B2) Effects on the two processes shown in A. Note that recommended treatment with varenicline almost completely activates nAChR protein chaperoning (inside-out process), but only slightly produces nAChR channel activation (outside-in process).

## 2.5 Discussion

The study quantifies the dynamics and extent of an early step in the inside-out pathway for nicotine: entry into the ER. Downstream steps have been studied and quantified in several a previous report using biochemistry, fluorescence microscopy, genetically altered mice, and immunocytochemistry (Henderson & Lester, 2015).

Development of the iNicSnFR family begins the field of optical subcellular pharmacokinetics for nicotine. We present data that extend to the sub- $\mu\text{M}$  nicotine concentration that exists in the plasma and CSF of a smoker or vaper. The genetically encoded nicotine biosensors iNicSnFR3a and -3b, trapped in the ER, reveal that nicotine appears in the ER within at most 10 s after it appears in the extracellular solution (Fig. 2.5, Fig. 2.6, Fig. 2.7, Fig. 2.14, and Fig. 2.15). The [nicotine] in the ER is equal to that in the extracellular solution, at a precision of twofold. These conclusions hold for each of the five cell types we have investigated: three types of human clonal cell lines (HeLa, Fig. 2.5; SH-SY5Y, Fig. 2.14 A; and HEK293, Fig. 2.14 B), human dopaminergic neurons differentiated from iPSCs (Fig. 2.6, E and F; and Fig. 2.15), and mouse hippocampal neurons (Fig. 2.6, A–D; and Fig. 2.7).

### Fluorescent biosensors for optical subcellular pharmacokinetics

Our strategy (Fig. 2.1) extends that used for iGluSnFR (Marvin, Borghuis, Tian, Cichon, Harnett, Akerboom, Gordus, Renninger, Chen, Bargmann, et al., 2013b). No known natural PBP binds nicotine; therefore, we engineered a PBP to bind a drug. That NicSnFRs also recognize ACh, and more weakly, choline, is useful for studies of compartmentalization. Related OpuBC proteins, further optimized to sense ACh itself, will also find use in neuroscience (Borden et al., 2020).

Although the directed evolution of the iNicSnFR family (Fig. 2.12) did not explicitly include assays for varenicline, varenicline is a highly potent full agonist for iNicSnFR3 fluorescence. Interestingly, varenicline is also more potent than ACh at both  $\alpha 4\beta 2$  and  $\alpha 7$  nAChRs (Coe et al., 2005; Mihalak et al., 2006). However, varenicline is a full agonist at  $\alpha 7$ , but not at  $\alpha 4\beta 2$  nAChRs. Thus, there are differences in the details of the binding site of the iNicSnFR constructs versus nAChRs. We found that the iNicSnFR3a and iNicSnFR3b constructs are less sensitive to other  $\alpha 4\beta 2$  agonists: cytisine, dianicline, and A-85380 (unpublished data).

Other neuronal drugs may also operate via inside-out pathways (Jong et al., 2009; Lester et al., 2012, 2015). With further modifications to the ligand site, preliminary data show that it may be possible to develop families of biosensors for optical

subcellular pharmacokinetics of several amine-containing drug classes (Muthusamy et al., 2018) (Shivange et al., 2017. Annual Meeting of the Society of General Physiologists. Abstract no. 32. J. Gen. Physiol.). Values for  $\log D_{7.4}$  of most neural drugs suggest that they enter organelles (Jong et al., 2018; Lester et al., 2012; Nickell et al., 2013), and melatonin probably also enters neutral organelles (Yu et al., 2016). The most important limitation, at present, is the extreme pH sensitivity of the biosensors. This constrains their usefulness in acidic organelles, where some neuronal drugs may also act (Stoeber et al., 2018).

Another class of fluorescent protein-based biosensors is derived from GPCRs rather than from PBPs (Jing et al., 2018; Patriarchi et al., 2018). In the GPCR-based biosensors, the ligand sites face the extracellular solution; they would presumably face the lumen of organelles like most (but not all) PBP-based SnFRs. However, in the GPCR-based biosensors, the fluorescent protein moiety faces the cytosol and therefore might be relatively insensitive to luminal pH. If GPCR-based biosensors can function in acidic organelles, they may also find use for subcellular pharmacokinetics.

### **Implications for the inside-out pathway**

Our data show that when [nicotine] in the extracellular solution falls to zero, nicotine completely leaves the ER, again within 10 s. Yet after a person receives a bolus of nicotine from a cigarette, [nicotine] in the body does not immediately fall to zero. The rather leisurely metabolism of nicotine (half-time, ~20 min in humans) (Benowitz et al., 1991) provides that a smoker's CSF [nicotine] decreases on the time scale shown in Fig. 8B1. Because of the highly nicotine-sensitive feature of pharmacological chaperoning, [nicotine] in the ER remains greater than the  $EC_{50}$  for pharmacological chaperoning during the entire 0.75–1-h interval between cigarettes. The inside-out pathway remains >50%-activated continually during the 12–16 h of our simulations (Fig. 2.8 B2). We conclude that the inside-out pathway, operating via pharmacological chaperoning, can readily account for up-regulation, an important component of nicotine dependence.



Our simulations also lead one to reexamine the relationship between the previously distinct concepts of “acute,” “repeated,” and “chronic” exposure to nicotine. In the “standard habit,” even a single cigarette, whose nicotine is fully ingested during 10 min, activates the inside-out pathway >50% until the next cigarette 1 h later (Fig. 8). Thus, a series of “acute” and “repeated” exposures, one per hour for 12 h, becomes “chronic” activation for the 12 h of smoking activity. By the next morning, nicotine levels have decreased below levels that activate pharmacological chaperoning; but the downstream trafficking and subsequent sequelae, including nAChR up-regulation, probably endure for several days (Marks et al., 1985).

Thus, subcellular pharmacokinetics readily explains dependence on smoked nicotine. Around the world at any time, several 100 million people have ingested tobacco within the past hour; they retain nicotine in every organelle of every cell. In the ER and cis-Golgi of the small percentage of cells that contain  $\alpha 4\beta 2$  nAChRs, these levels activate the inside-out pathway >50%, and therefore maintain one aspect of nicotine dependence.

Recently introduced ENDSs provide plasma levels with kinetics approaching those of cigarettes (Bowen & Xing, 2015). Thus, ENDSs can also maintain a key molecular/cellular basis of nicotine dependence: the inside-pathway at  $\alpha 4\beta 2$  nAChRs.

Can outside-in mechanisms, such as channel activation and  $\text{Ca}^{2+}$  influx, also account for cellular/molecular aspects of nicotine dependence? In contrast to pharmacological chaperoning, nAChR channels do not remain fully activated during the average smoker’s day; in fact, the average activation of PM nAChR channels is <20% (Fig. 2.8 B2). Some explanations of nicotine dependence assume that  $\text{Ca}^{2+}$  influx, either directly through nAChRs or indirectly through neuronal activity-induced  $\text{Ca}^{2+}$  channel influx, can account for nicotine addiction, even considering the rather modest level of nAChR channel activation shown by our simulations. Yet the rather general phenomenon of  $\text{Ca}^{2+}$  influx has not been shown to account for the highly specific aspects of nicotine addiction, such as post-translational nAChR up-regulation. Another frequently invoked explanation for nicotine dependence is desensitization of nAChR channels in response to the presence of nicotine. It is highly likely that some acute aspects of nicotine exposure arise from desensitization rather than activation (Miwa et al., 2011). However, no available data suggest that desensitized nAChRs begin an intracellular signaling pathway that could account for nicotine dependence.

### **Implications for varenicline-based therapy**

The present data show that varenicline also enters the ER (Fig. 2.9 and Fig. 2.16), and the simulations show that the resulting maintained level of varenicline in the ER could lead to pharmacological chaperoning by varenicline (Fig. 2.10). This explains the observations that varenicline also up-regulates  $\alpha 4\beta 2$  nAChRs (Govind et al., 2017; Marks et al., 2015; Turner et al., 2011). The usual explanation for varenicline as a smoking cessation agent is that, even though it produces negligible activation of  $\alpha 4\beta 2$  nAChR channels (Fig. 10B2), it does desensitize these nAChRs, blocking the action of nicotine itself. Our study supports the additional suggestion that the several-week taper regimen for varenicline also allows nicotine users to reverse up-regulation gradually. This, in turn, could help aspiring quitters to avoid craving and/or behavioral aspects of withdrawal. However, the persistence of up-regulated nAChRs could also cause some of the side effects of varenicline during the first days to weeks (Ashare et al., 2017); these side effects could underlie this drug's modest effectiveness in smoking cessation (Fagerström & Hughes, 2008).

Nicotine may also be neuroprotective in Parkinson's disease, and this effect may proceed via an inside-out pathway in the ER (Srinivasan et al., 2014, 2016). Therefore, we note recent reports that varenicline also displays neuroprotective effects in animal models of Parkinson's disease (McGregor et al., 2017) and another neurodegenerative disease (Sharma et al., 2018).

### **Quantitative aspects of reducing nicotine levels**

The prominence of the inside-out pathway in nicotine dependence has prompted us to simulate the activation of the inside-out pathway, as well as the outside-in pathway, during use of modified tobacco or ENDS (Table 2.1). United States Food and Drug Administration officials recently suggested decreasing the nicotine content of combustible tobacco. Our simulations show that a 3-fold reduction would nonetheless provide >40% average activation of the inside-out pathway; a 10-fold reduction (to 0.1 mg/cigarette) would reduce average activation to 20%. This conclusion would also hold for ingestion via an ENDS.

Our simulations deal with a "typical" smoker (Benowitz et al., 1991). These conclusions must be modified, at a personal level, for each smoker or vaper. Polymorphisms in cytochrome P450 2A6, the enzyme that primarily metabolizes nicotine, lead to dramatic (up to 10-fold) differences in nicotine lifetime among people (Dempsey et al., 2004). These result, in turn, to differences in the frequency of smoking (Tan-

ner et al., 2015). Future investigations must simulate the consequences of these variations for activation of the inside-out pathway.

If a nicotine-dependent person perceives desirable effects from up-regulated nAChRs, he or she might therefore prefer to inhale nicotine from an ENDS capable of delivering 1 mg of nicotine within a few minutes, rather than from a modified cigarette that, along with harmful smoke, delivers <0.1 mg, a dose that does not maintain full up-regulation. The harm reduction that results from such an individual behavioral choice about nicotine intake, (1) if stringently maintained by the nicotine-dependent individual and (2) if replicated in the entire nicotine-dependent population, would be considerable. One review suggests that such a complete transition would decrease tobacco-related diseases by 95% (London, 2016). Whether and how a society wishes to encourage such a transition from smoked tobacco to ENDS involves details both of policy and of science.

Nicotine dose (mg) per cigarette	Total daily cigarettes, intervals	Average [nicotine] in plasma/CSF/ER (nM)	Average nAChR activation on PM	Average activation of nAChR chaperoning in ER
<b>1</b>	12/d, 1 h	112	0.1	0.7
0.5	12/d, 1 h	56	0.05	0.55
0.3	12/d, 1 h	34	0.03	0.44
0.1	12/d, 1 h	11	0.01	0.2
0.05	12/d, 1 h	6	0.006	0.13
3	12/d, 1 h	321	0.23	0.83
1	6/d, 2 h	65	0.06	0.6
1	20/d, 0.8 h	148*	0.13*	0.75*

Table 2.1: Effect of dosing regimen variations on simulated nicotine concentrations in plasma/CSF/ER and on nAChR activation or chaperoning. Results have been averaged over 12 or 16 h. Asterisk (\*) denotes 16-h average. The first row (in bold) presents our definition of a standard habit, plotted in Fig. 8. The following five rows show simulations for increasingly “denicotinized” cigarettes. The row presenting a dose of 3 mg might be appropriate for a schizophrenic’s smoking strategy (Miwa et al., 2011).

## 2.6 Supplemental Information

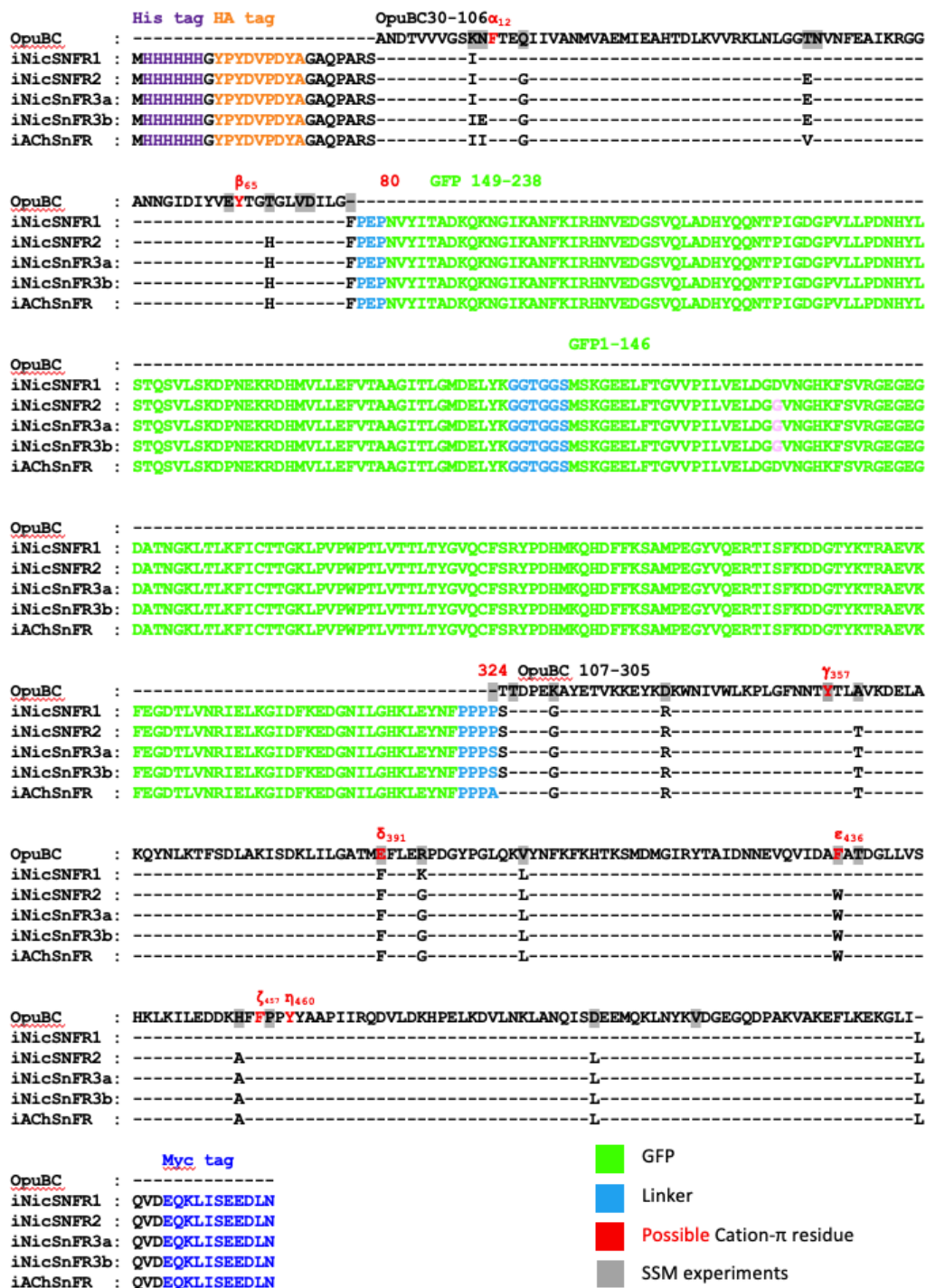
### Amine-containing buffers produce anomalous results

With Tris or HEPES buffers, experiments on purified iNicSnFRs gave elevated  $F_0$  values and decreased  $\Delta F$  values, compared with phosphate buffers. Isothermal titration calorimetry experiments with Tris buffers gave affinities much lower than with phosphate-containing buffers. We found similar anomalies with MOPS at >10 mM. In experiments on purified iNicSnFR proteins, like those of Fig. 3, MOPS buffer at  $\leq 10$  mM produced minimal perturbation. However, live-cell experiments with MOPS and iNicSnFR3a\_ER gave anomalously low  $\Delta F/F_0$ , probably because

this buffer allowed the ER to become acidic. Use of HEPES might have degraded the quality of the crystallographic data showing nicotine at the binding site. Even slight affinity to the buffer molecule might produce competition with the desired ligand. Examples of crystallized protein containing the amine buffer, rather than nicotine, ACh, or choline, are provided by the studies of ACh-binding protein (PDB file 1I9B) (Brejc et al., 2001) and of ProX (PDB file 3MAM) (Tschapek et al., 2011).

#### Acidic vesicles as candidates for the “sequestered compartment”

Our simulations include a “sequestered” compartment. This was previously termed a “peripheral” compartment (Benowitz et al., 1991), but the previous terminology would introduce confusion about nicotine in the peripheral nervous system. Working aside, where is this sequestered compartment, whose chief characteristic is that it remains inaccessible from metabolic enzymes? Early on, it was pointed out (De Duve et al., 1974) that weak bases accumulate, perhaps by factors of 100, in lysosomes or other acidic compartments. In 2009, it was suggested that nicotine could also become concentrated in this fashion (Lester et al., 2009). The pharmacokinetic literature points out that lysosomes (pH ~4.5), representing just ~1% of a cell’s volume, but concentrating a weakly basic drug by ~100-fold, could accumulate as much drug as the entire cellular and extracellular compartments (Mannhold et al., 2012). (Tischbirek et al., 2012) provided experimental evidence that antipsychotic drugs, which are also weak bases, accumulate in synaptic vesicles (pH ~5.5) and also presented a quantitative analysis including the dependence on logD and membrane permeation of the protonated, charged form (Trapp et al., 2008; Tischbirek et al., 2012). These concepts strengthen the recent suggestion that varenicline accumulates in lysosomes (Govind et al., 2017).







 GFP  
 Linker  
 Possible Cation- $\pi$  residue  
 SSM experiments

Figure 2.11: Sequences of PBPs and constructs described in this paper and/or studied in preliminary experiments.

The nicotine dose–response characteristics of iNicSnFR1 and iNicSnFR2 biosensors are given in Fig. S2 B. These constructs have not been studied systematically in mammalian cells with optimized methods. Experiments with iAChSnFR are described elsewhere (Borden et al., in preparation). Important domains are noted on the sequences. Based on a SwissDock simulation of nicotine in iNicSnFR1 (see Fig. 2 B), we have annotated the seven aromatic residues within 5 Å of the pyrrolidine nitrogen in nicotine. These are labeled  $\alpha$  through  $\eta$ . One or more of these side chains may be involved in a cation- $\pi$  interaction with the protonated pyrrolidine moiety of nicotine, with the quaternary amine of N' MeNic, and/or with the secondary amine of varenicline (Tavares et al., 2012; Post et al., 2017). The OpuBC sequence is annotated with a gray background at the 25 codons we subjected to SSM experiments. In communications among the collaborators on this project, we have used the following additional descriptions and temporary names. For iNicSNFR1: CC47, V4.6. For iNicSNFR2: CC90. For iNicSnFR3a: CC93. For iNicSnFR3a\_Y357A\_PM: CC105. For iNicSnFR3b: V7. For iAChSnFR: V9.

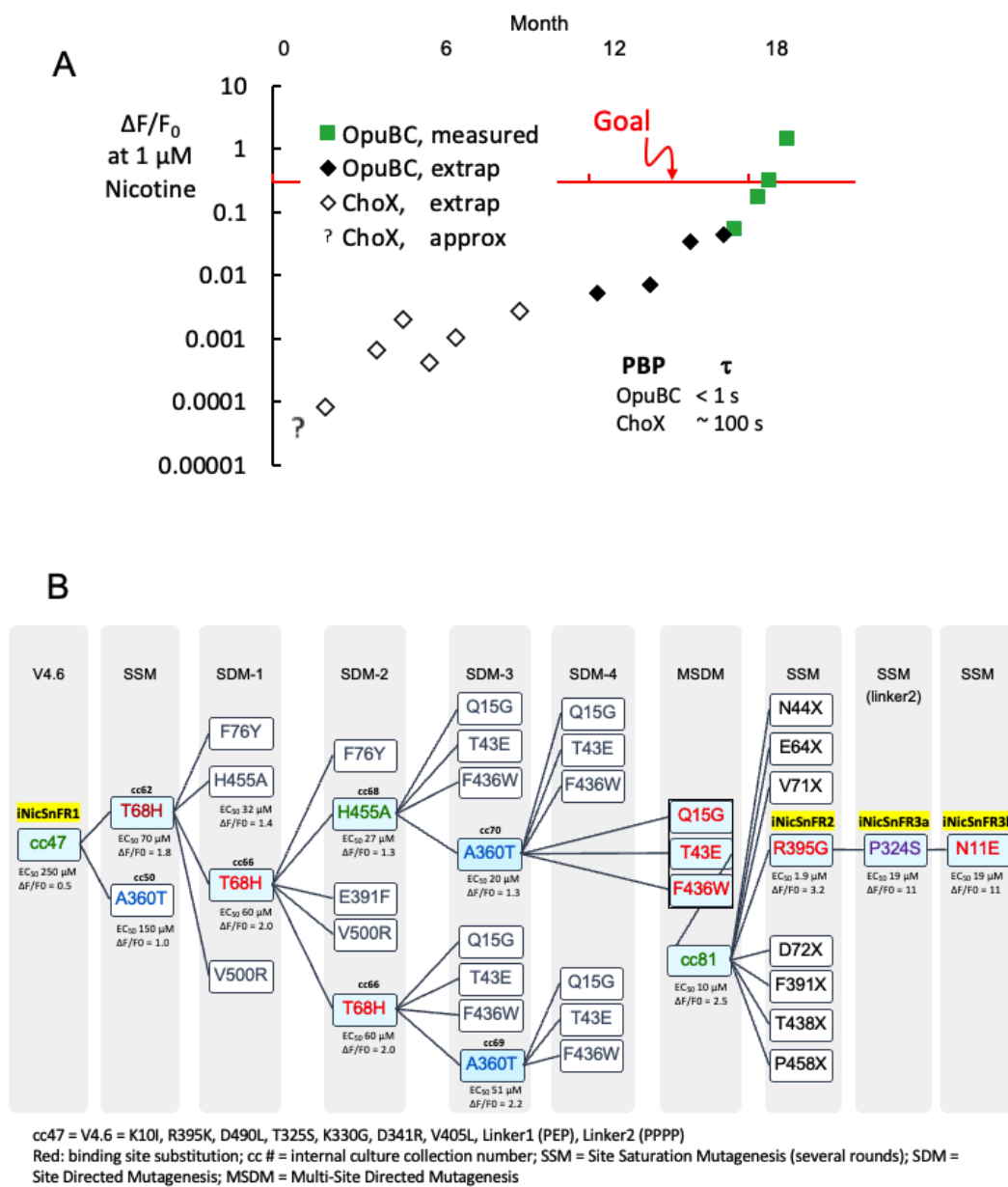


Figure 2.12: Directed evolution of the iNicSnFR family. (A) A history of our progress toward the goal of  $\Delta F/F_0 > 0.3$  at  $1\ \mu\text{M}$  nicotine. Initial experiments used ChoX, a choline PBP from *Sinorhizobium meliloti*. However, these constructs responded to ligands in solution with a time constant of  $\tau > 100\ \text{s}$  and were also poorly expressed in mammalian cells. We ceased systematic development of ChoX-based constructs. Later experiments used OpuBC from *T. spX513*, as described in the text and in Fig. 2. The reported values were measured in *Escherichia coli* cell lysates; values for key constructs were later verified with samples of the purified proteins. (B) Final stages in protein engineering of iNicSnFR constructs. For constructs denoted by black or white symbols,  $\Delta F/F_0$  at  $>1\ \mu\text{M}$  nicotine was extrapolated from measurements on bacterial lysates as  $[\Delta F/F_{\text{max}}]/EC_{50}$ .

For constructs denoted by green symbols,  $\Delta F/F_0$  at 0.3  $\mu\text{M}$  nicotine was measured directly on bacterial lysates. The designs of the mutant libraries were based on the iNicSnFR1 structure depicted in Fig. 2 A and the docking results of Fig. 2B. The sites selected for mutagenesis include the nicotine-binding pocket, linker residues, and the interface between OpuBC and cpGFP. Interestingly, the substitution A360T improved affinity despite its location “far” from the binding pocket (on a  $\beta$ -sheet next to one of the active site loops). The site A360 was selected based on the crystal structure of ACh-binding protein (AChBP) in complex with nicotine (PDB file 1UW6). Additional names for communications among collaborators are given in Fig. S1. Red: binding site substitution. Techniques: site saturation mutagenesis (several rounds), site-directed mutagenesis, and multisite-directed mutagenesis.

Traces are mean  $\pm$  SEM; three cells. At 30  $\mu\text{M}$  nicotine, photoswitching also proceeded more rapidly for 100% than for 10% intensity (time constant, 3.47 vs. 5.55 s, respectively). At 1  $\mu\text{M}$  nicotine, data were too noisy for systematic kinetic studies. (B) Photoswitching is reversible. HeLa cells transfected with iNicSnFR3a\_PM, imaging at 30  $\mu\text{M}$  nicotine. During an initial 20-s nicotine application,  $\Delta F$  reaches a peak, then decreases. During a second 200-s application,  $\Delta F$  reaches a peak, then recovers to a plateau. The laser is switched off for 60 s during the continued presence of nicotine. When the laser is switched on again,  $\Delta F$  appears to have recovered to its initial peak, then bleaches to its former plateau. Traces are normalized from five cells, and the gray bands show  $\pm$  SEM. (C) Further analysis of reversible photoswitching. HeLa cells transfected with iNicSnFR3a\_ER. Experiment at 100% laser intensity, 30  $\mu\text{M}$  versus 3  $\mu\text{M}$  nicotine. When 30  $\mu\text{M}$  nicotine is removed, the trace reveals a transient decrease in  $F_0$  (red arrow). In the absence of nicotine, when iNicSnFR is absorbing fewer photons,  $F_0$  recovers to its unbleached state over the next 10 s. Photoswitching was not observed with LED illumination.



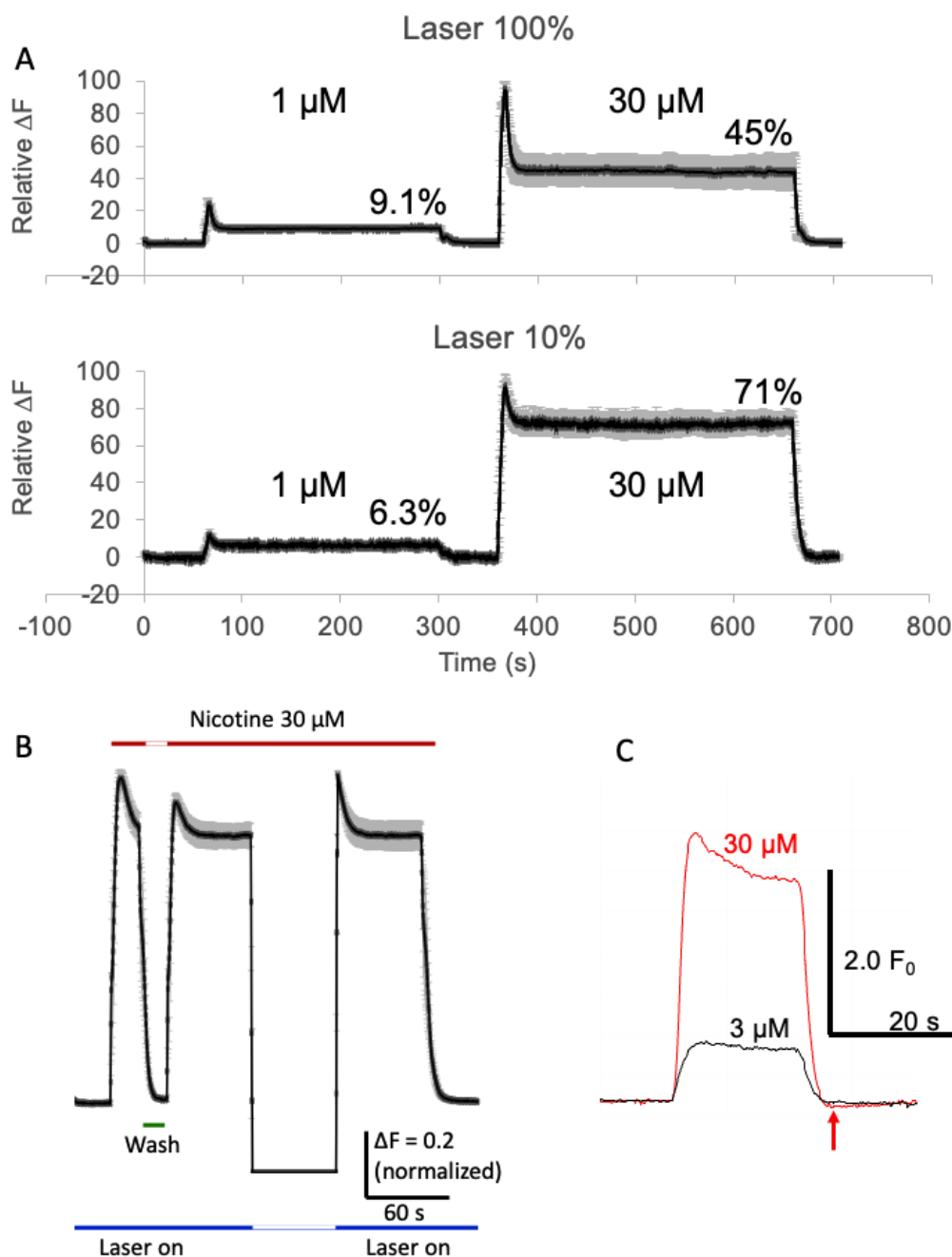


Figure 2.13: Photoswitching (bleaching) is noticeable at high [nicotine] with focused laser illumination. (A) Photoswitching (bleaching) increases at the highest illumination intensities and at higher [nicotine]. HeLa cells transfected with iNic-SnFR3a\_PM. Imaging at 1 and 30  $\mu M$  nicotine, with 100% and 10% laser intensity (top and bottom, respectively). At 30  $\mu M$  nicotine, photoswitching reduced the steady-state  $\Delta F$  to 45 versus 71% of the peak  $\Delta F$  for 100% and 10% laser intensity, respectively. The steady-state ratio,  $\Delta F(30 \mu M)$  to  $\Delta F(1 \mu M)$  was 4.92 versus 11.2 for 100% and 10%, respectively, indicating that high intensities artifactually shifted the dose-response relation ([nicotine] vs.  $\Delta F$ ) to lower [nicotine].

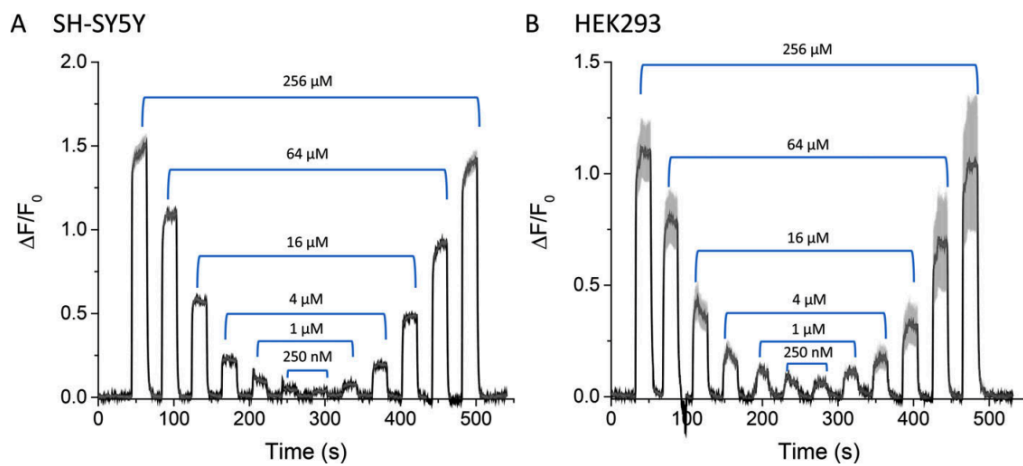


Figure 2.14: Responses to nicotine with iNicSnFR\_ER in SH-SY5Y cells and HEK293 cells. (A and B) iNicSnFR\_ER was transfected and imaged in SH-SY5Y (A) and HEK293 cells (B). Nicotine pulses were applied for 20 s at 40-s intervals. The nicotine concentration was stepped from 256  $\mu\text{M}$  to 250 nM and then from 250 nM to 256  $\mu\text{M}$  in 4 $\times$  concentration steps in HBSS. The mean of three cells is given as a solid black line, and the SEM is given as gray bounds.

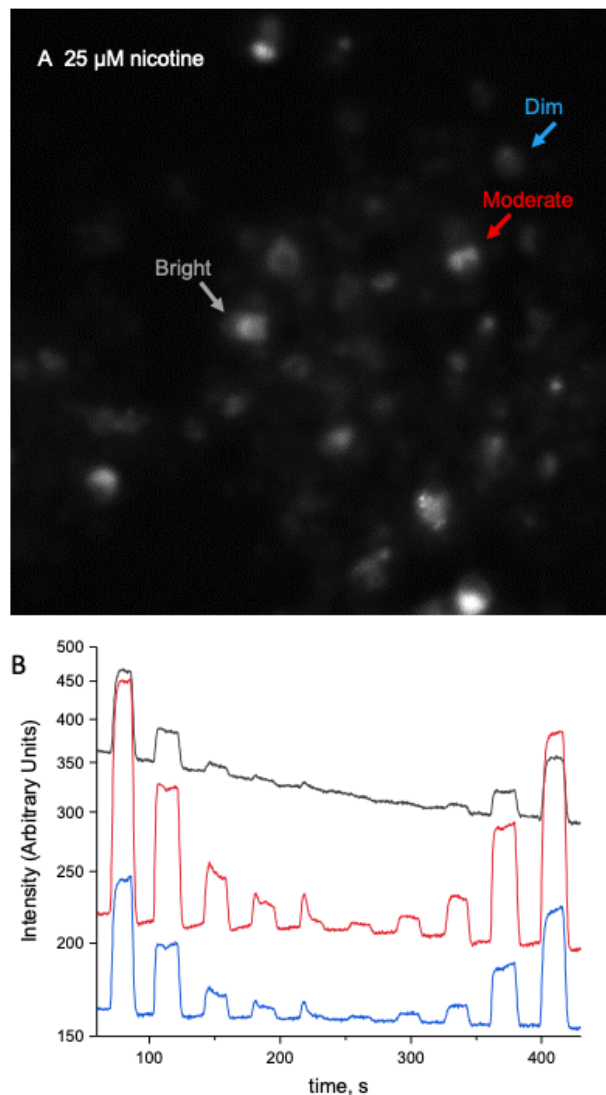


Figure 2.15: Human iPSCs, differentiated to dopaminergic neurons, transduced with AAV\_iNicSnFR3b\_ER. This figure accompanies the video of a descending, then ascending, series of nicotine concentrations at fivefold steps between 0.2 and 125  $\mu\text{M}$ . Concentrations and washes (“0  $\mu\text{M}$ ”) are marked on the video. (A) The image shows a single frame taken at 25  $\mu\text{M}$  nicotine, indicating three cells (dim, moderate, and bright). (B) Plots of the average absolute intensity of these images (log scale), without correction for sloping baseline or conversion to  $\Delta F/F_0$ . Note that in the descending phase, the responses begin more quickly and, at the lower [nicotine], show an initial transient. This is an artifactual result when solutions in a pH-regulated reservoir are allowed to remain in gaspermeable intermediate tubing, allowing  $\text{CO}_2$  to escape and rendering the solutions slightly more basic (see Materials and methods). The second application of each solution utilizes solution that has recently moved from the larger reservoir; the transients no longer appear.

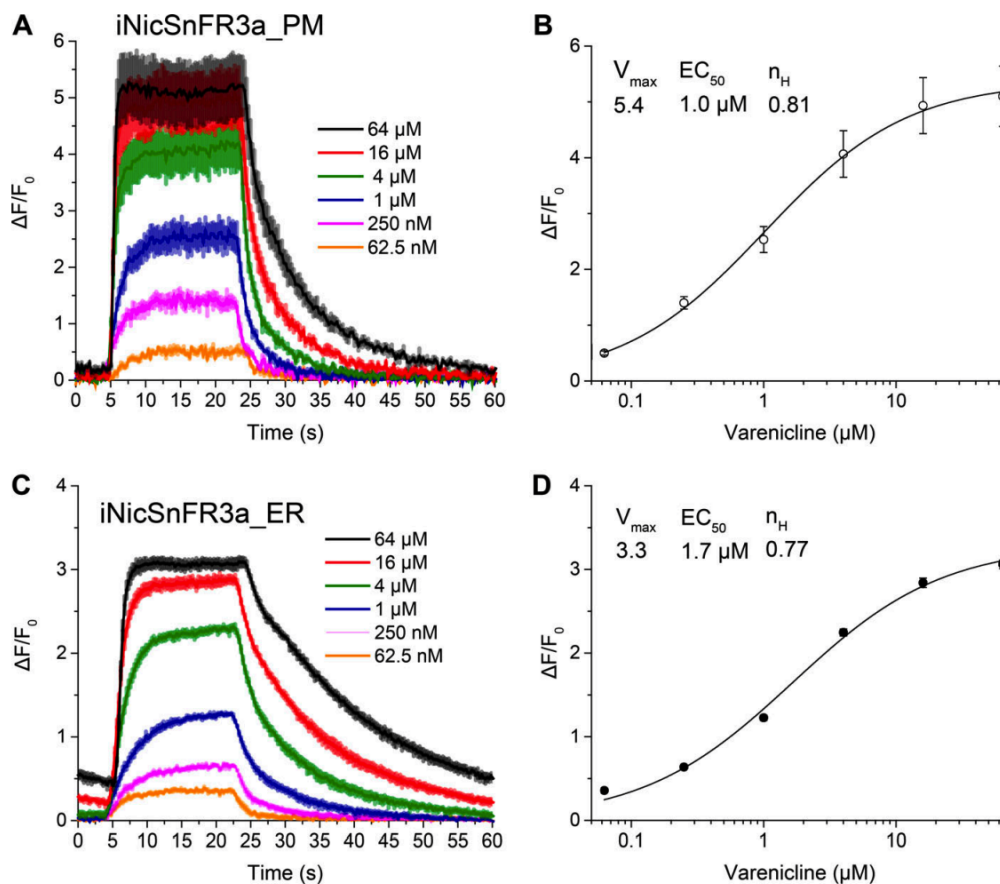


Figure 2.16: Varenicline at iNicSnFR3a expressed in HeLa cells. (A and C) Dose–response relations for varenicline-induced  $\Delta F/F_0$ . Mean  $\pm$  SEM; three measurements. (B and D) Dose–response plots for  $\Delta F/F_0$  at each response in A and C, against [varenicline]. Single-component Hill equation fit, including zero response at zero [varenicline]. Parameter values are shown.

Wavelength, Å	1.541
Resolution range, Å	61.64–2.4 (2.486–2.4)
Space group	I 2 2 2
Unit cell, Å	80.61, 95.64, 151.79, 90, 90, 90
Total reflections	758,695 (72898)
Unique reflections	23,162 (2253)
Multiplicity	32.8 (32.3)
Completeness, %	99.07 (98.82)
Mean I/ $\sigma$ (I)	47.79 (3.74)
Wilson B-factor	36.67
R <sub>merge</sub>	0.749 (1.909)
R <sub>meas</sub>	0.761 (1.939)
R <sub>pim</sub>	0.133 (0.342)
CC <sub>1/2</sub>	0.924 (0.737)
CC*	0.98 (0.921)
Reflections used in refinement	23,132 (2253)
Reflections used for R-free	1178 (100)
R <sub>work</sub>	0.1902 (0.2311)
R <sub>free</sub>	0.2521 (0.3714)
CC <sub>work</sub>	0.878 (0.811)
CC <sub>free</sub>	0.828 (0.381)
Number of non-hydrogen atoms	4,042
macromolecules	3,989
ligands	22
solvent	31
Protein residues	504
RMS deviation, bonds	0.009
RMS deviation angles	1.36
Ramachandran plot: favored %	95.56
Allowed %	4.44
Outliers %	0.00
Rotamer outliers %	0.23
Clash score	10.25
Average B-factor	45.07
macromolecules	45.17
ligands	29.03
solvent	42.60
Number of TLS groups	4

Statistics for the highest-resolution shell are shown in parentheses.

Table 2.2: Structure and refinement of iNicSnFR1 crystallized with nicotine.

	Parameter Name	Nicotine		Varenicline	
		Value	References	Value	References
Volume of distribution	Vd	200 liters	<a href="#">Benowitz et al. (1991)</a>	420 liters	<a href="#">Faessel et al. (2006)</a>
EC <sub>50</sub> for activating PM nAChR receptor channels	Activation k-/k+	1,000 nM		3,000 nM	<a href="#">Coe et al. (2005)</a> ; <a href="#">Rollema et al. (2007)</a>
EC <sub>50</sub> for chaperoning ER nAChR proteins	Chaperoning k-/k+	37 nM	<a href="#">Kuryatov et al. (2005)</a>	10 nM	<a href="#">Govind et al. (2017)</a>
PM nAChR Concentration	PM nAChR	0.1 nM		0.1 nM	
ER nAChR Concentration	ER nAChR	0.1 nM		0.1 nM	
Elimination rate constant	kel	0.706 1/h	<a href="#">Benowitz et al. (1991)</a>	2.6 1/h	<a href="#">Rollema et al. (2010)</a>
Rate constant, Plasma/CSF/ER to sequestered	kf	1.5 1/h	<a href="#">Benowitz et al. (1991)</a>	0.6 1/h	<a href="#">Rollema et al. (2010)</a>
Rate constant, sequestered to Plasma/CSF/ER	kr	1.2 1/h	<a href="#">Benowitz et al. (1991)</a>	2.5 1/h	<a href="#">Rollema et al. (2010)</a>
Absorption rate constant	ka_available	N/A		1.035 1/h	<a href="#">Rollema et al. (2010)</a>
Bioavailability	F	1		0.9	<a href="#">US Food and Drug Administration (2011)</a>

Assumed Vd: 2.86 liter/kg, 6 liter/kg; 70 kg person

Table 2.3: Parameters for nicotine and varenicline Matlab/SimBiology models.

Cell type	Drug	MP4 file number	Expression construct, LED voltage, Concentrations (if not labelled in the video)	Total time, s	Drug additions, s	Speed vs real time (fold)
<b>iDopaNeurons (iPSCs)</b>	Nicotine	1	AAV2-iNicSnFR3b_ER, 17days, 120mV, 125-25-5-1-0.2 μM	193	20	5.9
<b>HeLa cells</b>	Nicotine	2	iNicSnFR3a_PM, 30mV	285	20	9.5
		3	iNicSnFR_ER,30mV	289	20	9.6
	Varenicline	4	iNicSnFR3a, PM, 30mV	401	30	12.9
		5	iNicSnFR3a_ER, 30mV	396	30	13.2
<b>Hippocampal Cultures</b>	Nicotine	6	AAV2-iNicSnFR3b_ER, 62mV	342	20	12.2
		7	AAV2-iNicSnFR3b_PM, 125mV	335	20	12
	Varenicline	8	AAV2-iNicSnFRb_PM, 180mV	569	20	16.7
		9	AAV2-iNicSnFR3b_ER, 16mV	564	20	17.1

Each video is colored using the “fire” lookup table (blue < red < white). The lookup table is constant across the field and within each video, so that cells with varying levels of iNicSnFRs begin with varying colors. The general procedure is a series of steps in concentration of a single drug (either nicotine or varenicline), separated by control solution. Field of view is 211-μM wide. Please begin with Video 1 (nicotine). Its annotation is most complete, and it shows a “descending-increasing” series of nicotine concentrations. Figure S5 is a frame from this movie.

Table 2.4: Supplemental videos. Each video is colored using the “fire” lookup table (blue < red < white). The lookup table is constant across the field and within each video, so that cells with varying levels of iNicSnFRs begin with varying colors. The general procedure is a series of steps in concentration of a single drug (either nicotine or varenicline), separated by control solution. Field of view is 211-μM wide. Please begin with Video 1 (nicotine). Its annotation is most complete, and it shows a “descending-increasing” series of nicotine concentrations. Figure S5 is a frame from this movie.

## 2.7 Acknowledgements

Henry A. Lester and Amol V. Shivange thank the Janelia Research Campus for devoting hospitality and resources in the Visiting Scientist Program over a period of 3 y. We also thank Crystal N. Dilworth (early suggestion to use ProX-family PBPs), Jacob P. Keller (advice on pH and tubing), David P. Walton (analysis of N'MeNic), Michael R. Post (synthesis of N'MeNic), Peter H. Lee and Scott Sternson (purification of N'MeNic), Adela Nano and Jacqueline Barton (access to the ISS-K2 spectrofluorometer), Daniel Wagenaar (construction of LED light sources), Lauren M. Barnett (advice on photochemistry), Elizabeth K. Unger and Lin Tian (biosensors), Erik L. Snapp (ER imaging), Jennifer Lippincott-Schwartz (ER imaging), Eric R. Schreiter (biosensors), Tanner Lakin (cell culture), Kim Ritola and Melissa Ramirez (AAV constructs), Baljit S. Khakh (advice), Mark Lobas (advice), Victoria J. Orphan and Fabai Wu (use and instruction on structured illumination microscope), Stephen Grant (assisted in confocal microscopy), Margaret Jefferies (excellent laboratory management at Janelia), and Purnima Deshpande (excellent laboratory management at the California Institute of Technology).

This research was supported by grants from US National Institutes of Health (DA036061, DA037161, DA043829, GM123582, GM007616, MH061876, NS097362, and NS034407), the California Tobacco-Related Disease Research Project (23XT-0007), the California Institute for Regenerative Medicine (EDUC2-08398), the Brain and Behavior Research Foundation (National Alliance for Research on Schizophrenia and Depression), the Howard Hughes Medical Institute, the Della Martin Foundation, Louis and Janet Fletcher, and California Institute of Technology SURF donors Paraskeva N. Danailov and Maria Chan. E.R. Chapman is an Investigator of the Howard Hughes Medical Institute.

H.A. Lester previously had a consulting agreement with Pfizer, who manufacture varenicline. The authors declare no further competing financial interests.

Author contributions: A.V. Shivange, P.M. Borden, A.K. Muthusamy, A.L. Nichols, K. Bera, H. Bao, I. Bishara, M.J. Mulcahy, B. Cohen, E.R. Chapman, J. Marvin, L. Looger, and H.A. Lester designed experiments. A.V. Shivange, P.M. Borden, A.K. Muthusamy, A.L. Nichols, K. Bera, H. Bao, I. Bishara, J. Jeon, M.J. Mulcahy, B. Cohen, S.L. O'Riordan, C. Kim and H.A. Lester performed experiments. J. Jeon performed simulations. A.V. Shivange, P.M. Borden, A.K. Muthusamy, J. Jeon, K. Bera, H. Bao, I. Bishara, M.J. Mulcahy, L. Looger, and H.A. Lester wrote the paper. A.V. Shivange, P.M. Borden, A.K. Muthusamy, A.L. Nichols, K. Bera, H.

Bao, I. Bishara, J. Jeon, M.J. Mulcahy, B. Cohen, D.A. Dougherty, E.R. Chapman, L. Looger, and H.A. Lester revised the paper.

Merritt C. Maduke served as editor.

## 2.8 References

- Aronson, D. E., Costantini, L. M., & Snapp, E. L. (2011). Superfolder gfp is fluorescent in oxidizing environments when targeted via the sec translocon. *Traffic*, *12*(5), 543–548.
- Ashare, R. L., Lerman, C., Tyndale, R. F., Hawk, L. W., George, T. P., Cinciripini, P., & Schnoll, R. A. (2017). Sleep disturbance during smoking cessation: Withdrawal or side effect of treatment? *Journal of Smoking Cessation*, *12*(2), 63–70.
- Barnett, L. M., Hughes, T. E., & Drobizhev, M. (2017). Deciphering the molecular mechanism responsible for gcamp6m’s ca<sup>2+</sup>-dependent change in fluorescence. *PloS One*, *12*(2), e0170934.
- Beene, D. L., Brandt, G. S., Zhong, W., Zacharias, N. M., Lester, H. A., & Dougherty, D. A. (2002). Cation- $\pi$  interactions in ligand recognition by serotonergic (5-HT<sub>3A</sub>) and nicotinic acetylcholine receptors: The anomalous binding properties of nicotine. *Biochemistry*, *41*(32), 10262–10269.
- Benowitz, N. L., Jacob III, P., Denaro, C., & Jenkins, R. (1991). Stable isotope studies of nicotine kinetics and bioavailability. *Clinical Pharmacology & Therapeutics*, *49*(3), 270–277.
- Berntsson, R. P.-A., Smits, S. H., Schmitt, L., Slotboom, D.-J., & Poolman, B. (2010). A structural classification of substrate-binding proteins. *FEBS Letters*, *584*(12), 2606–2617.
- Borden, P. M., Zhang, P., Shivange, A. V., Marvin, J. S., Cichon, J., Dan, C., Podgorski, K., Figueiredo, A., Novak, O., Tanimoto, M., Shigetomi, E., Lobas, M. A., Kim, H., Zhu, P. K., Zhang, Y., Zheng, W. S., Fan, C., Wang, G., Xiang, B., . . . Looger, L. L. (2020). A fast genetically encoded fluorescent sensor for faithful in vivo acetylcholine detection in mice, fish, worms and flies. *BioRxiv*. <https://doi.org/10.1101/2020.02.07.939504>
- Bowen, A., & Xing, C. (2015, December). Nicotine salt formulations for aerosol devices and methods thereof [US Patent 9,215,895].
- Brejc, K., Van Dijk, W. J., Klaassen, R. V., Schuurmans, M., Van Der Oost, J., Smit, A. B., & Sixma, T. K. (2001). Crystal structure of an ACh-binding protein reveals the ligand-binding domain of nicotinic receptors. *Nature*, *411*(6835), 269–276.
- Casey, J. R., Grinstein, S., & Orlowski, J. (2010). Sensors and regulators of intracellular pH. *Nature Reviews Molecular Cell Biology*, *11*(1), 50–61.



- Chiu, C.-S., Jensen, K., Sokolova, I., Wang, D., Li, M., Deshpande, P., Davidson, N., Mody, I., Quick, M. W., Quake, S. R., et al. (2002). Number, density, and surface/cytoplasmic distribution of gaba transporters at presynaptic structures of knock-in mice carrying gaba transporter subtype 1–green fluorescent protein fusions. *Journal of Neuroscience*, *22*(23), 10251–10266.
- Coe, J. W., Brooks, P. R., Vetelino, M. G., Wirtz, M. C., Arnold, E. P., Huang, J., Sands, S. B., Davis, T. I., Lebel, L. A., Fox, C. B., et al. (2005). Varenicline: An  $\alpha 4\beta 2$  nicotinic receptor partial agonist for smoking cessation. *Journal of Medicinal Chemistry*, *48*(10), 3474–3477.
- Daly, J. W. (2005). Nicotinic agonists, antagonists, and modulators from natural sources. *Cellular and Molecular Neurobiology*, *25*, 513–552.
- De Duve, C., De Barsey, T., Poole, B., Trouet, A., Tulkens, P., & Van Hoof, F. (1974). Lysosomotropic agents. *Biochemical Pharmacology*, *23*(18), 2495–2531. [https://doi.org/10.1016/0006-2952\(74\)90174-9](https://doi.org/10.1016/0006-2952(74)90174-9)
- Del Castillo, J., & Katz, B. (1955). On the localization of acetylcholine receptors. *The Journal of Physiology*, *128*(1), 157.
- Dempsey, D., Tutka, P., Jacob III, P., Allen, F., Schoedel, K., Tyndale, R. F., & Benowitz, N. L. (2004). Nicotine metabolite ratio as an index of cytochrome p450 2a6 metabolic activity. *Clinical Pharmacology & Therapeutics*, *76*(1), 64–72.
- Du, Y., Shi, W.-W., He, Y.-X., Yang, Y.-H., Zhou, C.-Z., & Chen, Y. (2011). Structures of the substrate-binding protein provide insights into the multiple compatible solute binding specificities of the bacillus subtilis ABC transporter OpuC. *Biochemical Journal*, *436*(2), 283–289. <https://doi.org/10.1042/BJ20102097>
- Emsley, P., Lohkamp, B., Scott, W. G., & Cowtan, K. (2010). Features and development of coot. *Acta Crystallographica Section D: Biological Crystallography*, *66*(4), 486–501.
- Evans, P. R. (2011). An introduction to data reduction: Space-group determination, scaling and intensity statistics. *Acta Crystallographica Section D: Biological Crystallography*, *67*(4), 282–292.
- Faessel, H. M., Gibbs, M. A., Clark, D. J., Rohrbacher, K., Stolar, M., & Burstein, A. H. (2006). Multiple-dose pharmacokinetics of the selective nicotinic receptor partial agonist, varenicline, in healthy smokers. *The Journal of Clinical Pharmacology*, *46*(12), 1439–1448.
- Fagerström, K., & Hughes, J. (2008). Varenicline in the treatment of tobacco dependence. *Neuropsychiatric Disease and Treatment*, *4*(2), 353–363.
- Govind, A. P., Vallejo, Y. F., Stolz, J. R., Yan, J.-Z., Swanson, G. T., & Green, W. N. (2017). Selective and regulated trapping of nicotinic receptor weak base ligands and relevance to smoking cessation. *Elife*, *6*, e25651.

- Govind, A. P., Vezina, P., & Green, W. N. (2009). Nicotine-induced upregulation of nicotinic receptors: Underlying mechanisms and relevance to nicotine addiction. *Biochemical Pharmacology*, *78*(7), 756–765.
- Henderson, B. J., & Lester, H. A. (2015). Inside-out neuropharmacology of nicotinic drugs. *Neuropharmacology*, *96*, 178–193.
- Henderson, B. J., Wall, T. R., Henley, B. M., Kim, C. H., Nichols, W. A., Moaddel, R., Xiao, C., & Lester, H. A. (2016). Menthol alone upregulates midbrain nAChRs, alters nAChR subtype stoichiometry, alters dopamine neuron firing frequency, and prevents nicotine reward. *Journal of Neuroscience*, *36*(10), 2957–2974.
- Hussmann, G. P., Turner, J. R., Lomazzo, E., Venkatesh, R., Cousins, V., Xiao, Y., Yasuda, R. P., Wolfe, B. B., Perry, D. C., Rezvani, A. H., et al. (2012). Chronic sazetidine-a at behaviorally active doses does not increase nicotinic cholinergic receptors in rodent brain. *Journal of Pharmacology and Experimental Therapeutics*, *343*(2), 441–450.
- Jing, M., Zhang, P., Wang, G., Feng, J., Mesik, L., Zeng, J., Jiang, H., Wang, S., Looby, J. C., Guagliardo, N. A., et al. (2018). A genetically encoded fluorescent acetylcholine indicator for in vitro and in vivo studies. *Nature Biotechnology*, *36*(8), 726–737.
- Jong, Y.-J. I., Harmon, S. K., & O'Malley, K. L. (2018). Intracellular GPCRs play key roles in synaptic plasticity. *ACS chemical neuroscience*, *9*(9), 2162–2172.
- Klein, J., Köppen, A., Löffelholz, K., & Schmitthenner, J. (1992). Uptake and metabolism of choline by rat brain after acute choline administration. *Journal of Neurochemistry*, *58*(3), 870–876.
- Kuryatov, A., Luo, J., Cooper, J., & Lindstrom, J. (2005). Nicotine acts as a pharmacological chaperone to up-regulate human  $\alpha 4\beta 2$  acetylcholine receptors. *Molecular Pharmacology*, *68*(6), 1839–1851.
- Lester, H. A., Miwa, J. M., & Srinivasan, R. (2012). Psychiatric drugs bind to classical targets within early exocytotic pathways: Therapeutic effects. *Biological Psychiatry*, *72*(11), 907–915.
- Lester, H. A., Xiao, C., Srinivasan, R., Son, C. D., Miwa, J., Pantoja, R., Banghart, M. R., Dougherty, D. A., Goate, A. M., & Wang, J. C. (2009). Nicotine is a selective pharmacological chaperone of acetylcholine receptor number and stoichiometry. implications for drug discovery. *The AAPS Journal*, *11*, 167–177.
- London, R. O. P. O. (2016). Nicotine without smoke: Tobacco harm reduction. *RCP Lond*, *908*.
- Mannhold, R., Kubinyi, H., & Folkers, G. (2012). *Pharmacokinetics and metabolism in drug design* (Vol. 51). John Wiley & Sons.

- Marks, M. J., O'Neill, H. C., Wynalda-Camozzi, K. M., Ortiz, N. C., Simmons, E. E., Short, C. A., Butt, C. M., McIntosh, J. M., & Grady, S. R. (2015). Chronic treatment with varenicline changes expression of four nAChR binding sites in mice. *Neuropharmacology*, *99*, 142–155.
- Marks, M. J., Stitzel, J. A., & Collins, A. C. (1985). Time course study of the effects of chronic nicotine infusion on drug response and brain receptors. *Journal of Pharmacology and Experimental Therapeutics*, *235*(3), 619–628.
- Marvin, J. S., Borghuis, B. G., Tian, L., Cichon, J., Harnett, M. T., Akerboom, J., Gordus, A., Renninger, S. L., Chen, T.-W., Bargmann, C. I., et al. (2013a). An optimized fluorescent probe for visualizing glutamate neurotransmission. *Nature Methods*, *10*(2), 162–170.
- Marvin, J. S., Borghuis, B. G., Tian, L., Cichon, J., Harnett, M. T., Akerboom, J., Gordus, A., Renninger, S. L., Chen, T.-W., Bargmann, C. I., Orger, M. B., Schreiter, E. R., Demb, J. B., Gan, W.-B., Hires, S. A., & Looger, L. L. (2013b). An optimized fluorescent probe for visualizing glutamate neurotransmission. *Nature Methods*, *10*(2), 162–170. <https://doi.org/10.1038/nmeth.2333>
- Marvin, J. S., Scholl, B., Wilson, D. E., Podgorski, K., Kazemipour, A., Müller, J. A., Schoch, S., Quiroz, F. J. U., Rebola, N., Bao, H., Little, J. P., Tkachuk, A. N., Cai, E., Hantman, A. W., Wang, S. S.-H., DePiero, V. J., Borghuis, B. G., Chapman, E. R., Dietrich, D., . . . Looger, L. L. (2018). Stability, affinity, and chromatic variants of the glutamate sensor iGluSnFR. *Nature Methods*, *15*(11), 936–939. <https://doi.org/10.1038/s41592-018-0171-3>
- McGregor, A. L., D'Souza, G., Kim, D., & Tingle, M. D. (2017). Varenicline improves motor and cognitive deficits and decreases depressive-like behaviour in late-stage yac128 mice. *Neuropharmacology*, *116*, 233–246.
- Mihalak, K. B., Carroll, F. I., & Luetje, C. W. (2006). Varenicline is a partial agonist at  $\alpha 4\beta 2$  and a full agonist at  $\alpha 7$  neuronal nicotinic receptors. *Molecular pharmacology*, *70*(3), 801–805.
- Mitchell, P. (2011). Chemiosmotic coupling in oxidative and photosynthetic phosphorylation. *Biochimica et Biophysica Acta (BBA)-Bioenergetics*, *1807*(12), 1507–1538.
- Miwa, J. M., Freedman, R., & Lester, H. A. (2011). Neural systems governed by nicotinic acetylcholine receptors: Emerging hypotheses. *Neuron*, *70*(1), 20–33.
- Morales-Perez, C. L., Noviello, C. M., & Hibbs, R. E. (2016). X-ray structure of the human  $\alpha 4\beta 2$  nicotinic receptor. *Nature*, *538*(7625), 411–415.
- Moss, F. J., Imoukhuede, P., Scott, K., Hu, J., Jankowsky, J. L., Quick, M. W., & Lester, H. A. (2009). Gaba transporter function, oligomerization state, and anchoring: Correlates with subcellularly resolved fret. *Journal of General Physiology*, *134*(6), 489–521.

- Muthusamy, A. K., Shivange, A. V., Nichols, A. L., Kamajaya, A., Jeon, J., Borden, P. M., Marvin, J. S., Unger, E. K., Bao, H., Chapman, E. R., et al. (2018). Microscopy using fluorescent drug biosensors for “inside-out pharmacology”. *Biophysical Journal*, *114*(3), 358a.
- Naudé, J., Dongelmans, M., & Faure, P. (2015). Nicotinic alteration of decision-making. *Neuropharmacology*, *96*(Pt B), 244–254.
- Nees, F. (2015). The nicotinic cholinergic system function in the human brain. *Neuropharmacology*, *96*(Pt B), 289–301.
- Nickell, J. R., Grinevich, V. P., Siripurapu, K. B., Smith, A. M., & Dwoskin, L. P. (2013). Potential therapeutic uses of mecamylamine and its stereoisomers. *Pharmacology, Biochemistry, and Behavior*, *108*, 28–43.
- Oswald, C., Smits, S. H., ing, M., sser, L., Dupont, L., Le Rudulier, D., Schmitt, L., & Bremer, E. (2008). Crystal structures of the choline/acetylcholine substrate-binding protein ChoX from *Sinorhizobium meliloti* in the liganded and unliganded-closed states. *Journal of Biological Chemistry*, *283*(47), 32848–32859.
- Pantoja, R., Rodriguez, E. A., Dibas, M. I., Dougherty, D. A., & Lester, H. A. (2009). Single-molecule imaging of a fluorescent unnatural amino acid incorporated into nicotinic receptors. *Biophysical Journal*, *96*(1), 226–237.
- Patriarchi, T., Cho, J. R., Merten, K., Howe, M. W., Marley, A., Xiong, W. H., Folk, R. W., Broussard, G. J., Liang, R., Jang, M. J., Zhong, H., Dombeck, D., von Zastrow, M., Nimmerjahn, A., Gradinaru, V., Williams, J. T., & Tian, L. (2018). Ultrafast neuronal imaging of dopamine dynamics with designed genetically encoded sensors. *Science*, *360*(6396).
- Pédélecq, J. D., Cabantous, S., Tran, T., Terwilliger, T. C., & Waldo, G. S. (2006). Engineering and characterization of a superfolder green fluorescent protein. *Nature Biotechnology*, *24*(1), 79–88.
- Petersson, E. J., Choi, A., Dahan, D. S., Lester, H. A., & Dougherty, D. A. (2002). A perturbed pK(a) at the binding site of the nicotinic acetylcholine receptor: Implications for nicotine binding. *Journal of the American Chemical Society*, *124*(43), 12662–12663.
- Picciotto, M. R., Lewis, A. S., van Schalkwyk, G. I., & Mineur, Y. S. (2015). Mood and anxiety regulation by nicotinic acetylcholine receptors: A potential pathway to modulate aggression and related behavioral states. *Neuropharmacology*, *96*(Pt B), 235–243.
- Pittelkow, M., Tschapek, B., Smits, S. H., Schmitt, L., & Bremer, E. (2011). The crystal structure of the substrate-binding protein OpuBC from *Bacillus subtilis* in complex with choline. *Journal of Molecular Biology*, *411*(1), 53–67. <https://doi.org/10.1016/j.jmb.2011.05.037>

- Post, M. R., Lester, H. A., & Dougherty, D. A. (2017). 2 Nicotinic Acetylcholine Receptors. *Biochemistry*, *56*(13), 1836–1840.
- Powell, H. R., Battye, T. G. G., Kontogiannis, L., Johnson, O., & Leslie, A. G. W. (2017). Integrating macromolecular X-ray diffraction data with the graphical user interface iMosflm. *Nat Protoc*, *12*(7), 1310–1325.
- Richards, C. I., Srinivasan, R., Xiao, C., Mackey, E. D., Miwa, J. M., & Lester, H. A. (2011). Trafficking of alpha4\* nicotinic receptors revealed by superecliptic phluorin: effects of a beta4 amyotrophic lateral sclerosis-associated mutation and chronic exposure to nicotine. *Journal of Biological Chemistry*, *286*(36), 31241–31249.
- Rollema, H., Chambers, L. K., Coe, J. W., Glowa, J., Hurst, R. S., Lebel, L. A., Lu, Y., Mansbach, R. S., Mather, R. J., Rovetti, C. C., Sands, S. B., Schaeffer, E., Schulz, D. W., Tingley, F. D., & Williams, K. E. (2007). Pharmacological profile of the alpha4beta2 nicotinic acetylcholine receptor partial agonist varenicline, an effective smoking cessation aid. *Neuropharmacology*, *52*(3), 985–994.
- Rollema, H., Shrikhande, A., Ward, K. M., Tingley, F. D., Coe, J. W., O'Neill, B. T., Tseng, E., Wang, E. Q., Mather, R. J., Hurst, R. S., Williams, K. E., de Vries, M., Cremers, T., Bertrand, S., & Bertrand, D. (2010). Pre-clinical properties of the alpha4beta2 nicotinic acetylcholine receptor partial agonists varenicline, cytisine and dianicline translate to clinical efficacy for nicotine dependence. *British Journal of Pharmacology*, *160*(2), 334–345.
- Salette, J., Pons, S., Devillers-Thierry, A., Soudant, M., Prado de Carvalho, L., Changeux, J. P., & Corringer, P. J. (2005). Nicotine upregulates its own receptors through enhanced intracellular maturation. *Neuron*, *46*(4), 595–607.
- Schiefner, A., Breed, J., sser, L., Kneip, S., Gade, J., Holtmann, G., Diederichs, K., Welte, W., & Bremer, E. (2004). Cation-pi interactions as determinants for binding of the compatible solutes glycine betaine and proline betaine by the periplasmic ligand-binding protein ProX from *Escherichia coli*. *J Biol Chem*, *279*(7), 5588–5596.
- Sharma, A. K., Gupta, S., Patel, R. K., & Wardhan, N. (2018). Haloperidol-induced parkinsonism is attenuated by varenicline in mice. *Journal of Basic and Clinical Physiology and Pharmacology*, *29*(4), 395–401.
- Srinivasan, R., Henderson, B. J., Lester, H. A., & Richards, C. I. (2014). Pharmacological chaperoning of nAChRs: A therapeutic target for Parkinson's disease. *Pharmacological Research*, *83*, 20–29.
- Srinivasan, R., Henley, B. M., Henderson, B. J., Indersmitten, T., Cohen, B. N., Kim, C. H., McKinney, S., Deshpande, P., Xiao, C., & Lester, H. A. (2016). Smoking-relevant nicotine concentration attenuates the unfolded protein response in dopaminergic neurons. *Journal of Neuroscience*, *36*(1), 65–79.

- Srinivasan, R., Pantoja, R., Moss, F. J., Mackey, E. D., Son, C. D., Miwa, J., & Lester, H. A. (2011). Nicotine up-regulates alpha4beta2 nicotinic receptors and ER exit sites via stoichiometry-dependent chaperoning. *Journal of General Physiology*, *137*(1), 59–79.
- Srinivasan, R., Richards, C. I., Xiao, C., Rhee, D., Pantoja, R., Dougherty, D. A., Miwa, J. M., & Lester, H. A. (2012). Pharmacological chaperoning of nicotinic acetylcholine receptors reduces the endoplasmic reticulum stress response. *Molecular Pharmacology*, *81*(6), 759–769.
- Stoeber, M., Jullié, D., Lobingier, B. T., Laeremans, T., Steyaert, J., Schiller, P. W., Manglik, A., & von Zastrow, M. (2018). A genetically encoded biosensor reveals location bias of opioid drug action. *Neuron*, *98*(5), 963–976.e5. <https://doi.org/10.1016/j.neuron.2018.04.021>
- Subramaniam, M., & Dani, J. A. (2015). Dopaminergic and cholinergic learning mechanisms in nicotine addiction. *Annals of the New York Academy of Sciences*, *1349*(1), 46–63.
- Tanner, J. A., Chenoweth, M. J., & Tyndale, R. F. (2015). Pharmacogenetics of nicotine and associated smoking behaviors. *Current Topics in Behavioral Neurosciences*, *23*, 37–86.
- Tischbirek, C. H., Wenzel, E. M., Zheng, F., Huth, T., Amato, D., Trapp, S., Denker, A., Welzel, O., Lueke, K., Svetlitchny, A., et al. (2012). Use-dependent inhibition of synaptic transmission by the secretion of intravesicularly accumulated antipsychotic drugs. *Neuron*, *74*(5), 830–844.
- Tschapek, B., Pittelkow, M., Sohn-Bösser, L., Holtmann, G., Smits, S. H., Gohlke, H., Bremer, E., & Schmitt, L. (2011). Arg149 is involved in switching the low affinity, open state of the binding protein afprox into its high affinity, closed state. *Journal of Molecular Biology*, *411*(1), 36–52.
- Turner, J. R., Castellano, L. M., & Blendy, J. A. (2011). Parallel anxiolytic-like effects and upregulation of neuronal nicotinic acetylcholine receptors following chronic nicotine and varenicline. *Nicotine Tobacco Research*, *13*(1), 41–46.
- Van Arnam, E. B., Blythe, E. E., Lester, H. A., & Dougherty, D. A. (2013). 7 nicotinic acetylcholine receptor, with implications for the binding of varenicline. *Molecular Pharmacology*, *84*(2), 201–207.
- Van Arnam, E. B., & Dougherty, D. A. (2014). Functional probes of drug-receptor interactions implicated by structural studies: Cys-loop receptors provide a fertile testing ground. *Journal of Medicinal Chemistry*, *57*(15), 6289–6300.
- Wolters, J. C., Berntsson, R. P., Gul, N., Karasawa, A., Thunnissen, A. M., Slotboom, D. J., & Poolman, B. (2010). Ligand binding and crystal structures of the substrate-binding domain of the ABC transporter OpuA. *PLoS One*, *5*(4), e10361.

- Yu, H., Dickson, E. J., Jung, S. R., Koh, D. S., & Hille, B. (2016). High membrane permeability for melatonin. *Journal of General Physiology*, *147*(1), 63–76.
- Zhong, W., Gallivan, J. P., Zhang, Y., Li, L., Lester, H. A., & Dougherty, D. A. (1998). From ab initio quantum mechanics to molecular neurobiology: a cation- $\pi$  binding site in the nicotinic receptor. *PNAS*, *95*(21), 12088–12093.

## Chapter 3

## Evolution of iS-methadoneSnFR for Subcellular Pharmacokinetics and Biofluid Measurements

**Muthusamy, A. K.**, Kim, C. H., Virgil, S. C., Knox, H. J., Marvin, J. S., Nichols, A. L., Cohen, B. N., Dougherty, D. A., Looger, L. L., & Lester, H. A. (2022). Three mutations convert the selectivity of a protein sensor from nicotinic agonists to S-methadone for use in cells, organelles, and biofluids. *Journal of the American Chemical Society*, 144(19), 8480-8486. <https://doi.org/10.1021/jacs.2c02323>

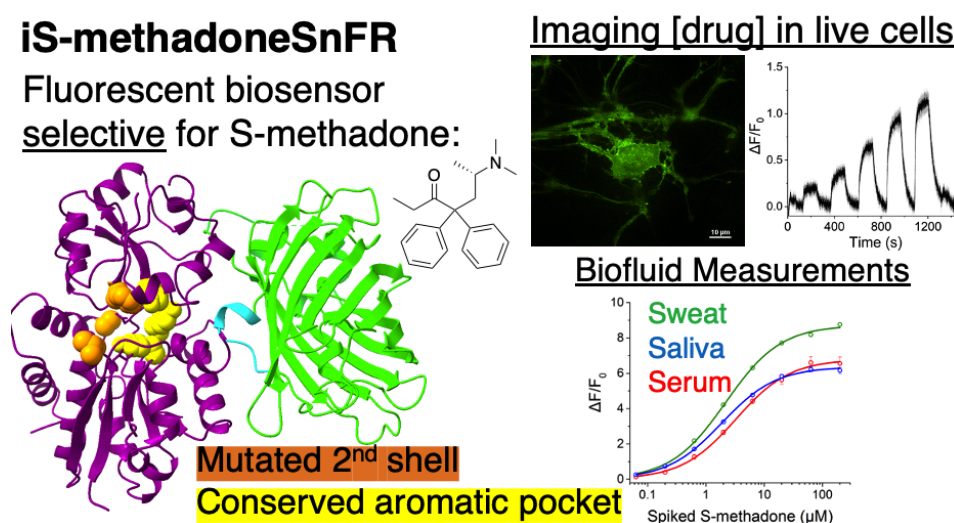


Figure 3.1: iS-methadoneSnFR in primary culture and human biofluids.

### 3.1 Abstract

We report a reagentless, intensity-based S-methadone fluorescent sensor, iS-methadoneSnFR, consisting of a circularly permuted GFP inserted within the sequence of a mutated bacterial periplasmic binding protein (PBP). We evolved a previously reported nicotine-binding PBP to become a selective S-methadone-binding sensor, via three mutations in the PBP's second shell and hinge regions. iS-methadoneSnFR displays the necessary sensitivity, kinetics, and selectivity—notably enantioselectivity against R-methadone—for biological applications. Robust iS-methadoneSnFR responses in human sweat and saliva and mouse serum enable diagnostic uses. Expression and imaging in mammalian cells demonstrate that S-methadone enters at least two organelles and undergoes acid trapping in the Golgi apparatus, where



opioid receptors can signal. This work shows a straightforward strategy in adapting existing PBPs to serve real-time applications ranging from subcellular to personal pharmacokinetics.

### 3.2 Introduction

We report the first selective real-time fluorescent biosensor for a small molecule opioid, “intensity-based S-methadone sensing fluorescent reporter” or “iS-methadoneSnFR” (Figure 3.1). To employ the indicator for quantitative dynamic opioid measurements in cells and biofluids, we engineered iS-methadoneSnFR to meet necessary criteria: (1) sensitivity in the pharmacological range, (2) selectivity against endogenous molecules, (3) selectivity against exogenous drugs, including those of the same drug class, (4) photostability for the duration of measurements, (5) physical stability outside cells, and (6) reversible binding with ~second resolution.

The risk of opioid-use disorder and death by overdose has increased alongside the worldwide access to highly potent opioid agonists (Althoff et al., 2020). Nevertheless, opioids remain essential analgesics. Since the 1960s, methadone maintenance therapy (MMT) has served to reduce harm from opioid addiction (Dole, 1965, 1971). MMT relies on pharmacokinetics: oral methadone’s onset is slower than that of injected or inhaled  $\mu$ -opioids, and its effects last much longer due to a ~24 h half-life (Cruciani and Knotkova, n.d.). Therefore, despite acting as a  $\mu$ -opioid agonist, methadone staves off withdrawal symptoms without producing the euphoria associated with other agonists Cruciani and Knotkova, n.d. However, interindividual variability in the metabolism of methadone, partially due to polymorphisms in cytochrome P450 isotypes, (Eap et al., 2002; Li et al., 2008) can lead to therapeutic failures (Nilsson et al., 1983).

Methadone is clinically administered as the racemate and measuring either enantiomer is suitable for therapeutic drug monitoring (Foster et al., 2000). Drug metabolism is conventionally addressed by blood draw, but this method is laborious, invasive, and restricted to the clinic. An optimal methadone readout would enable personalized dosing regimens, by producing real-time tracking of [methadone] in biological fluids and facilitating tapering from potent opioids. Within a subject, opioid pharmacokinetics also vary at the level of intracellular compartments to produce acid trapping and diverse interactions with receptors including chaperoning and activation (Lester et al., 2012; Petäjä-Repo and Lackman, 2014; Stoeber et al., 2018). In both cases, a sensor with *in situ* readout and ~second resolution is required.

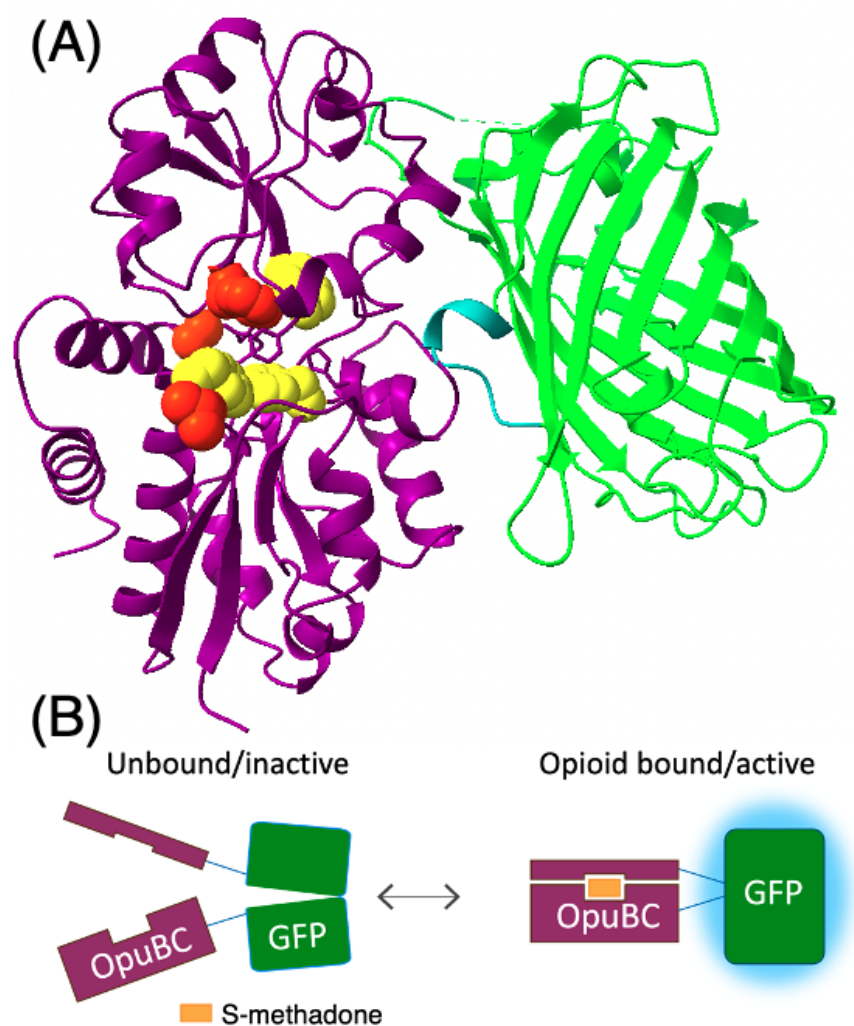


Figure 3.2: Biosensing Scheme for iS-methadoneSnFR. (a) Crystal structure of iNicSnFR3a (PDB:7S7T) mutated in silico to iS-methadoneSnFR (mutations shown in orange spheres). All but one putative cation $\pi$  residue in iNicSnFR3a were maintained in iS-methadoneSnFR's binding pocket (critical residues Y65, Y357, and Y460 shown as yellow spheres). (b) Biosensor mechanism: in the unbound state, GFP's chromophore has a poor environment for fluorescence. The PBP binds S-methadone with a "Venus fly trap" conformational change, increasing the brightness of the GFP chromophore.

Conventional small molecule detection methods have been extended to methadone but may be limited in specificity, temporal resolution, or spatial resolution (Ahmed et al., 2020). An antibody against methadone was used in a lateral flow test of human sweat (limited to a single time point) (Hudson et al., 2019). Electrochemical methods provide continuous measurements but vary in selectivity against other

opioids (Ardeshiri and Jalali, 2016; Khorablou et al., 2021; Rezaei et al., 2020) and, in all cases, cannot be used for subcellular measurements. A pioneering de novo protein design campaign for an opioid sensor, the binding of fentanyl produced a conformational switch in a transcription factor (Bick et al., 2017) but required a cellular readout and hours-to-days temporal resolution.

### 3.3 Lead Discovery: Methadone Isomer x Nicotinic Biosensor Library Screen

We hypothesized that all the required criteria could be satisfied by a single-chain sensor comprising a mutated bacterial periplasmic binding protein (PBP), a variant of the choline-binding protein OpuBC from *Thermoanaerobacter sp513*, interrupted by a circularly permuted GFP (cpGFP) (Figure 3.1) (Borden et al., 2020; Marvin et al., 2013; Shivange et al., 2019). The cpGFP insertion approach has also been used in Ca<sup>2+</sup> sensors (the GCaMP series) and in neurotransmitter sensors (Marvin et al., 2013; Tian et al., 2009). Our strategy consisted of (1) screening each methadone enantiomer against a previously reported nicotine biosensor, iNicSnFR3a, and its variants (Shivange et al., 2019) and (2) iterative site-saturation mutagenesis to select for S-methadone and against cholinergic ligands (Figure 3.2a). We performed chiral resolution on racemic methadone to isolate (+)-S-methadone and (-)-R-methadone (assigned by optical rotation) (Larsen et al., 1948) with analytical purity and 99% enantiomeric excess (Figure 3.8).

While there is no structural homology or pharmacological overlap between nicotinic and  $\mu$ -opioid receptors, several variants of nicotinic drug biosensors displayed weak fluorescence responses to S-methadone (Figure 3.2b). Although the PBP had no enantioselective pressure for binding its achiral ligand choline, all variants screened to date displayed enantioselectivity for S-methadone (Figure 3.9). Dose-response relations were fit to the Hill equation to determine an EC<sub>50</sub> and  $\Delta F_{\max}/F_0$ . In the linear portion of the dose-response relation we define the increase in fluorescence per micromolar, “S-slope,” as a metric of biosensor sensitivity:  $(\Delta(F/F_0)/(\Delta[\text{ligand}]])$  at  $[\text{drug}] = EC_{50}/23$ . For a Hill coefficient of  $\sim 1.0$ , the S-slope equals the ratio  $(\Delta F_{\max}/F_0)/EC_{50}$ . A variant of iNicSnFR3a, iNicSnFR3b, provided the largest dynamic range for both S-methadone and R-methadone (Figure 3.9) and served as the input to several rounds of directed evolution.

### 3.4 Directed Evolution of iS-methadoneSnFR

We selected for both an increase in sensitivity to S-methadone and a decrease in sensitivity to nicotinic ligands. We chose mutation sites based on a crystal structure

of iNicSnFR1 (PDB:6EFR) and directed evolution of iNicSnFR3a(Shivange et al., 2019).

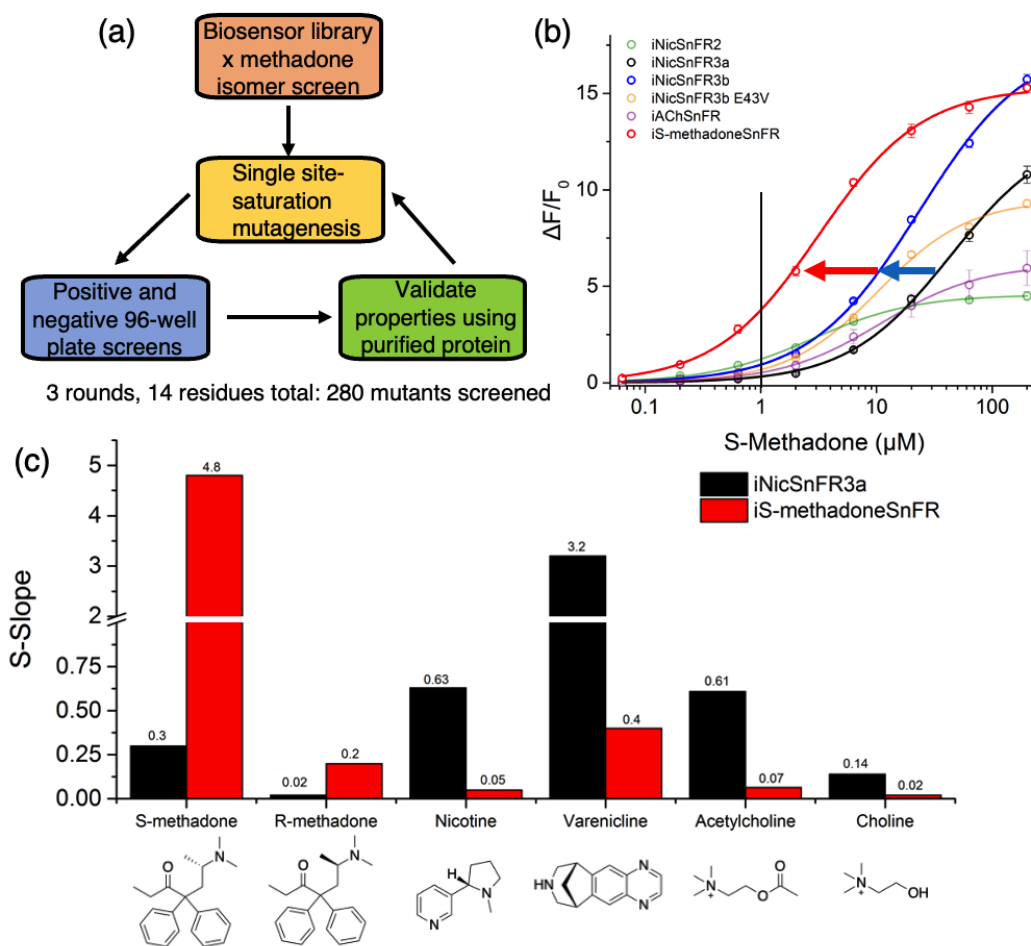


Figure 3.3: Improving Sensitivity and Selectivity Toward iS-methadoneSnFR. (a) Directed evolution strategy. (b) Fluorescence responses to S-methadone. iNicSnFR3a (black) has several variants (faded curves), of which one has markedly better sensitivity, owing to the N11E mutation (blue). This lead was evolved to iS-methadoneSnFR (red), which included reoptimization at position 11. Only the final biosensor had sufficient sensitivity at 1  $\mu\text{M}$  (vertical black line; the relevant maintenance concentration). (c) Shift in selectivity from iNicSnFR3a (black) to iS-methadoneSnFR (red) measured by S-slope (see text). Note the scale change at the axis break.

The resulting sensor displayed a ~16-fold improvement in sensitivity over iNicSnFR3a;  $\Delta F/F_0$  increased to  $3.76 \pm 0.16$  at 1  $\mu\text{M}$ , the representative plasma maintenance concentration<sup>8</sup> (Figure 3.2b). Notably, iS-methadoneSnFR displayed sensitivity to S-methadone that exceeded the sensitivity for any of the original cholinergic ligands and displayed a marked shift in ligand selectivity (Figure 3.2c).

iS-methadoneSnFR displayed near-zero response for physiologically or pharmacologically relevant steady-state acetylcholine (ACh), choline, varenicline, and nicotine concentrations ( $\sim 1 \mu\text{M}$ , 10 to 20  $\mu\text{M}$  (Zeisel et al., 1980), 0 to 100 nM (Faessel et al., 2010), and  $\sim 25$  to  $\sim 500$  nM, respectively (Russell et al., 1980) (see Figure 3.4a)).

### 3.5 Biophysical Characterization of iS-methadoneSnFR

We characterized iS-methadoneSnFR's binding using docking and biochemical studies. Although only three mutations were required to generate iS-methadoneSnFR from iNicSnFR3a/3b, advantageous mutations were rare:  $\sim 1\%$  of all mutations screened were accepted as improvements. Docking S-methadone into recently reported structures of liganded iNicSnFR3a27 showed that the N-methyl groups of S-methadone lie 4.6 and 5.5 Å from the aromatic groups of Y357 and Y65, respectively (slightly greater than the distance from the beta carbons of varenicline to these two groups). In the initial round of mutations, most sites yielded no improvement, except for a W436F mutation spatially near Y65 and Y357 (Figure 3.10). We previously reported nicotine and varenicline making cation- $\pi$  interactions with Y65 and Y357 in iNicSnFR3a (PDB:7S7T and 7S7U, respectively).<sup>27</sup> Each nicotinic ligand bears a protonated nitrogen lying midway on the axis of the aromatic centroids of Y65 and Y357 (Figure 3.3a). In the subsequent round, second-shell mutation N11V created additional volume next to F12, in the second shell. Finally, the third round yielded L490A, allowing for greater flexibility in the hinging of the PBP.

Leucine mutagenesis among individual binding pocket aromatic residues showed the primacy of Y65, Y357, F12, and Y460 (Figure 3.3b). An aromatic side-chain screen across these four positions revealed a necessity of Tyr in the first shell positions Y65, Y357, and Y460 (Figure 3.3c). Substituting a noncanonical side chain, O-methyltyrosine, yielded a near-null biosensor at residue 65 but not at 12 (Figure 3.11). These data suggest that S-methadone's amine directly interacts with the first shell residues, as with nicotinic drugs, and the phenolic -OH is necessary for hydrogen bonding. The three accepted mutations represent a 94 Å<sup>3</sup> reduction in van der Waals' volume, comparable to the 132 Å<sup>3</sup> increase in ligand volume from varenicline to methadone, as though the accepted mutations allowed S-methadone better access to aromatic residues critical to binding both classes of drugs. Therefore, the PBP has an aromatic binding pocket for protonated amines, and other regions of the binding site can be tuned to accommodate the remainder of the ligand's steric bulk and functional groups.

iS-methadoneSnFR satisfied our sensitivity, selectivity, and biophysical criteria for a useful biosensor. Fluorescence dose- response relations showed an excellent dynamic range,  $\Delta F_{\max}/F_0$  of  $15.3 \pm 0.2$ , and an  $EC_{50}$ ,  $3.2 \pm 0.2 \mu\text{M}$ , near the relevant plasma concentrations for maintenance therapy.<sup>8</sup> Isothermal titration calorimetry (ITC) determined a  $K_d$  of  $1.9 \pm 0.2 \mu\text{M}$ , in good agreement with the fluorescence  $EC_{50}$  (Figure 3.4c). ITC also demonstrated a single binding site (stoichiometry = 0.92) with an entropically driven conformational change. iSmethadoneSnFR had little or no response (S-slope  $< 0.1 \mu\text{M}^{-1}$ ) to other neurotransmitters (Figure 3.14a) and other opioids (Figure 3.4b). The S-slope for S-methadone was  $\sim 20\times$  that for R-methadone. When we added R-methadone to Smethadone, fluorescence was modestly elevated at lower [Smethadone], but all responses converged at the  $\Delta F_{\max}/F_0$  for S-methadone alone (Figure 3.12). 1 s stopped flow kinetics were obtained using racemic methadone (Figure 3.11) and determined an apparent  $k_{\text{on}}$  of  $0.13 \mu\text{M}^{-1} \text{ s}^{-1}$  (Figure 3.4d). The final 10 ms of the 1 s stopped-flow traces were fitted by a Hill equation with  $EC_{50} \sim 8 \mu\text{M}$  (Figure 3.13) for the racemate, which was approximately double the  $EC_{50}$  for S-methadone alone (as expected if the binding strongly favors the (s) enantiomer).

### 3.6 Application in Mammalian Biofluids and Cells

#### Biofluid Application

Therapeutic use of opioids would be improved by quantitative, real-time, minimally invasive or noninvasive measurements in sweat, saliva, and interstitial fluid.<sup>28,29</sup> The selectivity and high aqueous solubility of iS-methadoneSnFR enable its use in such applications. We tested the biosensor in PBS:biofluid samples and found robust responses in the pharmacologically relevant concentration range (Figure 3.5). iSmethadoneSnFR, like all GFP-based biosensors, displays smaller responses at  $\text{pH} < \sim 7$  (Figure 3.14). Because biofluids, particularly sweat, have variable and/or acidic pH,  $3\times$  PBS pH 7.4 was used to partially buffer a mixture with the biofluid. Still, the response at  $1 \mu\text{M}$  and below in the biofluids provide at least  $\sim 200\%$  dynamic range.

#### Subcellular Pharmacokinetics in HeLa

At the subcellular level, membrane-permeant weakly basic opioid drugs, but not impermeant derivatives or endogenous opioid peptides, enter the endoplasmic reticulum, and can act as pharmacological chaperones, altering the folding and trafficking of their receptors (Petäjä-Repo and Lackman, 2014). Opioid drugs also activate their receptors in endosomes and the Golgi apparatus (Stoeber et al., 2018). We

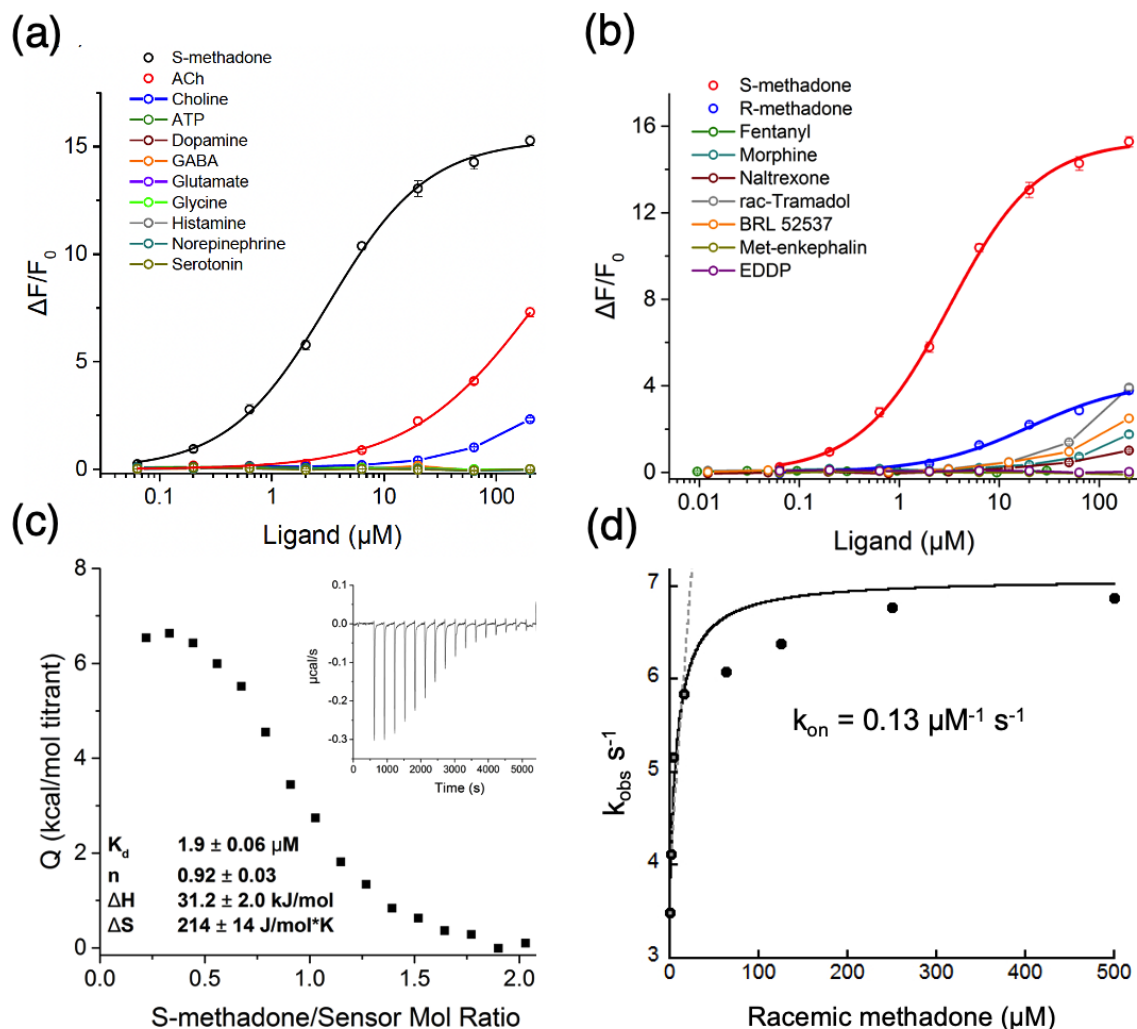


Figure 3.4: Selectivity and biophysical properties of iS-methadoneSnFR. (a) iS-methadoneSnFR vs endogenous neurotransmitters and choline. Responses to ACh and choline had S-slopes  $< 0.1 \mu\text{M}^{-1}$ . (b) iS-methadoneSnFR vs other clinically used opioids. The response to R-methadone was near zero at  $\sim 1 \mu\text{M}$ . Weak or no responses were observed for other drugs tested. EDDP is 2-ethylidene-1,5-dimethyl-3,3-diphenylpyrrolidine, the major metabolite of methadone. (c) Isothermal titration calorimetry of purified iS-methadoneSnFR. Thirty  $\mu\text{M}$  of the biosensor was mixed with  $2 \mu\text{L}$  injections of  $300 \mu\text{M}$  S-methadone. (d) Stopped-flow kinetic measurements with racemic methadone.

targeted iS-methadoneSnFR to the plasma membrane (Figure 3.6a), endoplasmic reticulum (Figure 3.6b), and Golgi apparatus (Figure 3.6c) of HeLa cells using targeting sequences. We applied pulses of S-methadone (0 to 250 nM in 50 nM steps) to measure the linear portion of the dose-response relation (S-slope) in widefield imaging (Figure 3.15). The results indicate that ample S-methadone is available in

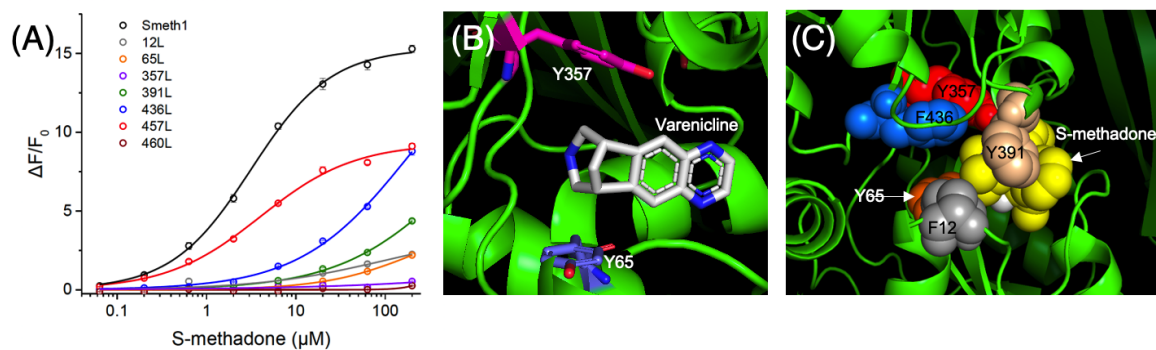


Figure 3.5: Structural Basis of S-methadone Recognition. (a) PDB:7S7T(iNicSnFR3a, varenicline bound) showing cation- $\pi$  interactions with Y65 and Y357. S-methadone was docked into 7S7T. (b) Fluorescence dose-response relations of cation- $\pi$  residue Leu mutants. (c) Aromatic side-chain screen through critical positions identified in (b) with resulting S-slope. Note the break in y-axis.

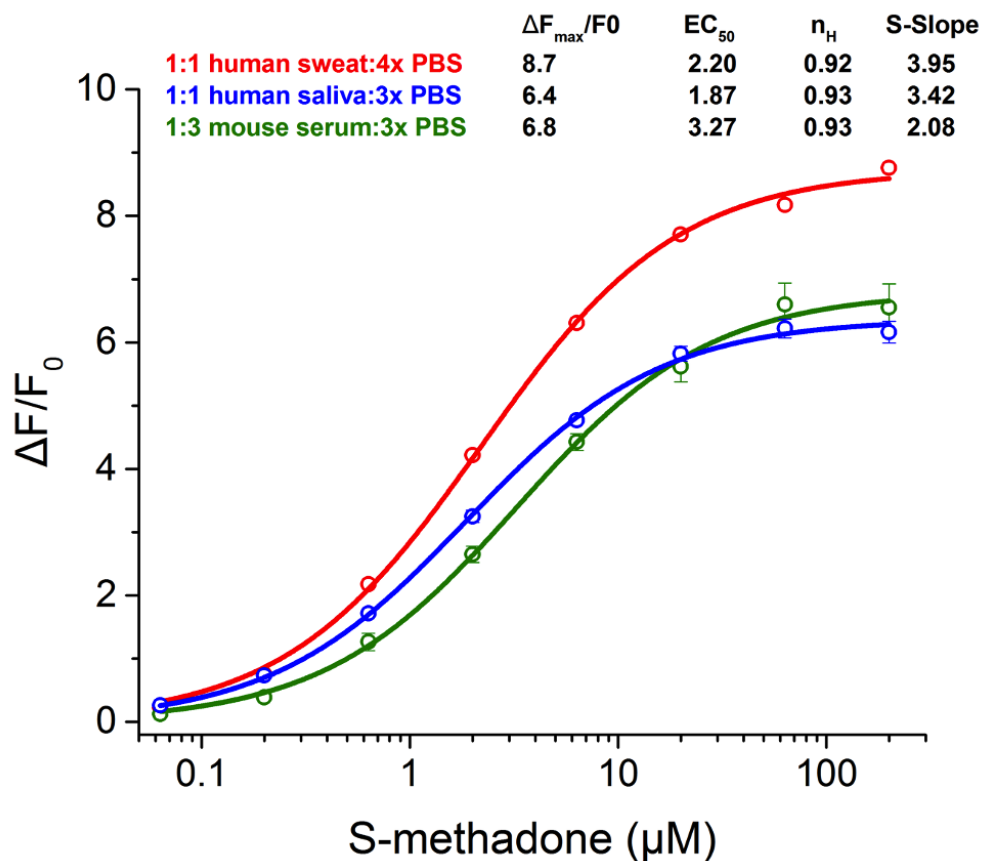


Figure 3.6: iS-methadoneSnFR dose-response relation in biofluids. 1:1 mixture of drug:biosensor in 3 $\times$  PBS pH 7.4 with either human sweat or human saliva and 1:3 mixture with mouse serum (no pH adjustment of any biofluid).



the ER for potential chaperoning. The Golgi showed the largest S-slope among the three compartments ( $1.7\times$  that of PM), despite having the lowest pH (Figure 3.6d). After correcting the S-slope for pH dependence, we find an accumulation factor of  $2.9\times$  to  $4.4\times$  across the Golgi pH range of 6.3 to 6.830 (Figure 3.15). Accumulation of opioids such as methadone in acidic compartments<sup>31</sup> may lead to intensified G-protein coupled signaling. We also validated iS-methadoneSnFR for time-resolved measurements in primary hippocampal neurons, encouraging mechanistic studies in tissues and *in vivo* (Figure 3.16).

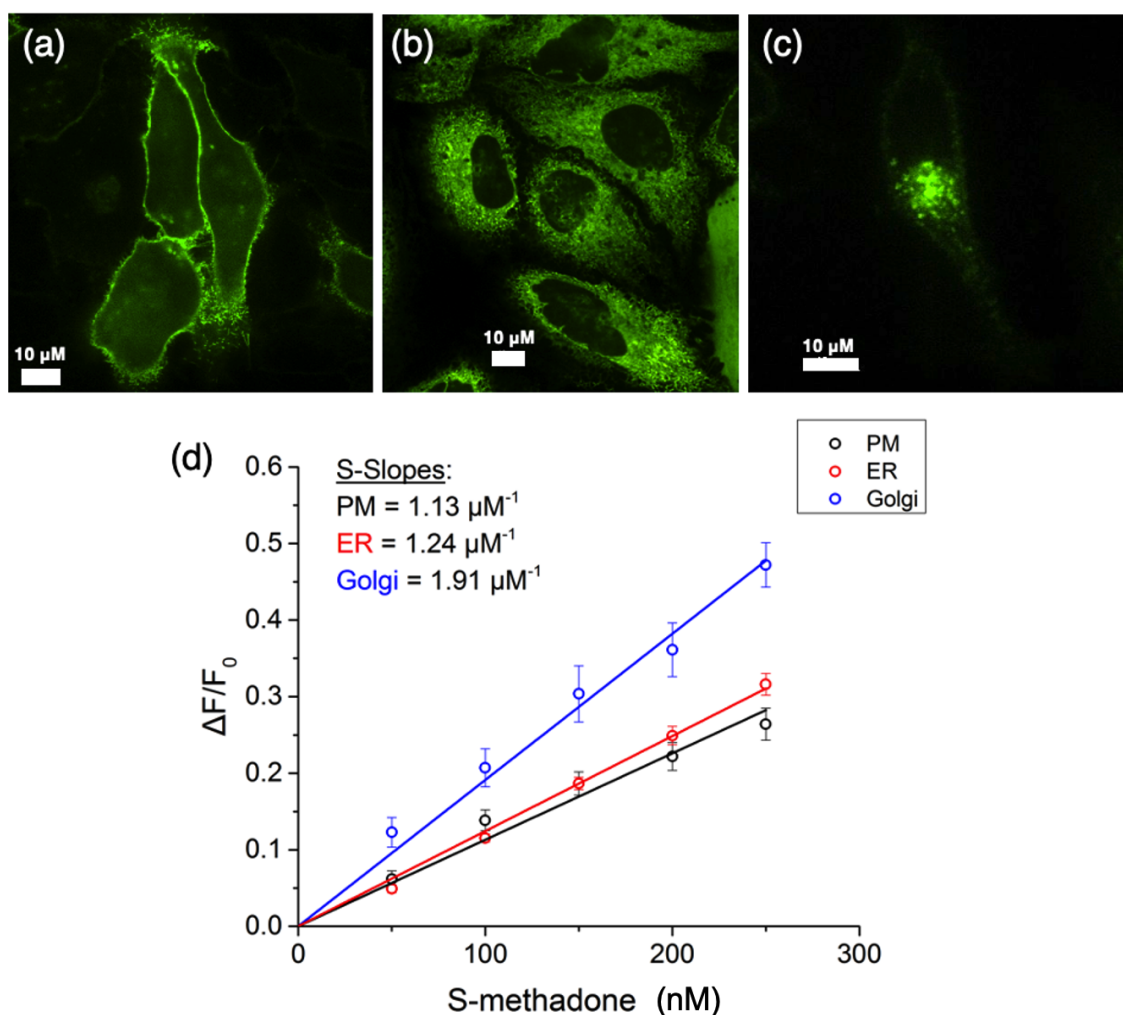


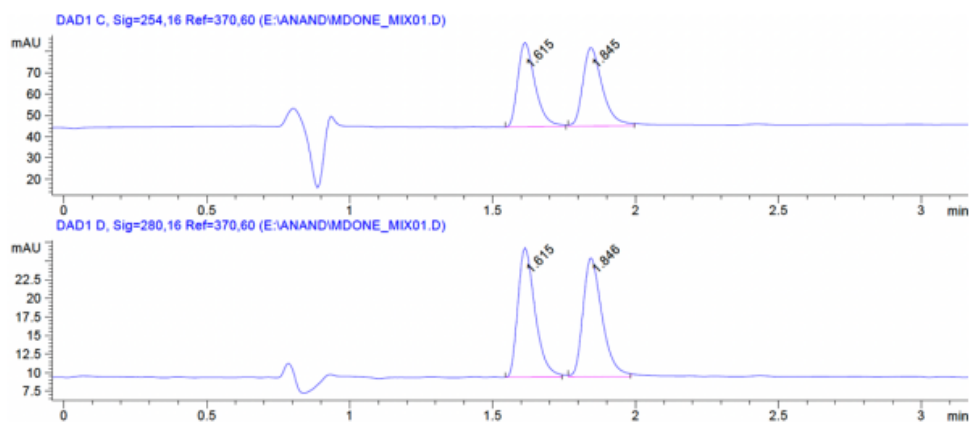
Figure 3.7: Spinning disk confocal imaging of HeLa cells transfected with (a) iS-methadoneSnFR\_PM, (b) \_ER, and (c) \_Golgi (470 nm excitation, 535 nm emission,  $100\times$  1.4 NA objective). Scale bar = 10  $\mu\text{m}$ . (d) S-slope plotted for each organelle response at 0–250 nM S-methadone. Points are average responses to a 1 min pulse of [S-methadone]. PM n = 11 cells; ER n = 10; Golgi n = 11.

### 3.7 Discussion

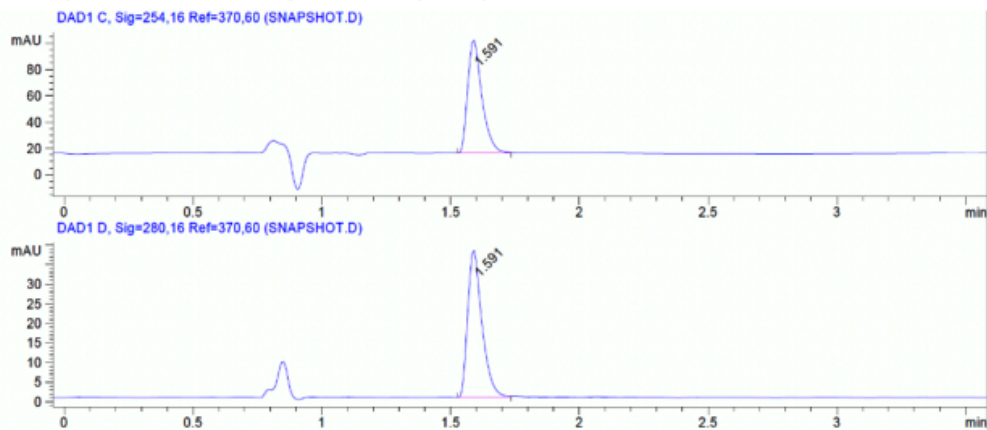
Along with other sensors of opioid signaling, (Abraham et al., 2021; Stoeber et al., 2018) this study establishes the first genetically encoded fluorescent protein biosensor for an opioid drug, enabling real-time quantification. Furthermore, the enantioselectivity encourages biosensor development to investigate “chiral switching” of other drugs where a single enantiomer substitutes a clinically used racemate (Long et al., 2021). One enantiomer may serve previously unstudied indications. For example, S-methadone is now under clinical investigation as a rapidly acting antidepressant via nonopioid mechanism(s) (Fogaça et al., 2019). The directed evolution results demonstrate that the nicotinic PBP may be converted to detect nonnicotinic small molecule amines by tuning residues around the aromatic first shell. Drug biosensors *in vivo* can monitor drug concentration near receptors during administration by the experimenter or the subject, a common manipulation for studying mechanisms of reward, analgesia, and drug abuse. To meet immediate needs for diagnostics, iS-methadoneSnFR can also provide *in situ* readouts in the laboratory or home.

### 3.8 Supplemental Data

#### a) Racemic methadone (peaks found at ~1.6 and ~1.8 min)



#### b) R-methadone (~1.6 min peak)



#### c) S-methadone (~1.8 min peak)

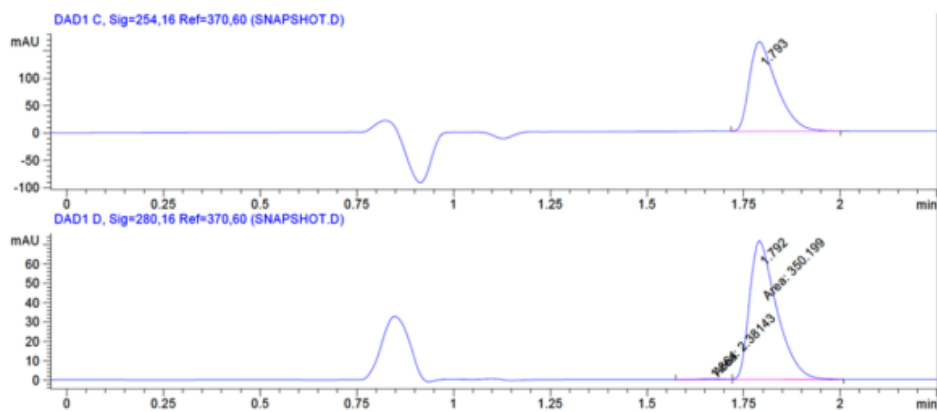


Figure 3.8: Chiral resolution of racemic methadone.

LC-MS analysis of (a) racemic, (b) R-methadone (peak at 1.591 min) and (c) S-methadone (peak at 1.793 min) batches after chiral resolution using the same chiral column (10x250 mm OJ-H, Chiral Technologies). Each trace shows ~100% of the desired enantiomer and ~0% of the other enantiomer. Early minor peaks are from vehicle solvent. Identity of each isomer was determined by optical rotation and the sign was matched to known enantiomer assignments: +30.4° for S-methadone and -32.0° for R-methadone.

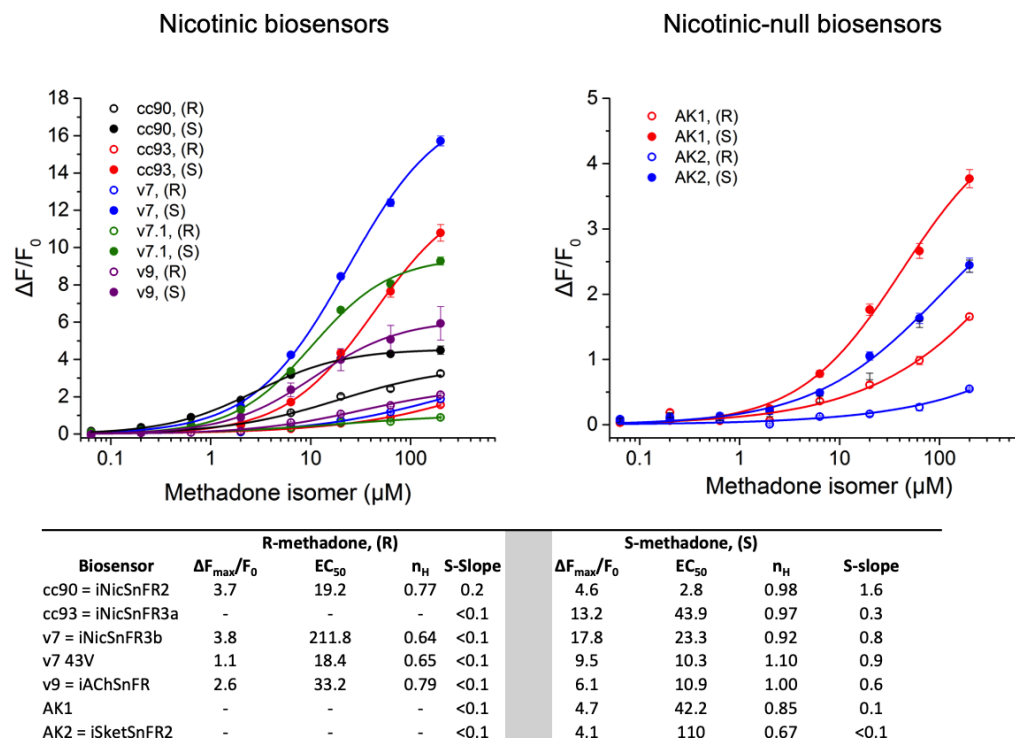


Figure 3.9: Dose-response relations for previously developed biosensor variants against R-methadone and S-methadone. Top left: nicotinic biosensors originally developed for iNicSnFR and iAChSnFR campaigns<sup>1,11</sup>. Top right: nicotinic-null biosensors originally developed for iSketSnFR (ketamine biosensor) campaigns<sup>12</sup>. Table: Hill fit parameters for every biosensor-methadone enantiomer pair dose response. iNicSnFR3b displayed the greatest S-slope for both S-methadone and R-methadone while preserving dynamic range of  $\Delta F_{max}/F_0 > 10$ .

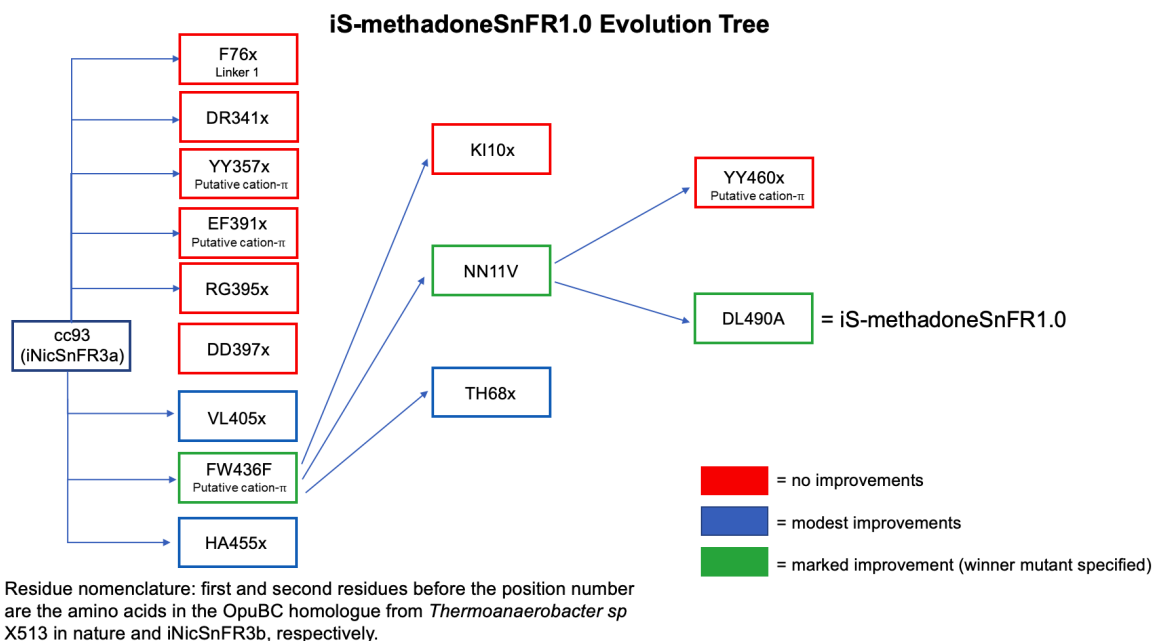
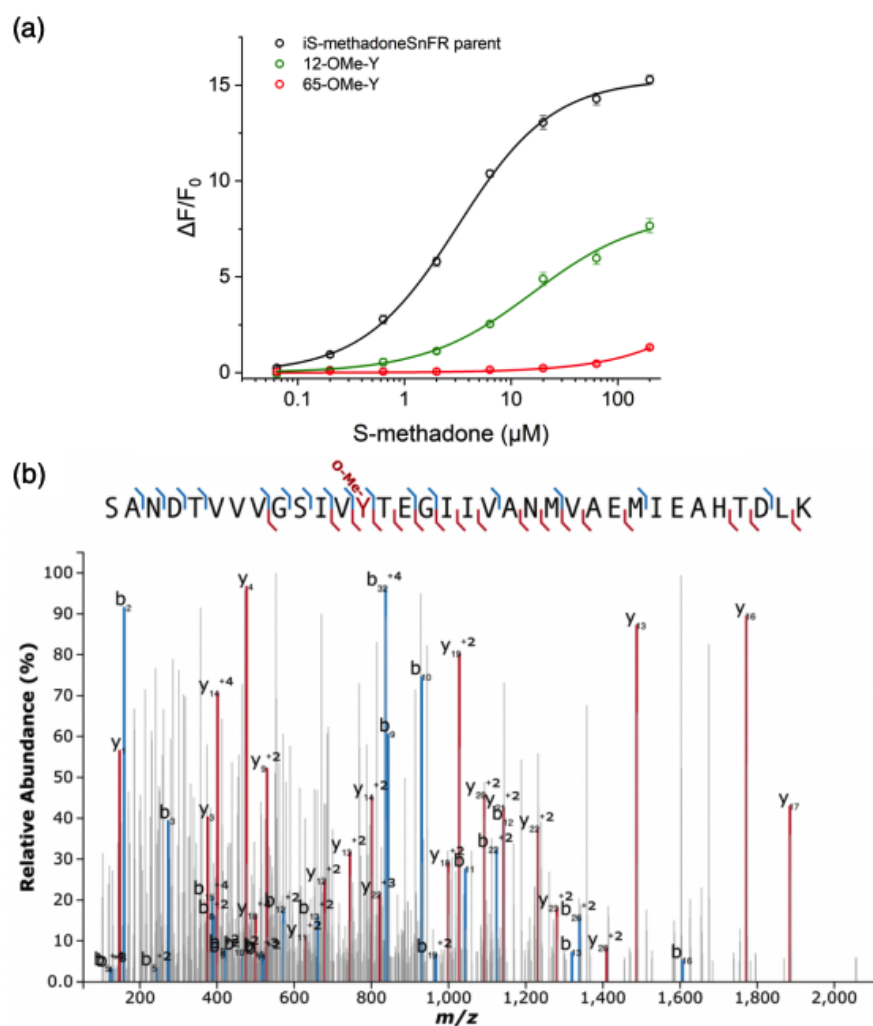
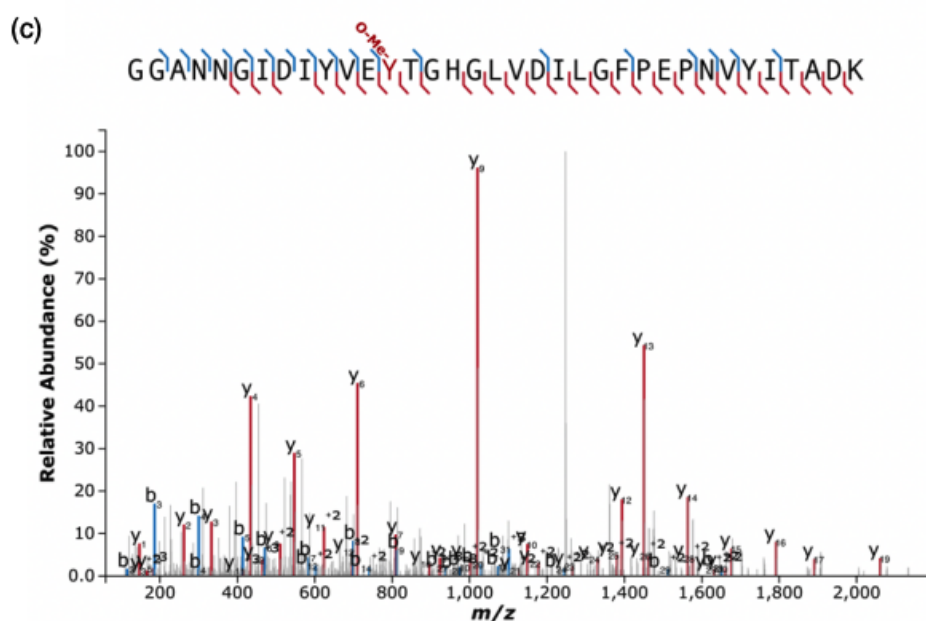


Figure 3.10: Evolution tree from iNicSnFR3a to iS-methadoneSnFR. Residue nomenclature: first and second residues before the position number are the amino acids in the OpuBC homologue from *Thermoanaerobacter* sp X513 and iNicSnFR3b, respectively. Functional role of the residue is noted. Each arrow and box pair represents a single residue site-saturation experiment. Red outlined boxes indicate positions that yielded only variants inferior to the parent. Blue outlined boxes indicate residues that yielded variants with modest improvements, typically 10-20% increases in S-slope. Green outlined boxes indicate mutations that yielded marked improvements accepted for additional mutagenesis rounds or, finally, for iS-methadoneSnFR.



UAA Fragment	Charge (z)	Experimental m/z	Theoretical m/z	Mass Error (Da)
b13	1	1319.6825	1319.6845	-0.002
b13	2	660.3418	660.3459	-0.0041
b15	3	517.2863	517.2631	0.0232
b15	4	388.1996	388.1992	0.0004
b16	1	1606.8046	1606.7962	0.0083
b19	2	966.521	966.52	0.001
b22	2	1124.5962	1124.5803	0.0159
b26	2	1339.6737	1339.6746	-0.0009
b32	4	836.9033	836.9153	-0.012
y22	2	1231.6143	1231.6191	-0.0048
y22	3	821.3989	821.4151	-0.0163
y23	2	1281.1467	1281.1533	-0.0066
y26	2	1409.694	1409.7221	-0.0281

(a)



UAA Fragment	Charge (z)	Experimental m/z	Theoretical m/z	Mass Error (Da)
b20	2	1030.4974	1030.4898	0.0077
b27	3	938.4449	938.4643	-0.0194
b31	2	1651.8505	1651.8222	0.0282
b31	3	1101.5284	1101.5506	-0.0221
y26	2	1462.7508	1462.7396	0.0112
y28	2	1576.8031	1576.7951	0.008

(b)

Figure 3.11: Amber suppression unnatural amino acid mutagenesis was used to incorporate the unnatural amino acid (UAA) O-methyltyrosine into positions 12 and 65 in separate constructs. (a) The dose responses for these two mutants are compared to the fully canonical sequence. Substitution at position 12 decreases dynamic range but roughly maintains  $EC_{50}$ ; however, methylation of 65Y sidechain led to a near-null mutant. (b) Mass spectrometry validation of UAA incorporation at position 12: peptide containing the UAA was identified by mass fragments. ‘b’ fragments (blue) are numbered for the fragment length starting from N-terminal end of the peptide. ‘y’ fragments (red) are numbered for the fragment length starting from the C-terminal end of the peptide. The table lists the expected and theoretical mass difference for peptide fragments containing the UAA. (c) Mass spectrometry validation of UAA incorporation at position 65 using the same method in (b).

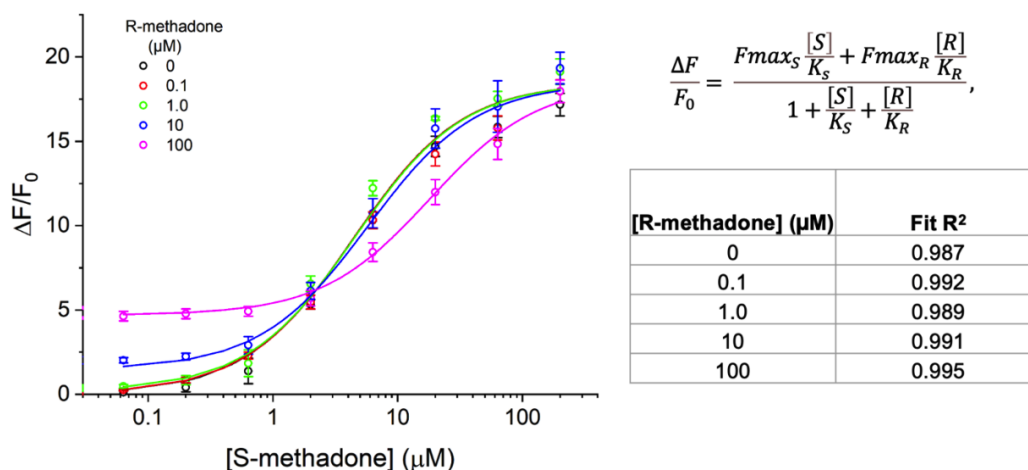


Figure 3.12: Interactions between R- and S-methadone at iS-methadoneSnFR. Dose-response relations were measured for S-methadone in the additional presence of five R-methadone concentrations. A model of competitive inhibition with mixed alternative substrates was used to account for R-methadone and Smethadone competitive binding with partial R-methadone agonism. Consistent with the model, R-methadone right-shifted the [S-methadone] concentration-response relation but did not significantly affect the maximum response.

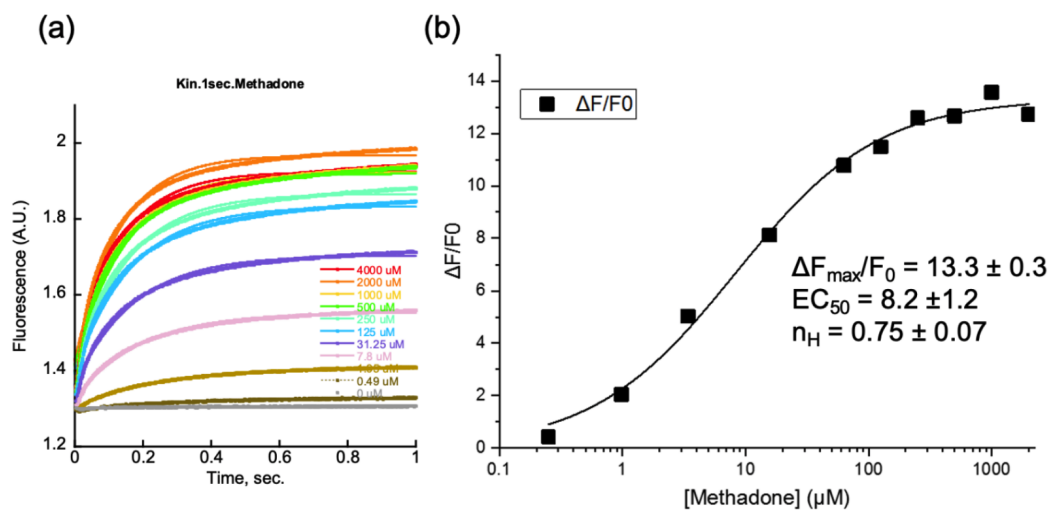


Figure 3.13: Kinetics of iS-methadoneSnFR's Response. (a) 1 s stopped-flow data. Racemic methadone was mixed with purified iSmethadoneSnFR in a chamber while monitoring fluorescence. Concentrations listed are twice the final [Smethadone]. (b) The mean response for the final 10 ms of the relaxation [methadone] was fitted to the Hill equation. The EC<sub>50</sub> of 8.2 μM is ~double that of the fluorescence dose-response EC<sub>50</sub> measured for Smethadone alone (Fig. 4B).



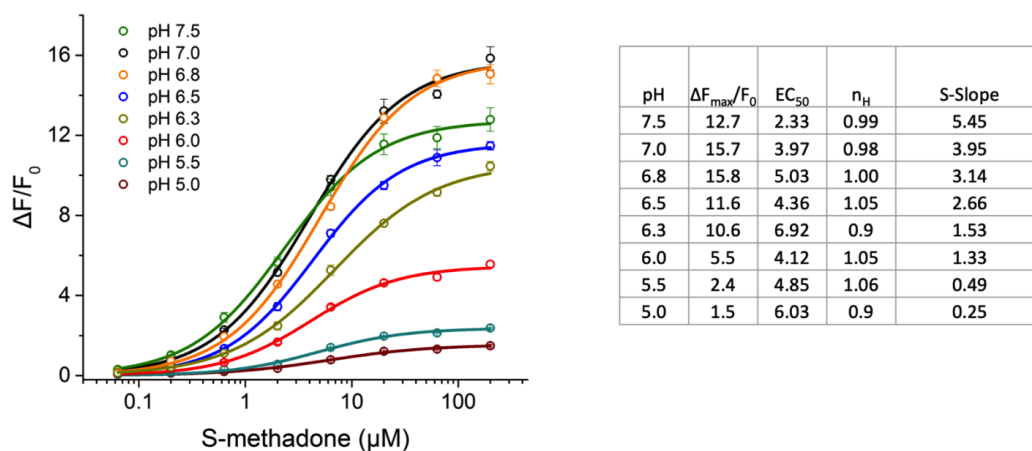


Figure 3.14: Effect of pH on the S-methadone dose-response relation. 3x PBS buffers were prepared from pH 5.0 to 7.5 in half-unit increments. Dose-response data were collected in each buffer and plotted. Hill fit parameters and computed S-slope are given in the righthand table. Like other GFP-based biosensors, the iS-methadoneSnFR response decreased at acidic pH. The S-slope remained  $> 1 \mu\text{M}^{-1}$  at pH 6.0, enabling measurements across the Golgi pH range. S-slope at pH 7.5 was 1.7x larger than that at pH 6.8 and 2.6x larger than that at pH 6.3.

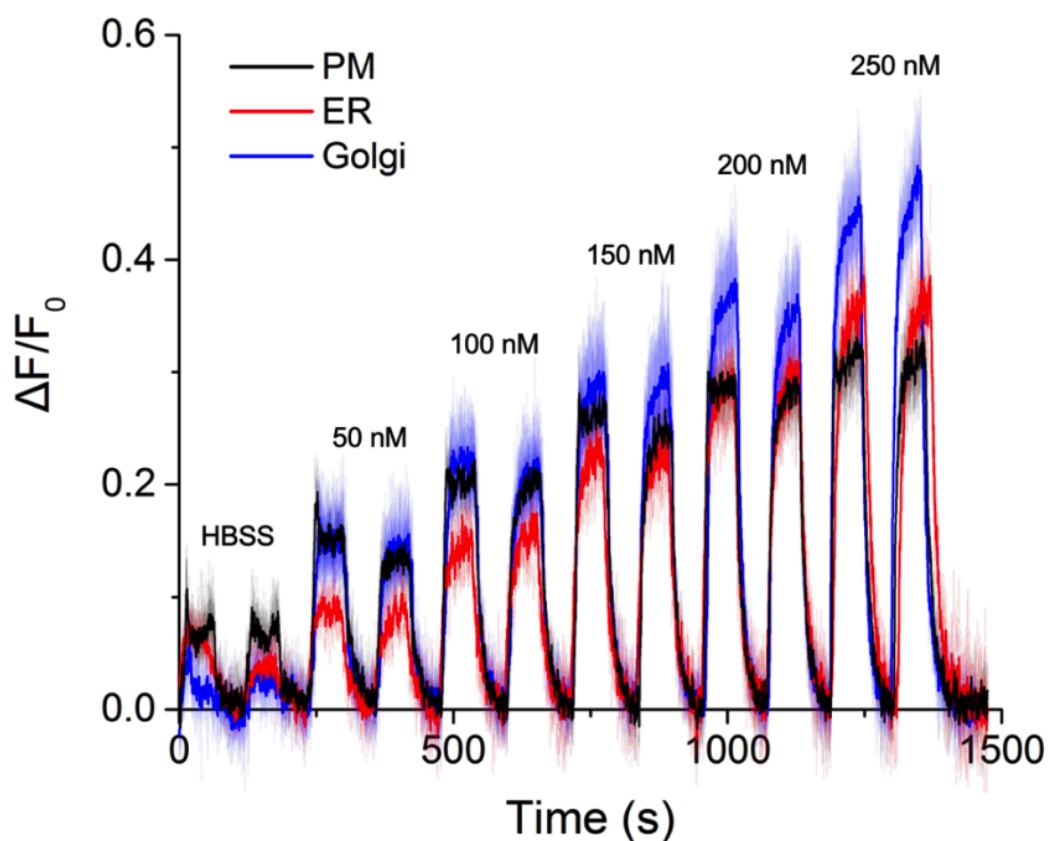


Figure 3.15: Time-resolved dose-response data from imaging experiments for iS-methadoneSnFR targeted to various HeLa cellular compartments. A “stuttered step” perfusion method (1 min S-methadone on, 1 min wash, each dose applied twice) was used to minimize pH effects. Fluorescence images (40x, 1.0 NA, 470 nm excitation) were acquired at 4 Hz. Traces show mean responses (PM n = 11 cells; ER n = 10; Golgi n = 11). Data were smoothed using a 4-point moving average. SEM denoted by faint bands.

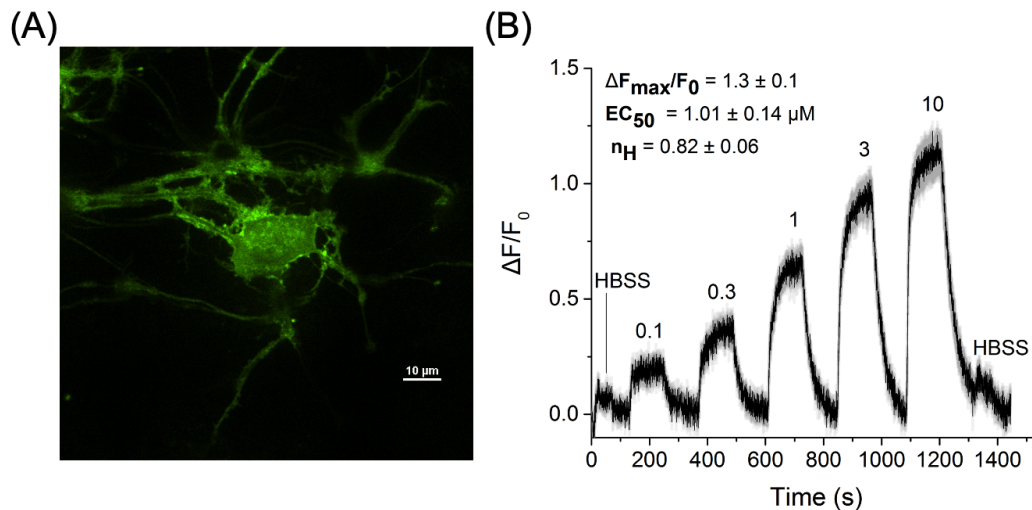


Figure 3.16: Validation in primary hippocampal neurons. (a) Spinning disc confocal imaging of a cultured mouse hippocampal neuron transduced with PHP.eB-hSyn-iS-methadoneSnFR-PM-WPRE (100 $\times$ , 1.4 NA objective; 488 nm excitation, 535 nm emission. Scale bar = 10  $\mu$ m.) (b) Responses to pulses of S-methadone (2 min drug application followed by 2 min rinse). iS-methadoneSnFR detected S-methadone in neuronal cultures across the pharmacologically relevant range (50 nM to 3  $\mu$ M). Traces are mean response  $\pm$  SEM ( $n = 12$  neurons, SEM as gray bounds). Smethadone concentration is given above traces (in  $\mu$ M). The final 10 s of the S-methadone response was averaged across the cells and the response to vehicle alone (HBSS) was subtracted to measure the doseresponse relation. The Hill fit parameters of the dose-response were  $F_{\max}/F_0 = 1.3 \pm 0.1$ ,  $EC_{50} = 1.01 \pm 0.14 \mu$ M, and  $n_H = 0.82 \pm 0.06$ .

### 3.9 Materials and Methods

#### Materials

Reagents The 10x250 mm OJ-H column (Chiral Technologies, p/n 17335) was used for both analytical and preparative experiments for the chiral resolution of racemic methadone. The following reagents were purchased from Thermo Fisher Scientific: DMEM, FBS, penicillin/streptomycin solution, trypsin, DPBS, B27, Neurobasal medium, HBSS, OptiMEM, donor equine serum, and Lipofectamine 3000. The following reagents were purchased from Sigma Aldrich: ascorbic acid, BSA, racemic methadone hydrochloride, and DNase. Papain was purchased from Worthington Biochemical Corporation. Cell culture dishes were purchased from MatTek Life Sciences. HeLa and HEK293T cells were purchased from ATCC. Dpn1, Phusion polymerase, and dNTP mixture were purchased from New England Biolabs.

Cloning: we previously reported a bacterial expression vector pHHM.X513-iNicSnFR3b-(V7) (Addgene plasmid #124881) and mutated this plasmid during this work's directed evolution<sup>1</sup>. We previously reported pMinDis.X513-iNicSnFR3a-(CC93)-ER (Addgene plasmid #125121) and pMinDis.X513-iNicSnFR3a-(CC93)-PM (Addgene plasmid #125122), targeting the endoplasmic reticulum and plasma membrane, respectively. We cloned iS-methadoneSnFR into these mammalian expression vectors. mApple-Golgi-7 was a gift from Michael Davidson (Addgene plasmid #54907; <http://n2t.net/addgene:54907>; RRID: Addgene 54907) and used for the sequence targeting the fusion protein to the Golgi apparatus by appending the Golgi-targeting sequence to the biosensor's N-terminus and removing the plasma membrane targeting sequence in pMinDis.X513-iNicSnFR3a-(CC93)-PM. Animal use statement: C57BL/6 mice were used for a terminal cardiac puncture procedure to collect blood. Animal care was conducted in accordance with the guidelines for care and use of animals recommended by the National Institutes of Health, as stated in IACUC protocol #1386 at the California Institute of Technology. Animals were kept on a 12 h light/dark cycle and given food and water ad libitum.

#### Methods

##### Chiral resolution of racemic methadone

Racemic methadone (>98% purity, Sigma Aldrich) was dissolved in ethanol containing 0.1% triethylamine and purified with ethanol containing 0.1% triethylamine on a 10x250 mm OJ-H column (Chiral Technologies, p/n 17335). From a 400 mg sample of racemic methadone hydrochloride, ~50 preparative injections afforded S-methadone, after recrystallization of each antipode from ethanol. The enantiomeric

excesses of each resolved isomer were measured by supercritical fluid chromatography using eluant on 4.6x250 mm OJ-H columns. The optical rotations of the two methadone isomers agreed with published values. Optical rotation was measured in water to match each fraction to the stereochemical identity: +30.4° and -32.0° for S-methadone and R-methadone, respectively, compared to +26° and -26° optical rotation reference values for the dextro- and levo- isomers of the free base<sup>2</sup>.

#### Docking in iNicSnFR3a

AutoDock Vina was used to perform docking<sup>3</sup>. The structure of iNicSnFR3a bound to varenicline was obtained from the Protein Data Bank (ID: 7S7T). The structure was prepared in AutoDockTools by removing waters, adding polar hydrogens, and assigning Gasteiger charges. Ligands were allowed torsional freedom in the docking routine. To verify the structure, varenicline was docked initially into the prepared structure. The highest scoring pose showed only a ~1 Å deviation from the nitrogens in varenicline of 7S7T. Then, S-methadone was docked into the structure. The highest scoring conformation with methadone's amine directed into the binding pocket was chosen for further analysis.

#### Biosensor expression by autoinduction

pHHMI plasmids bearing a biosensor gene were transformed into chemically competent BL21 (DE3) cells and grown on ampicillin plates overnight at 37 °C. Autoinduction LB was prepared according to the method of Studier 2005<sup>4</sup> with ampicillin (100 mg/L). A single colony was picked to inoculate each vessel with autoinduction medium. The vessel was incubated at 30 °C with shaking at 250 rpm for 28-30 h, shielded from light. Biosensor expression produced yellow-green colored cultures.

#### Protein purification by FPLC

Biosensors were expressed in 200 mL autoinduction cultures. Bacteria were pelleted and resuspended in 1x PBS, pH 7.4. The suspension was sonicated to lyse cells and centrifuged. The supernatant contained soluble biosensor and was applied to a Ni-NTA column on an Akta Start FPLC. The biosensor was eluted with a linear gradient from 10 to 200 mM imidazole in 1x PBS, pH 7.4. Fractions (5 mL) were collected and analyzed by SDS-PAGE to confirm purity. Pure fractions were combined and concentrated in a spin column with a 30 kDa cutoff (Amicon). The protein was buffer-exchanged into 3x PBS, pH 7.0, and concentrated to ~500 µL. Biosensor concentration was determined by absorbance at 280 nm using the extinction coefficient calculated for aromatic residues. Final pooled and concentrated protein purity was assessed by SDS-PAGE to find greater than 95% purity in samples used

for both kinetic and equilibrium experiments. Unnatural amino acid mutagenesis “Amber codon suppression” was performed by introducing TAG codons at positions 12, 65, and 357. A permissive aminoacyl synthetase/tRNA pair (pCNF) was used to incorporate O-methyl-L-tyrosine derivatives<sup>5</sup>. pEVOL-pCNF and the biosensor plasmid were co-transformed into BL21 (DE3) cells. Cells were plated on double antibiotic selection plates (spectinomycin/ampicillin). A single colony was picked to inoculate a 5 mL primary LB culture, then allowed to grow overnight at 37 °C. This culture was used to inoculate a 200 mL autoinduction culture as described above. At OD<sub>600</sub> ~0.7, the unnatural amino acid was added to the culture dropwise while agitating. The culture was then incubated for 30-32 h with shaking at 30 °C. The biosensor protein was purified by FPLC.

#### Protein Digestion for Mass Spectrometry

Purified iS-methadoneSnFR samples with canonical sequence and with O-methyl-L-tyrosine substituted at positions 12 and 65 (100 µg each) was dissolved in 100 µL HEPES (50 mM, pH 8.0) containing 8 M urea. TCEP (1 µL, 500 mM in 50 mM HEPES, pH 8.0) was added, and the sample was incubated with shaking (750 rpm) at 37 °C for 20 min. 2-chloroacetamide (3 µL, 500 mM in 50 mM HEPES, pH 8.0) was added, and the sample was incubated with shaking (750 rpm) at 37 °C. Endoproteinase Lys-C (2 µL, 100 ng/µL) was added, and the sample was incubated with shaking (750 rpm) at 37 °C for 4 h. HEPES buffer (375 µL, 50 mM, pH 8.0) was added to dilute urea to a final concentration of < 2 mM. CaCl<sub>2</sub> (5 µL, 100 mM) was added, followed by trypsin (3 µL, 100 ng/µL), and the sample was incubated with shaking (750 rpm) at 37 °C overnight. The sample was acidified with TFA (15 µL, 20% v/v) and centrifuged for 30 s at 13,000 x g. Desalting was performed using ThermoFisher C18 spin columns (cat #89870) according to the manufacturer’s protocol. Desalted samples were freeze-dried and stored at -20 °C prior to analysis.

#### Mass spectrometry validation of unnatural amino acid incorporation

Peptides were suspended in the water containing 0.2% formic acid and 2% acetonitrile for further LC-MS/MS analysis. LC-MS/MS analysis was performed with an EASY-nLC 1200 (ThermoFisher Scientific, San Jose, CA) coupled to a Q Exactive HF hybrid quadrupole-Orbitrap mass spectrometer (ThermoFisher Scientific, San Jose, CA). Peptides were separated on an Aurora UHPLC Column (25 cm × 75 µm, 1.6 µm C18, AUR2-25075C18A, IonOpticks) with a flow rate of 0.35 µL/min for a total duration of 43 min and ionized at 1.6 kV in the positive ion mode. The gradient was composed of 6% solvent B (2 min), 6-50% B (20.5 min), 50-80% B

(7.5 min), 80-98% B (1 min) and 98% B (12 min); solvent A: 2% ACN and 0.2% formic acid in water; solvent B: 80% ACN and 0.2% formic acid. MS1 scans were acquired at the resolution of 60,000 from 375 to 2,000 m/z, AGC target 3e6, and maximum injection time 15 ms. The 12 most abundant ions in MS2 scans were acquired at a resolution of 30,000, AGC target 1e5, maximum injection time 60 ms, and normalized collision energy of 28. Dynamic exclusion was set to 30 s and ions with charge +1, +7, +8 and >+8 were excluded. The temperature of ion transfer tube was 275 °C and the S-lens RF level was set to 60. MS2 fragmentation spectra were searched with Proteome Discoverer SEQUEST (version 2.5, Thermo Scientific) against in silico tryptic digested Uniprot database of Escherichia coli (strain K12) and iS-methadoneSnFR1.0 protein. The maximum missed cleavages were set to 2. Dynamic modifications were set to oxidation (M, +15.995 Da), deamidation (N and Q, +0.984 Da), O-Me-Tyr (F, +30.011Da; Y, +14.016 Da), protein N-terminal acetylation (+42.011 Da) and Met-loss (-131.040 Da). Carbamidomethylation on cysteine residues (C, +57.021 Da) was set as a fixed modification. The maximum parental mass error was set to 10 ppm, and the MS2 mass tolerance was set to 0.03 Da. The false discovery threshold was set strictly to 0.01 using the Percolator Node validated by q-value. The relative abundance of parental peptides was calculated by integration of the area under the curve of the MS1 peaks using the Minora LFQ node. Spectral annotation was generated by the Interactive Peptide Spectral Annotator (IPSA, <http://www.interactivepeptidespectralannotator.com/>)<sup>6</sup> The mass spectra of the peptides containing the unnatural amino acid were taken. The fragmentation pattern and mass/charge value matched expected values in both cases.

#### Fluorescence dose-response relation and calculation

Biosensor and drug solutions were mixed by a liquid handling robot (epMotion) to yield 100 nM final [biosensor] and the desired [drug]. The drug plate consisted of a serial dilution of 100.5 over each of seven steps and vehicle alone. Samples were prepared in triplicate. All solutions were 3x PBS, pH 7.0, unless otherwise stated. The plate was read using a Tecan Spark 10M with 485 nm excitation and 535 nm emission wavelengths to measure GFP fluorescence. Mean  $\Delta F/F_0$  was calculated for the response to each [ligand] where  $\Delta F/F_0 = (F_{\text{drug+biosensor}} - F_{\text{biosensor}}) / F_{\text{biosensor}}$ . Error bars are given for the standard error of the mean. The resulting data were fit with the Origin 9.2 software (OriginLabs).

Directed evolution Directed evolution consisted of (A) DNA library preparation, (B) culturing in 96-well plates, and (C) screening for response to ligands and obtaining

winning sequences. (A) A 22-codon method was used to create mutant DNA libraries<sup>7</sup>. The PCR product library was transformed into TOP10 cells to amplify the DNA. Several variants from each library were sequenced to verify randomization. (B) 300 ng of the library was transformed into BL21 (DE3) cells, plated on ampicillin selection plates, and incubated overnight at 37 °C. Autoinduction medium was prepared and 800  $\mu$ L were added to each well in a 96-deep well plate. A single colony was picked to inoculate each well. AeraSeal film was used to cover the plate while allowing oxygenation. The plate was incubated at 30 °C with shaking at 250 rpm for 30 h. The culture was pelleted, resuspended in 3x PBS, pH 7.0, frozen in liquid nitrogen, and thawed at room temperature to lyse bacteria. The plate was centrifuged again, providing biosensor solubilized in the lysate. (C) Lysates were transferred to a 96-well flat black plate and fluorescence in each well was read. 11  $\mu$ L of 10x drug solution was added to each well and mixed by shaking. The fluorescence was measured after ligand application.  $\Delta F/F_0$  was computed for each well. The top ~8 mutants were sequenced. Non-parent mutants were then transformed into BL21 (DE3) cells and used to inoculate a 10 mL autoinduction culture. The lysate was then used for a full dose response to verify the advantageous mutation.

Isothermal titration calorimetry ITC was conducted using an Affinity ITC (TA Instruments). S-methadone stock solution and buffer-exchanged stock solution of purified biosensor were prepared using 3x PBS, pH 7.0. 40  $\mu$ M of biosensor solution was added to the cell and 400  $\mu$ M S-methadone (titrant) was added to the syringe. 2  $\mu$ L injections of the titrant were injected at 300 s intervals 20 times. NanoAnalyze software (TA Instruments) was used to process the data. The baseline correction was applied to account for drug solvation energy. The resulting heat curve was fitted with an “independent” model to determine enthalpy, entropy, binding affinity, and stoichiometry.

Stopped-flow kinetics Stopped-flow kinetics were measured using an Applied Photophysics SX20 stopped-flow fluorimeter with a 490 nm excitation LED and 510 nm long-pass filter at room temperature (22 °C). Equal volumes of 0.2  $\mu$ M iS-methadoneSnFR and varying concentrations of racemic methadone were mixed (5 replicates). The first 3 ms were not analyzed to ignore mixing artifacts and instrument dead time. Data were plotted and time courses were fitted, when possible, to a single exponential approach to a plateau, using Kaleidagraph (version 4.4).  $k_{obs}$  was plotted as a function of [ligand]. The linear portion of that graph was fitted, with the slope reporting  $k_1$  and the y-intercept reporting  $k_{-1}$ . When the time course



did not fit well to a single exponential component, it was fitted to the sum of two exponentials, and the faster phase ( $k_{\text{obs1}}$ ) was treated as above to determine  $k_1$  and  $k_{-1}$ . Generation and analysis of racemic methadone steady-state concentration-response relation The relaxation data were sampled at intervals of one ms. We measured the steady-state concentration-response relation for  $\Delta F/F_0$  vs [racemic methadone] by taking the mean  $\Delta F/F_0$  for the final 10 ms of the 1 s methadone stopped-flow relaxations. We computed  $\Delta F$  by subtracting the fluorescence in methadone from that in 0  $\mu\text{M}$  methadone. After correcting for instrumental offset, the value of  $F_0$  was 0.05. The data were fit to the Hill equation without weighting using the nonlinear regression routine provided by the Origin 2018 software.

Analysis of R- and S-methadone interaction To determine whether R- and S-methadone bound competitively to the sensor, we measured the effect of fixed R-methadone concentrations (0, 0.1, 1, 10, 100  $\mu\text{M}$ ) on the S-methadone concentration-response relation. R-methadone is not a simple competitive inhibitor because it also partially activates the sensor. Therefore, we adapted a model from enzyme kinetics for competitive inhibition with mixed alternative substrates<sup>8</sup>.

Adeno-associated virus preparation iS-methadoneSnFR gene was cloned into a pAAV vector with a synapsin-1 promoter and a PDGFR plasma membrane-targeting sequence<sup>9</sup>. Integrity of the inverted terminal repeat sequence was confirmed by SmaI digest. Mammalian tissue culture, virus harvesting, and virus purification were performed according to the protocol of Challis 2019<sup>10</sup>. HEK293T cells were transfected with the pAAV, pHelper, and PHP.eB capsid genes. The medium was harvested at 3 and 5 days post-transfection and the cells were harvested at 5 days post-transfection. Digestion produced a lysate with soluble viral particles. The lysate was purified by gradient ultracentrifugation. Viral titer was determined by qPCR.

Tissue culture and transfection HeLa cells (ATCC) were thawed and passaged twice before use in imaging studies. Cell culture followed ATCC recommended protocols. For each imaging study, 100,000 HeLa cells were plated onto a 35 mm dish with a 14 mm coverslip (MatTek) and incubated at 37 °C, 5%  $\text{CO}_2$  for 24 h. Cells were then transfected with Lipofectamine 3000 using 500 ng for  $\_PM$ , 250 ng for  $\_ER$ , and 600 ng for  $\_Golgi$  constructs in OptiMEM. Cells were kept in OptiMEM transfection medium for 24 h and then switched to standard growth medium for an additional 24 h before imaging.

Primary neuron culturing and transduction A pregnant mouse was euthanized at

embryonic day 16. The uterine sac was removed, and each embryo was decapitated before dissection. The hippocampi from several embryos were combined and digested with 15 U of papain at 37 °C for 15 min. After DNase treatment, the cells were triturated in Hanks' balanced salt solution (HBSS) with 5% donor equine serum and spun through a layer of 4% BSA and HBSS. Dishes with a 10 mm poly-D-lysine-coated glass bottom (MatTek) were coated with poly-L-ornithine and laminin 24 h prior to plating. The cells were then plated at a density of 90,000/dish in 130  $\mu$ L of plating medium. After 1 h, 3 mL of complete culture medium was added to each dish. Half of the medium was changed twice a week. After 4 days, the neurons were transduced by mixing virus into the medium. After ~2 weeks, the dishes were used in imaging experiments. Mouse serum collection Mice were anesthetized with 5% isoflurane in air. Anesthesia was verified by slowed breathing and insensitivity to toe pinch. A needle was inserted in the left lateral thoracic wall and punctured the ventricle; 0.5-0.75 mL of blood was withdrawn into a syringe. The sample was allowed to coagulate at room temperature for 1 h and then centrifuged. The supernatant was pipetted off and used for dose response studies without any other processing. Time-resolved measurements in cultured cells An Olympus XI-80 microscope was equipped with an LED centered at 470 nm (LZ1- 10DB00; Led Engin), a 40- nm band-pass filter, centered at 470 nm (ET 470/40X; Chroma Technology) and an iXon DU-897 EM chargecoupled device camera (Andor Technology). Imaging was performed at 4 Hz. A programmable 8-valve perfusion system (Automate Scientific) was used to deliver solutions. Serial dilutions of S-methadone were prepared in Hanks' balanced salt solution (HBSS). PTFE-coated tubing was used to minimize gas diffusion; nonetheless, some CO<sub>2</sub> diffused out of the tubing between the solution reservoir and cell chamber, slightly alkalizing the bicarbonate-based buffer. Hence, vehicle application without drug elicited an F<sub>0</sub> increase (Figure 3.15). Therefore, we used a "stuttered step" program in which each drug application was repeated to flush the solution in the tubing. The second response was taken for analysis. This response was subtracted from the mean peak response at each [S-methadone]. Analysis of cellular imaging time series data ImageJ plugin "Time Series Analyzer" was used to calculate the average pixel intensity in the region of interest (ROI) drawn (PM, ER, or Golgi) and a background region in each frame. These data were further analyzed using the OriginLabs software. The background values were subtracted from the ROI at each frame to calculate F. A baseline was drawn with a spline to determine F<sub>0</sub> at each frame.  $\Delta F/F_0$  was then calculated as  $(F-F_0)/F_0$  for each frame. The steady-state response was taken as the average of the

final 20 frames in each response. For the slope measurements, the HBSS response was subtracted from each of the responses at 50-250 nM drug. The linear fit was constrained to a y-intercept of zero. Spinning disc confocal imaging Images were captured using a Nikon Ti2 spinning disc confocal microscope. An environmental chamber around the stage was set to 37 °C and 5% CO<sub>2</sub>. “Perfect Focus” was used to maintain z-position before, during, and after drug solution addition. A 2x drug stock was prepared in HBSS and applied after a “baseline” image was taken. 1 min was given to allow for diffusion before capturing the post-drug image. Nikon’s software was used to tile the acquisition and stitch the final image.

### Methods References

- (1) Shivange, A. V.; Borden, P. M.; Muthusamy, A. K.; Nichols, A. L.; Bera, K.; Bao, H.; Bishara, I.; Jeon, J.; Mulcahy, M. J.; Cohen, B.; O’Riordan, S. L.; Kim, C.; Dougherty, D. A.; Chapman, E. R.; Marvin, J. S.; Looger, L. L.; Lester, H. A. Determining the Pharmacokinetics of Nicotinic Drugs in the Endoplasmic Reticulum Using Biosensors. *Journal of General Physiology* 2019, 151 (6), 738–757. <https://doi.org/10.1085/jgp.201812201>.
- (2) Larsen, A. A.; Tullar, B. F.; Elpern, B.; Buck, J. S. The Resolution of Methadone and Related Compounds. *Journal of the American Chemical Society* 1948, 70 (12), 4194–4197.
- (3) Trott, O.; Olson, A. J. AutoDock Vina: Improving the Speed and Accuracy of Docking with a New Scoring Function, Efficient Optimization, and Multithreading. *J. Comput. Chem.* 2009.
- (4) Studier, F. W. Protein Production by Auto-Induction in High-Density Shaking Cultures. *Protein Expression and Purification* 2005, 41 (1), 207–234.
- (5) Young, D. D.; Young, T. S.; Jahnz, M.; Ahmad, I.; Spraggon, G.; Schultz, P. G. An Evolved AminoacylTRNA Synthetase with Atypical Polysubstrate Specificity. *Biochemistry* 2011, 50 (11), 1894–1900.
- (6) Brademan, D. R.; Riley, N. M.; Kwiecien, N. W.; Coon, J. J. Interactive Peptide Spectral Annotator: A Versatile Web-Based Tool for Proteomic Applications. *Molecular Cellular Proteomics* 2019, 18 (8), S193–S201.
- (7) Kille, S.; Acevedo-Rocha, C. G.; Parra, L. P.; Zhang, Z.-G.; Opperman, D. J.; Reetz, M. T.; Acevedo, J. P. Reducing Codon Redundancy and Screening Effort of Combinatorial Protein Libraries Created by Saturation Mutagenesis. *ACS Synthetic*

*Biology* 2013, 2 (2), 83–92.

(8) Irwin Segel. Simple Inhibition Systems. In *Enzyme Kinetics: Behavior and Analysis of Rapid Equilibrium and Steady-State Enzyme Systems*; Wiley Classics Library, 1993; pp 113–118.

(9) Leopold, A. V.; Shcherbakova, D. M.; Verkhusha, V. V. Fluorescent Biosensors for Neurotransmission and Neuromodulation: Engineering and Applications. *Frontiers in Cellular Neuroscience* 2019, 13, 474.

(10) Challis, R. C.; Ravindra Kumar, S.; Chan, K. Y.; Challis, C.; Beadle, K.; Jang, M. J.; Kim, H. M.; Rajendran, P. S.; Tompkins, J. D.; Shivkumar, K.; Deverman, B. E.; Gradinaru, V. Systemic AAV Vectors for Widespread and Targeted Gene Delivery in Rodents. *Nature Protocols* 2019, 14 (2), 379–414.

(11) Borden, P. M.; Zhang, P.; Shivange, A. V.; Marvin, J. S.; Cichon, J.; Dan, C.; Podgorski, K.; Figueiredo, A.; Novak, O.; Tanimoto, M.; Shigetomi, E.; Lobas, M. A.; Kim, H.; Zhu, P. K.; Zhang, Y.; Zheng, W. S.; Fan, C.; Wang, G.; Xiang, B.; Gan, L.; Zhang, G.-X.; Guo, K.; Lin, L.; Cai, Y.; Yee, A. G.; Aggarwal, A.; Ford, C. P.; Rees, D. C.; Dietrich, D.; Khakh, B. S.; Dittman, J. S.; Gan, W.-B.; Koyama, M.; Jayaraman, V.; Cheer, J. F.; Lester, H. A.; Zhu, J. J.; Looger, L. L. A Fast Genetically Encoded Fluorescent Sensor for Faithful in Vivo Acetylcholine Detection in Mice, Fish, Worms and Flies. *BioRxiv* 2020. <https://doi.org/10.1101/2020.02.07.939504>.

(12) Bera, K.; Kamajaya, A.; Shivange, A. V.; Muthusamy, A. K.; Nichols, A. L.; Borden, P. M.; Grant, S.; Jeon, J.; Lin, E.; Bishara, I.; Chin, T. M.; Cohen, B. N.; Kim, C. H.; Unger, E. K.; Tian, L.; Marvin, J. S.; Looger, L. L.; Lester, H. A. Biosensors Show the Pharmacokinetics of S-Ketamine in the Endoplasmic Reticulum. *Frontiers in Cellular Neuroscience* 2019, 13, 499.

## Sequences

iS-methadoneSnFR nucleotide sequence:

```
ATGCATCATCATCATCATCATGGTTATCCCTATGATGTTCCAGATTATG
CTGGGGCCCAGCCGGCCAGATCTGCGAACGACACCGTAGTTGTGGGCT
CGATCGTGTTTACAGAAGGGATTATCGTCGCAAACATGGTGGCAGAGA
TGATTGAGGCGCATAACAGACCTTAAGGTGGTTCGCAAACCTGAACCTTG
GCGGGGAGAACGTAACTTTGAAGCCATTAACGCGGAGGTGCGAAT
AATGGTATTGACATTTACGTGGAGTACACTGGGCACGGTCTTGTGGAT
ATTCTGGGGTTCCCGGAGCCGAACGTCTATATCACCGCCGACAAGCAG
```

AAGAACGGCATCAAGGCGAACTTCAAGATCCGCCACAACGTGGAGGA  
CGGCAGCGTGCAGCTCGCCGACCACTACCAGCAGAACACCCCCATCGG  
CGACGGCCCCGTGCTGCTGCCCGACAACCACTACCTGAGCACCCAGTC  
CGTGCTGAGCAAAGACCCCAACGAGAAGCGCGATCACATGGTCCTGCT  
GGAGTTCGTGACCGCCGCCGGGATCACTCTCGGCATGGACGAGCTGTA  
CAAGGGCGGTACCGGAGGGAGCATGAGCAAGGGCGAGGAGCTGTTCA  
CCGGGGTGGTGCCCATCCTGGTCGAGCTGGACGGCGACGTAAACGGCC  
ACAAGTTCAGCGTGC GCGGGCGAGGGCGAGGGCGATGCCACCAACGGC  
AAGCTGACCCTGAAGTTCATCTGCACCACCGGCAAGCTGCCCGTGCC  
TGGCCACCCTCGTGACCACCCTGACCTACGGCGTG CAGTGCTTCAGC  
CGTACCCCGACCACATGAAGCAGCACGACTTCTTCAAGTCCGCCATG  
CCCGAAGGCTACGTCCAGGAGCGCACCATCAGCTTCAAGGACGACGG  
CACCTACAAGACCCGCGCCGAGGTGAAGTTCGAGGGCGACACCCTGGT  
GAACCGCATCGAGCTGAAGGGCATCGACTTCAAGGAGGACGGCAACA  
TCCTGGGGCACAAGCTGGAGTACAAC TTTCCGCCGCCAGCTCTACTG  
ATCCAGAAGGTGCATACGAAACCGTGAAGAAGGAGTACAAACGTAAA  
TGGAATATTGTATGGCTCAAACCACTGGGATTCAACAATACGTATACG  
CTTACCGTTAAAGACGAACTGGCGAAACAGTATAACCTTAAAACCTTC  
AGTGACTTAGCGAAAATCTCGGATAAGCTGATTCTGGGTGCAACGATG  
TTCTTTTTAGAAAGGGCCCGATGGTTACCCAGGCCTGCAAAA ACTGTAC  
AATTTCAAATTCAAGCACACCAAAAAGCATGGACATGGGTATTCGCTAT  
ACCGCCATTGATAATAACGAAGTTCAGGTAATTGATGCCTTCGCCACT  
GATGGCTTGCTGGTGAGCCACAAATTA AAAAATTCTGGAGGATGATAAA  
GCGTTCTTCCCGCCGTATTATGCTGCCCCATCATCCGTCAGGATGTCT  
TAGATAAGCATCCTGAACTGAAGGACGTGCTGAACAAACTCGCGAATC  
AAATTT CAGCGGAAGAAATGCAGAACTGAATTACAAGGTGGACGGT  
GAGGGTCAGGACCCAGCGAAAGTAGCTAAGGAGTTTTTTGAAAGAGAA  
AGGTTTAATTCTGCAGGTGACGAACAAAAACTCATCTCAGAAGAGGA  
TCTGAATTAA

iS-methadoneSnFR amino acid sequence:

MHHHHHHGYPYDVPDYAGAQPARSANDTVVVGSIVFTEGIIIVANMVAE  
MIEAHTDLKVVVRKLNLGGENVNEAIKRGGANNGIDIYVEYTGHGLVDILG  
FPEPNVYITADKQKNGIKANFKIRHNVEDGSVQLADHYQQNTIGDGPVLL  
PDNHYLSTQSVLSKDPNEKRDHMLLEFVTAAGITLGMDELYKGGTGGS  
MSKGEELFTGVVPLVELDGDVNGHKFSVRGEGEGDATNGKLTCLKFICTTG  
KLPVPWPTLVTTLTYGVCFSRYPDHMKQHDFFSAMPEGYVQERTISFKD  
DGTYKTRAEVKFEGDTLVNRIELKGIDFKEDGNILGHKLEYNFPPPSSTDP  
EGYETVKKEYKRKWNIVWLKPLGFNNTYTLTVKDELAQYNLKTFSDLA  
KISDKLILGATMFFLEGPDGYPGQKLYNFKFKHTSMDMGIRYTAIDNNEV  
QVIDAFATDGLLVSHKLEDDKAFFPPYYAAPIIRQDVLDKPELKDVLN  
KLANQISAEEMQKLNKVDGEGQDPAKVAKEFLKEKGLILQVDEQKLISE  
EDLN

### 3.10 References

- Abraham, A. D., Casello, S. M., Schattauer, S. S., Wong, B. A., Mizuno, G. O., Mahe, K., Tian, L., Land, B. B., & Chavkin, C. (2021). Release of endogenous dynorphin opioids in the prefrontal cortex disrupts cognition. *Neuropsychopharmacology*, *46*(13), 2330–2339. <https://doi.org/10.1038/s41386-021-01168-2>
- Ahmed, S. R., Chand, R., Kumar, S., Mittal, N., Srinivasan, S., & Rajabzadeh, A. R. (2020). Recent biosensing advances in the rapid detection of illicit drugs. *TrAC Trends in Analytical Chemistry*, *131*, 116006. <https://doi.org/10.1016/j.trac.2020.116006>
- Althoff, K. N., Leifheit, K. M., Park, J. N., Chandran, A., & Sherman, S. G. (2020). Opioid-related overdose mortality in the era of fentanyl: Monitoring a shifting epidemic by person, place, and time. *Drug and Alcohol Dependence*, *216*, 108321. <https://doi.org/10.1016/j.drugalcdep.2020.108321>
- Ardeshiri, M., & Jalali, F. (2016). Highly selective electrode for potentiometric analysis of methadone in biological fluids and pharmaceutical formulations. *Materials Science and Engineering: C*, *63*, 30–36. <https://doi.org/10.1016/j.msec.2016.02.050>
- Bick, M. J., Greisen, P. J., Morey, K. J., Antunes, M. S., La, D., Sankaran, B., Reymond, L., Johnsson, K., Medford, J. I., & Baker, D. (2017). Computational design of environmental sensors for the potent opioid fentanyl. *eLife*, *6*, e28909. <https://doi.org/10.7554/eLife.28909>
- Borden, P. M., Zhang, P., Shivange, A. V., Marvin, J. S., Cichon, J., Dan, C., Podgorski, K., Figueiredo, A., Novak, O., Tanimoto, M., Shigetomi, E., Lobas, M. A., Kim, H., Zhu, P. K., Zhang, Y., Zheng, W. S., Fan, C., Wang, G., Xiang, B., . . . Looger, L. L. (2020). A fast genetically encoded fluorescent sensor for faithful in vivo acetylcholine detection in mice, fish, worms and flies. *BioRxiv*. <https://doi.org/10.1101/2020.02.07.939504>
- Cruciani, R., & Knotkova, H. (Eds.). (n.d.). *Handbook of methadone prescribing and buprenorphine therapy* (1st ed.). Springer. <https://link.springer.com/book/10.1007%2F978-1-4614-6974-2#toc>
- Dole, V. P. (1965). A medical treatment for diacetylmorphine (heroin) addiction. *198*(8), 646–650. <https://doi.org/10.1001/jama.1965.03090080008002>
- Dole, V. P. (1971). Methadone maintenance treatment for 25,000 heroin addicts. *Journal of the American Medical Association*, *215*(7), 1131–1134.
- Eap, C. B., Buclin, T., & Baumann, P. (2002). Interindividual variability of the clinical pharmacokinetics of methadone: Implications for the treatment of opioid dependence. *Clinical Pharmacokinetics*, *41*(14), 1153–1193. <https://doi.org/10.2165/00003088-200241140-00003>

- Faessel, H. M., Obach, R. S., Rollema, H., Ravva, P., Williams, K. E., & Burstein, A. H. (2010). A review of the clinical pharmacokinetics and pharmacodynamics of varenicline for smoking cessation. *Clinical Pharmacokinetics*, *49*(12), 799–816. <https://doi.org/10.2165/11537850-000000000-00000>
- Fogaça, M. V., Fukumoto, K., Franklin, T., Liu, R.-J., Duman, C. H., Vitolo, O. V., & Duman, R. S. (2019). N-methyl-d-aspartate receptor antagonist d-methadone produces rapid, mTORC1-dependent antidepressant effects. *Neuropsychopharmacology*, *44*(13), 2230–2238. <https://doi.org/10.1038/s41386-019-0501-x>
- Foster, D. J. R., Somogyi, A. A., Dyer, K. R., White, J. M., & Bochner, F. (2000). Steady-state pharmacokinetics of (r)- and (s)-methadone in methadone maintenance patients: Pharmacokinetics of (r)- and (s)-methadone. *British Journal of Clinical Pharmacology*, *50*(5), 427–440. <https://doi.org/10.1046/j.1365-2125.2000.00272.x>
- Hudson, M., Stuchinskaya, T., Ramma, S., Patel, J., Sievers, C., Goetz, S., Hines, S., Menzies, E., & Russell, D. A. (2019). Drug screening using the sweat of a fingerprint: Lateral flow detection of  $\delta$ 9-tetrahydrocannabinol, cocaine, opiates and amphetamine. *Journal of Analytical Toxicology*, *43*(2), 88–95. <https://doi.org/10.1093/jat/bky068>
- Khorablou, Z., Shahdost-Fard, F., & Razmi, H. (2021). Flexible and highly sensitive methadone sensor based on gold nanoparticles/polythiophene modified carbon cloth platform. *Sensors and Actuators B: Chemical*, *344*, 130284. <https://doi.org/10.1016/j.snb.2021.130284>
- Larsen, A. A., Tullar, B. F., Elpern, B., & Buck, J. S. (1948). The resolution of methadone and related compounds. *Journal of the American Chemical Society*, *70*(12), 4194–4197. <https://doi.org/10.1021/ja01192a065>
- Lester, H. A., Miwa, J. M., & Srinivasan, R. (2012). Psychiatric drugs bind to classical targets within early exocytotic pathways: Therapeutic effects. *Biological Psychiatry*, *72*(11), 907–915. <https://doi.org/10.1016/j.biopsych.2012.05.020>
- Li, Y., Kantelip, J.-P., Schieveen, P. G.-v., & Davani, S. (2008). Interindividual variability of methadone response: Impact of genetic polymorphism. *Molecular Diagnosis & Therapy*, *12*(2), 109–124. <https://doi.org/10.1007/BF03256276>
- Long, A. S., Zhang, A. D., Meyer, C. E., Egilman, A. C., Ross, J. S., & Wallach, J. D. (2021). Evaluation of trials comparing single-enantiomer drugs to their racemic precursors: A systematic review. *Journal of the American Medical Association Network Open*, *4*(5), e215731. <https://doi.org/10.1001/jamanetworkopen.2021.5731>
- Marvin, J. S., Borghuis, B. G., Tian, L., Cichon, J., Harnett, M. T., Akerboom, J., Gordus, A., Renninger, S. L., Chen, T.-W., Bargmann, C. I., Orger, M. B., Schreiter, E. R., Demb, J. B., Gan, W.-B., Hires, S. A., & Looger, L. L. (2013).



- An optimized fluorescent probe for visualizing glutamate neurotransmission. *Nature Methods*, 10(2), 162–170. <https://doi.org/10.1038/nmeth.2333>
- Nilsson, M. .-, Grnbladh, L., Widerlv, E., & nggrd, E. (1983). Pharmacokinetics of methadone in methadone maintenance treatment: Characterization of therapeutic failures. *European Journal of Clinical Pharmacology*, 25(4), 497–501. <https://doi.org/10.1007/BF00542117>
- Petäjä-Repo, U. E., & Lackman, J. J. (2014). Targeting opioid receptors with pharmacological chaperones. *Pharmacological Research*, 83, 52–62. <https://doi.org/10.1016/j.phrs.2013.12.001>
- Rezaei, B., Tajaddodi, A., & Ensafi, A. A. (2020). An innovative highly sensitive electrochemical sensor based on modified electrode with carbon quantum dots and multiwall carbon nanotubes for determination of methadone hydrochloride in real samples. *Analytical Methods*, 12(43), 5210–5218. <https://doi.org/10.1039/D0AY01374A>
- Russell, M. A., Jarvis, M., Iyer, R., & Feyerabend, C. (1980). Relation of nicotine yield of cigarettes to blood nicotine concentrations in smokers. *British Medical Journal*, 280(6219), 972–976. <https://doi.org/10.1136/bmj.280.6219.972>
- Shivange, A. V., Borden, P. M., Muthusamy, A. K., Nichols, A. L., Bera, K., Bao, H., Bishara, I., Jeon, J., Mulcahy, M. J., Cohen, B., O’Riordan, S. L., Kim, C., Dougherty, D. A., Chapman, E. R., Marvin, J. S., Looger, L. L., & Lester, H. A. (2019). Determining the pharmacokinetics of nicotinic drugs in the endoplasmic reticulum using biosensors. *Journal of General Physiology*, 151(6), 738–757. <https://doi.org/10.1085/jgp.201812201>
- Stoeber, M., Jullié, D., Lobingier, B. T., Laeremans, T., Steyaert, J., Schiller, P. W., Manglik, A., & von Zastrow, M. (2018). A genetically encoded biosensor reveals location bias of opioid drug action. *Neuron*, 98(5), 963–976.e5. <https://doi.org/10.1016/j.neuron.2018.04.021>
- Tian, L., Hires, S. A., Mao, T., Huber, D., Chiappe, M. E., Chalasani, S. H., Petreanu, L., Akerboom, J., McKinney, S. A., Schreiter, E. R., Bargmann, C. I., Jayaraman, V., Svoboda, K., & Looger, L. L. (2009). Imaging neural activity in worms, flies and mice with improved GCaMP calcium indicators. *Nature Methods*, 6(12), 875–881. <https://doi.org/10.1038/nmeth.1398>
- Zeisel, S. H., Epstein, M. F., & Wurtman, R. J. (1980). Elevated choline concentration in neonatal plasma. *Life Sciences*, 26(21), 1827–1831. [https://doi.org/10.1016/0024-3205\(80\)90585-8](https://doi.org/10.1016/0024-3205(80)90585-8)

*Chapter 4***FLUORESCENCE SCREENS FOR IDENTIFYING CENTRAL NERVOUS SYSTEM–ACTING DRUG–BIOSENSOR PAIRS FOR SUBCELLULAR AND SUPRACELLULAR PHARMACOKINETICS**

Beatty, Z. G., **Muthusamy, A. K.**, Unger, E. K., Dougherty, D. A., Tian, L., Looger, L. L., Shivange, A. V., Bera, K., Lester, H. A., & Nichols, A. L. (2022). Fluorescence screens for identifying central nervous system-acting drug-biosensor pairs for subcellular and supracellular pharmacokinetics. *Bio-protocol*, 12(22), e4551-e4551. <https://doi.org/10.21769/BioProtoc.4551>

**4.1 Abstract**

Subcellular pharmacokinetic measurements have informed the study of central nervous system (CNS)–acting drug mechanisms. Recent investigations have been enhanced by the use of genetically encoded fluorescent biosensors for drugs of interest at the plasma membrane and in organelles. We describe screening and validation protocols for identifying hit pairs comprising a drug and biosensor, with each screen including 13–18 candidate biosensors and 44–84 candidate drugs. After a favorable hit pair is identified and validated via these protocols, the biosensor is then optimized, as described in other papers, for sensitivity and selectivity to the drug. We also show sample hit pair data that may lead to future intensity-based drug-sensing fluorescent reporters (iDrugSnFRs). These protocols will assist scientists to use fluorescence responses as criteria in identifying favorable fluorescent biosensor variants for CNS-acting drugs that presently have no corresponding biosensor partner.

**4.2 Background: CNS Drugs & Sensors**

Low-molecular-weight central nervous system (CNS)–acting drugs typically bind to receptors, transporters, and ion channels (both ligand- and neurotransmitter-gated). Such CNS-acting drugs have therapeutic uses, but some are also abused (Henderson & Lester, 2015; Lester et al., 2012). Sources for new drug compounds typically include nature (mostly plants) or medicinal chemistry.

The protein targets of CNS-acting drugs are synthesized, assembled, and processed

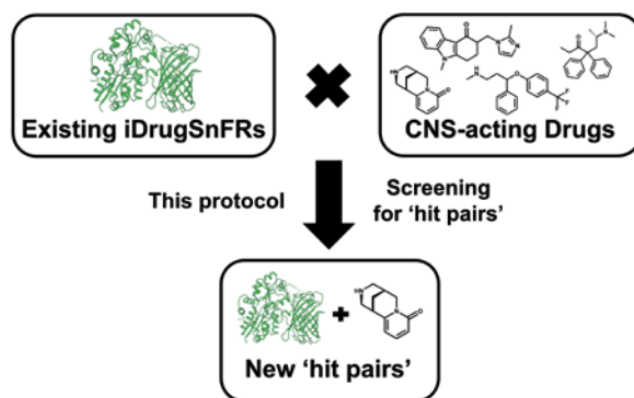


Figure 4.1: Graphical abstract.

within intracellular exocytotic pathways before eventually reaching the plasma membrane. In some cases, membrane-permeant drugs also interact with their targets in intracellular compartments. For this reason, many papers report on pharmacokinetic characteristics of CNS-acting drugs at the subcellular scale: dynamics and intracellular concentrations. Optical methods provide appropriate time and distance scales, and the genetically encoded fluorescent biosensors we have developed bear strong resemblance to those developed for individual neurotransmitters (Marvin et al., 2018; Unger et al., 2020). The reversibility and linearity of such sensors also render them useful for the more conventional application of monitoring within extracellular biofluids (Muthusamy et al., 2022).

A general term we use to describe our biosensors is iDrugSnFR (intensity-based drug-sensing fluorescent reporter), following the lead of iGluSnFR (an early sensor for the neurotransmitter glutamate) (Marvin et al., 2018). All the iDrugSnFRs described here consist of circularly permuted green fluorescent proteins (cpGFP) inserted into a suitably mutated OpuBC periplasmic choline binding protein (PBP) from *Thermoanaerobacter sp513*. Upon the development of the first iDrugSnFR (iNicSnFR3a for nicotine), we conducted several screens with the goal of developing iDrugSnFRs for other drugs (Bera, Kamajaya, Shivange, Muthusamy, Nichols, Borden, Grant, Jeon, Lin, Bishara, et al., 2019b; Muthusamy et al., 2022; Nichols et al., 2022; Shivange et al., 2019). The present report shows the protocol for such screens.

In most cases, screening is required to develop a novel biosensor because, at present, we cannot predict atomicscale details of the interaction between a drug of interest and the PBP site. Some pharmacological structure–activity relations (such as cation-

$\pi$  boxes) that govern the interaction between a CNS-acting drug and its putative binding partner are recapitulated in the drug-iDrugSnFR binding site, while others are not (Bera, Kamajaya, Shivange, Muthusamy, Nichols, Borden, Grant, Jeon, Lin, Bishara, et al., 2019b; Muthusamy et al., 2022; Nichols et al., 2022) (Protein Data Bank files 7S7T, 7S7U, 7S7X, and 7S7Z). Screens reported here have two classes of molecular input: purified biosensor candidate proteins (13–18 per screen) and drugs of interest (DOIs, 44–84 drugs per screen). The DOIs we have chosen to study typically contain nitrogen (i.e., are alkaloids), have molecular weights (MW) below 500, and are weak bases ( $6 < \text{pK}_a < 10$ ). The weakly basic nature of these molecules allows passive diffusion through membranes into cells and organelles, enabling us to study their subcellular pharmacokinetics.

We define a hit pair as a drug–biosensor pair that displays an acceptable fluorescence signal ( $\Delta F/F_0 > 1$ ). This definition of a hit arises from our experience that  $\Delta F/F_0 > 1$  is required for subsequent directed evolution of an optimal biosensor variant. This report describes screens with single DOI concentrations and validations with full dose-response relations (several concentrations of the DOI) (Bera, Kamajaya, Shivange, Muthusamy, Nichols, Borden, Grant, Jeon, Lin, Bishara, et al., 2019a).

In general, the biosensor of the hit pair becomes the starting construct for directed evolution of an optimized variant that senses the DOI. Other papers describe the directed evolution of optimized variants (Bera, Kamajaya, Shivange, Muthusamy, Nichols, Borden, Grant, Jeon, Lin, Bishara, et al., 2019b; Muthusamy et al., 2022; Nichols et al., 2022; Shivange et al., 2019). In all cases, the directed evolution also includes optimizing the selectivity against other drugs. This workflow has resulted in iDrugSnFRs for cholinergic compounds, opioids, and the rapidly acting antidepressant S-ketamine (Muthusamy et al., 2022; Nichols et al., 2022; Shivange et al., 2019). Reports on additional iDrugSnFRs are in preparation.

### **4.3 2017 Screen: Psychiatric Drugs**

In 2017, a single concentration drug–biosensor fluorescence screen was conducted with a primary focus on drugs used to treat psychiatric disorders (Figure 4.2). Drugs were chosen both based on clinical importance and to encompass a range of pharmacological or therapeutic classes; classes present included opioids, anticholinergics, antipsychotics, antidepressants, benzodiazepines, anti-seizure medications, and sedatives. In total, 84 drugs and 13 biosensors were screened. We also grouped results into general categories based on the most common treatment use: schizophre-

nia, major depressive disorder, anxiety disorders, epilepsy, and other. As noted, a hit pair comprises a pair of molecules: drug and biosensor. In total, 190 drug–biosensor hit pairs were identified, with  $\Delta F/F_0$  ranging from 1.0 to 18.5. From these, 108 hit pairs had  $1 < \Delta F/F_0 < 3$  and thus could likely be used to generate optimized biosensor variants through directed evolution. The remaining 82 hits had  $\Delta F/F_0 > 3$  and thus could likely be used for cellular imaging without further mutations. Hit pairs were concentrated in three clinical use categories (schizophrenia, major depressive disorder, and other), with no hit pairs identified for anxiety and epilepsy drugs. The v7.1.2 biosensor participated in the largest number of hit pairs; these also had the highest  $\Delta F/F_0$  values (Figure 4.2).

This screen allowed for the identification of drug–biosensor pairs, from which the biosensor could potentially be evolved for engineering of novel variant biosensors for various neuropsychiatric medications. Biosensors for two nicotinic agonists, cytisine and dianicline, were engineered based on hit pairs obtained from this screen. The directed evolution of these sensors, as well as associated experiments on the subcellular pharmacokinetics of these drugs, are detailed in Nichols et al. (2022). The hit pair involving methadone became the basis for a selective variant, iS-methadoneSnFR (Muthusamy et al., 2022).

Because many of the drugs included in this screen are sparingly water-soluble, DMSO was often used for dissolution. However, this screen showed that DMSO interacts with several biosensor candidates, even in the absence of a DOI. This phenomenon resulted in the presence of many negative  $\Delta F/F_0$ s, as the baseline biosensor fluorescence was higher than would be reasonable if the biosensor and solvent were not interacting. This showed that additional normalizations and corrections would be required when DMSO was used as a solvent with iDrugSnFRs (see Notes). We have not systematically studied the residues responsible for DMSO sensitivity.

The 2017 screen was also informative in showing a failure: we found no hit pairs involving S-ketamine, its enantiomers, or its metabolites. Faute de mieux, we performed site-saturated mutagenesis on a residue, Tyr357, that makes a key cation- $\pi$  interaction with nicotinic drugs (Shivange et al., 2019; Unger et al., 2020). This resulted in the S-ketamine responsive Tyr357Gly construct termed AK1, and we evolved AK1 into variants that satisfactorily sense S-ketamine. We included these variants in subsequent screens described below.

Biosensor Nickname	v4.6	v4.8.1.2	v6	v7	v7.1	v7.1.2	v8	v9	cc70	cc93	AK1	L121G4	L194D
Published Name	iNicSnFR1	--	--	iNicSnFR3b	--	--	--	iAChSnFR	--	iNicSnFR3a	--	--	--
iSnFRBase Number	S002	S099	S004	S007	S085	S086	S098	S008	S364	S006	S291	S015	S097
<b>SCHIZOPHRENIA</b>													
Melperone	-0.1	0	0	2.5	0.2	9.1	0.8	-0.1	-0.1	1.6	-0.2	0	0
Loxapine	0	0.1	-0.2	-0.2	-1.9	0.3	-2.1	-1.3	-0.3	-0.6	-0.1	-0.1	0
Ziprasidone	-0.1	-0.1	-0.4	-5.1	-5.2	-0.4	-3.3	-3.4	-0.9	-4.4	0	0.1	0.2
Paliperidone	0	-0.1	-0.2	-2.4	-2.3	-0.2	-3.5	-1	-0.3	-2.3	0.6	-0.8	-0.1
Risperidone	-0.2	-0.6	-1.5	-9	-8.4	-4	-8.8	-2.5	-2	-10.3	0	-9	-0.6
Sulpiride	0.2	0.5	0.2	12	4.8	18.5	3.6	1	0.2	10.3	1.5	-0.1	0.1
Clozapine	0.1	0.3	0.3	1.1	2.8	4.1	1	0.4	0.1	1.4	0.2	0.2	0.3
Clotiapine	0.3	0.4	0.6	7.2	2.5	3.2	2	-0.2	0.3	4.8	0.8	1.7	0.3
Remoxipride	0	0	0	-1.5	-3.3	2.6	-3.2	-0.4	-0.1	-1.3	0.2	-0.3	-0.1
Aripiprazole	0	0	0	1	1.1	8.1	1.1	0.4	0	0.8	0.2	0	0.1
Olanzapine	-0.1	-0.1	-0.3	-4	-4.7	0.4	-4.3	-1.7	-0.6	-3.9	0.1	-0.1	-0.1
Quetiapine	-0.1	-0.1	-0.1	-2.8	-2.7	-0.2	-2.2	-0.6	-0.3	-2.6	0.2	-0.1	0.1
Fluperlapine	-0.2	0.3	0.4	5.2	3.2	6.7	3.2	1.3	0.4	4.4	0.4	0.2	0.3
Bifeprunox	0.1	0	0.5	-1.3	-1.2	1.6	-0.3	-0.5	0	-0.9	0.1	0.9	1.1
Blonanserin	0	0	0	1.5	-0.1	0.1	0.1	0	0.1	-0.1	0	0	0
Lurasidone	0	0.1	0.3	0.7	0.2	0.6	0.4	0.3	0.2	-0.3	-0.1	1.1	0.1
Molindone	-0.1	0	-0.2	-0.4	-1.5	0	-0.9	-0.2	-0.2	-0.8	0.1	0	0
Perospirone	-0.1	0	-0.1	-1.8	-2.1	-0.1	-1.4	-0.1	-0.1	-1.7	1	0.1	0
Pimvanserin	0.1	0.1	0.3	4.5	2.4	8.2	1.9	1.2	0.3	2.3	0.2	0.1	0.1
Sertindole	0.1	0.2	0.3	-0.5	0	1	0.5	0.7	0.3	-0.3	1.4	0.4	0.8
Zotepine	0.5	0.8	0.6	6.7	1.7	3.3	1	0.3	0.7	4.4	1.6	0.2	0.1
Haloperidol	0	0	0	0.3	-1.8	0	-0.2	-0.2	-0.1	-0.2	0.6	0.1	0.2
L-741,626	0.1	0.2	0.6	0.6	0.5	4.2	0.5	0.4	0.4	0.4	0.6	6.3	7.3
Asenapine	0	0.1	0	-3.5	-3.6	0.3	-2.8	-1.1	-0.2	-3.2	1.6	0.9	1.6
Chlorpromazine	0.8	1.2	1	-4.4	-5	7.4	-4.6	-1.9	0.6	-3.8	1.3	3	5.4
Flupentixol	0.2	0.1	0.3	-4.6	-5.2	-0.2	-3.6	-1.4	0	-3.8	0.3	0.7	0.8
Fluphenazine	0.3	0.2	0.8	-3.6	-3	1	-2	-0.6	0.3	-2.9	0.1	1.2	2.9
Trifluoperazine	0.8	1.5	0.9	-1.7	-3.4	6.5	-3.4	-1.2	0.2	-1.5	1	0.8	1.8
Lexomepromazine	0.3	1	0.5	-3.9	-3.4	1.6	-3.4	-1.1	0.1	-3.1	1.2	2.2	4.5
Prochlorperazine	0.7	1.7	0.4	-3.3	-4.7	4.6	-4	-1.9	-0.2	-2.5	1.2	1.1	3.1
Thiothixene	0.3	0.7	0.6	-1.8	-3	2.6	-1.9	-0.3	0.5	-1.4	0.9	0.5	0.4
<b>MAJOR DEPRESSIVE DISORDER</b>													
Mirtazapine	0.1	0.1	0.1	-0.5	-0.8	1.3	-0.7	0	0.1	-0.3	1.6	0.1	0.4
Vortioxetine	0.1	0.2	0.2	0.2	-1.4	0.9	-0.9	0.1	0.2	-0.2	4.1	0.4	0.6
Desvenlafaxine	-0.1	-0.1	-0.2	-1.9	-2.6	-0.3	-2.4	-1	-0.4	-2.1	0.4	-0.1	-0.1
Duloxetine	0	0	0	1.6	0	1.9	-0.3	-0.4	-0.1	1.1	0.3	1.6	1
Nortriptyline	0.1	0.2	0.2	-2.5	-4.2	1.1	-3.5	-0.6	0	-3	1.3	0.5	0.8
Fluvoxamine	0	0	-0.1	-1.7	-1.5	0	-1.1	-0.3	-0.1	-1.4	-0.1	0	0
Amoxapine	-0.2	0	-0.3	-7.9	-7.8	-1.2	-7.1	-5.2	-1	-7.1	-0.2	-0.1	-0.1
Clomipramine	0.8	1.4	1	-5.8	-6.3	4.8	-5.9	-2.5	0.2	-5	1.1	1	1.6
Escitalopram	0.6	1.3	0.4	8.2	-0.6	6.3	-2.3	-0.5	0.2	5.9	0.8	0	0
Amitriptyline	0.2	1.9	0.4	-3.1	-5.1	6.3	-5.2	-1.4	0.4	-3	2.7	0.3	0.6
Citalopram	0.6	1.1	0.7	8.9	-0.1	6.8	-1.6	0.2	0.5	6.4	0.8	0.1	0.1
Sertraline	0.1	0.1	0.2	-1.9	-3.9	2.4	-3.6	-0.6	0.1	-1	3.9	0.4	0.7
Venlafaxine	0	0	0	1.8	0.3	0.4	0.1	0.1	0	-0.1	0.3	0	0
Fluoxetine	0.1	0.1	0.1	-0.4	-1.2	0.8	-0.6	0.2	0.2	-0.4	0.1	1.1	0.9
Paroxetine	0.1	0.1	0.1	-2.1	-1.7	0.1	-1.4	-0.3	0.1	-1.6	1.7	0.1	0.4
Hydroxybupropion	0.1	0.1	0.2	4.2	0.2	0.7	0.4	0.7	0.3	1.6	0.2	0.2	0.1
Vilazodone	0	-0.1	-0.2	-1.4	-1.3	-1.5	-1.8	-0.2	-0.2	-1	0.4	0.5	0.2
<b>ANXIETY DISORDERS</b>													
Trazodone	-0.1	-0.1	-0.1	-2.3	-1.5	-0.3	-1.4	-0.5	-0.1	-1.6	-0.1	0	0.1
GBL 345	0	-0.1	-0.1	-1.9	-1.2	-0.5	-2.3	-1	-0.2	-2.1	0	0.1	0.1
Clonazepam	0	0	0	0.2	-0.6	-0.2	-0.6	-0.3	-0.1	-0.6	0.1	-0.1	0.1
Diazepam	0	0	0	-2.3	-1.3	0	-1.4	-0.4	-0.1	-1.2	0.9	0	0
Lorazepam	-0.1	0	-0.1	-0.8	-0.8	0.1	-0.9	-0.2	-0.1	-0.4	0.2	0	0.2
<b>EPILEPSY</b>													
Natoxetine	0	0	0	0.6	-0.3	-0.1	-0.4	-0.2	-0.1	-0.2	0	0	-0.1
Scopolamine	0	0	0	0.5	-0.4	0	-0.4	0	0	-0.2	0	0	0.1
Tramadol	0	0	0	0.1	-0.2	-0.1	-0.5	-0.3	0	0.2	0	0	0.1
<b>OTHER</b>													
Natoxetine	0	0	0	-0.5	-0.7	1.2	-0.7	-0.4	-0.1	-0.3	0.2	0	0
Scopolamine	0.4	0.9	0.4	7.5	4.6	9.2	3.1	0.1	0	6.8	0.2	0	0
Tramadol	0	0	0	1.8	-0.2	0.2	-0.7	-0.3	-0.1	-0.1	0.8	0	0
Droperidol	0	0	-0.1	-1.6	-3.2	-0.3	-1.1	-0.2	-0.6	-2.4	0.7	-1	0.2
Bupropion	0	0	0	1.2	-1.5	3.9	-1	-0.3	0	0.5	0.2	0	0.1
Eszopiclone	0	0	0	-0.9	-1.6	0.1	-1.9	-0.5	-0.1	-1.6	0.1	0	0
Pregabalin	-0.1	0	-0.1	-7.7	-7.7	-1.1	-7	-5	-0.8	-6.9	-0.2	0	0
Zaleplon	-0.1	0	-0.1	-1.3	-2	0	-2.2	-0.6	-0.2	-1.5	-0.3	0	0
L-963,403	0	-0.1	-0.2	-1.4	-1.3	-1.5	-1.8	-0.2	-0.2	-1	0.4	0.5	0.2
GR 135351	0	0	-0.1	0.1	-0.5	-0.2	-0.6	-0.3	-0.1	-0.7	0	0.1	0.2
2-Phenylmelatonin	0.1	0	0.2	-0.4	-1.3	-0.2	-0.7	-0.3	0	-0.8	0.1	0.3	0.4
Raclopride	-0.1	0.1	-0.3	-3.3	-6	3.4	-6	-2.3	-0.6	-3.6	0	-0.2	-0.3
Metoclopramide	0.1	0.1	0.2	6	2	9.5	2.3	0.1	0	3.9	0.5	0.3	0.5
Flumazenil	0	0	-0.1	-2.2	-2.7	-0.3	-2.2	0.6	-0.2	-2.1	0.9	0	0
Gabapentin	0	0	0	0.4	-0.7	-0.1	-0.4	-0.2	-0.1	-0.2	0	0	0
BTCP	-0.1	-0.1	-0.2	-2.1	-2.7	0.3	-2.1	-1	-0.3	-2	1	-0.1	-0.1
Vanoxerine	-0.1	-0.1	-0.1	-3.3	-3.2	1.7	-3.3	-2.4	-0.4	-3.3	0.4	1.5	1.3
Phaclofen	5.5	8.7	-0.1	-2.1	1.4	-0.8	-7.1	-5.2	-1	-4.5	10	-0.7	16.3
Baclofen	0	-0.1	0	0.3	0	0	-0.1	0	0	-0.2	0	0	0
Cinanserin	0.4	0.6	0.5	6.4	6.8	8.5	5.3	0.5	1	6.3	5.2	0	0.2
6-Nitroquipazine	0	0	-0.2	0.6	-0.4	2.3	-0.4	-0.4	-0.3	0.4	0.7	0	0.1
3-CPMT	0.7	1.2	1	8.1	2.1	12.8	3.2	0.9	0.4	5.1	0.8	0.2	0.2
CAS 202646-03-5	0.7	1.8	1.1	6.9	1.6	11.3	2.1	0.3	0.4	3.2	1.1	0.2	0.4
Radafaxine	0	0	0.1	1.5	-1.9	0.4	-0.8	0.1	0.1	1.1	0.1	0	0.2
Methadone	1	2.5	1	6	-1.9	3.2	-2.1	-0.2	0.3	2.2	3.6	0	0
<b>2018 MINI-SCREEN</b>													
Cytisine	0.1	0.2	0.2	1.8	1.6	1.6	1.1	2.3	0.2	0.8	0.3		
Dianicline	1.4	3.9	2.9	11.2	9.9	7.6	6.6	7.4	0.9	7.2	0.7		
A85380	0.2	0.6	0.5	4.2	3.9	1.8	2.1	4.4	0.5	2.2	0.5		

Figure 4.2: Results map from the 2017 single concentration drug–biosensor fluorescence screen. Fluorescence response (as represented by  $\Delta F/F_0$ ) for drug–biosensor pairs included in the 2017 screen. Fluorescent response shading from green ( $\Delta F/F_0 \geq 3$ ) to white ( $\Delta F/F_0 = 0$ ), in which stronger hits are represented by darker green, weaker hits by lighter green, and non-hits by white. Drug–biosensor pairs that were not screened are in black.

#### 4.4 2018 Screen: Opioids

The 2018 screen was conducted to identify biosensor–drug hit pairs for opioids of several categories (Figure 4.5). Drugs included in the screen were chosen based on clinical importance, as well as presence in the existing literature. Most opioids included activate the  $\mu$  opioid receptor, though several drugs target  $\kappa$  and  $\delta$  opioid receptors. An Other category was composed of opioid inhibitors. In total, 48 drugs and 16 biosensors were included. From these pairs, 205 total drug–biosensor hits were identified. Of these, 128 hits had  $1 < \Delta F/F_0 < 3$ , while 76 had  $\Delta F/F_0 > 3$ . Thirty of the 48 drugs tested participated in at least one hit pair, with most having hit pairs with several biosensors (one drug had a single hit pair). Additionally, each biosensor participated in a hit pair with at least one drug. The proportion of hit pairs varied by drug category. No hit pairs were found for  $\delta$  opioids ligands, while the largest proportion of hit pairs were found for  $\mu$  opioid ligands. Hit pairs also varied in fluorescence response, with the weakest pair having a  $\Delta F/F_0$  of 1.0 (our at least definition for a hit pair) and the strongest pair having a  $\Delta F/F_0$  of 19.0 (tapentadol  $\times$  biosensor v7). Generally, the v7 biosensor series (including v7, v7.1, v7.1.2, v8, and v9) had strong responses with  $\mu$  opioids (Figure 4.3). This screen allowed for the identification of drug–biosensor pairs that could lead to the engineering of novel opioid biosensor variants. Furthermore, this screen showed many strong hit pairs involving clinically relevant  $\mu$  opioid ligands, which could allow for direct cellular imaging or efficient generation of novel biosensors for this drug class.

Biosensor Nickname	v4.6	v4.8.1.2	v6	v7	v7.1	v7.1.2	v8	v9	cc70	cc90	cc93	AK1	AK2	AK3	AK4	L194D1
Published Name	iNicSnFR1	--	--	iNicSnFR3b	--	--	--	iAChSnFR	--	iNicSnFR2	iNicSnFR3a	--	iSKetSnFR1	--	--	--
iSnFRBase Number	S002	S099	S004	S007	S085	S086	S098	S008	S364	S005	S006	S291	S120	S121	S122	S097
<b>KAPPA</b>																
U-69,593	0	0.1	0.1	0.1	0.1	0.2	0.2	0.2	0.2	0.1	0.2	1	0.2	0.1	0.2	0.1
Salvinorin B	0.1	0.1	0.1	0	0.1	0.1	0	0.1	0.1	0.1	0.1	0	0	0.1	0	0.4
Salvinorin A	0	0	0.1	0	0	0	0	0.1	0	0.1	0.1	0.3	0	0	0	0.3
nor-Binaltorphimine	0.1	0.1	0.2	0.4	0.1	0.5	0.2	0	0.1	0.4	0.2	-0.5	-0.2	-0.1	-0.3	0.2
ML138	0.4	1.6	2.2	-0.2	-0.2	0.5	-0.3	-0.3	-0.2	-0.2	-0.3	0.3	-0.2	0.2	-0.1	2
GR 896996	0	0.1	0.1	0.8	0.3	0.8	0.3	0.5	0.1	1.1	0.4	1	0.5	0.1	0.6	0.1
BRL 52537	0.4	0.8	0.5	12.3	5.9	8.9	4.3	4.5	0.6	3.9	3.5	1.3	1.6	1	2.2	0.3
Amentoflavone	0.1	0.9	0.7	-0.9	-0.5	0.7	-0.7	-0.6	-0.5	-0.5	-0.3	0.2	-0.3	-0.1	-0.4	1.2
<b>DELTA</b>																
ARM390	0.2	0.1	0.2	0.1	0.1	0.1	0.1	0.1	0.2	0.2	0.1	0.2	0	0.2	0	0.1
SNC80	0.2	0	0.2	0.1	0.1	0.2	0.1	0.1	0.2	0.2	0.1	0	0	0.1	0	0.1
Naltrindole	0	0.1	0.1	-0.7	-0.6	0.5	-0.5	-0.2	0	-0.2	-0.6	0	0	0	0.1	0.2
Naltrexone	-0.1	-0.1	-0.1	-0.3	-0.3	-0.2	-0.2	-0.1	-0.1	-0.1	-0.2	-0.1	-0.1	0	-0.1	0.2
Desmethylozapine	0.1	0.2	0.2	0	0.1	0.1	0	0.1	0.1	0.1	0	0.1	-0.1	0	-0.2	0.4
6'-GNTI	-0.1	0.1	0	0.6	0.3	0.7	0.3	0.6	-0.2	0.5	0.2	0.2	0.6	0.2	0.6	0.2
Tianeptine	0.3	0.2	0.2	0.2	0.2	0.4	0.2	0.2	0.3	0.4	0.1	0.2	0	0	0	0.1
<b>MU</b>																
Codeine	1.6	3.9	2.7	3.3	3.3	2.9	2.9	4.9	0.7	3.4	1.3	0.2	0.1	0.1	0	0.1
Oxymorphone	0.4	0.5	0.4	1.9	1.9	1.5	1.5	2.3	0.4	2.3	0.5	0.5	0	0	-0.1	-0.3
Nalorphine	0	0.1	0	2.8	0.9	1.4	0.7	1.6	0.1	2.6	1.1	0	0	-0.1	0.2	0
Hydromorphone	0.8	1.3	1.4	2.3	2.8	1.9	3.5	4.9	1.2	2.5	0.9	0.5	0.1	0	-0.1	-0.3
Morphine-6-glucuronide	-0.1	-0.2	-0.2	0.6	0.5	-0.5	-0.2	1.3	0	1.3	-0.1	-0.1	-0.1	-0.1	-0.2	-0.1
Hydrocodone	0.8	1.6	1.2	1.4	1.4	1.8	1.8	2.8	1.1	2.1	0.5	0	-0.2	-0.1	-0.3	-0.1
Naltrexone	0.2	0.3	0.3	5.6	2.1	6.9	2.1	3.7	0.1	3.4	2.3	0	0.2	0.1	0.6	0
Nalmefene	0.2	0.4	0.3	8.4	5	4.5	5.7	5.2	0.1	3.2	3.6	0.2	0.3	0.2	0.5	0.1
Oxycodone	0.1	0.2	0.1	0.1	0	0.2	0.1	0.1	0.1	0.1	0.1	0.1	0.1	0.1	0	0
Noroxymorphone	0	0.1	0	0	0	0	0	0.1	0	0	0	0.1	0	0	0	0
Butorphanol	0.4	0.8	0.8	5.2	2.3	6.1	2.3	3	0.2	2.7	2.2	1.2	1.8	0.4	2.8	-0.1
Levallorphan	0.4	0.3	0.3	6.8	5	2.3	5	4.3	0.2	3.2	3.7	1.5	0.4	0	0.5	0
Levorphanol	1.3	4	3.7	8	6.3	5.3	5.3	5.5	1.7	3.2	3.4	1.7	0.5	0.4	0.5	-0.4
Alfentanil	0	0	0	0	0	0.1	0.1	0.1	0	0.1	0	-0.1	1.2	0.7	1.6	0
Sufentanil	-0.3	-0.3	-0.3	-0.1	-0.2	0.1	0.1	-0.1	-0.3	-0.1	-0.1	0.7	0.1	-0.1	0.2	0
Fentanyl	-0.2	-0.1	-0.2	-0.1	-0.2	0.1	0.1	-0.1	-0.2	0.1	0	0.9	0.7	1.2	1.1	0
Carefentanyl	0.2	0.1	0.2	0.2	0.3	0.2	0.1	0.1	0.1	0.2	0	0.2	0.1	0.1	0.1	0
Norfentanyl	0.6	1.1	1.1	1.5	1.8	2.5	1.2	2.5	0.5	2.3	0.4	0.3	0.2	0.2	0.3	0.2
Meperidine	0.7	1.1	0.7	4.6	4.6	4	4	4.5	1	3	1.3	0.5	0.3	0	0.3	0.1
ML-335	0.3	0.1	0.3	0.1	0.2	0.2	0.1	0.1	0.2	0.2	0.1	0	0.3	0.5	0.6	0.2
Loperamide	0	0	0	-0.2	-0.2	-0.1	-0.2	0	0	-0.3	-0.2	0.5	0.6	0.7	0	0
Mepizolinol	1	1.3	1	3.9	4	12.2	5.5	5.8	1.3	3.8	3.8	2.2	1	1	1.3	0
Mitragynine	1	1.8	0.5	0.1	0.1	5.9	2.7	0.2	1.6	0.3	1.2	1.4	1.7	0.8	1.8	1.3
Tapentadol	0.9	4.4	4	19	9.2	14	14	6.4	2.1	4	7.3	1.1	1.5	0.3	2	0
Tramadol	0.2	0.1	0.1	3.1	1.3	0.7	0.6	1	0.2	2.4	0.7	1.8	0.3	0.1	0.3	0.1
desMe-Tramadol	0.3	0.4	0.5	4.9	2.8	1.7	1.6	2.4	0.7	2.9	1.1	1.6	0.3	0	0.4	0
DMS-986122	0	1.9	2.5	-0.5	-0.6	0.2	-0.5	-0.4	-0.4	-0.5	-0.6	0	-0.3	0.1	0	3.5
<b>OTHER</b>																
Lofexidine	0.7	1.2	1	6.3	3.5	2.5	4.1	4.8	1.7	3.7	2.7	0.7	0.3	0.1	0.5	0
Glucuronic acid	-0.1	-0.1	-0.1	0	-0.1	0	0.1	0	0.1	0.1	0	-0.1	0	0	0	0
Cimetidine	1	1.4	1.5	2.5	1.3	3.3	1.1	1.7	0.7	2.9	0.7	1.5	0.7	0.3	0.1	0.4
Amiodarone	1.1	1.9	2.7	0.2	0.2	2.4	0.1	-0.1	0.3	0.1	0.3	0.4	0.1	0.4	0	3.1
Norepinephrine	0	0	-0.1	0	-0.1	-0.1	-0.1	-0.1	-0.1	0	-0.1	-0.1	-0.1	-0.1	-0.1	-0.1
Allopregnalone	0.3	1.1	1.3	-0.2	-0.2	0.4	-0.3	-0.2	-0.1	-0.2	-0.3	-0.1	-0.1	0.1	-0.1	1.6

Figure 4.3: Results map from the 2018 single concentration drug–biosensor fluorescence screen. Fluorescence response (as represented by  $\Delta F/F_0$ ) for drug–biosensor pairs included in the 2018 single concentration drug–biosensor fluorescence screen. Drugs are grouped by opioid category. Fluorescent response shading from green ( $\Delta F/F_0 \geq 3$ ) to white ( $\Delta F/F_0 = 0$ ), in which stronger hits are represented by darker green, weaker hits by lighter green, and non-hits by white.



#### 4.5 2019 Screen: 5-HT<sub>3</sub> Ligands, CB<sub>1</sub>/CB<sub>2</sub> Ligands, and Neonicotinoids

The 2019 screen was completed to identify hit pairs involving previously unscreened classes of CNS-acting drugs (Figure 4.4). Several drugs were included from each of five classes: 5-HT<sub>3</sub> antagonists, anticholinergics, CB<sub>1</sub>/CB<sub>2</sub> ligands, opioids, and neonicotinoids. Individual drugs of interest from a range of classes were also included and designated by an Other category. In total, 44 drugs were included and tested against 18 biosensor proteins. A total of 106 drug–biosensor hit pairs were identified, with 81 having  $1 < \Delta F/F_0 < 3$  and 24 having  $\Delta F/F_0 > 3$ . Twenty-one of the 44 drugs chosen participated in a hit pair with at least one biosensor. Additionally, each biosensor had a hit pair with at least one drug. Certain biosensors showed strong responses with several drugs in the same class. For example, L194D1 [a precursor to the biosensor iSeroSnFR, which detects serotonin (Unger et al., 2020)] displayed hit pairs for six CB<sub>1</sub>/CB<sub>2</sub> ligands, with responses ranging from  $\Delta F/F_0$  of 3.5–5.0. Several other biosensors (v4.6, v4.8.1.2, v7 436A, and Scop4) also participated in hit pairs with several CB<sub>1</sub>/CB<sub>2</sub> ligands, albeit less strongly (Figure 4.4). This screen expanded the number of drug–biosensor hit pairs identified that could be used for engineering of novel variants, as well as the range of drug classes. 5-HT<sub>3</sub> antagonists participated in many hit pairs and also showed promising results in validation through dose-response measurements.

Biosensor Nickname	AK1	AK2	AK8	cc70	cc90	cc93	v4.6	v4.8.1.2	v7	v7A	v7.1	v7.1.2	v8	v9	v9 SH	AK1 AG	Scop4	L194D
Published Name	--	iSKetSnFR1	iSKetSnFR2	--	iNicSnFR2	iNicSnFR3a	iNicSnFR1	--	iNicSnFR3b	--	--	--	--	iAChSnFR	--	--	--	--
iSnFRBase Number	S291	S120	S128	S364	S005	S006	S002	S099	S007	S280	S085	S086	S098	S008	S037	S302	S136	S097
<b>5HT3 ANTAGONISTS</b>																		
Ondansetron	1.4	0.4	0.1	1.2	0.8	-0.7	0.2	0.0	0.0	0.2	0.4	2.1	0.2	0.3	0.0	0.3	1.9	0.1
Tropisetron	2.2	1.1	-0.1	0.5	1.2	0.3	0.8	0.4	2.2	0.6	4.1	7.2	4.0	0.5	0.6	0.8	1.6	0.2
Palanasetron	2.7	0.3	0.2	1.7	1.1	-0.1	0.0	-0.3	1.1	0.8	2.4	5.3	1.9	0.4	0.9	0.0	2.6	0.2
Alosetron	-0.1	0.0	0.1	0.0	0.2	0.1	0.1	-0.6	0.0	0.3	0.1	0.3	0.0	0.1	0.5	0.0	0.0	0.1
<b>ANTICHOLINERGICS</b>																		
Mecamylamine	0.4	-0.1	-0.1	0.0	1.2	-0.6	-0.2	-0.5	0.4	-0.2	0.3	2.6	0.2	-0.1	-0.5	-0.3	0.8	0.2
Tacrine	1.2	1.3	0.4	1.3	-0.4	-0.9	-0.2	-0.5	-0.7	-0.2	-0.6	0.7	-0.6	-0.5	-0.3	-0.3	2.5	1.0
Tiotropium	0.4	-0.3	-0.5	-0.2	-0.2	1.2	1.5	2.1	0.4	3.6	0.3	4.7	0.2	-0.3	1.0	-0.2	0.4	-0.3
Hamicholinium	2.2	0.9	0.4	1.7	0.8	-0.3	0.8	2.7	0.5	3.6	1.6	3.3	1.1	0.1	0.8	1.0	3.2	0.2
<b>NEONICOTINOIDS</b>																		
Nitenpyram	0.0	-0.2	0.0	-0.1	-0.1	-1.0	-0.3	-0.7	0.1	-0.4	-0.4	-0.2	-0.1	-0.2	-0.6	-0.1	-0.1	-0.2
Acetamiprid	0.3	1.0	0.0	0.8	-0.3	-0.9	-0.4	-0.7	-0.1	-0.3	-0.5	-0.5	-0.1	-0.2	-0.5	-0.3	0.0	-0.1
Thiacloprid	0.0	0.0	-0.2	0.0	0.0	-1.0	0.1	-0.1	-0.1	0.3	-0.2	-0.1	-0.1	0.0	-0.3	-0.1	-0.1	-0.1
Clothianidin	-0.1	-0.2	-0.1	-0.1	0.2	-0.8	-0.2	-0.3	-0.2	-0.3	-0.2	0.1	-0.2	0.3	-0.2	0.0	-0.2	-0.2
Dinotefuran	-0.1	-0.1	-0.3	0.0	-0.5	-0.9	-0.3	-0.8	-0.1	-0.3	-0.7	-0.6	-0.1	-0.1	-0.6	-0.3	-0.1	-0.1
Imidacloprid	0.0	0.0	0.0	0.0	-0.9	0.3	-0.2	0.0	-0.4	0.0	0.0	0.0	0.0	0.0	-0.4	0.0	-0.1	0.1
Thiamethoxam	0.0	0.4	0.1	0.4	-0.1	-0.9	-0.3	-0.5	-0.1	-0.1	0.0	-0.2	-0.2	-0.2	-0.4	-0.4	0.0	-0.1
<b>OPPIOIDS</b>																		
Buprenorphine	-0.2	-0.2	0.0	-0.2	0.1	-0.9	-0.1	-0.2	-0.2	-0.3	-0.2	-0.2	-0.1	-0.2	-0.3	0.0	-0.1	-0.1
DADLE	-0.1	-0.1	0.0	-0.1	0.0	-0.9	-0.3	-0.6	0.1	-0.3	-0.3	-0.2	0.0	-0.2	-0.6	-0.2	0.0	-0.1
DAMGO	-0.1	-0.2	-0.1	-0.2	-0.5	-1.0	-0.2	-0.6	0.0	-0.3	-0.6	-0.6	0.0	-0.2	-0.6	-0.3	0.0	-0.2
Mitragynine	0.0	0.2	-0.7	0.1	0.1	6.1	-0.1	-0.9	-0.1	0.0	0.1	-0.1	-0.2	0.0	0.6	-0.1	-0.2	-0.5
Met-enkephalin	-0.2	-0.2	-0.1	-0.2	-0.5	-1.0	-0.3	-0.6	-0.1	-0.4	-0.6	-0.6	0.0	-0.2	-0.6	-0.3	-0.1	-0.2
EDDP	2.4	1.0	0.1	1.5	0.2	-0.9	0.0	-0.2	-0.3	2.5	-0.5	0.0	-0.4	-0.4	-0.2	-0.1	1.8	-0.1
ML 190	-0.3	-0.1	-0.1	-0.4	0.1	-0.6	0.3	-0.1	-0.3	-0.2	-0.2	0.1	-0.2	0.0	-0.1	0.0	-0.4	0.2
BNTX	-0.1	-0.1	-0.1	0.0	0.0	-1.0	0.1	-0.6	-0.1	0.1	-0.2	-0.1	-0.1	-0.1	-0.5	-0.1	0.0	-0.1
7-OH Mitragynine	0.2	0.0	0.1	0.1	0.1	-1.4	0.3	-0.6	0.1	0.1	0.0	0.0	0.0	0.1	-0.5	0.1	0.1	-0.1
<b>CB1/CB2 LIGANDS</b>																		
SLV 319	0.8	-0.1	0.1	-0.2	-0.4	-0.7	1.5	0.6	-0.4	1.4	-0.5	0.4	-0.4	-0.3	0.4	-0.2	0.6	4.4
O-2050	-0.1	0.0	-0.1	0.2	-0.1	-1.2	-0.2	-0.3	0.1	-0.2	-0.5	-0.3	0.9	0.0	-0.2	0.0	-0.2	0.3
AM 6545	1.6	0.2	0.8	0.4	0.0	-0.7	1.9	1.5	-0.2	2.9	-0.3	1.1	-0.4	-0.4	0.5	0.4	1.4	4.6
Leelamine	-0.6	-0.8	-0.7	-0.7	-0.9	-1.1	-0.4	-0.8	-0.7	-0.7	-0.9	-0.8	-0.8	-0.6	-0.6	-0.8	-0.6	-0.5
CP 94545	-0.1	-0.1	0.0	-0.1	0.0	-0.4	0.2	-0.4	-0.1	0.0	0.0	0.4	-0.1	0.1	-0.4	0.0	-0.1	0.0
Nida 41020	0.9	-0.1	0.3	0.0	-0.3	-0.7	1.5	1.3	-0.5	1.0	-0.6	0.2	-0.5	-0.1	1.1	0.0	1.1	3.8
Rimonabant	1.4	0.1	0.5	0.1	-0.2	-0.8	1.7	1.1	-0.4	1.6	-0.4	0.7	-0.6	-0.3	0.6	0.1	1.3	5.0
Win 55	0.9	0.0	0.5	0.1	-0.1	-0.7	1.3	1.7	-0.1	2.9	-0.1	1.0	-0.2	-0.2	1.1	0.3	0.9	3.5
PSNCBAM-1	1.4	0.3	0.7	0.2	-0.1	-0.3	2.1	0.7	-0.1	2.8	-0.1	1.2	-0.2	-0.3	0.4	0.0	1.5	4.2
<b>OTHER</b>																		
Clazosporin A	0.1	0.1	0.1	0.1	0.2	-0.1	0.6	-0.6	0.3	-0.4	0.3	0.2	0.3	0.4	-0.3	0.1	0.0	0.0
Caffeine	0.7	1.7	0.1	1.2	-0.6	-0.9	-0.3	-0.6	-0.1	-0.3	-0.7	-0.6	-0.1	-0.2	-0.4	-0.2	0.4	-0.1
Stachydrine	0.0	0.0	0.0	0.0	0.0	-0.9	0.3	-0.2	0.1	0.3	0.0	0.0	0.0	0.0	-0.3	0.0	0.0	0.0
Theophylline	0.0	0.0	-0.1	0.1	-0.5	-0.9	-0.3	-0.7	0.0	-0.3	-0.7	-0.6	-0.1	-0.2	-0.5	-0.3	-0.1	0.0
Melastatin	0.0	-0.1	-0.1	0.0	0.0	-1.0	0.3	-0.2	0.0	0.3	0.0	0.0	0.0	0.0	-0.3	0.0	0.0	0.1
Cyanemazine	0.3	0.0	0.1	0.1	0.1	-0.8	0.5	-0.3	0.1	0.4	-0.1	0.3	0.0	0.1	-0.2	0.1	0.9	0.6
AT-1001	-0.1	-0.3	-0.1	-0.2	-0.2	-1.0	0.4	-0.6	0.0	0.3	-0.3	3.1	-0.4	-0.3	-0.8	-0.2	0.7	0.1
Glycine Betaine	0.0	0.1	0.0	0.2	0.3	5.6	0.3	0.0	0.0	0.0	0.2	0.2	0.4	0.4	0.4	0.5	0.0	0.1
Reserpine	2.5	1.3	1.9	1.5	0.5	23.0	3.1	4.6	0.2	6.9	1.0	2.2	0.2	0.1	3.9	1.0	3.0	4.1
Sazetidine A	0.3	0.3	0.2	1.1	1.1	-0.8	-0.2	-0.2	0.1	0.4	2.1	1.0	0.0	0.0	-0.2	0.7	0.9	-0.1
Theobromine	0.1	0.1	0.1	0.1	0.1	-1.0	0.3	-0.1	0.0	0.4	0.1	0.0	0.0	0.0	-0.3	0.0	0.1	0.1

Figure 4.4: Fluorescence response (as represented by  $\Delta F/F_0$ ) for drug–biosensor pairs included in the 2019 single concentration drug–biosensor fluorescence screen. Drugs are grouped by class. Fluorescent response shading from green ( $\Delta F/F_0 \geq 3$ ) to white ( $\Delta F/F_0 = 0$ ), in which stronger hits are represented by darker green, weaker hits by lighter green, and non-hits by white.

#### 4.6 Notes on Generalizability of OpuBC-Based Biosensors

Through our single concentration screens, over 500 drug–biosensor hit pairs were identified that show promise for creation of novel biosensors for CNS-acting drugs. While most hit pairs had  $1 < \Delta F/F_0 < 3$  (approximately 65%) and thus will likely require further directed evolution before they can be used for imaging with their paired drug, a substantial portion (approximately 35%) had  $\Delta F/F_0 > 3$  and thus could likely be directly used for cellular imaging. However, one must note that the screened biosensors were engineered to bind another drug, so directed evolution will still need to be conducted to establish selectivity for the new drug of interest. Once hit pairs have been successfully identified, they can be further assessed by multiple concentration validations. This is particularly useful in cases where a single drug participates in multiple hit pairs, and a single sensor needs to be chosen to begin directed evolution.

Several idiosyncrasies underlie the described protocols. First, many iDrugSnFRs of the OpuBC family bind and respond to amine-containing buffers at the tens of mM concentrations used in typical biological and molecular experiments. This is likely due to the amine-binding OpuBC parentage with the cation- $\pi$  box at the binding site (Bera, Kamajaya, Shivange, Muthusamy, Nichols, Borden, Grant, Jeon, Lin, Bishara, et al., 2019b; Muthusamy et al., 2022; Nichols et al., 2022) (PDB files 7S7T, 7S7U, 7S7X, 7S7Z). Thus, we use only phosphate- and/or bicarbonate-based buffers. Second, most cpGFP-based biosensors are sensitive to pH, which is likely due to the proton candle snuffer mechanism (Barnett et al., 2017; Muthusamy et al., 2022; Nichols et al., 2022). Thus, one is limited to imaging in nearly pH-neutral organelles such as the cytoplasm, endoplasmic reticulum, and cis-Golgi apparatus. Third, many iDrugSnFRs are activated by DMSO alone, which implies that one cannot use commercially available screening libraries formatted in DMSO and must be cautious when using DMSO for water-insoluble drugs. Lastly, one must consider the fact that some drugs may have detectable fluorescence independent of biosensor interaction and require correction for this fluorescence in  $\Delta F/F_0$  calculations (as outlined in Equation 1 above). Additionally, the protocol has been revised with each screen to increase efficiency. Given the wide range of drugs for which hit pairs were identified in the screens shown, our fluorescence screening protocol is probably generalizable for drug classes other than those we have studied. There are several rubrics for describing drug classes.

One definition of drug class invokes chemistry. We do not know the upper limit for MW of ligands that could participate in hit pairs; we have not screened drugs with MW > 500. Wild-type OpuBC and its orthologs bind permanently charged quaternary amines such as choline, betaine, and proline betaine. Only a few clinically useful drugs (for instance tiotropium) are quaternary amines. Our screens have concentrated on primary, secondary, and tertiary amines that are partially protonated at neutral pH, i.e., they are weakly basic. We assume that only the protonated form of the drug makes a cation- $\pi$  interaction with the iDrugSnFR (Bera, Kamajaya, Shivange, Muthusamy, Nichols, Borden, Grant, Jeon, Lin, Bishara, et al., 2019b; Muthusamy et al., 2022; Nichols et al., 2022) (Protein Data Bank files 7S7T, 7S7U, 7S7X, and 7S7Z). In many alkaloids, the nitrogen remains unprotonated at neutral pH. For instance, the iDrugSnFRs that bind nicotinic drugs do not sense cotinine, an amide, and we doubt that OpuBC-based iDrugSnFRs would detect amides. In unpublished work related to the 2018 screen (Figure 4.3), we found no hit pairs involving opioid peptides (the peptide bond is an amide bond). Another rubric for drug class invokes target pharmacology (receptor, channel, transporter, or enzyme). As noted in the Introduction, the screens we describe are necessary because little correlation exists between the structure–activity relations that govern, on one hand, target binding and, on the other hand, binding to OpuBC variants, other than the presence of a weakly basic amine.

Other rubrics for drug class invoke the disorder being treated or the type of drug abuse. Within the former rubric, the figures show hit pairs for classical antidepressants, rapidly acting antidepressants, smoking cessation therapeutics, analgesics, antiemetics, antipsychotics, and appetite suppressants. Our unpublished data show hit pairs including the antimentia drug tacrine. Within the latter rubric, we found hit pairs including nicotine dependence, opioid dependence, and dissociative effects. We have not screened US Drug Enforcement Administration Schedule 1 drugs; among these, it is likely that hit pairs could be identified for some psychedelics (especially psilocin and analogs), cocaine, and MDMA. Hit pairs for other drug classes (however one defines the classes) should probably be approached by merging circularly permuted fluorescent protein GFP with variants of a different PBP (Scheepers et al., 2016). Hit pairs for amino acid drugs might be generated by mutating the binding site in the glutamate-sensing iGluSnFR variants (Marvin et al., 2018). Many drugs that inhibit intracellular enzymes are amides; we have not considered the likeliest PBPs for binding amides. Finally, several scientists have proposed the intriguing challenge of generating PBP-based sensors for peptides.

#### 4.7 Acknowledgments

We have been supported by The Brain and Behavior Research Foundation (NARSAD Award 2014-23069), California Tobacco-Related Disease Research Program (Aaron L. Nichols, 27FT-0022) (Dennis A. Dougherty, 27IP0057), The Della Martin Foundation (Kallol Bera), Howard Hughes Medical Institute (Jonathan S Marvin and Loren L Looger), National Institute on Drug Abuse (Henry A Lester, DA043829) (Henry A Lester and Anand K Muthusamy, DA049140), National Institute of General Medical Sciences (Henry A Lester, GM-12358) (Anand K Muthusamy T32-GM7616), National Institute of Mental Health (Henry A Lester, 213MH120823), National Institute of Neurological Disorders and Stroke fellowship (Anand K Muthusamy T32NS105595), the Caltech CI2 program, and Caltech SURF donors Samuel P. and Frances Krown (Zoe G Beatty). This protocol was derived from the original research paper “Fluorescence activation mechanism and imaging of drug permeation with new sensors for smoking cessation ligands” (Nichols et al., 2022).

**Competing interests:** Anand Muthusamy, Henry Lester, Loren Looger, and Jonathan Marvin have filed a patent application that includes opioid biosensors. Lin Tian is a co-founder of Seven Biosciences.

**Ethics:** There are no ethical concerns relevant to this paper.

#### 4.8 References

- Barnett, L. M., Hughes, T. E., & Drobizhev, M. (2017). Deciphering the molecular mechanism responsible for gcamp6m’s  $Ca^{2+}$ -dependent change in fluorescence. *PloS One*, *12*(2), e0170934.
- Bera, K., Kamajaya, A., Shivange, A. V., Muthusamy, A. K., Nichols, A. L., Borden, P. M., Grant, S., Jeon, J., Lin, E., Bishara, I., et al. (2019a). Biosensors show the pharmacokinetics of s-ketamine in the endoplasmic reticulum. *Frontiers in cellular neuroscience*, *13*, 499.
- Bera, K., Kamajaya, A., Shivange, A. V., Muthusamy, A. K., Nichols, A. L., Borden, P. M., Grant, S., Jeon, J., Lin, E., Bishara, I., Chin, T. M., Cohen, B. N., Kim, C. H., Unger, E. K., Tian, L., Marvin, J. S., Looger, L. L., & Lester, H. A. (2019b). Biosensors show the pharmacokinetics of s-ketamine in the endoplasmic reticulum. *Frontiers in Cellular Neuroscience*, *13*, 499. <https://doi.org/10.3389/fncel.2019.00499>
- Henderson, B. J., & Lester, H. A. (2015). Inside-out neuropharmacology of nicotinic drugs. *Neuropharmacology*, *96*, 178–193.

- Lester, H. A., Miwa, J. M., & Srinivasan, R. (2012). Psychiatric drugs bind to classical targets within early exocytotic pathways: Therapeutic effects. *Biological Psychiatry*, *72*(11), 907–915.
- Marvin, J. S., Scholl, B., Wilson, D. E., Podgorski, K., Kazemipour, A., Müller, J. A., Schoch, S., Quiroz, F. J. U., Rebola, N., Bao, H., Little, J. P., Tkachuk, A. N., Cai, E., Hantman, A. W., Wang, S. S.-H., DePiero, V. J., Borghuis, B. G., Chapman, E. R., Dietrich, D., . . . Looger, L. L. (2018). Stability, affinity, and chromatic variants of the glutamate sensor iGluSnFR. *Nature Methods*, *15*(11), 936–939. <https://doi.org/10.1038/s41592-018-0171-3>
- Muthusamy, A. K., Kim, C. H., Virgil, S. C., Knox, H. J., Marvin, J. S., Nichols, A. L., Cohen, B. N., Dougherty, D. A., Looger, L. L., & Lester, H. A. (2022). Three mutations convert the selectivity of a protein sensor from nicotinic agonists to s-methadone for use in cells, organelles, and biofluids. *Journal of the American Chemical Society*, *144*(19), 8480–8486.
- Nichols, A. L., Blumenfeld, Z., Fan, C., Luebbert, L., Blom, A. E., Cohen, B. N., Marvin, J. S., Borden, P. M., Kim, C. H., Muthusamy, A. K., et al. (2022). Fluorescence activation mechanism and imaging of drug permeation with new sensors for smoking-cessation ligands. *Elife*, *11*, e74648.
- Scheepers, G. H., Lycklama a Nijeholt, J. A., & Poolman, B. (2016). An updated structural classification of substrate-binding proteins. *FEBS letters*, *590*(23), 4393–4401.
- Shivange, A. V., Borden, P. M., Muthusamy, A. K., Nichols, A. L., Bera, K., Bao, H., Bishara, I., Jeon, J., Mulcahy, M. J., Cohen, B., O’Riordan, S. L., Kim, C., Dougherty, D. A., Chapman, E. R., Marvin, J. S., Looger, L. L., & Lester, H. A. (2019). Determining the pharmacokinetics of nicotinic drugs in the endoplasmic reticulum using biosensors. *Journal of General Physiology*, *151*(6), 738–757. <https://doi.org/10.1085/jgp.201812201>
- Unger, E. K., Keller, J. P., Altermatt, M., Liang, R., Matsui, A., Dong, C., Hon, O. J., Yao, Z., Sun, J., Banala, S., et al. (2020). Directed evolution of a selective and sensitive serotonin sensor via machine learning. *Cell*, *183*(7), 1986–2002.

*Chapter 5*

CHEMICAL AND PHARMACOKINETIC PERSPECTIVE ON  
FREELS ET AL., 2020: CANNABIS EXTRACT COMPOSITION  
DETERMINES REINFORCEMENT IN A VAPOR  
SELF-ADMINISTRATION PARADIGM

**Muthusamy, A. K.** (2020). Cannabis extract composition determines reinforcement in a vapor self-administration paradigm. *Journal of Neuroscience*, 40(33), 6264-6266. <https://doi.org/10.1523/JNEUROSCI.0814-20.2020>

### 5.1 Perspective on Freels et al, 2020

The legalization of cannabis and shifting cultural attitudes have driven an increase in cannabis use and the proliferation of vapor delivery devices. The DSM-V recognizes “cannabis use disorder” under the umbrella of substance use disorders, but its neural mechanisms require greater clarity (Oleson & Cheer, 2012). Debate in the scientific community and the public sphere alike primarily asks, “is cannabis addictive?” and “are there negative effects from chronic use?” The first issue magnifies the second: if users compulsively seek cannabis or become dependent, then safe regimens become difficult to maintain.

Drug abuse studies in human populations generally are confounded by use of other drugs, medical history, and varying genetic background. Self-administration in animal models sidesteps these issues and has good construct validity given the volitional consumption (Koob et al., 2012). Unlike cocaine and opioid self-administration studies, however, self-administration of cannabis or  $\Delta^9$ -tetrahydrocannabinol (THC) alone has been notoriously difficult to establish across several species because of THC’s weak rewarding effect and aversive effects at high doses (Fuchs et al., 2019; Justinova et al., 2005). Although THC is the primary psychoactive compound in cannabis, extracts may have over 120 other phytocannabinoids, including cannabidiol (CBD), which has its own effects as an inverse agonist at cannabinoid receptors (Ibsen et al., 2017). Further complicating self-administration is the varying pharmacokinetics of different delivery methods. In particular, intravenous delivery, which is used for other addictive drugs, leads to fast infusion rates that trigger aversive effects for THC (Carbuto et al., 2012).

Freels et al. addressed these long-standing issues by designing a vapor-delivery method to successfully establish cannabis self-administration in rodents (2020). Their paradigm bears the greatest similarity to human use to date by allowing volitional and titratable vapor delivery of cannabis extracts (MacCallum & Russo, 2018). The National Institute on Drug Abuse drug supply program provided whole cannabis extract enriched with either THC ( $CAN_{THC}$ ) or CBD ( $CAN_{CBD}$ ). In the apparatus, rats could nose-poke to activate one of two ports indicated by a 60 s light cue. When one port was activated, one of three vapors was delivered: organic solvent vehicle,  $CAN_{THC}$ , or  $CAN_{CBD}$ ; when the other port was activated, nothing was delivered.

### **$CAN_{THC}$ uniquely reinforces self-administration by acting on cannabinoid receptor type 1 ( $CB_1$ )**

This work demonstrated that Sprague Dawley rats will stably self-administer  $CAN_{THC}$  and perform more work for a single delivery of  $CAN_{THC}$  vapor than for  $CAN_{CBD}$  or vehicle (Freels et al., 2020). Across fixed ratios of nose-pokes to vapor deliveries, rats maintained a consistent number of  $CAN_{THC}$  vapor deliveries in each session, and the number of deliveries was significantly higher than for  $CAN_{CBD}$  or vehicle (~5 to ~12 deliveries/day, a baseline for nose-poking). In all experiments, Freels et al. observed some level of nose-poking for the vehicle delivery, suggesting some interest in the cue light and/or solvent vapor. Even under the 1:1 ratio, however, rats did not respond significantly more for  $CAN_{CBD}$  than for vehicle. Furthermore, when the rats faced a sequentially increasing number of nose-pokes required to earn vapor delivery, they worked significantly more for  $CAN_{THC}$ , but not for  $CAN_{CBD}$ , than for vehicle. Notably, rats nose-poked for  $CAN_{THC}$  most often in the first 15 min of each 1 h session. These results suggest that rats learn to nose-poke at a certain rate to achieve a desired THC level. Maintaining  $CAN_{THC}$  consumption under a mounting workload points to the drug's reinforcing efficacy and is comparable with the human motivation to devote time and effort to seek an appealing stimulus (Fuchs et al., 2019).

Freels et al. found that systemic injection of AM251, a  $CB_1$ -selective antagonist, reduced the  $CAN_{THC}$  vapor seeking rate to vehicle control levels, whereas the  $CAN_{CBD}$  group was unaffected. While  $CB_1$  is widely expressed across the mammalian brain, a well-characterized midbrain reward mechanism implicated in the self-administration of other addictive substances likely underlies  $CAN_{THC}$ 's effect (Gardner, 2005). THC acts as partial agonist of  $CB_1$ , which is abundantly expressed



in VTA GABAergic terminals (Sperlágh et al., 2009). In the VTA, the activation of CB<sub>1</sub> diminishes the GABAergic inhibition of dopaminergic neurons that project to the NAc (Gardner, 2005; Oleson & Cheer, 2012). The resulting increase in dopaminergic tone in the NAc is rewarding and can establish drug addiction (Oleson & Cheer, 2012).

### **THC:CBD ratio in extracts determines selectivity in self-administration and presentation of the tetrad response**

Surprisingly, although rats were not willing to work as hard to earn CAN<sub>CBD</sub> as they were to earn CAN<sub>THC</sub>, they self-administered CAN<sub>CBD</sub> more selectively. In the behavior apparatus, the rats could learn which port provided any vapor as opposed to no outcome. Only the rats earning CAN<sub>CBD</sub> achieved a fraction of nose-pokes at the active port that was significantly greater than the vehicle group. Quantification of cannabinoid concentrations in the rat brain likely explains this finding. Each of the two cannabis extracts had a small quantity of the nonenriched compound. CAN<sub>THC</sub> extract had a THC concentration nearly 30× that of CAN<sub>CBD</sub> and a CBD concentration only 1/40 that of CAN<sub>CBD</sub>. Nonetheless, after self-administration, brain THC concentrations were similar regardless of which extract was delivered, whereas the concentration of CBD was ~3× greater in rats receiving CAN<sub>CBD</sub> than in those receiving CAN<sub>THC</sub>. These results demonstrate that rats achieve pharmacologically relevant increases in brain THC with both extracts; the enrichment of THC in the CAN<sub>CBD</sub> group might result from inhibition of THC metabolism by CBD (Jones & Pertwee, 1972). Furthermore, because THC disrupts spatial memory and acquisition of operant tasks in rats, it may increase the error in discrimination (Delatte et al., 2002; Varvel et al., 2001). Finally, CBD counteracts the psychotropic and aversive effects of THC particularly through action in the ventral hippocampus (Hudson et al., 2019). A balance between THC-driven motivation and CBD-protected learning may therefore underlie the discrimination disparity across CAN<sub>THC</sub> and CAN<sub>CBD</sub> groups.

In a separate experiment, the rats' locomotion and metabolic parameters were measured over 10 d of fixed-ratio self-administration. Only rats that self-administered CAN<sub>THC</sub> exhibited some features of the classical physiological "tetrad" response: lowered spontaneous activity, antinociception, hypothermia, and catalepsy (Metna-Laurent et al., 2017). Rats self-administering CAN<sub>THC</sub> spent more time inactive than those receiving CAN<sub>CBD</sub> but also displayed significantly greater food consumption and energy expenditure. In contrast, locomotor and metabolic signatures were indis-

tinguishable in the  $CAN_{CBD}$  and vehicle groups. This demonstrates that the extracts have different effects on some internal states (e.g., arousal and appetite). Still, the mechanism that relates drug action to internal state and physiological adaptations that lead to self-administration selectivity or chronic drug seeking is not yet clear.

**Self-administration of  $CAN_{CBD}$  is more resistant to extinguishing while  $CAN_{THC}$  elicits stronger reinstatement, raising questions about the underlying circuit adaptations**

Freels et al. trained another cohort of rats to self-administer vapor over 19 d and then continued sessions with both ports set as inactive over 7 d. The  $CAN_{CBD}$  group, but not the  $CAN_{THC}$  group, required significantly more trials than the vehicle group to extinguish nose-poking (defined as a 50% decrease in nose-pokes at the previously active port since the last session with vapor delivery). Transitioning the rats off of the vapor thus raised an apparent inconsistency with the prior results: rats were more resistant to extinguishing the seeking of  $CAN_{CBD}$  despite their greater motivation to consume  $CAN_{THC}$ . This observation is especially curious given that CBD disrupts the association between rewarding effect and the spatial location where rats consume cocaine or opioids (de Carvalho & Takahashi, 2017; Mahmud et al., 2017). The result might be explained by a difference in learning rates due to reward prediction error for dopamine reinforcement (Glimcher, 2011). The light cue or vapor smell may be more salient to the  $CAN_{THC}$  group because they experience the reinforcing effect of higher THC concentrations immediately. The  $CAN_{THC}$  group may have then experienced a greater unexpected result under extinguishing conditions, eliciting a faster rate of learning to stop nose-poking.

Finally, to test the reinstatement of vapor seeking, Freels et al. provided an additional session after extinction, in which nose-poking the previously active port triggered the light cue, but no vapor delivery. Only rats previously receiving  $CAN_{THC}$  increased their nose-poking relative to the vehicle group. This result indicates a sustained stronger motivation to seek  $CAN_{THC}$  and is consistent with the previous results indicating that  $CAN_{THC}$  has a greater reinforcing efficacy compared with that of  $CAN_{CBD}$ . This drive to seek  $CAN_{THC}$  could be motivated by reward-seeking, withdrawal avoidance, or a combination of both factors (Fuchs et al., 2019).

The study of cannabis use disorder is now challenged with distinguishing the actions of each cannabis constituent in the development and reinforcement of maladaptive behaviors. Future work should characterize the pharmacokinetics for the method developed by Freels et al., given that human use of electronic cannabis vaporization

demands considerable optimization (Hazekamp et al., 2006). Then, one could determine whether synthetic agonists, purified THC and CBD, or cannabis extracts are sufficient to establish self-administration. The work by Freels et al. also raises questions about reward encoding and prediction mechanisms. The critical question for addiction studies remains: what, if any, factor could transition an animal from controlled to compulsive cannabis seeking that forgoes well-being (Everitt et al., 2008)? Freels et al. have provided the behavioral neuroscience field with a method to address these questions with excellent fidelity to the human experience of cannabis use.

Footnotes:

I thank my adviser Dr. Henry A. Lester for guidance in the neuroscience of addiction; and Vinicius S. Ferreira for helpful comments on the manuscript. This work was supported by the National Institute on Drug Abuse grant DA049140.

## 5.2 References

- Carbuto, M., Sewell, R. A., Williams, A., Forselius-Bielen, K., Braley, G., Elander, J., Pittman, B., Schnakenberg, A., Bhakta, S., Perry, E., et al. (2012). The safety of studies with intravenous  $\Delta$  9-tetrahydrocannabinol in humans, with case histories. *Psychopharmacology*, *219*, 885–896.
- de Carvalho, C. R., & Takahashi, R. N. (2017). Cannabidiol disrupts the reconsolidation of contextual drug-associated memories in wistar rats. *Addiction Biology*, *22*(3), 742–751.
- Delatte, M., Winsauer, P., & Moerschbaeche, J. (2002). Tolerance to the disruptive effects of  $\Delta$ 9-thc on learning in rats. *Pharmacology Biochemistry and Behavior*, *74*(1), 129–140.
- Everitt, B. J., Belin, D., Economidou, D., Pelloux, Y., Dalley, J. W., & Robbins, T. W. (2008). Neural mechanisms underlying the vulnerability to develop compulsive drug-seeking habits and addiction. *Philosophical Transactions of the Royal Society B: Biological Sciences*, *363*(1507), 3125–3135.
- Freels, T. G., Baxter-Potter, L. N., Lugo, J. M., Glodosky, N. C., Wright, H. R., Baglot, S. L., Petrie, G. N., Yu, Z., Clowers, B. H., Cuttler, C., et al. (2020). Vaporized cannabis extracts have reinforcing properties and support conditioned drug-seeking behavior in rats. *Journal of Neuroscience*, *40*(9), 1897–1908.
- Fuchs, R. A., Higginbotham, J. A., & Hansen, E. J. (2019). Animal models of addiction. *Neural Mechanisms of Addiction*, 3–22.

- Gardner, E. L. (2005). Endocannabinoid signaling system and brain reward: Emphasis on dopamine. *Pharmacology Biochemistry and Behavior*, *81*(2), 263–284.
- Glimcher, P. W. (2011). Understanding dopamine and reinforcement learning: The dopamine reward prediction error hypothesis. *Proceedings of the National Academy of Sciences*, *108*(supplement\_3), 15647–15654.
- Hazekamp, A., Ruhaak, R., Zuurman, L., Van Gerven, J., & Verpoorte, R. (2006). Evaluation of a vaporizing device (volcano®) for the pulmonary administration of tetrahydrocannabinol. *Journal of Pharmaceutical Sciences*, *95*(6), 1308–1317.
- Hudson, M., Stuchinskaya, T., Ramma, S., Patel, J., Sievers, C., Goetz, S., Hines, S., Menzies, E., & Russell, D. A. (2019). Drug screening using the sweat of a fingerprint: Lateral flow detection of  $\delta^9$ -tetrahydrocannabinol, cocaine, opiates and amphetamine. *Journal of Analytical Toxicology*, *43*(2), 88–95. <https://doi.org/10.1093/jat/bky068>
- Ibsen, M. S., Connor, M., & Glass, M. (2017). Cannabinoid cb1 and cb2 receptor signaling and bias. *Cannabis and Cannabinoid Research*, *2*(1), 48–60.
- Jones, G., & Pertwee, R. (1972). A metabolic interaction in vivo between cannabidiol and  $\Delta^1$ -tetrahydrocannabinol. *British Journal of Pharmacology*, *45*(2), 375.
- Justinova, Z., Goldberg, S. R., Heishman, S. J., & Tanda, G. (2005). Self-administration of cannabinoids by experimental animals and human marijuana smokers. *Pharmacology Biochemistry and Behavior*, *81*(2), 285–299.
- Koob, G. F., Bloom, F., & Kupfer, D. (2012). Animal models of drug addiction. *Psychopharmacology: The fourth generation in progress/Bloom FE, Kupfer DJ—1995.—345 p.*
- MacCallum, C. A., & Russo, E. B. (2018). Practical considerations in medical cannabis administration and dosing. *European Journal of Internal Medicine*, *49*, 12–19.
- Mahmud, A., Gallant, S., Sedki, F., D’Cunha, T., & Shalev, U. (2017). Effects of an acute cannabidiol treatment on cocaine self-administration and cue-induced cocaine seeking in male rats. *Journal of Psychopharmacology*, *31*(1), 96–104.
- Metna-Laurent, M., Mondésir, M., Grel, A., Vallée, M., & Piazza, P.-V. (2017). Cannabinoid-induced tetrad in mice. *Current Protocols in Neuroscience*, *80*(1), 9–59.
- Oleson, E. B., & Cheer, J. F. (2012). A brain on cannabinoids: The role of dopamine release in reward seeking. *Cold Spring Harbor Perspectives in Medicine*, *2*(8).

- Sperlágh, B., Windisch, K., Andó, R. D., & Vizi, E. S. (2009). Neurochemical evidence that stimulation of cb1 cannabinoid receptors on gabaergic nerve terminals activates the dopaminergic reward system by increasing dopamine release in the rat nucleus accumbens. *Neurochemistry International*, *54*(7), 452–457.
- Varvel, S., Hamm, R., Martin, B., & Lichtman, A. (2001). Differential effects of  $\Delta$  9-thc on spatial reference and working memory in mice. *Psychopharmacology*, *157*, 142–150.

*Chapter 6***iOpioidSnFRs & Recording Fentanyl *in vivo* Alongside A Computer Vision Routine for Quantifying Behavior**

**Muthusamy, A. K.**, Rosenberg, M. H., Kim, C. H., Wang, A. Z., Ebisu, H., Chin, T. M., Koranne, A., Marvin, J. S., Cohen, B. N., Looger, L. L., Oka, Y., Meister, M., & Lester, H. A. (2024). Correspondence of fentanyl brain pharmacokinetics and behavior measured via engineering opioids biosensors and computational ethology. *bioRxiv*. <https://doi.org/10.1101/2024.03.15.584894v1>.

**6.1 Abstract**

Despite the ongoing epidemic of opioid use disorder and death by fentanyl overdose, opioids remain the gold standard for analgesics. Pharmacokinetics (PK) dictates the individual's experience and utility of drugs; however, PK and behavioral outcomes have been conventionally studied in separate groups, even in preclinical models. To bridge this gap, we developed the first class of sensitive, selective, and genetically encodable fluorescent opioid biosensors, iOpioidSnFRs, including the fentanyl sensor, iFentanylSnFR. We expressed iFentanylSnFR in the ventral tegmental area of mice and recorded [fentanyl] alongside videos of behaviors before and after administration. We developed a machine vision routine to quantify the effects of the behavior on locomotor activity. We found that mice receiving fentanyl exhibited a repetitive locomotor pattern that paralleled the [fentanyl] time course. In a separate experiment, mice navigating a complex maze for water showed a dose-dependent impairment in navigation, in which animals repeated incorrect paths to the exclusion of most of the unexplored maze for the duration of the average fentanyl time course. This approach introduces self-maintenance, a key feature of human addiction, to rodent models. Finally, we demonstrate the utility of iFentanylSnFR in detecting fentanyl spiked into human biofluids and the generalizability of engineering methods to evolve selective biosensors of other opioids, such as tapentadol and levorphanol. These results encourage diagnostic and continuous monitoring approaches to personalizing opioid regimens for humans.

## 6.2 Introduction: Opioid Use Disorder, Pharmacokinetics, & Behavior Paradigms

Humans have used opioids from plants for over 5,000 years and continue to consume them for their euphoric and analgesic properties (Brownstein, 1993). Since ~1870, the development of even more potent opioid agonists, such as heroin and fentanyl, has driven an increase in opioid use disorder (OUD). Today, OUD affects ~16 million people worldwide, including ~2 million in the U.S. (Chang et al., 2018). Among the ~110,000 drug overdose deaths in the United States in 2022, fentanyl and other synthetic opioids alone account for ~70% (Farida B. Ahmad et al., 2023). Still, opioids remain the gold standard for severe and chronic pain despite the burden of OUD. These opioids are unmatched by other classes of analgesics in blunting not only physical pain but also the perceptual and emotional factors of pain (Atlas et al., 2014; Friedman & Nabong, 2020; Saulo C. Riberio et al., 2005). At least 50% of OUD these cases begin with an opioid prescription, raising the issue of managing opioid use in daily life (Cicero et al., 2014; Committee on Pain Management and Regulatory Strategies to Address Prescription Opioid Abuse et al., 2017; Lankenau et al., 2012; Pradip K. Muhuri et al., 2013).

A core tenet of behavioral neuropharmacology is the existence of some stereotyped relationship between the time course of a drug and behavioral outcomes such as OUD. Interindividual variability in pharmacokinetics complicates the problem of optimized opioid dosing, especially outside the clinic (Saiz-Rodríguez et al., 2019). The problem of personalizing pharmacokinetics is severe in substance use disorders: the patient must receive opioid levels that relieve pain, minimize tolerance and other side effects, and remain within a therapeutic window to maximize adherence. That ideal window is a “moving target” due to tolerance that leads to a decreased response to the drug. A central tension in opioid administration lies in the differing tolerance rates for the  $\mu$ -opioid receptor’s activity in circuits driving reward, analgesia, and respiratory depression (Montandon & Slutsky, 2019). These differences lead to withdrawal periods and dose escalation that can lead to undesirable side effects and, potentially, death by overdose. The mechanisms of tolerance and dependence are incompletely understood but involve several levels of effects. Cellular neurobiology reveals a “location bias”: the cellular compartment in which a drug interacts with the  $\mu$ -opioid receptor affects signaling dynamics (Lobingier & Von Zastrow, 2019; Radoux-Mergault et al., 2022; Stoeber et al., 2018). Circuit adaptations are sensitive to variations in opioid dose regimens and their interruptions (Cahill, 2020; Lefevre et al., 2020; Muntean et al., 2019). Therefore, progress in neurobiology requires improved methods of monitoring opioids and their receptors across time

and space (Julli  et al., 2020; Muthusamy et al., 2022; Wang et al., 2022). Along the range from organelle to behaving animals, one asks, “What is the time course of the drug in the relevant compartment?” followed by “How does the animal respond?” In this work, we developed iOpioidSnFRs for sufficient sensitivity, selectivity, and kinetics to enable pharmacokinetic measurements at both subcellular and whole animal levels (Figure 6.1 A, B).

Rodent models are critical for therapeutic development, conserving several receptors and circuits involved in biological phenomena related to OUD (Kimmey et al., 2022). Established paradigms show that  $\mu$ -opioids elicit analgesic, rewarding, reinforcing, place preferent, anxiolytic, respiratory depressive, and hyperactive effects in rodents (Le Merrer et al., 2009; Tzschentke, 1998). One now asks how the cumulative physiological effects influence higher-order behaviors that lead to and constitute OUD (Belin et al., 2016). The next critical open question is when and how animals switch from impulsive use to compulsive use despite the negative tradeoffs in life goals and survival (Belin et al., 2016). The DSM-V defines aspects of this tradeoff in terms of human obligations (e.g., responsibilities to family and work) (Glasheen et al., n.d.); however, there is no comparable, ethologically relevant, and readily quantifiable task for rodents (Iversen et al., 1977). To this end, the field has recently sought endophenotypes for phenomena in addiction related to the ability to maintain self-control and achieve goals.

First, we developed an assay where we genetically encoded iFentanylSnFR to record brain fentanyl levels alongside video recording. This recording is the longest continuous measurement of the brain [drug] alongside behavior (4 hours) and a first for OUD. Using a custom machine vision analysis, we found a stereotypic, repetitive motor pattern that tracked the entire fentanyl time course despite variable PK across individuals. This result challenges current models of cellular desensitization and acute tolerance that occur on  $\sim 10$  min and  $\sim 1$  h timescales, respectively. Second, we asked if this stereotypical pattern impaired mice in a survival task. We developed a paradigm based on foraging for water through a labyrinth maze (Rosenberg et al., 2021). Like in the open arena, mice in the maze exhibited circling/stalling for  $\sim 3$  h, to the complete exclusion of successful foraging for water. Critically, this paradigm offers a normative definition of a deficit useful for future studies of OUD, as mice ought to have a baseline level of successful foraging to survive. Finally, we use these biosensors as purified protein and lyophilized powder to detect opioids in solution and human biofluids, enabling continuous drug monitors for humans.



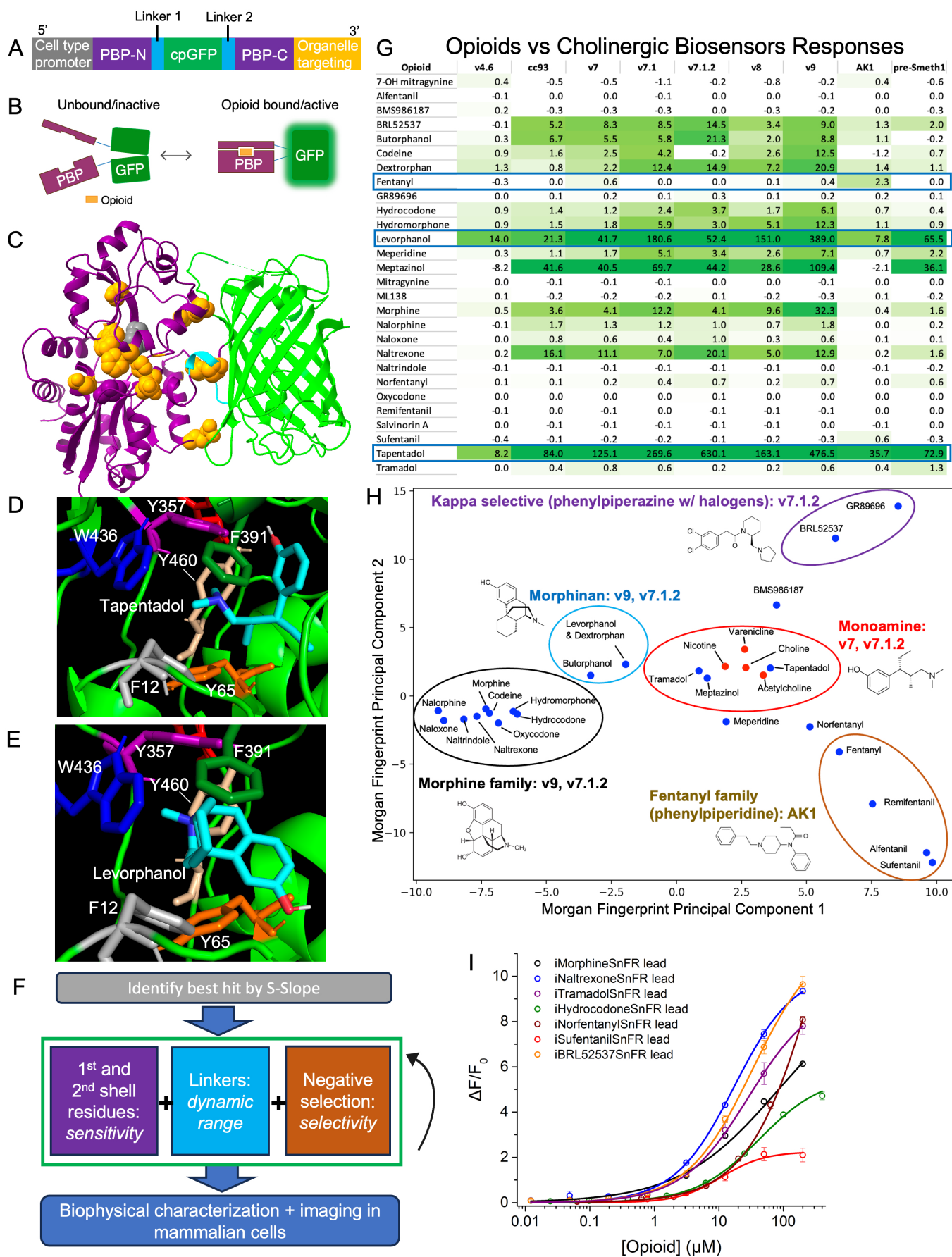


Figure 6.1: A general strategy to evolve opioid biosensors from cholinergic biosensors.

- (A) The biosensor gene construct. The periplasmic binding protein (PBP) gene (purple) is interrupted by a circularly permuted GFP (green), connected by two linker sequences (cyan). A 5' promoter sequence restricts expression to the desired cell type, and a C-terminal tag directs the biosensor to the desired cellular compartment.
- (B) Scheme for ligand gating of GFP fluorescence.
- (C) Crystal structure of iNicSnFR3a (PDB: 7S7V) annotated with variable regions exploited in directed evolution: sites mutated to improve cholinergic binding (orange spheres) and a critical cation- $\pi$  residue, Y357 (grey spheres).
- (D & E) Docking of two exemplar opioids, tapentadol, and levorphanol, in iNicSnFR3a (PDB: 7S7V) using AutoDock Vina. Binding pocket residues (labeled) form an aromatic box.
- (F) General strategy for the directed evolution of iOpioidSnFRs.
- (G) "Green map" of the response of cholinergic biosensors to opioids expressed as the  $\delta$ -Slope  $\times$  100 (0-4, white to light green, and 4-40+, light green to dark green) ( $n = 3$  dose responses averaged).
- (H) Mapping the OpuBC mutant hit sequences to opioid structural classes (encircled and given representative structures). Opioids (blue) and cholinergic ligands (red) were represented as Morgan fingerprint vectors and subjected to a principal component analysis. Mitragynine and 7-OH mitragynine were omitted for their outlying alkaloid structures, atypical of clinically used opioids.
- (I) After one to three rounds of directed evolution, iOpioidSnFR leads display detection limits of  $< 2 \mu\text{M}$  in bacterial lysates. SEM is shown as error bars ( $n = 3$  dose responses).

### 6.3 Results

#### A general approach to detecting opioids using OpuBC mutants

A common strategy in generating optical biosensors involves merging a conformation switching protein with circularly permuted GFP (cpGFP) so that ligand binding elicits an increase in fluorescence (Dong et al., 2022; Patriarchi et al., 2018; S. Singh et al., 2023; Sun et al., 2020; Tian et al., 2009; Wu et al., 2023; Zhang et al., 2023). The  $\mu$ -opioid receptor is a natural choice for detecting opioid drugs; however, unlike several other GPCRs, the  $\mu$ -opioid receptor merged with cpGFP has been only minimally responsive to its ligands (Tian et al., 2023). Bacterial periplasmic binding proteins (PBPs) are attractive for their stereotypically large Venus flytrap motion upon ligand binding. PBPs have served as conformational switches in genetically encoded biosensors such as iGluSnFR (Marvin et al., 2013). However, unlike neu-

rotransmitters, neural drugs do not have cognate PBPs found in nature. Therefore, this work utilized a previously reported family of biosensors based on the choline-binding protein PBP, OpuBC merged with cpGFP (Beatty et al., 2022; Muthusamy et al., 2022; Nichols et al., 2021; Shivange et al., 2019). One of these biosensors, iAChSnFR, has been deployed *in vivo* and demonstrated sub-second time resolution across several animal models (Borden et al., 2020). We have previously reported only one opioid biosensor, iS-methadoneSnFR, demonstrated *in vitro* and in living cells (Muthusamy et al., 2022). The remaining challenges were to diversify the substrate scope for a variety of opioids and apply them *in vivo*.

We report a class of iOpioidSnFRs based on mutated OpuBC variants (Figure 6.1 A, B, PDB: 7S7V). We first tested the hypothesis that the binding pocket could be adapted to various opioids regardless of their activity at the  $\mu$ -OR (e.g., agonists, partial agonists, and antagonists). We found that ligand binding to the PBP results in a conformational change, causing a glutamate residue in the 1st linker to withdraw from quenching GFP's chromophore. This allosteric linker-GFP mechanism appears agnostic to the binding pocket residues and ligands (Beatty et al., 2022; Muthusamy et al., 2022; Nichols et al., 2021). Docking simulations using a crystal structure of iNicSnFR3a indicated that the binding pocket could accept opioids (Figure 6.11 D, E). The top-scoring poses placed the protonated tertiary amines of some opioids, such as tapentadol and levorphanol, where they could participate in cation- $\pi$  interactions analogous to those between nicotinic ligands and their optimized biosensors (Haloi et al., 2024; Nichols et al., 2021).

Based on these results, we formulated a strategy to generalize OpuBC mutants toward various clinically used opioids (Figure 6.11 F). We measured dose response relations between 28 opioids and nine biosensors based on OpuBC and previously reported for detecting nicotinic ligands ('v4.6'- 'v9'), ketamine ('AK1'), and S-methadone ('pre-Smeth1') (SI Figure 6.8, SI Table 1).  $\Delta F/F_0 = (F_{\text{sensor+drug}} - F_{\text{sensor}})/F_{\text{sensor}}$  was calculated at each dose, and the low-concentration, linear portion of each dose response was fit with a linear regression. We have previously defined the  $\delta$ -Slope for fluorescent biosensors as the slope of that linear regression with units  $\mu\text{M}^{-1}$ . Higher  $\delta$ -Slopes result from higher  $\Delta F_{\text{max}}/F_0$  and lower  $K_d$ . The  $\delta$ -Slope for the library screen is visualized in shades of green, presenting at least an appreciable response to nearly all opioids (Figure 6.1 G). A principal component analysis of the opioid structures' Morgan fingerprints revealed clustering into the conventional pharmacological subclasses which could be assigned to one or two biosensors

displaying the greatest  $\delta$ -Slope for each subclass. The monoamine opioids, such as tapentadol, showed structural similarity to nicotine and were best detected by iNicSnFR3b. Most notably, 'AK1' represents a distinct branch of the biosensors with Y357G mutation that renders it null in response to nicotnics but allows for a minuscule but appreciable response to fentanyl and its analogs. Notably, we previously evolved 'AK1' toward a biosensor of ketamine shares a comparable arylcyclohexamine motif to fentanyl.

Using this mapping, we selected biosensor starting points and performed directed evolution in *E. coli*. The initial biosensor-opioid hit pairs typically required improved sensitivity, dynamic range, and selectivity, so we mutated sites throughout the biosensor sequences. Remarkably, the OpuBC fitness landscape has been smooth enough for this approach and we have not yet encountered any "dead-ends" where the response could not be further improved. Examples of evolved leads for various clinically used opioids and one  $\kappa$ -selective opioid demonstrate the detection of their drug at  $< 2 \mu\text{M}$  (Figure 6.1 I). Given that there is some mapping between OpuBC mutant sequences and opioid structures, we can narrow the search space to generate any next opioid sensor.

### **Improving Sensitivity by ~500x through iFentanylSnFR2.0**

Given the immediate human health relevance of detecting fentanyl, we then sought to take one of the weakest hits and generate the most sensitive iOpioidSnFR to date. The best biosensor hit for fentanyl, AK1, presented a relatively weak response with an  $\delta$ -Slope of  $0.023 \mu\text{M}^{-1}$ . This hit was ~100x weaker than our founding iNicSnFR3a's sensitivity for nicotine and ~3000x weaker than the best hit for tapentadol. Fentanyl's six rotatable bonds and largely hydrophobic surface with few functional groups make it a challenging ligand for designing binders (Bick et al., 2017). Fentanyl also poses a unique challenge for the putative binding pocket interaction in OpuBC because its tertiary amine is placed near the middle of its linear structure, unlike choline. The docked pose, where fentanyl's protonated amine is deepest in the binding pocket, places the nitrogen ~6 Å from aromatic residues and the substituent carbons, off-axis and directed away from the aromatic residues likely not allowing cation- $\pi$  interactions (Figure 6.2 A).

We evolved AK1 further with the most extensive SSM experiments of all iOpioid-SnFRs, spanning the 2nd shell, hinge, and linkers (SI Figure 6.10). Two second-shell mutations, KI10G and RG395A, yielded a biosensor with  $\Delta F/F_0 \sim 1$  at  $\sim 1 \mu\text{M}$  that

we termed iFentanylSnFR1.0 (orange trace, Figure 6.2 B). Additional mutations across the PBP and the 2nd linker yielded a sensor with  $\Delta F/F_0 \sim 1$  at 100 nM and S-Slope = 11.8 that we termed iFentanylSnFR2.0 (black trace, Figure 6.2 B). This evolution campaign represents > 500x improvement in sensitivity from the initial hit to iFentanylSnFR2.0.

Still, only seven mutations, a ~2% difference in the PBP's sequence identity, separate this biosensor from iNicSnFR3a. Notably, all accepted mutations in the PBP selected alanine or glycine, and the sole linker mutation converted a proline to leucine. iFentanylSnFR2.0 preserves the overall fold in the PBP structure generated by AlphaFold2 with an RMSD = 1.66 Å with respect to the iNicSnFR3a's PBP crystal structure (PDB: 7S7W) (Figure 6.3 C). We scanned leucine through the binding pocket aromatic residues and found that preserving aromaticity at each residue was essential to binding fentanyl (Figure 6.2 D). This screen also yielded the W436L mutant, the “null sensor” used in later experiments *in vivo*. Remarkably, the G357L mutation also yielded a null sensor, suggesting that increasing flexibility and/or reducing steric bulk at this position is critical to binding fentanyl.

Biophysical assays confirmed iFentanylSnFR2.0 met our affinity and kinetic criteria. ITC determined a  $K_d = 391 \pm 61.3$  nM with a stoichiometry  $n = 0.91 \pm 0.01$  in agreement with the  $EC_{50} = 389$  nM from the fluorescence dose response and the single binding site in the PBP (Figure 6.2 E). iFentanylSnFR2.0 displayed an entropically driven binding interaction with its ligand, like the parent cholinergic biosensors and other iOpioidSnFRs. Stopped-flow kinetics in a 1 s experiment determined a  $k_{on} = 0.27 \mu\text{M}^{-1} \text{s}^{-1}$  (Figure 6.2 F, raw data in SI Figure 6.9 C). An extended measurement of iFentanylSnFR2.0 showed > 95% of the maximum response in ~1 min after the concentration jump from 0 to 1  $\mu\text{M}$  (SI Figure 6.9 F). Accordingly, we later analyzed the *in vivo* photometry data with filtering with a similar time constant.

iFentanylSnFR2.0 exhibited exquisite selectivity with no detectable response to any neurotransmitter or endogenous opioid peptide (Figure 6.2 G and SI Figure 6.9 F) and ~zero response to other opioid drugs at ~3  $\mu\text{M}$  and below, more than inclusive of their pharmacologically relevant ranges (Figure 2H). iFentanylSnFR2.0 discriminates even among its major metabolite, norfentanyl, and its analogs, sufentanil, alfentanil, and remifentanil (Figure 2I). Whereas the  $\mu$ -OR displays an  $IC_{50} \sim 3x$  lower for sufentanil than fentanyl<sub>44</sub>, iFentanylSnFR2.0 displays a ~20x greater response to fentanyl in terms of S-Slope.

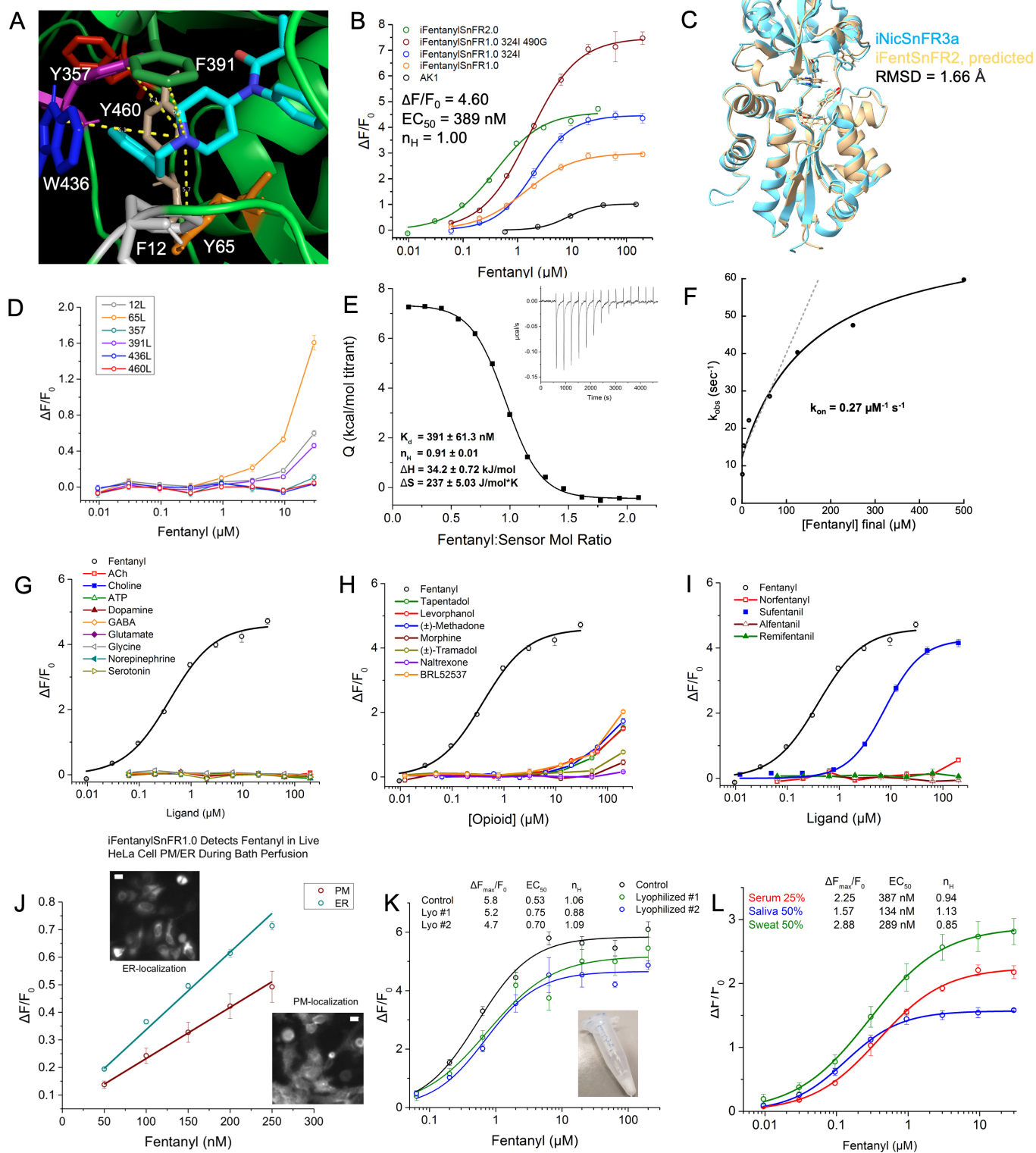


Figure 6.2: iFentSnFR evolution, characterization, and application in cells and biofluids.

- (A) Docking fentanyl in iNicSnFR3b (PDB: 7S7V). The top-scoring conformation shows fentanyl's phenyl ring directed into the pocket, preventing full insertion of the tertiary amine into the aromatic box.
- (B) Directed evolution of iFentanylSnFR2.0 via, AK1, the initial hit bearing the founding Y357G mutation.
- (C) Overlay of the iNicSnFR3b PBP crystal structure (PDB: 7S7W, cyan) and the AlphaFold2 prediction of iFentanylSnFR2.0's PBP structure (wheat). RMSD = 1.66 Å.
- (D) Leucine mutagenesis scan through the aromatic box diminishes dose responses.
- (E) Isothermal titration calorimetry: 2.5  $\mu$ L of 200  $\mu$ M fentanyl was injected into a cell with 20  $\mu$ M iFentanylSnFR2.0 at 300 s intervals. Raw heat (figure inset) and thermodynamic parameters and stoichiometry are given.
- (F)  $k_{\text{obs}}$  vs. [fentanyl] in a 1 s stopped-flow kinetic response experiment. The  $k_{\text{on}}$  was determined by a linear fit of the first four points.
- (G) Dose response against neurotransmitters demonstrates complete selectivity.
- (H) Selectivity against other opioids shows complete selectivity beyond their pharmacologically relevant concentration ranges.
- (I) Dose responses against other fentanyl analogs: 20x selectivity against Sufentanil based on S-Slope and complete selectivity against the other analogs and the major metabolite, norfentanyl.
- (J) iFentanylSnFR1.0 monitors fentanyl permeation in living cells. HeLa cells were transfected with iFentanylSnFR1.0\_PM and \_ER. Dose responses ranging 50-250 nM show a linear response in both compartments with the S-Slope within a factor of 2x of each. Widefield imaging (figure insets for \_PM and \_ER constructs), 40x, 1.0 NA objective, 470 nm excitation, scale bars = 20  $\mu$ m.
- (K) Simulated field of iFentanylSnFR1.0 324I 490G: the purified protein was lyophilized (figure inset), stored in the dark at room temperature and humidity for 3 weeks, reconstituted in solution, and used in a dose response ( $n = 2$ ).
- (L) iFentanylSnFR2.0's dose response in biofluids spiked with fentanyl. Final v/v for serum = 25%, saliva = 50%, and sweat 50% mixed into a biosensor solution prepared in 3x PBS pH 7.4. For all dose responses: SEM is shown as error bars ( $n = 3$  dose responses averaged).

As we evolved iFentanylSnFR, we found all intermediate candidates to be functional and applied some in various biological preparations. HeLa cells were transfected with iFentanylSnFR1.0\_PM and \_ER, directed to the plasma membrane (PM) and endoplasmic reticulum (ER), respectively (Figure 2J). Fentanyl equilibrated in ~sec-

onds in each compartment, and the S-Slopes were within a factor of 2x within each compartment, indicating that fentanyl rapidly (~sec time constant) permeates cells. In a simulated field test, lyophilized samples of the predecessor mutant of iFentanyl-SnFR2.0 maintained at least 60% of the S-Slope and at least ~80% of the dynamic range (Figure 6.2 K). Finally, in diluted pooled serum, saliva, and sweat spiked with fentanyl, iFentanylSnFR2.0 maintained its S-Slope within a factor of 2x, with minimal decline in response in the pharmacologically relevant range (Figure 6.2 L).

### **iFentanylSnFR2.0 in primary neurons, acute slices, and the living brain of freely behaving mice**

We transduced biological preparations with AAV9-hSyn-iFentanylSnFR2.0-cyto-WPRE to continuously monitor fentanyl. Given that fentanyl rapidly equilibrates across membranes, the cytoplasm affords a superior imaging volume suitable for studying PK. In primary hippocampal neurons, iFentanylSnFR2.0 displayed the desired localization (Figure 6.3 A) and a linear dose response in the low nM regime with S-Slope =  $4.8 \mu\text{M}^{-1}$  (Figure 6.3 B, C). A full dose-response ranging from 30 nM to 3  $\mu\text{M}$  fitted to a Hill equation showed  $\text{EC}_{50} = 104 \text{ nM}$  with  $\Delta F_{\text{max}}/F_0 = 0.97$  (SI Figures 6.11 A-C). Both measures of the S-Slope demonstrate that iFentanylSnFR2.0 maintains its sensitivity within a factor of 2x relative to the purified protein's dose response.

We chose to measure fentanyl waveforms in acute slices to validate iFentanyl-SnFR2.0's localization and kinetics en route to *in vivo* experiments. the VTA for the region's central role in rodent models for substance use disorders, involved in the rewarding and locomotor effects (Cooper et al., 2017; Steidl et al., 2017). In acute VTA slices, iFentanylSnFR2.0 exhibited widespread transduction (4x view, Figure 6.3 D) and cytoplasmic localization (40x view, Figure 6.3 E). The biosensor exhibited a similar response magnitude to a bath application of 1  $\mu\text{M}$  fentanyl as in primary culture. The imaging focal plane was 3 to 4 layers of neurons into the slice, ~50  $\mu\text{m}$  from the top surface. In this case, the biosensor's response takes ~3.5 min to plateau compared to ~2 min in the primary neuron culture.



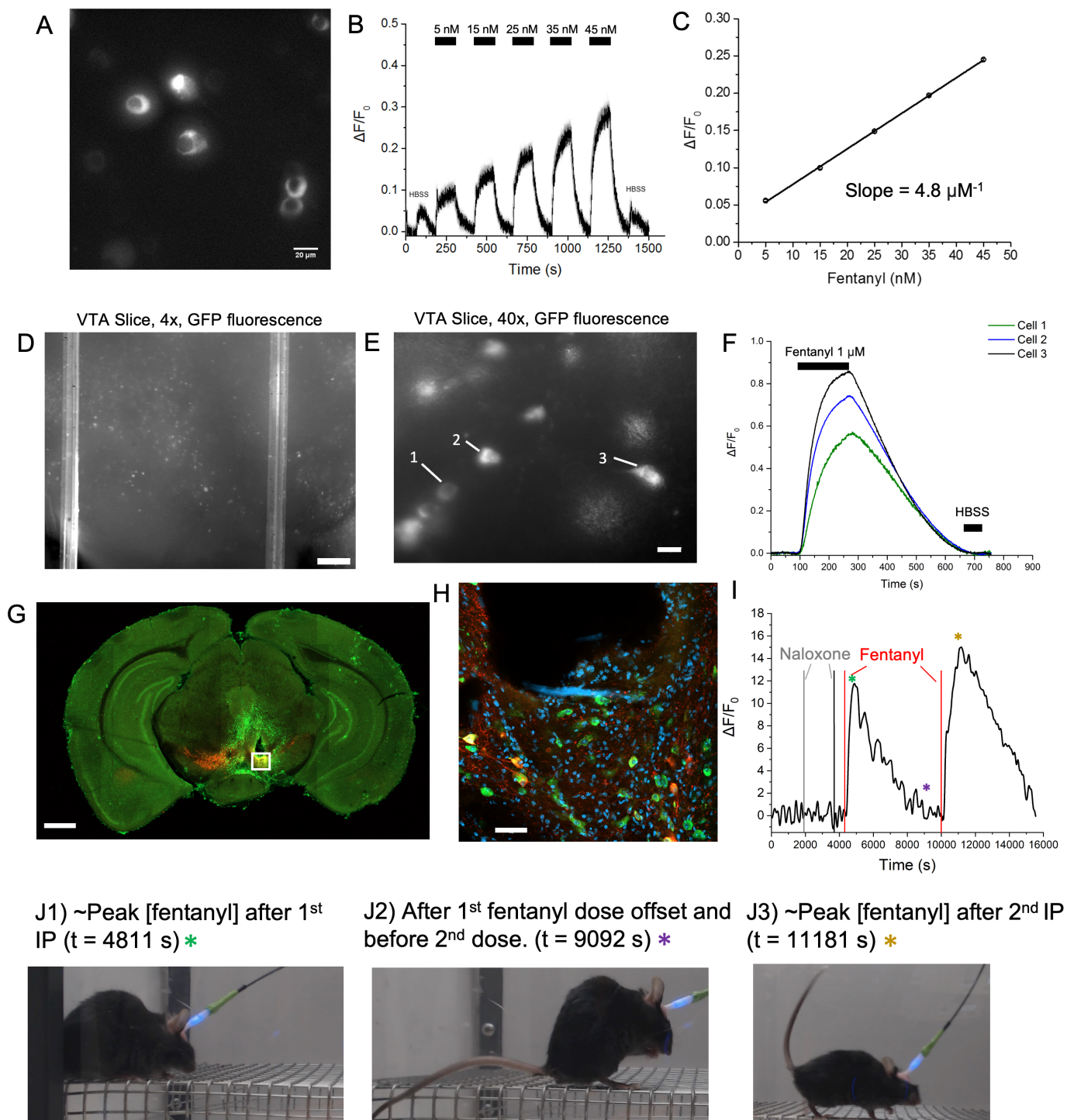


Figure 6.3: Detecting fentanyl in neurons enables real-time dosing in a freely behaving animal.

AAV9-iFentanylSnFR2.0-cyto-WPRE was used for all experiments.

(A-C): Linear dose response of iFentanylSnFR2.0 in primary hippocampal neurons.

(A) Widefield fluorescence image (40x, NA = 1.0, 470 nm excitation) at peak response to fentanyl.

(B) The dose-response waveform during continuous imaging. A HBSS control (1 min wash in/wash out) was used to begin and end the experiment. Fentanyl applications (2 min wash in/wash out) were stepped by 10 nM from 5 nM to 45 nM.

(C) Linear regression fit of responses corrected for the pH artifact (average of HBSS controls).

(D-F): Imaging iFentanylSnFR2.0 in acute VTA slices. (D) Acute VTA slice (4x objective). Scale bar = 100 microns; brightness increased by 20%. (E) Individual cells show cytoplasmic targeting (40x objective). Cells in the focal plane used for analysis are annotated. Scale bar = 20  $\mu$ m. (F) Waveform during the bath perfusion of 1  $\mu$ M fentanyl (first arrow, t = 90 s) and washout (second arrow, t = 270 s). Bath exchange time ~10 s.

(G-H): Immunohistochemistry validation of VTA targeting. (G) The coronal brain slice confirms fiber placement coordinates above the VTA. Tyrosine hydroxylase (Th, red) and GFP (green) channels are shown. Scale bar = 1 mm. The area below the fiber tract is denoted by the white box outline. (H) Zoom in on the fiber tract area (Th, GFP, and DAPI channels shown). Scale bar = 50  $\mu$ m.

(I-J) Real-time dosing of fentanyl in an exemplar rodent via photometry. A mouse was pre-treated with 1 mg/kg and then 10 mg/kg naloxone (grey and black vertical lines). During the course of the first 1 mg/kg fentanyl dose (first vertical red line), no change in behavior was observed (J1, J2). The experimenter watched for the subsidence of the first dose and then administered the second fentanyl dose (second vertical red line). The animal then displayed the stereotypical Straub tail and circling behavior (J3). Asterisks match snapshots to time in the waveform in (I).

We injected the viral vector for functional and null variants of iFentanylSnFR2.0 in the VTA of live mice, followed by the implantation of a fiber optic element. Immunohistochemistry confirmed the desired fiber targeting above the VTA (Figure 6.3 G). A magnified region below the tract shows GFP-positive neurons partially colocalized with Th-positive neurons, as expected for pan-neuronal expression. Photometry measurements in the animals after 1 mg/kg fentanyl IP showed no significant change (n = 3, SI Figures 6.11 D-F; Figure 6.4 A). Therefore, any photometry signal is the result of fentanyl interacting with the binding pocket of iFentanylSnFR2.0 to elicit increased GFP fluorescence in the tissue.

### **Real-time dosing in an individual animal via photometry**

We demonstrated that photometry allows an experimenter-in-the-loop approach to dosing a drug in an animal. We recorded from an animal while the experimenter observed and administered naloxone, a pan-opioid competitive antagonist, and fentanyl, a selective  $\mu$ -OR agonist, by intraperitoneal (IP) injection. iFentanylSnFR2.0 showed no response to naloxone and then responded to the first fentanyl dose (1 mg/kg) with a relatively steep rise followed by metabolism/clearance (Figure 6.3 I). During the majority of the first fentanyl waveform, the animal did not display behavioral indications of fentanyl's effects (Figure 6.3 J1, J2). The experimenter watched for the complete subsidence of the fentanyl waveform in real time and then provided a second dose of 1 mg/kg fentanyl. During the 2nd fentanyl waveform peak, the animal exhibited a stark Straub tail (elevated tail with a hunched, rigid body) and hyperactivity characteristic of  $\mu$ -OR activation (Figure 6.3 J3). This correlation between  $\mu$ -OR agonism and the biosensor signal in the VTA encouraged a population behavioral study where the time course may vary between individuals.

### **Machine vision pose estimation alongside the photometry measurement in freely behaving mice**

We then systematically quantified photometry recorded simultaneously with behavior in 16 animals in an open arena. Cameras were centered above and on one side of an open rectangular arena, and we used DeepLabCut to train separate neural nets for each camera view using experimenter-labeled frames<sup>47,48</sup>. In the top view, the animal's midline, ears, and fiber were labeled with key points (Figure 6.4 B1). The "mid\_1" point was used for the body's displacement, and "fiber" was used for the head position in over 97% of frames (SI Table 2). In the side view, the tail was extensively labeled in addition to the fiber and midline to determine the tail-body angle (Figure 4B) in over 93% of frames where the tail was visible (SI Table 3).

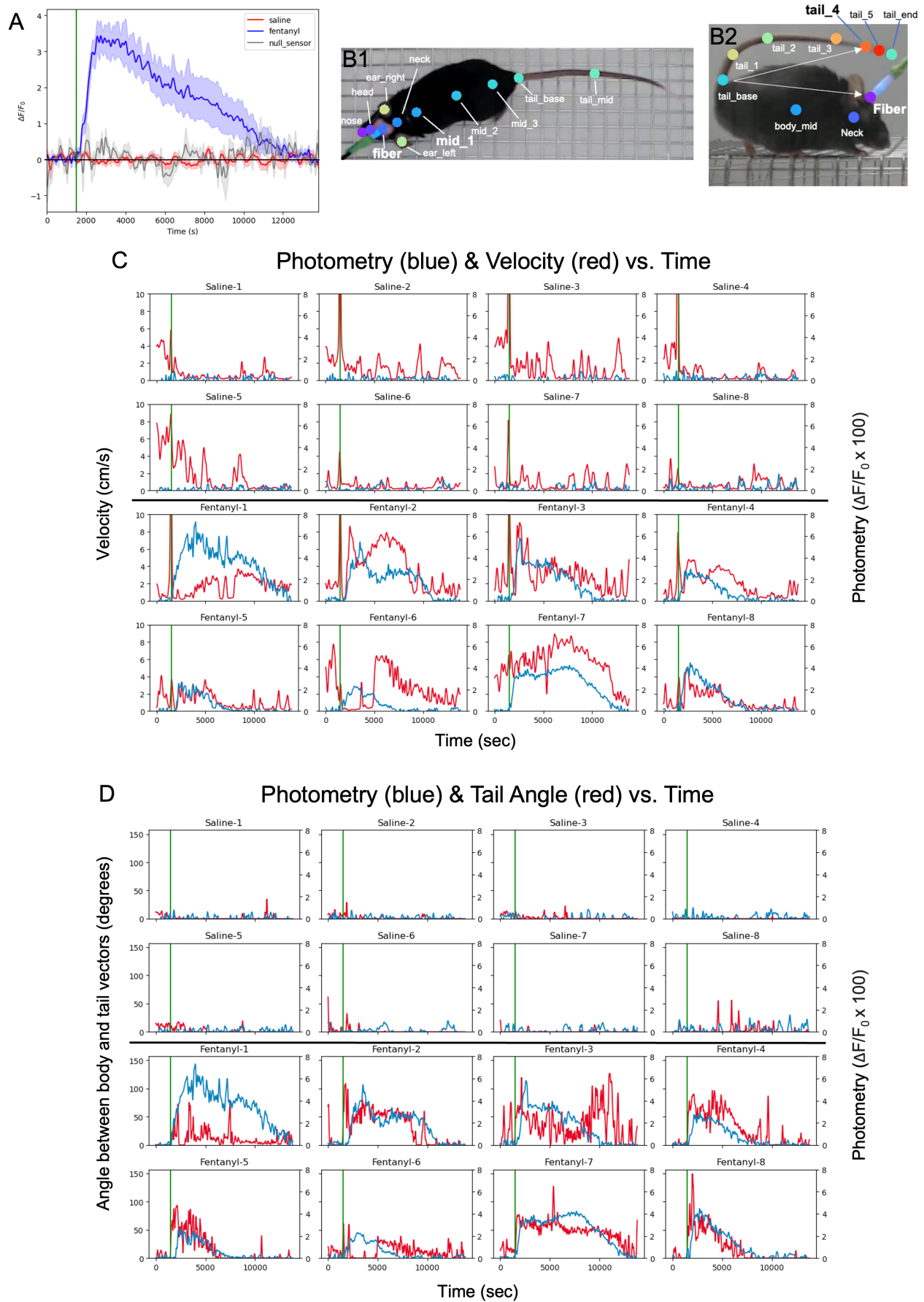
### **Population versus individual [fentanyl] waveforms**

The fentanyl treatment group ( $n = 8$ ) and received a 1 mg/kg fentanyl IP injection; they displayed a significant positive waveform, whereas saline group ( $n = 8$ ) showed no appreciable change from baseline (Figure 6.4 A). The fentanyl treatment group average shows a  $\sim 3$  h time course, consistent with prior population studies of fentanyl brain PK. Conventionally, fentanyl pharmacokinetics has been performed by blood draws or tissue homogenization for a single time point analyzed by LC-MS. A previous study by Kalvass et al. sacrificed cohorts of animals at several time

points and reported the population averages for blood and brain pharmacokinetics of fentanyl after a 0.9 mg/kg subcutaneous injection in mice. Kalvass et al. found that the [fentanyl] in the brain resembled that of serum within a ~few min with a  $t_{1/2}$  of 4.9 min in the brain (Kalvass et al., 2007). The results from Kalvass et al. displayed a similar overall time course and time constants for each phase, as observed in this work (Kalvass et al., 2007). In the present study, individual animals displayed time courses ranging from ~2 h (e.g., animal Fentanyl-5) to ~3.5 h (e.g., Fentanyl-1) (Figure 6.4 C). This variability is evident in the population average, where the standard error is the largest mid-way through the subsidence of the waveform (Figure 6.4 A). This result highlights the importance of measuring the relationship between drug PK and behavior within the same individual. Whereas microdialysis could be performed in situ, it is less robust at ~nM concentrations and in detecting highly hydrophobic molecules (Srinivas et al., 2018).

### **The [fentanyl] waveform drives phasic locomotor activity and Straub tail**

The photometry waveform for each animal is plotted against the velocity (Figure 6.4 C) and tail angle (Figure 6.4 D). The saline cohort remained motionless in a corner, occasionally moved to another corner, and occasionally groomed themselves. These animals displayed an elevated tail only incidentally, typically when their rears were pressed into a corner (SI Figures 6.12 A, B). In contrast, the fentanyl treatment group showed phasic hyperactivity and Straub tail that tracked the fentanyl waveform. The beginning of this correlation is seen within a few min after IP injection (SI Figure 6.13 A). Cross-correlations between each behavioral measure and the photometry waveform show a peak with a lag of 0-10 min for the fentanyl cohort except for the two animals that stalled and no appreciable correlation for the saline cohort (SI Figures 6.13 B, C). Fentanyl-1's velocity dropped to ~zero at ~1.5 h as it pauses in the corner. Fent-3 displayed a high sensitization to the Straub tail effect; the first apparent phase is a typically elevated tail while circling, while the second phase tracked with the animal rearing frequently with a modestly elevated tail. Fent-6 displayed a ~30 min period of inactivity and apparent low tail angle; however, inspection of the video shows that this individual collapsed from the fentanyl effect during this period.



(A) Averaged photometry recordings of fentanyl in the VTA of freely behaving mice. Two cohorts expressing the functional biosensor received an IP injection of 1 mg/kg fentanyl ( $n = 8$ , blue) or saline ( $n = 8$ , red). A cohort expressing the null biosensor received an IP injection of 1 mg/kg fentanyl (dark gray). Waveforms are aligned to the time of IP (green line). SEM is shown as the shaded region.

(B1-2) Machine vision tracking of mouse behavior designed by this work using top (B1) and side (B2) views.

(C) Overlay of photometry waveform (blue, 60 s FFT filter) and the animal's velocity (red) for each animal in the two cohorts: saline (top half) and fentanyl (bottom half). Velocity was calculated using a 3.33 s rolling window and was Gaussian smoothed ( $\sigma = 60$  s). The vertical green line indicates the time of IP.

(D) Overlay of photometry waveform (blue, 60 s FFT filter) and the animal's tail angle elevation (red, Gaussian smoothed,  $\sigma = 60$  s).

### **A stereotypical and paradoxical repetitive locomotor pattern**

While hyperactivity, respiratory depression, and Straub tail have been observed after opioid agonism, short-term tolerance and how these effects interplay to produce overarching behavioral patterns are incompletely defined. This work shows that “repetitiveness,” including those effects, appears to be the predominant, integrated effect. We define circling as the animal completing a circuit around the corners of the arena and the midpoints in between within 30 s. The saline cohort exhibits virtually zero circling as animals largely move from one corner to another, where they spend most time sitting. In contrast, the fentanyl cohort displays phasic circling in which the animal may spend up to ~90% of a 5 min window circling, subsiding with the fentanyl waveform (Figure 6.6 B). We define “nose in corner” as any period where the animal's fiber is within one cm of a corner, facing into that corner. This behavior is highly unusual insofar as prey animals prefer to stay close to the perimeter of arenas but facing outward. The saline cohort scarcely triggers this criterion, whereas the fentanyl cohort dwells facing into the corner, sometimes standing on all four paws facing in and other times reared stationary, holding a Straub tail posture. After the fentanyl IP, the animals display up to ~100% of their time faced into the corner in a 5 min bin (Figure 6.6 C). In sum, the fentanyl cohort shows a significantly higher total distance traveled and time spent circling and with nose-in-corner than the saline cohort (Figure 6.6 D).

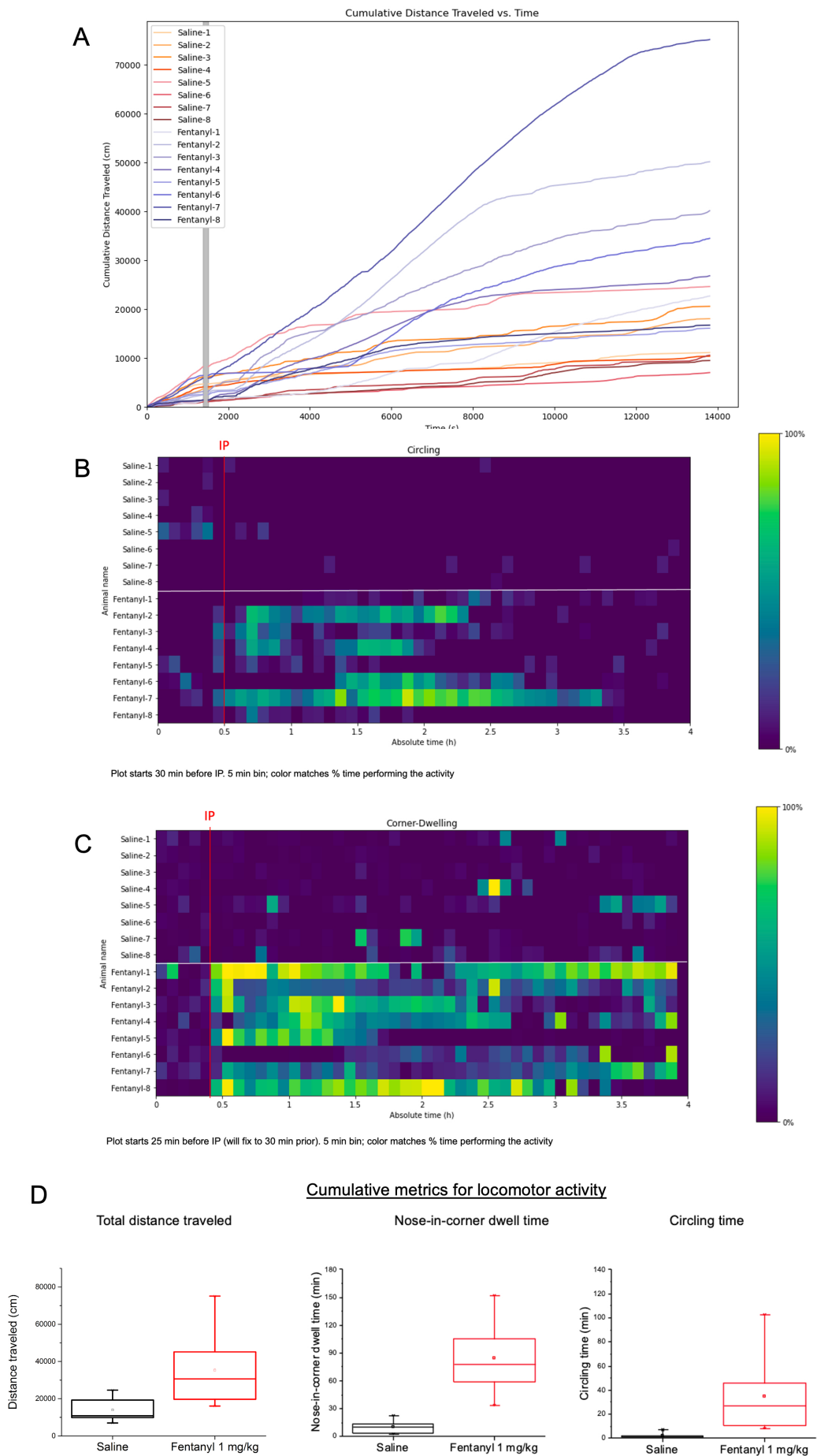


Figure 6.5: The stereotyped fentanyl effect demonstrated in cumulative statistics.

- (A) Cumulative distance traveled for each animal over the entire experiment (4 h). Individual traces are labeled for each animal. Time of IP indicated by vertical green line.
- (B) Time series heat map of circling behavior. Circling is defined as the animal passing through the center of each side of the arena within 30 s. Bins are 5 min.
- (C) Time series heat map of nose-in-corner behavior defined as periods where the animal places its nose into a corner of the arena continuously for at least 3 s. Bins are 5 min.
- (D) Comparison of cumulative locomotor behaviors between fentanyl (red) and saline (black) cohorts. The box denotes 25, 50, 75 percentiles and outlier whiskers denote the individual lowest/highest values.

This work shows that “repetitiveness,” including those effects, appears to be the predominant, integrated effect. The saline cohort exhibits little or no circling: as animals largely move from one corner to another, where they spend most time sitting. In contrast, the fentanyl cohort displays phasic circling: the animal may spend up to ~90% of a 5 min window circling, subsiding with the fentanyl waveform (Figure 5B). The “nose in corner” behavior is highly unusual insofar as prey animals prefer to stay close to the perimeter of arenas but face outward. The fentanyl cohort dwells facing into the corner, sometimes standing on all four paws facing in and other times reared stationary, holding a Straub tail posture. After the fentanyl IP, the animals display up to ~100% of their time faced into the corner in a 5 min bin (Figure 5C). In sum, the fentanyl cohort shows a significantly higher total distance traveled and time spent circling and with nose-in-corner than the saline cohort (Figure 5D). The cumulative key point location heat maps confirm this stark circling pattern in the top view (SI Figure 6.12 A) and elevated tail position throughout the cage (SI Figure 6.12 B) for the fentanyl group and not the saline group.

We term the “fentanyl-driven stereotypical locomotor pattern” as a hyperactive repetitive pattern of circling, stalling, and Straub tail that follows the fentanyl time course. This pattern appears paradoxical in that animals on fentanyl show stalling by collapsing with visible respiratory depression or holding their “nose in the corner” but also display hyperactivity in terms of cumulative displacement. However, the apparent paradox is resolved when considering the time series data and the multiple circuits bearing  $\mu$ -ORs. Although animals cannot simultaneously circle and dwell faced into the corner, they can display both behaviors within a 5 min bin. There



is a phasic tradeoff between the rates of circling and dwelling with the nose in the corner.

### **Assessing the effect of fentanyl in an ethologically relevant survival task**

We then tested the hypothesis that the stereotypical locomotor pattern due to fentanyl exposure is detrimental to self-maintenance. We used a foraging paradigm where the animals learn to navigate through a labyrinth maze to find a water port (Figure 6.6 A) (Rosenberg et al., 2021). Animals entered the maze on their own volition via a tube connected to their home cage. A single water port in the maze provided their only source of hydration (food is provided ad libitum in the home cage). Zero training was required for this paradigm, and the entire experiment was conducted during the animal's dark cycle (active period) for 10 h. The maze consists of 128 numbered nodes (SI Figure 6.14 A), allowing for quantification via a machine vision routine and comparison of trajectories. A camera placed below the maze's IR-transparent bottom recorded the animal in the maze (Figure 6.6 B). This maze was reported previously in a study that showed animals exhibited "sudden insight" to learn direct routes to the water port (Rosenberg et al., 2021).

In this work, one group of animals was deprived of water for 22 h prior to the experiment ("water-deprived") and administered either saline ("Sal"), 0.1 mg/kg fentanyl ("Fent-low"), or 1.0 mg/kg fentanyl ("Fent-high") IP at the start of the experiment (n = 8, each treatment). To assess intrinsic interest and navigation in the maze, another group of animals had food and water ad libitum in the home cage ("intrinsically motivated", animal aliases given prefix "i-") and was administered either saline (n = 6) or 1.0 mg/kg fentanyl (n = 4) to assess the impact of the drug on exploration in the absence of a foraging task.

The experimental groups initially deprived of water displayed stark fentanyl dose- and time-dependent effects in navigating the maze and earning water. The water-deprived animals injected with saline showed immediate interest in exploring the maze and performed bouts typically < 5 min (Figure 6.6 C). This group showed rapid (< 30 min) discovery of the water port and persistent successful foraging (Figure 6.6 D). The animals receiving 0.1 mg/kg fentanyl remained in their cage for 0.5-3 h before entering the maze. A side view of the home cage showed that these animals displayed the hallmarks of opioid agonism (e.g., circling and Straub tail) (SI Video 3). However, once these animals entered the maze at a later clock time compared to the saline group, they displayed rapid learning of the route to the water port. The

water-deprived animals treated with 1.0 mg/kg fentanyl readily entered the maze and remained there for ~3 h in a single bout. Fent-high-2 is the exception as it entered the maze for the first time with ~15 min remaining in the 10 h experiment. No water-deprived animal treated with 1.0 mg/kg earned water from the port for that first ~2 h (wall or maze clock), and most animals only began earning water rewards 2.5 h or later into the experiment. However, beyond this period, all animals learned direct routes and earned plentiful water rewards.

During their extended initial bouts in the water-deprived groups, the animals receiving 1.0 mg/kg fentanyl typically moved in a circling or figure-eight pattern in a 1/16 region of the maze, occasionally moving to another subsection but never finding the water port or drinking during this period. Notably, animals in this group will repeatedly press their face into a dead-end wall or corner, not immediately turning around. In contrast, animals receiving 0.1 mg/kg fentanyl display modest and brief or no such circling and stalling in the maze (after an extended period in the home cage – Figure 6.6 C), and animals receiving saline never display impaired locomotion (representative traces, Figure 6.6 E). The repetitive locomotion is characterized by revisiting a small number ( $< 16$ ) of nodes without exploring other regions of the maze. This effect is visualized through representative raster plots of the nodes visited over time for an animal receiving saline versus 1.0 mg/kg fentanyl (Figure 6F). Another contrast in locomotor pattern between the groups is captured in part by the average speed over time. The 1.0 mg/kg fentanyl group initially displays ~1/2 the speed of the saline and 0.1 mg/kg fentanyl groups while in the maze and eventually converges with these two groups after ~3 h (Figure 6G). The repetitive circling locomotor pattern is also captured in a lower average entropy for the 1.0 mg/kg fentanyl group, converging with the saline group on a similar time course (Figure 6.6 H).

In another set of experiments, the intrinsically motivated animals were treated with either saline or 1.0 mg/kg fentanyl IP and were allowed to enter the maze of their own volition. Animals receiving saline exhibited maze exploration behavior similar to the water-rewarded experiments (SI Figure 6.14 B-D). As in the prior study establishing the maze paradigm, animals normally have an intrinsic interest in entering and exploring the maze thoroughly (Rosenberg et al., 2021). The animals receiving 1.0 mg/kg fentanyl also displayed similar locomotor and exploration results as in the water-deprived case: low entropy (SI Figure 6.14 B) and repetitive circling (SI Figure 6.14 E) despite extended residence in the maze (SI Figure 6.14 C). 3 of 4

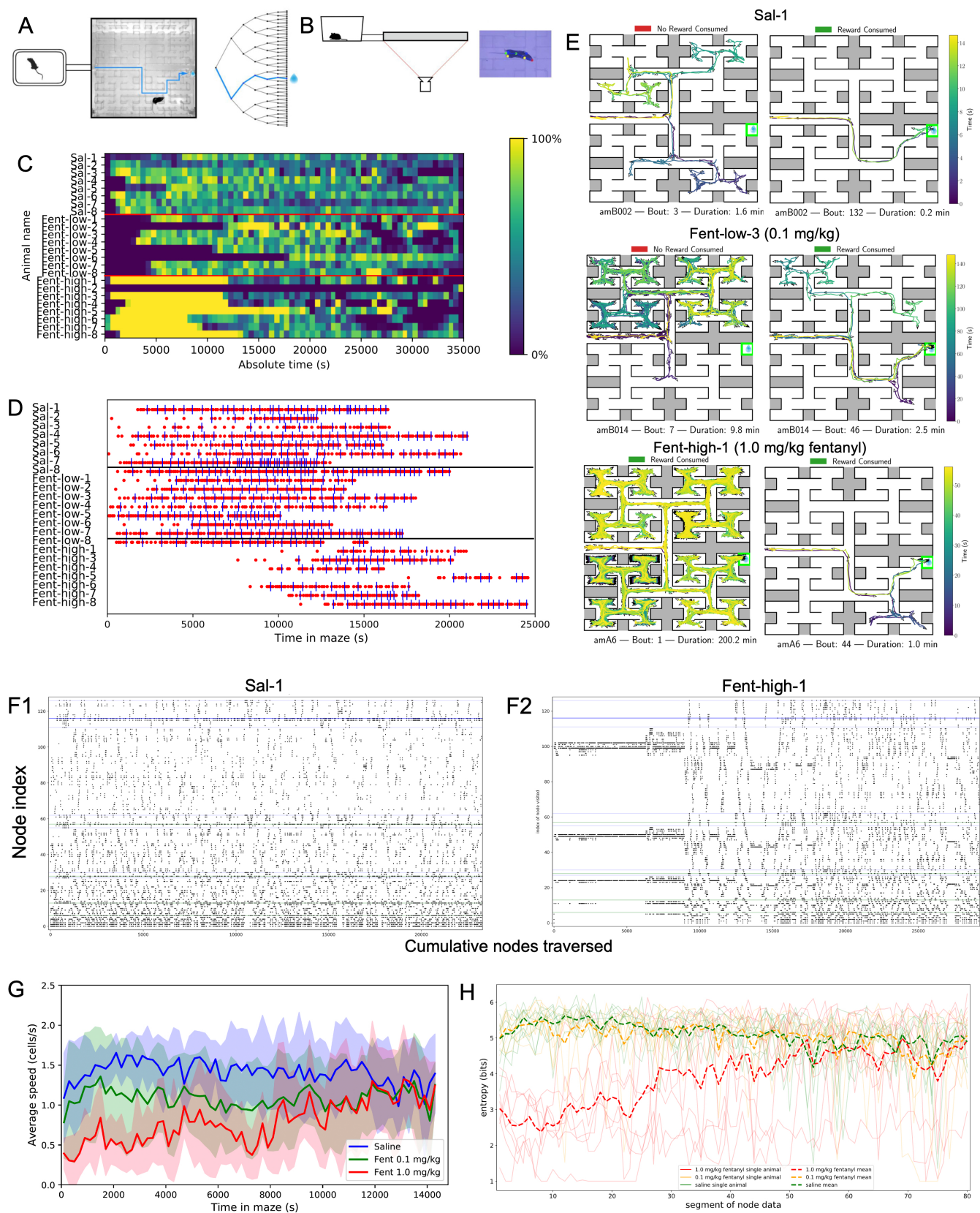


Figure 6.6: Fentanyl effects on animals foraging for water in a labyrinth maze.

(A) Labyrinth maze paradigm with 2<sup>6</sup> binary decision branches and a single water port accessible at a terminal node. Mice were placed in a home cage with no water and ad. lib. food and could voluntarily enter the maze via a tube. The animals could earn 35  $\mu$ L water for nose-poking into a port at the end of the maze (90 s timeout after dispensing). The experiment lasted 10 h during the animal's dark (active) cycle.

(B) Videography scheme: the maze was constructed using IR-transparent plastic. An IR camera was placed underneath the maze to capture the animal's movements, and the IR indicator light for water rewards at the water port.

(C) Time series heat map for the occupancy of the maze over the entire experiment (0 to 100%, dark blue to yellow). Bins = 500 s.

(D) Water rewards earned (red dot for each and blue tick mark for every 5th) over the cumulative time in the maze. amA7 was excluded from this analysis due to the first entry occurring at 9.5+ h.

(E) Bouts from representative animals by fentanyl dose at early and mid-experiment time points. The path is traced as a line time series colored using a gradient from dark blue to yellow to represent the beginning and end of the bout. The duration of each bout is noted below the image.

(F) Representative visualization of node visitation pattern for an animal that received saline (Sal-1, F1) or 1 mg/kg fentanyl (Fent-high-1, F2).

(G) Velocity in the maze for saline (blue), 0.1 mg/kg fentanyl (green), and 1.0 mg/kg fentanyl (red) cohorts. The standard deviation is shown as a shaded region.

(H) Entropy measure of each of the three groups of animals foraging for water in the maze (individuals are represented by solid traces and the group averages by dashed line).

animals receiving 1.0 mg/kg fentanyl displayed extended bouts ranging from 2.5 to 4 h, and the 4th animal did not enter the maze until 4 h into the experiment (SI Figure 6.14 C), comparable to the outlier animal in the water-deprived, 1.0 mg/kg fentanyl treatment group. Therefore, the locomotor and exploration deficits from fentanyl administration appear to be independent of the water-deprivation and specific goal.

### **Evolving selective sensors from pan-activating ligands: iTapentadolSnFR and iLevorphanolSnFR**

Finally, we sought to further evolve iOpioidSnFRs for opioids with varying activity profiles and pharmacokinetics that contrast with fentanyl. Given the biosensor

library's engineered responses to nicotinic ligands, particularly choline and acetylcholine, we sought to test the most challenging cases for improving selectivity. A principal component analysis of the S-Slopes from the "biosensor x opioid" library screen revealed that tapentadol, levorphanol, and meptazinol were outliers in their strong pan-activation of the cholinergic biosensors (Figure 6.7 A). We then prioritized tapentadol and levorphanol because of their unique activities and pharmacokinetic profiles. Tapentadol, a  $\mu$ -opioid agonist and norepinephrine reuptake inhibitor, is the most recent FDA approval for an opioid with a novel mechanism of action (Langford et al., 2016; D. Singh et al., 2013). The combination of these two mechanisms allows for lower effective doses and has opened a route to less addictive opioids (Schröder et al., 2011). Levorphanol's lack of cross-tolerance with respect to prior morphine use (Moulin et al., 1988) and its longer duration of action (~11 h half-life in humans) provide a pharmacokinetic basis for improved treatment of chronic pain (Prommer, 2007).

We found that a small number of mutations was sufficient to engender the desired selectivity in these iOpioidSnFRs. OpuBC's lack of affinity for endogenous ligands in mammals, save for choline, simplified the search space to a positive selection for the opioid and a negative selection against acetylcholine/choline. For iTapentadolSnFR, one mutation at a cation- $\pi$  residue, W436A, in iNicSnFR3b, ablated all sensitivity to cholinergic ligands while improving an already strong response to tapentadol (Figure 6.7 B). iLevorphanolSnFR was generated via two mutations in the second shell, G15T and A455P, diminishing the sensitivity to ACh outside the physiologically relevant range (Figure 6.7 C). Both variants show little or no response to other neurotransmitters (SI Figures 6.9 A, B) and endogenous opioid peptides (SI Figures 6.9 D, E). iTapentadolSnFR displays ~zero sensitivity to other opioids at ~1  $\mu$ M and below. iLevorphanolSnFR displayed selectivity against all tested drugs except S-methadone (Figure 6.7 G). The two biosensors are well-behaved insofar as their  $K_d$  values, determined by ITC, are within a factor of 2x of their  $EC_{50}$  from fluorescence with a stoichiometry near 1.0 (Figures 6.7 E, H). Stopped-flow kinetics showed that iLevorphanolSnFR's  $k_{on}$  is approximately unchanged from the  $k_{on}$  for its parent, iAChSnFR41. iTapentadolSnFR has an ~order of magnitude larger  $k_{on}$  than its predecessor, iNicSnFR3a38 (Figures 6.7 F, I; raw data in SI Figures 6.9 A, B).

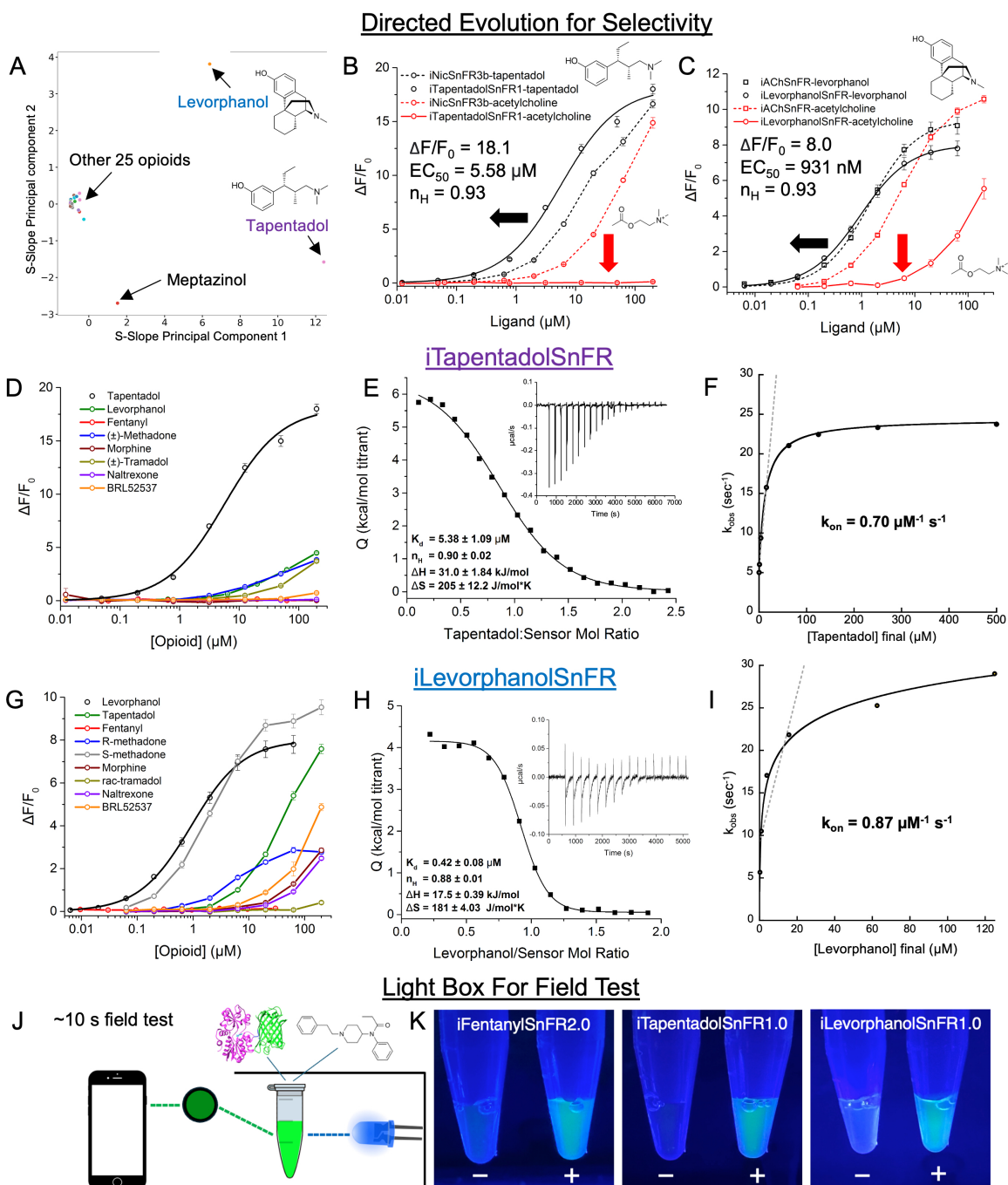


Figure 6.7: Evolving the two best hits for increased selectivity, yielding iTapentadol-SnFR and iLevorphanolSnFR & application to a reagentless field test. (A) Principal component analysis of the cholinergic biosensor-opioid pair S-Slopes with outlier structures noted for tapentadol, levorphanol, and meptazinol. (B) A single point mutation, W436A, generates iTapentadolSnFR. Hill fit parameters for tapentadol against iTapentadolSnFR are listed. (C) Two point mutations in the 2nd shell residues, QG15T and HA455P generate iLevorphanolSnFR and shift sensitivity to acetylcholine outside the physiological range. Hill fit parameters for levorphanol against iLevorphanolSnFR are listed. (D-F) iTapentadolSnFR characterization. (D) Selectivity against other opioid drugs show no response in their pharmacologically relevant ranges. (E) Isothermal titration calorimetry: 2  $\mu\text{L}$  of 450  $\mu\text{M}$  tapentadol was injected into a cell with 45  $\mu\text{M}$  iTapentadolSnFR at 300 s intervals (raw heat, figure inset).

Thermodynamic parameters given with fit error. (F)  $k_{\text{obs}}$  vs. [tapentadol] in a 1 s stopped-flow kinetic response experiment. (G-I) iLevorphanolSnFR characterization. (G) Selectivity against other opioid drugs demonstrated for all but S-methadone. (H) Isothermal titration calorimetry: 2  $\mu\text{L}$  of 500  $\mu\text{M}$  levorphanol was injected into a cell with 50  $\mu\text{M}$  iLevorphanolSnFR at 300 s intervals (raw heat, figure inset). Thermodynamic parameters are given with fit error. (I)  $k_{\text{obs}}$  vs. [levorphanol] in a 1 s stopped-flow kinetic response experiment. For all dose responses: SEM is shown as error bars ( $n = 3$  dose responses averaged). (J-K) Field test using a light box. (J) Light box apparatus was constructed using blue LED strips on either side. A bandpass filter (50 nm band centered at 560 nm) was positioned in front of a phone camera. (K) Pairs of solutions of the three exemplary biosensors were prepared (5  $\mu\text{M}$ ) and one was spiked with the drug of interest (20  $\mu\text{M}$ ) and immediately photographed with the phone.

In sum, we can generate sensitive and selective responses to opioids even if they display promiscuous binding to the starting points. Most notably, nine variants based on OpuBC provide enough diversity in starting points so that a small number of mutations can yield the desired selectivity. These results point to “activity cliffs” in sequence space where small steps in the sequence landscape result in dramatic changes in function. Activity cliffs represent a weakness in current machine learning approaches to protein engineering; however, this weakness can be resolved by collecting training data like these, and including a training criterion assessing performance with activity cliffs (van Tilborg et al., 2022). These results suggest that the binding pocket and 2nd shell residues in OpuBC harbor the potential for activity cliffs, exploited for converting selectivity from one drug class to another.

### **Field test: immediate, cost-effective, & robust opioid detection via a phone camera**

While our initial motivation in developing iOpioidSnFRs was to genetically encode them in living cells, their biophysical properties make them attractive probes for field tests, especially in resource-constrained settings. In particular, the sufficient aqueous solubility, dynamic range, sensitivity, selectivity, kinetics, and emission in the visible range allow for a fluorescence-based field test. We used a lightbox using readily available parts, namely a blue LED strip in a black box, a smartphone, and a green bandpass filter for our simulated field test (Figure 6.7 J). Solutions of iFentanylSnFR2.0, iTapentadolSnFR, and iLevorphanolSnFR were prepared with and without spiked drug and photographed using an iPhone 14 camera. No post-

processing was required; the immediately captured images are shown (Figure 6.7 K). That the biosensors tolerate lyophilization, allows for future versions of this field test not to require any solutions in storage or transit. This test could be used to determine the presence of a health hazard in the environment (e.g., fentanyl) or determine the exposure level in a person provided 10s of microliters of a relevant biofluid can be collected.

#### 6.4 Discussion

We report the first class of sensitive and selective genetically encodable biosensors of synthetic opioid drugs. We focused on the relation between whole-body PK (as measured in the brain, specifically VTA) and rodent behavior to get a comprehensive view of the opioid time course. While prior studies have shown various behavioral effects, the observation times were often limited to ~1 h and did not include [fentanyl] measurements alongside, so correlations could not be determined. In a simple model, behavioral effects are directly mediated by neuronal dynamics, which include receptor kinetics and cellular allostatic mechanisms. In the ligand bias model of GPCR activity, fentanyl displays strong  $\beta$ -arrestin bias, and we expected it to induce strong, fast desensitization (Williams et al., 2013). That the stereotypical pattern tracks the entire fentanyl waveform was unanticipated: conventional models show desensitization and “short-term tolerance” on time scales of ~10 min and ~1 h, respectively (Williams et al., 2013). Instead, we observed that the fentanyl time course, ranging from 1.5 to 3 hours across individuals, drove locomotor activity with similar kinetics. These periods are well beyond the conventional regime of cellular desensitization and call for the reconciliation of the dynamics in cellular and circuit models with the observed opioid-related behavioral time courses.

Additionally, our results motivate additional mechanistic study of the unique behavioral effects in rodents not seen in humans. While “high doses” of fentanyl would be normally associated with incapacity in humans, they elicit erratic hyperactivity in rodents. Other work has shown a monotonic relationship between increased fentanyl dose and increased respiratory depression (Chamoun et al., 2023) and peak hyperactivity at 1.0 mg/kg fentanyl (Varshneya et al., 2021), the dose used in this work. However, prior works had not reconciled the apparent paradox of Straub tail/respiratory depression alongside hyperactivity. There is some similarity between the rigid posture of the rodent Straub tail and chest wall rigidity (“wooden chest syndrome”) in humans (Pergolizzi et al., 2021). However, to our knowledge, there are no reports of hyperactivity and repetitive locomotor behavior in humans.



This work shows that an individual animal administered fentanyl can display periods of hypo- and hyper-activity, switching every few ~min. During chronic opioid exposure, humans display Cheyne-Stokes or Biot's breathing (switching between periodic high- and low-breathing rates) (Owens, 2020). Mice may also display alternation between hypo- and hyper-activity from hypoxia-dependent compensatory activity. Our work provides a reference to ask if a circuit manipulation can re-create these effects with similar time constants.

This work introduces a naturalistic paradigm to address opioid effects on self-maintenance. Critically, the maze task provides an integrated view of all the fentanyl effects (e.g., motor, cognitive, etc.) in a quantifiable, ethologically relevant task over a longer-than-average 10 hour experiment. Conventionally, the substance use disorder field has relied on tasks like the 5-choice serial reaction time task to assess the drug's effect on an animal's self-control (Asinof & Paine, 2014); however, this task requires weeks of training and non-natural activities. In contrast, mice readily forage in complex environments for resources, both in the wild and in our experiments. That mice do not require any prior training whatsoever suggests that this navigation task assesses a core capacity necessary for survival. In this sense, the maze navigation task more closely matches the DSM-V criteria than conventional cognitive tasks. Indeed, we see fentanyl dose-dependent deficits in exploration and foraging compared to the saline cohort. The 1.0 mg/kg fentanyl cohort showed circling in a small portion of the maze for several hours. The animals show a rapid recovery in foraging performance after ~3 hours and sustain it for the rest of the night; they are not completely debilitated during their first withdrawal period. Future studies will investigate repeated opioid exposure to determine if deficits are restricted to the period of the drug time course and the threshold at which repeated exposures lead to failure in survival tasks (Belin et al., 2016).

Long-term tolerance is a critical feature of OUD, driving escalated intake and, potentially, death by overdose. This work's continuous monitoring method suggests one future tactic to assess long-term tolerance: identify administration regimens that lead to behavior deviating from the fentanyl waveform. We know that other neural drugs, generally, including some other opioids, lack a straightforward relationship between free concentration and activity (Lutfy & Cowan, 2004). In contrast, fentanyl offers straightforward pharmacology as it is not a prodrug, lacks active metabolites, and selectively binds to  $\mu$ -OR. With the present work, we have a straightforward mapping between [fentanyl] waveform and locomotor behavior.

Continuous monitoring devices to perform analogous studies in humans would allow researchers and drug use therapy providers to personalize dosing methods to minimize side effects, particularly in reducing tolerance. With advances in diagnostic device fabrication, the bottleneck in continuous monitors has moved to generating selective, sensitive, and robust sensor molecules paired with appropriate signal transduction mechanisms (Campuzano et al., 2020; Liu, 2021). iOpioidSnFR2.0's optical response can be calibrated to the biofluid, meeting existing form factors for both rapid point-of-care tests and continuous monitors comparable to a fluorescence-based continuous glucose monitor (Joseph, 2021). This result is particularly useful for addressing the proliferation of synthetic fentanyl analogs (Armenian et al., 2018; O'Donnell et al., 2017) and research compounds such as unconventional  $\mu$ -opioids and synthetic kappa opioids under consideration in therapeutic applications (Beck et al., 2019; Rosalyn Chen et al., 2021).

This work demonstrates a protein with excellent conformational switching ability with little or no affinity for the drug of interest can be evolved to become an optimal binder. At present, we believe that the OpuBC-based tactic will succeed for many drugs of MW < ~700 capable of making cation- $\pi$  interaction. This work further generalizes the concept of exploiting minute promiscuous binding to develop an eventually sensitive and selective protein function (Arnold, 2018). Most notably, nine variants based on OpuBC provide enough diversity in starting points to generate iOpioidSnFRs with a small number of mutations. Most starkly, we observed "activity cliffs" as in some binders like iTapentadolSnFR where small steps in the sequence landscape result in dramatic changes in function. These cliffs represent a weakness in current machine learning approaches to protein engineering; however, collecting training data like the leucine screen in the binding pocket aromatic residues can address this limitation (van Tilborg et al., 2022). These results suggest that the binding pocket and 2nd shell residues in OpuBC harbor the potential for activity cliffs, exploited for rapidly converting selectivity from one drug class to another without sacrificing the attractive biophysical properties for continuous measurements.

These tactics could be applied to other scaffolds that exploit the many naturally occurring and synthetic conformation-switching proteins. While genetically encoded sensors have been reported for many neurotransmitters, there remain many small molecule drugs and metabolites to monitor in situ for metabolic, cell signaling, and pharmacokinetic interests. Nature has afforded ~25,000 bacterial ligand-binding

proteins alone, and a recent work demonstrated a technique to screen for sites where one can insert reporters, including the present cpGFP. PBPs offer excellent physical properties, including large (10-20 Å) conformational changes, aqueous solubility, localizability within organelles, a lack of crosstalk with mammalian cells, and stability as a lyophilized powder. Recent advances in signal transduction techniques, such as nanopores, have been applied to use PBPs in electronic circuits, offering another approach to continuous monitoring devices (Zernia et al., 2020). The protein engineering and computational ethology approaches together serve the goal of detecting molecules in living organisms in a minimally invasive and continuous manner. These approaches enable us to study animals as they behave in more naturalistic contexts, and, ultimately, in their ecological niches.

## **6.5 Acknowledgements and Funding**

### Acknowledgements:

Christopher Evans provided advice about the construction of the opioid panel. Dalibor Sames provided mitragynine and 7-OH mitragynine. Viviana Gradinaru, Zhe Qu, and Timothy Miles at the CLOVER Center provided training in virus production. Brandon Henderson advised in adapting the acute slice protocol. Brandon Henderson, Carsten Tishberek, and Elizabeth Unger provided feedback on this manuscript. Giada Spigolon and Andres Collazo managed the Biological Imaging Facility supported by the Beckman Institute and advised on confocal imaging. Nicole McMillan and Karen Lencioni assisted in IACUC protocol development and oversaw animal care. Purnima Deshpande provided laboratory management.

### Funding:

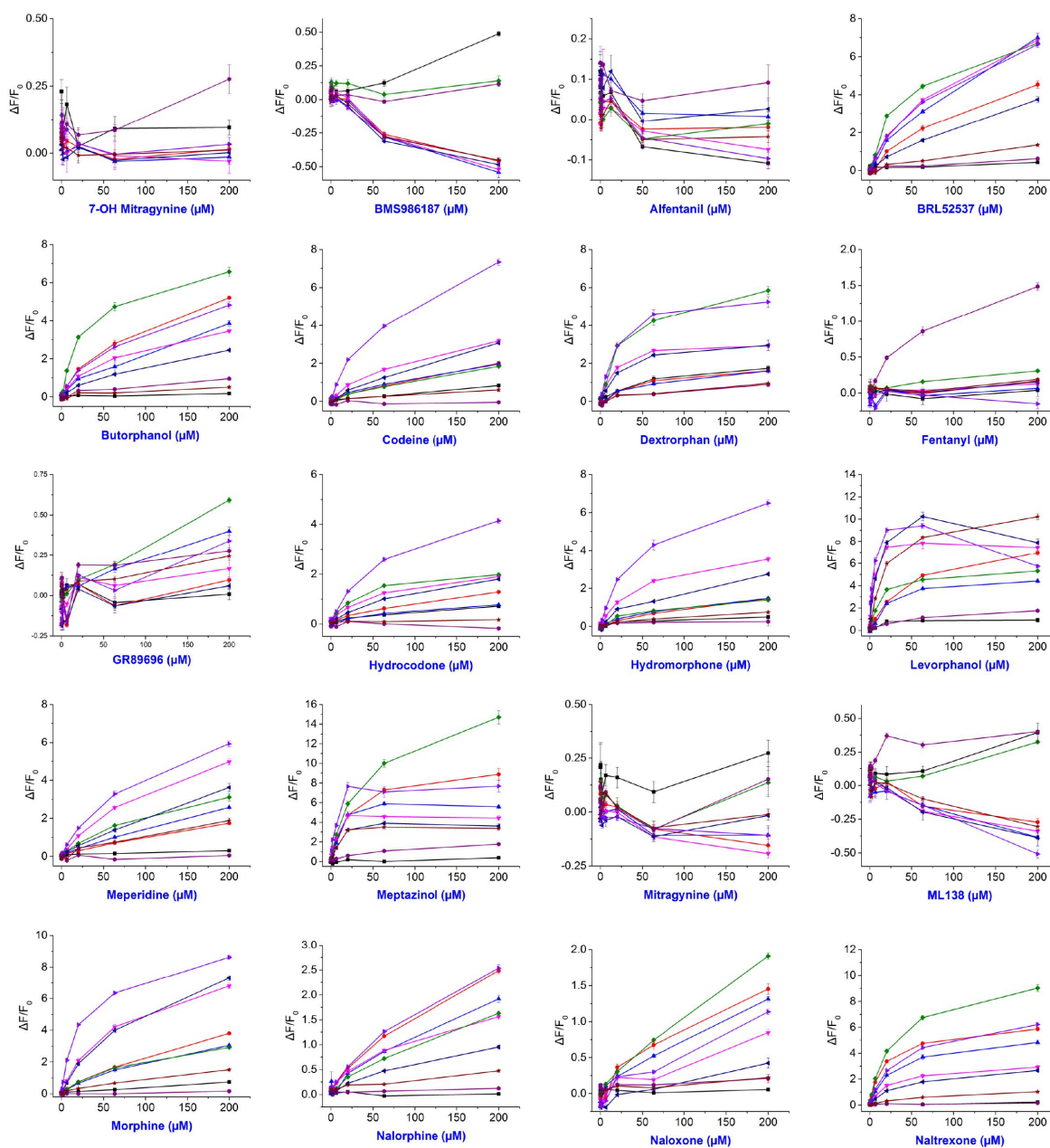
This work was supported by the National Institute on Drug Abuse (NIDA) Grant DA043829, National Institute of General Medical Sciences (NIGMS) Grant GM-123582, and Janelia Research Campus, Howard Hughes Medical Institute (HHMI). H.A.L. was supported by DA043829 and GM-123582. A.K.M. was supported by DA043829, NIGMS fellowship 5T32GM007616, and National Institute of Neurological Disorders and Stroke fellowship T32NS105595. A.K.M. and M.H.R. were supported by a Chen Innovator Grant provided by the Chen Institute at Caltech. L.L.L. and J.S.M. were supported by Janelia Research Campus, HHMI.

### Declaration of competing interests:

A.K.M., H.A.L., L.L.L., and J.S.M. have filed a patent application (US20220196642A1) regarding iOpioidSnFRs and their applications.

## 6.6 Supplemental Figures

Biosensor Legend: v4.6, cc93, v7, v7.1, v7.1.2, v8, v9, AK1, v7 436F 11V



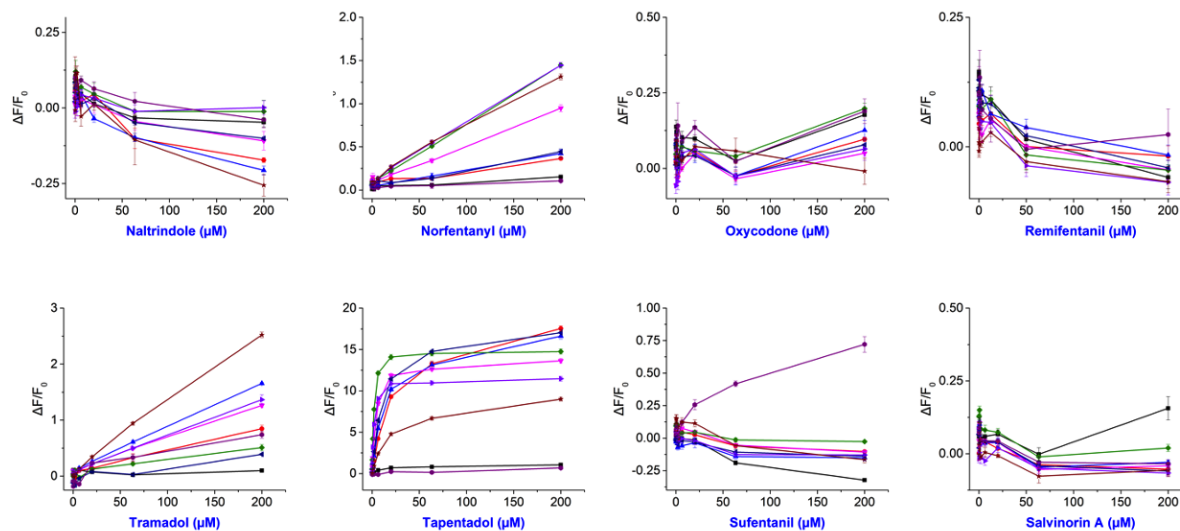


Figure 6.8: SI Figure 1 related to Figure 6.1: Raw data for biosensor responses plotted against each opioid ligand. A serial dilution of each opioid was prepared and mixed into a biosensor solution to achieve a final [opioid] ranging from 200  $\mu\text{M}$  to 63.3 nM with a constant [biosensor] of 100 nM. Each dose response is shown as a line graph (color legend identifies biosensor sequence). These dose responses determined the linear range for the regression for each opioid vs. biosensor. The SEM is shown as error bars ( $n = 3$  dose responses averaged).

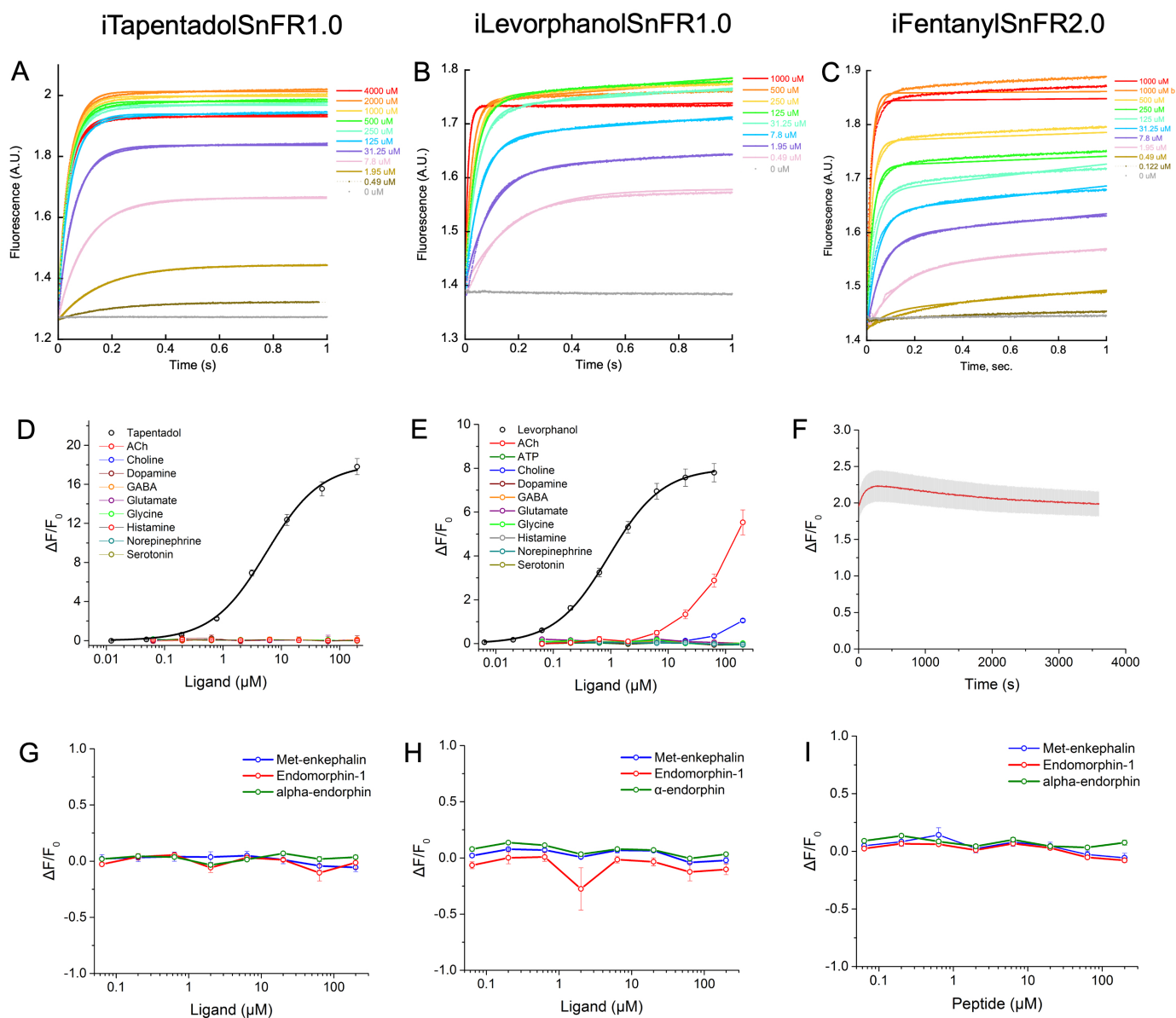


Figure 6.9: SI Figure 2 related to Figure 6.2 & 6.3: Raw data and additional characterization of iTapentadolSnFR, iLevorphanolSnFR, and iFentanylSnFR2.0. (A-C): 1 s stopped-flow kinetic data. 200 nM of each biosensor was mixed in equal volume to each ligand in varying concentrations as labeled. The final [opioid] in the chamber was one-half of this value. (F) 1-hour measurement of iFentanylSnFR2.0's response to 1  $\mu\text{M}$  fentanyl shows  $\sim 90\%$  of the response immediately ( $\sim 3$  s) after mixing followed by a  $\sim 4$  min equilibration for the remaining  $\sim 10\%$  of the signal and then linear bleaching. (D-E): Selectivity against neurotransmitters (iFentanylSnFR2.0's response shown in the main text). (D) iTapentadolSnFR shows no response to any neurotransmitter, including acetylcholine, owing to a mutation in a critical cation- $\pi$  residue, like iFentanylSnFR2.0. (E) iLevorphanolSnFR shows diminished response to acetylcholine with  $S$ -Slope  $< 0.05$  and  $\sim$ zero response at the physiologically relevant concentrations (at  $\sim 2$   $\mu\text{M}$  and below). (G-I): Selectivity against endogenous opioid peptides in fluorescent dose responses. No significant response is observed for [peptide] at the highest tested dose (200  $\mu\text{M}$ ) or below for any sensor. For all dose responses: SEM shown as error bars ( $n = 3$  dose responses averaged).

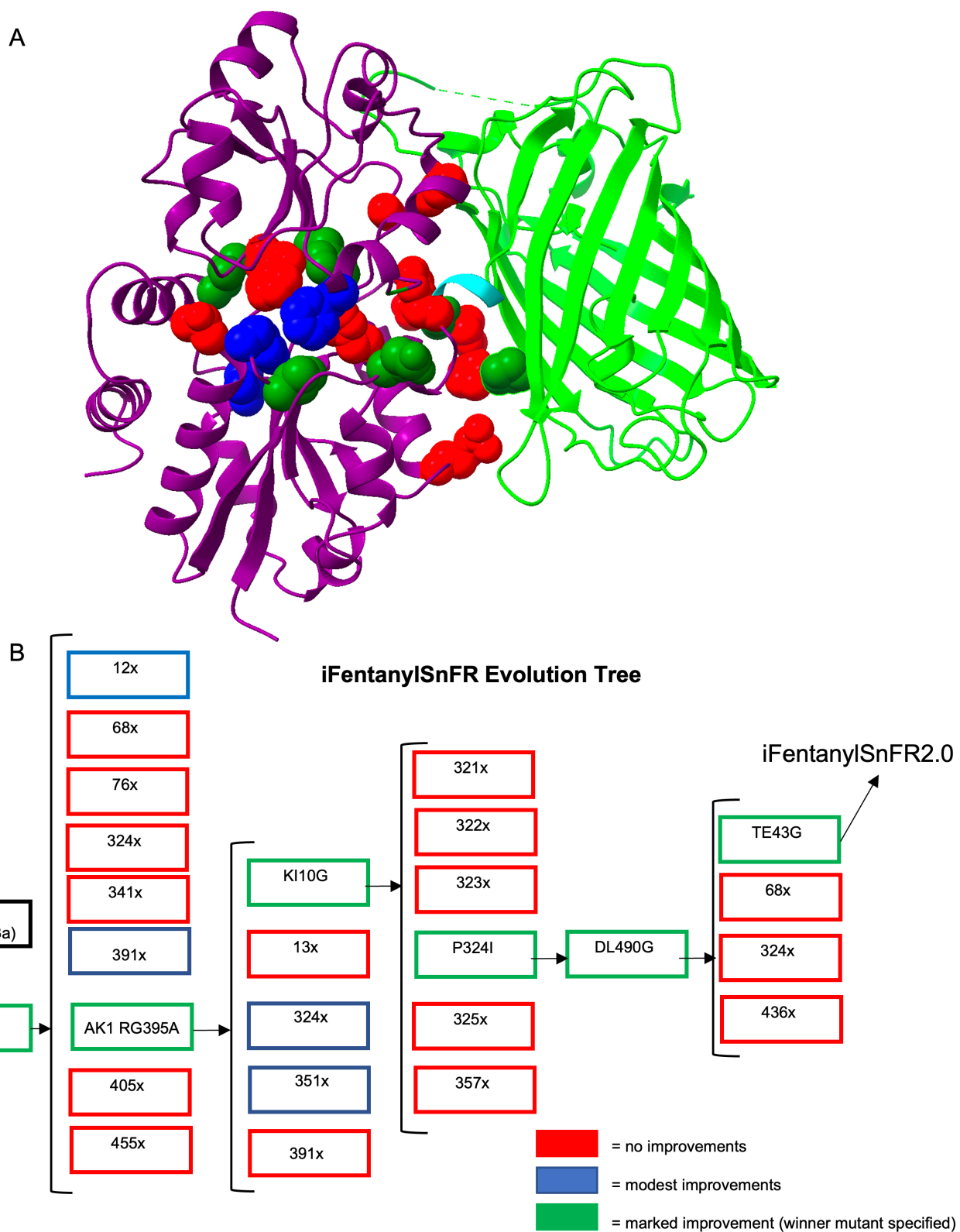


Figure 6.10: SI Figure 3 related to Figure 6.3: iFentanylSnFR2.0 Directed Evolution Tree.

Crystal structure of iNicSnFR3b (PDB: 7S7V) annotated with residues mutated in the directed evolution towards iFentanylSnFR2.0. Side chains mutated are shown as spheres: failed mutations (red spheres), modest improvements not taken forward (blue spheres), and accepted mutations (dark green spheres). Evolution tree representing site saturation mutagenesis experiments. Residue nomenclature: first and second residues before the position number are the amino acids in the OpuBC homologue from *Thermoanaerobacter* sp X513 in nature and iNicSnFR3b, respectively. The residue listed after the position number is the amino acid found in iFentanylSnFR2.0.



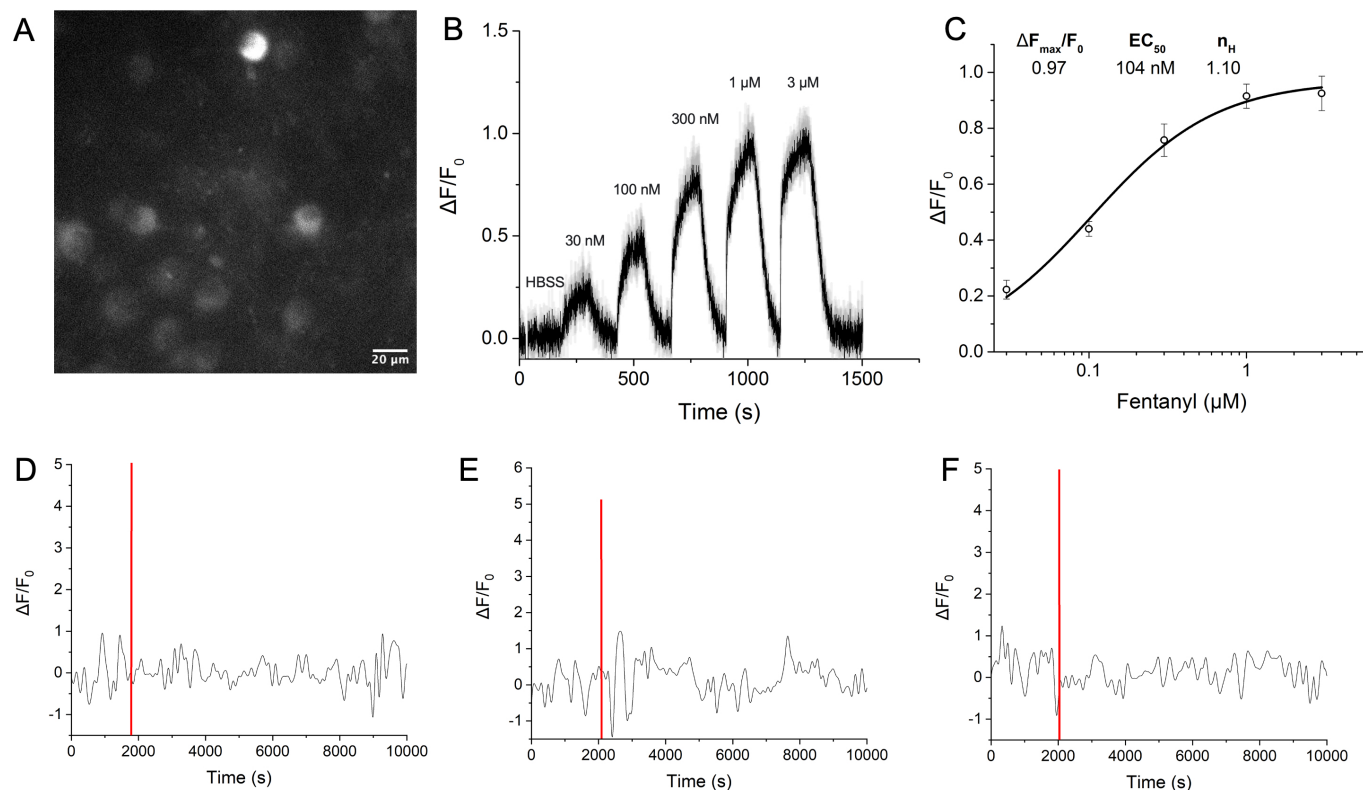


Figure 6.11: SI Figure 4 related to Figure 6.4 & 6.5. (A-C) iFentanylSnFR2.0 response in primary hippocampal neurons under saturating [fentanyl]. (A) Widefield image of the neurons transduced with iFentanylSnFR2.0 (scale bar = 20 microns). 40x objective, 1.0 NA, 470 nm excitation. (B) The waveform of biosensor response during widefield fluorescence imaging. The HBSS control and then increasing [fentanyl] bath application (2 min on, 2 min washout) was applied. (C) The steady-state response after correcting for the HBSS artifact was fit with the Hill equation (parameters shown). The dynamic range observed in primary cell culture is comparable to that of the acute slice response to 1 micromolar fentanyl bath perfusion. (D-F) Individual traces from the “null” negative control experiment. iFentanylSnFR2.0 W436L (null sensor) was cloned into the same pAAV vector, packaged in AAV9, and injected into same coordinates in the VTA, replicating the protocol used for the functional sensor. Photometry recordings were conducted before and after administration (1 mg/kg fentanyl IP time noted by vertical red line). No appreciable response was observed in response to the IP.

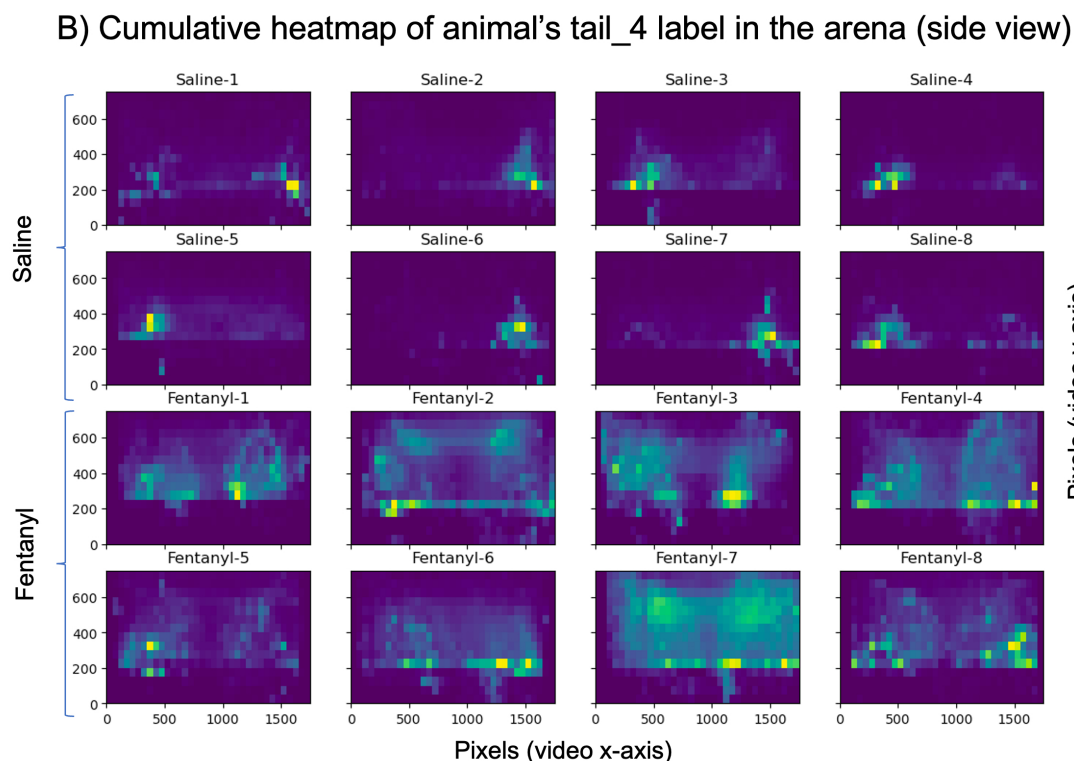
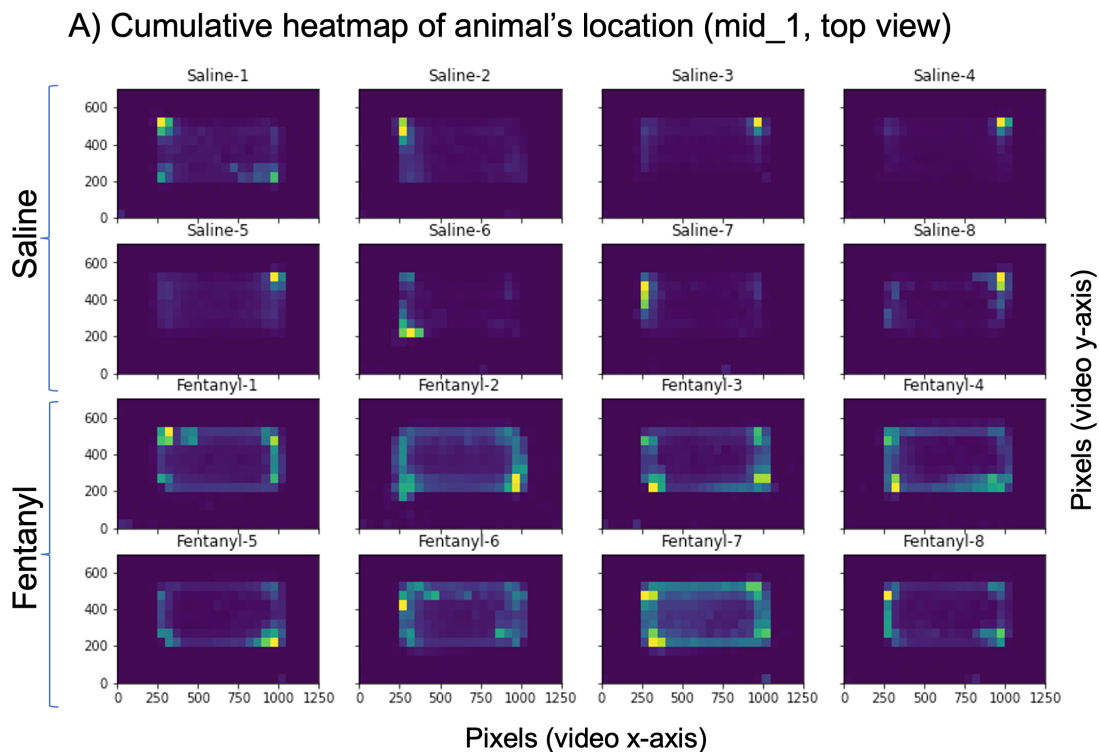
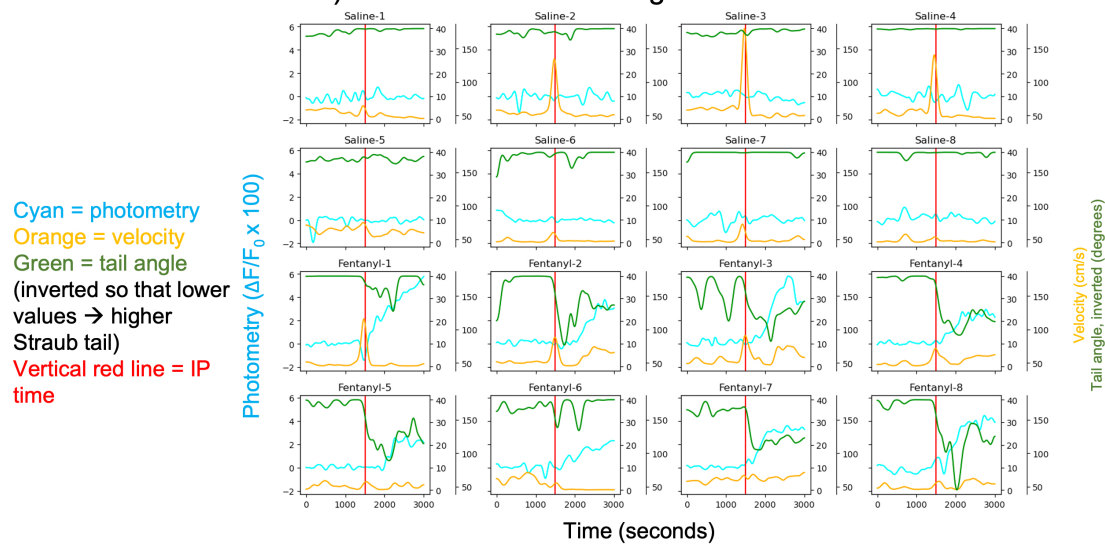
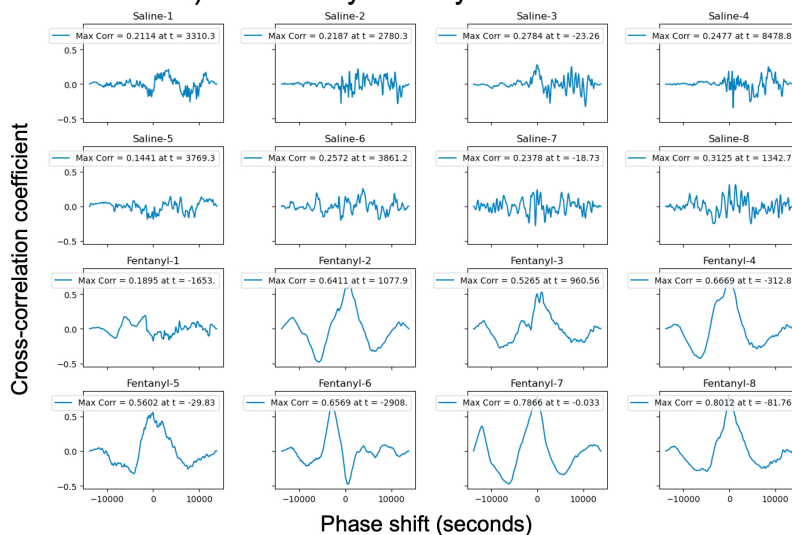


Figure 6.12: SI Figure 5 related to Figure 6.5 & 6.6: intermediate checks on raw machine vision data. (A) X-Y position heat map (top view) of the animal's posterior body label. Animals receiving fentanyl show a circling pattern whereas the saline cohort spends most time sitting/grooming in the corners of the arena. (B) X-Z position heat map (side view) of the second to last label on the animal's tail ("tail\_4," arrow in inset image of the cage). Animals receiving fentanyl show an elevated tail throughout the cage (i.e., moving around the arena displaying Straub tail). Animals receiving saline show the tail largely lies on the floor, hangs below the mesh, or is pushed up the wall when sitting in a corner.

### A) Zoom-in on main text figure +/- 25 min from IP time



### B) Photometry-velocity cross-correlation



### C) Photometry-tail angle cross-correlation

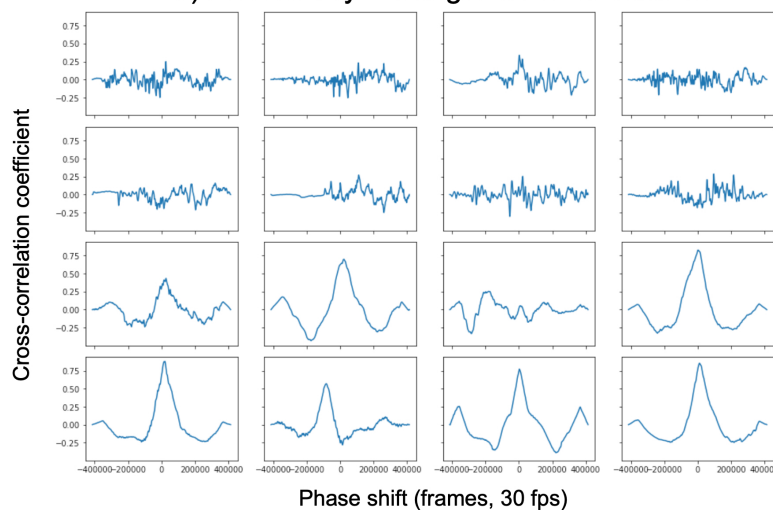


Figure 6.13: SI Figure 6 related to Figure 6.5 & 6.6: Cross-correlations of photometry and behavioral measures.

(A) Zoom in on Figures 6.5 & 6.6 immediately before/after IP time with photometry (cyan), velocity (orange), and tail angle (dark green) traces overlaid. Straub tail metric is inverted with respect to the main text for clarity in the overlaid traces (depressed angle trace corresponds to a greater degree of Straub tail). (B-C) Cross-correlations between photometry and behavior. X-axes are in video frames. (B) Cross-correlation of the entire velocity vs. photometry waveforms. (C) Cross-correlation of the entire tail angle vs. photometry waveforms.

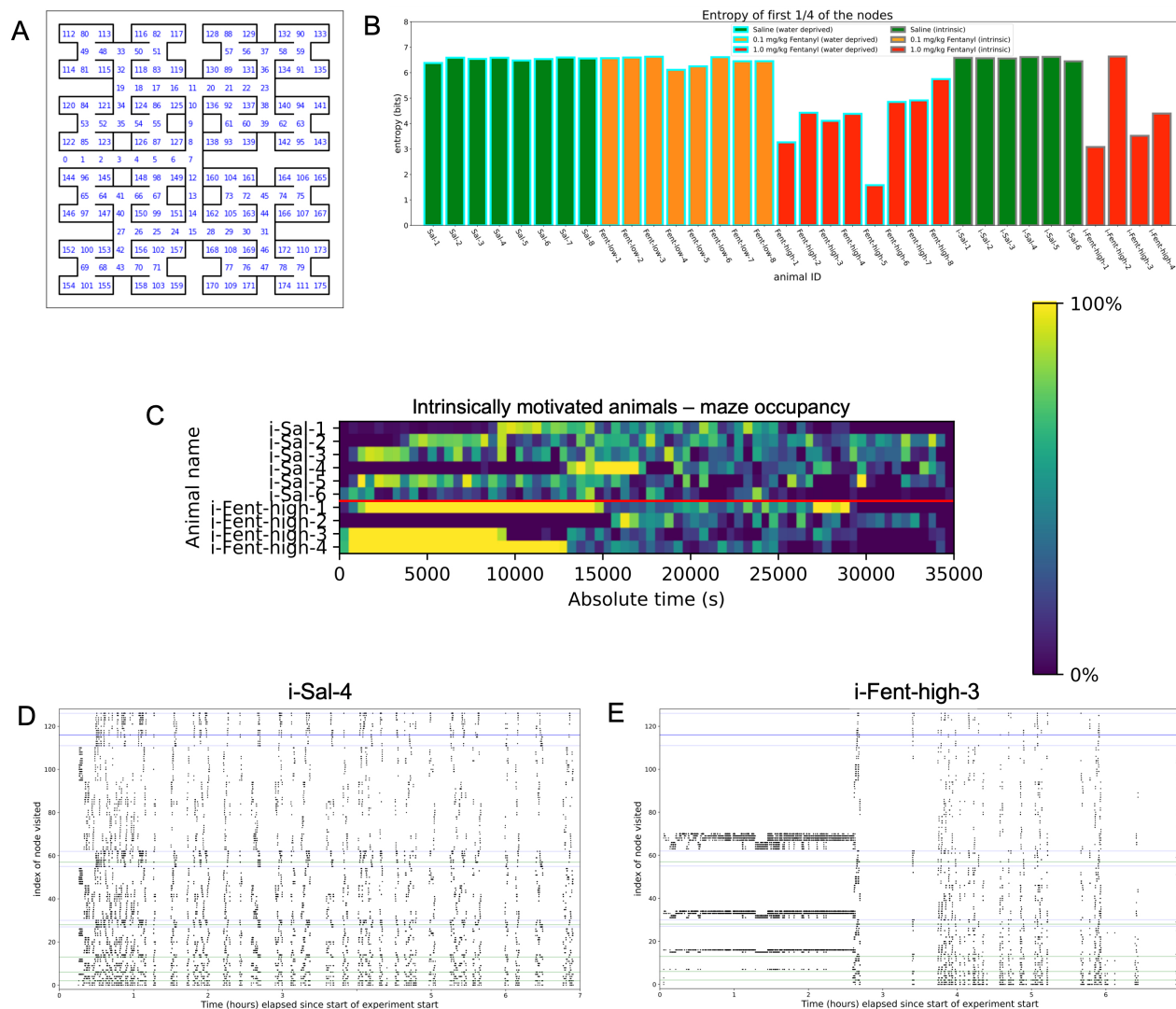


Figure 6.14: SI Figure 7 related to Figure 6.7.

(A) Maze with node numbering used for Figure 6.7.

(B) Right: entropy of the maze navigation for the first 1/4 nodes visited in the maze for each animal.

(C-E) “Intrinsic” negative control experiment—without water deprivation, animals receiving fentanyl still show repetitive navigation in the maze. Mice not deprived of water and given ad. lib. food and water in the home cage during the maze experiment. One group received saline IP and the other group received 1 mg/kg fentanyl IP. (C) Maze occupancy vs absolute time. Representative node navigation plots comparing an animal receiving saline IP (i-Sal-4 in D) vs. an animal receiving 1 mg/kg fentanyl IP (i-Fent-high-3 in E).

## 6.7 Supplemental Tables

Animal ID	Fiber	Mid_1	Accounted
Saline-1	99.6	98.7	99.2
Saline-2	99.2	93.5	95.1
Saline-3	99.6	98.9	99.5
Saline-4	99.4	98.3	99.1
Saline-5	99.6	95.7	97.0
Saline-6	99.7	97.3	97.9
Saline-7	99.4	98.1	99.0
Saline-8	99.7	98.3	98.7
Avg	99.5	97.4	98.2
Stdev	0.2	1.9	1.5
Fentanyl-1	99.7	97.2	97.7
Fentanyl-2	99.5	93.5	96.0
Fentanyl-3	99.7	98.8	99.3
Fentanyl-4	99.7	94.1	96.6
Fentanyl-5	99.7	99.4	99.6
Fentanyl-6	99.2	92.5	96.3
Fentanyl-7	99.7	96.2	97.4
Fentanyl-8	99.6	99.3	99.7
Avg	99.6	96.4	97.8
Stdev	0.2	2.7	1.5

Table 6.1: Check on DeepLabCut pose estimation quality, top view. The percent of frames with acceptable confidence for given keypoints (“Fiber” and “Mid\_1”) and frames used in final analysis (“Accounted”) are given for each animal and statistics are given for each cohort.

Animal ID	Fiber	Tail clear	Accounted
Saline-1	98.5	15.2	92.0
Saline-2	98.6	9.4	96.0
Saline-3	99.5	17.5	91.8
Saline-4	99.4	4.5	91.7
Saline-5	98.6	20.4	94.5
Saline-6	97.2	12.8	93.7
Saline-7	99.1	19.1	91.6
Saline-8	99.3	28.1	92.9
Avg	98.8	15.9	93.0
Stdev	0.7	7.2	1.6
Fentanyl-1	99.2	61.7	98.7
Fentanyl-2	98.3	59.9	92.6
Fentanyl-3	98.7	63.7	93.7
Fentanyl-4	99.0	66.0	97.5
Fentanyl-5	98.7	43.2	96.1
Fentanyl-6	98.5	61.9	93.4
Fentanyl-7	97.9	65.5	91.6
Fentanyl-8	98.7	50.0	97.5
Avg	98.6	59.0	95.1
Stdev	0.4	8.1	2.7

Table 6.2: Check on DeepLabCut pose estimation quality, side view. The percent of frames with acceptable confidence for the fiber, the tail position, and, final computed tail angle (“Accounted”) are given for each animal and statistics are given for each cohort.

## 6.8 Methods

### EXPERIMENTAL MODEL AND SUBJECT DETAILS

#### Mice

All animal care and experimental procedures were carried out in accordance with the National Institutes of Health (NIH) Guide for the Care and Use of Laboratory Animals and approved by the Institute Animal Care and Use Committee and the Institute Biosafety Committee at the California Institute of Technology. Both males and females were used in equal numbers in each experiment. The animals were housed in a temperature- and humidity-controlled facility with a 13:11 h light:dark cycle with food and water available ad libitum. The animals were group-housed when possible. Following surgery, subjects were singly housed for two weeks prior to experiments and monitored daily for a full recovery. Mice in the experimental arm of the maze foraging experiment were deprived of water for 21 h before the experiment.

#### METHOD DETAILS

##### Cloning and DNA Preparation

###### *Cloning*

Gibson assembly was used to construct several biosensor-vector combinations. We used NEBuilder (<https://nebuilder.neb.com/>) to design primers to generate DNA fragments with the requisite overlaps. These fragments were combined using Gibson assembly reactions (Gibson Assembly® Master Mix, NEB) according to the manufacturer's protocol. Each type of vector, bacterial, mammalian, and viral, served different experiments and dictated additional steps:

Bacterial expression vector: we used our previously reported vector pHHM.X513-iNicSnFR3b-(V7) (Addgene #124881) and replaced iNicSnFR3a with the new gene of interest. Directed evolution experiments mutated the resulting plasmids directly.

Mammalian expression vectors: we used our previously reported pMinDis.X513-iNicSnFR3a-(CC93)-ER (Addgene #125121) and pMinDis.X513-iNicSnFR3a-(CC93)-PM (Addgene #125122), targeting the endoplasmic reticulum and plasma membrane, respectively. We replaced the gene for iNicSnFR3a with the new biosensor gene of interest.

pAAV construction for AAV packaging: pAAV-hSyn-iGluSnFR-WPRE-SV40 (AddGene #98929) was used as the backbone for the viral construct. The PDGFR-

targeting sequence was excluded in the final construct. Without any targeting sequences, biosensors are directed to the cytoplasm of neurons. PCR reactions involving the vector backbone required 3% DMSO due to the secondary structure of the inverted terminal repeat (ITR) regions. SmaI digest was used to confirm the integrity of the ITR regions. The resulting plasmid, pAAV-hSyn-iFentanylSnFR2.0-cyto-WPRE, was used for AAV production.

#### *DNA preparation and purification*

Plasmids used for bacterial expression were transformed into DH5 $\alpha$  cells and cultured on ampicillin selection plates for 16-20 h at 37 °C. A 5 mL LB culture with ampicillin was inoculated with one colony and incubated while shaking at 250 rpm at 37 °C for 16-18 h. The DNA was purified using the QIAprep Spin Miniprep Kit (Qiagen) according to the manufacturer's protocol. The resulting DNA was submitted for Sanger sequencing to verify its identity (Laragen Inc., Culver City, CA).

pAAV plasmids used for AAV production were transformed into NEB Stable cells using the NEB Stable media and cultured on ampicillin selection plates at 30 °C for 30 h. All culturing tubes and flasks were pyrogen-free and specified for AAV production. A 5 mL primary culture using Plasmid+® media (Thomson Instrument Company) and ampicillin was inoculated with a single colony and incubated while shaking at 250 rpm at 30 °C for 6-8 h. The primary culture was diluted 1:200 into a secondary culture of 100 mL Plasmid+® media with ampicillin and incubated while shaking at 250 rpm at 30 °C for 16-20 h. The DNA was purified using EndoFree Plasmid Maxi Kit (Qiagen) according to the manufacturer's protocol. SmaI digest was used to confirm the integrity of the inverted terminal repeat (ITR) regions. The region between the ITRs was sequenced using custom hSyn-forward and WPRE-reverse primers (Laragen Inc., Culver City, CA). The DNA concentration and purity were verified using a Nanodrop.

#### Drug solution preparation

##### *Safety for handling fentanyl and its analogs*

During the procedure, the experimenter wore a disposable lab coat, sleeve covers, a safety mask, and eye protection. Two observers, trained in administering Narcan and in emergency response procedures related to opioid exposure, stood by for the duration of the procedure. The powder was weighed, transferred to a container, and dissolved in an aqueous solution. The bench space was wiped down with water



and 70% ethanol solution. The plastic waste was triple-rinsed, and all waste was disposed of using standard chemical hazard procedures.

#### *Stock solution preparation*

Controlled substances were procured under a Schedule II DEA license (PI: Henry Lester) and stored in lockboxes at room temperature, 4 °C, or -20 °C, according to the manufacturer's suggested conditions. An analytical balance with 0.0001 g precision was used to weigh compounds. Stock solutions were prepared in 3x PBS pH 7.0 or sterile saline for *in vitro* and *in vivo* experiments, respectively. Drug solutions were sterile-filtered using a 0.2-  $\mu$ M syringe filter before injections in mice. Stock solutions were serially diluted and stored in deep well plates for dose-response experiments. All solutions and plates were stored at -20 °C.

#### Protein Purification and Lyophilization

##### *Protein purification*

A bacterial expression vector bearing the biosensor gene of interest was used to transform chemically competent BL21 DE3 gold cells (Agilent Technologies). Bacteria were plated on LB agar selection plates (100 mg/L ampicillin). A single colony was used to inoculate 200 mL of autoinduction media (Studier 2005) with 100 mg/L ampicillin. The culture was incubated at 30 °C while shaking at 250 rpm for 28-30 h. The resuspended cell pellet was sonicated on ice three times, 30 sec each, with 2 min recovery periods in between. The cell debris was pelleted by centrifugation. The supernatant was filtered through a 0.2  $\mu$ m filter and loaded onto an ÄKTA Start FPLC equipped with a 5 mL Ni-NTA column. The protein was eluted using a 10-200 mM imidazole gradient in 1x PBS, pH 7.4. The fractions were analyzed by SDS-PAGE gel for the expected mass and fraction purity. Pure fractions were pooled, concentrated, and buffer exchanged into 3x PBS pH 7.0 using a spin column with a 30 kDa cutoff (Amicon). Protein concentration was determined by measuring the sample's absorbance at 280 nm. Purified protein was stored at 4 °C.

##### *Lyophilization and simulated field test*

100  $\mu$ L samples of the purified fentanyl biosensor were flash-frozen in liquid nitrogen and lyophilized. The biosensor powder was stored in the dark to prevent the photobleaching of GFP. The tube containing the powder was punctured so that the samples could be exposed to room temperature and humidity. After three weeks, the powder was redissolved into 100  $\mu$ L molecular biology grade deionized water, and the concentration was verified unchanged by this process. A control sample from

the same batch of purified protein was flash-frozen and stored at  $-80\text{ }^{\circ}\text{C}$  during the same period. The lyophilized and control biosensor samples were then tested using the general dose-response method.

### General methods of dose-response measurements

#### *General Tecan plate reader method*

Plates were read using a Tecan Spark 10M with 485 nm excitation (20 nm bandwidth) and 535 nm emission (25 nm bandwidth) wavelengths in top read mode and manual gain set to “60” to measure GFP fluorescence. Samples were mixed by pipette in the plate and then inserted into the instrument, where it is shaken for 10 seconds using a double orbital pattern prior to recording from the designated wells. All dose-response experiments were carried out at room temperature.

#### *Dose-responses in PBS*

Purified biosensor protein and drug solution plates were mixed using a robotic liquid handler (epMotion, Eppendorf). 11  $\mu\text{L}$  of a drug solution from the 10x concentration stock plate was mixed into 100  $\mu\text{L}$  biosensor solution in 3x PBS pH 7.0 in triplicate for each dose. The concentrations of biosensor and drug were chosen to observe interactions surpassing the ligand depletion regime. The final [biosensor] = 100 nM in each well for experiments involving purified protein. One set of three wells was reserved for buffer control (zero [drug] to determine  $F_0$ ).

#### *Dose responses in biofluids*

Biofluids were frozen and thawed once to aliquot prior to the experiment and were not filtered, pH-adjusted, or otherwise modified, thereby maintaining their composition. A series of biosensor/drug solutions were prepared with 2x the final target concentration in a final volume of 50  $\mu\text{L}$ . These solutions were manually pipetted into a Costar flat black 96 well plate. The biofluid was pipetted and mixed thoroughly in each well to yield the final drug-spiked biofluid-biosensor solution. The fluorescence was read using the general Tecan plate reader method.

#### *Directed Evolution*

Mutant library generation by site saturation mutagenesis (SSM) Residues for site saturation mutagenesis were chosen based on previously reported crystal structures and mutagenesis data. Generally, sites in the linker region and hinge were chosen to improve dynamic range, and sites in the binding pocket and second shell were chosen to improve affinity for the target opioid. DNA libraries were constructed using the

“22-codon method,” where three sets of primers bearing ‘NDT’, ‘VHG’, and ‘TGG’ encode for 12, 9, and 1 codons, respectively, at the site of interest (Kille 2013). The 22-codon method covers all 20 amino acids with near-equal selection probability while excluding all stop codons. A PCR reaction using Phusion polymerase, an equimolar solution of each primer, and the biosensor parent plasmid as the template DNA generated the “SSM library.” The PCR product was purified and treated with a Dpn1 digest to remove all template DNA. The DNA libraries were transformed into electrochemically competent TOP10 cells and plated on LB agar ampicillin selection plates. Typically, we found ~300 colonies on a plate, ensuring sufficient sampling of the DNA library. Five colonies were selected at random to inoculate miniprep cultures (5 mL LB with ampicillin). The DNA was isolated and sequenced to verify codon randomization from the 22-codon method. The remainder colonies on the selection plate were resuspended in LB and centrifuged. The DNA was extracted using a miniprep kit to yield an amplified SSM DNA library.

#### *Bacterial lysate screening of mutant libraries*

Separate aliquots of BL21 DE3 cells were transformed with 300 ng of the SSM library and the parent biosensor plasmid and cultured on LB agar ampicillin (100 mg/L) selection plates. Autoinduction medium was prepared according to the Studier method (Studier 2005), and 800  $\mu$ L was pipetted into each well in a 96-deep well plate. 92 wells were inoculated with a colony randomly picked from the SSM library plate, three with colonies with the parent biosensor (positive control), and one with no inoculation (negative control). The plate was sealed with a 0.2  $\mu$ m breathable mesh (AeraSeal, Sigma Aldrich) and incubated while shaking at 250 rpm at 30 °C for 28 h.

After culturing, 100  $\mu$ L from each well was transferred to the corresponding wells in a 96-well Costar flat black plate and stored at -80 °C to create a replica plate. The remainder culture in deep well plate was centrifuged to yield a yellow-green pellet. The supernatant was removed, and the pellet was washed once with 1x PBS pH 7.0 to remove residual media. The pellet was then resuspended in 3x PBS pH 7.0, flash-frozen in liquid nitrogen, and thawed to lyse the cells. The plate was centrifuged again, yielding solubilized mutant biosensors in the lysate. The mutants were then screened in parallel using positive and negative screens (if applicable) against the opioid of interest and acetylcholine, respectively. The concentrations of the ligands used in the screens were their EC<sub>50</sub> in activating the parent biosensor. 100  $\mu$ L of the lysate from each well was transferred to each Costar flat black plate. The plate reader

was programmed to read GFP fluorescence, add 11  $\mu\text{L}$  of a 10x stock of the ligand to each well, shake in a double orbital pattern to mix, and then read GFP fluorescence again. These data provided the  $F_0$  and  $\Delta F$  values to determine the strength of the response in each well. The DNA of mutants that showed considerable improvement was isolated by culturing the BL21 DE3 from the replica plate, extracting the DNA using a miniprep kit, and sequencing to determine the winning residue identity.

#### *Full dose responses in lysate for winning mutants*

To compare the winning mutations from the plate screen, the top several constructs were compared in full dose responses before selecting one for further directed evolution. BL21 DE3 cells were transformed with the DNA of the winning mutants and plated on selection plates with ampicillin. A 10 mL culture with autoinduction media and ampicillin was inoculated for each winner and incubated at 30 °C while shaking (250 rpm) for 28 h. The culture was centrifuged to yield a yellow-green pellet. The pellet was resuspended in 8 mL of 3x PBS pH 7.0, flash-frozen in liquid nitrogen, and thawed to lyse the cells. The lysate was centrifuged, and the supernatant was pipetted to yield the solubilized biosensor. A serial dilution of the lysate was performed, and fluorescence was measured on the plate reader to determine the appropriate dilution that provided a baseline fluorescence of  $\sim 1/20$  of the detector's dynamic range under the given settings. Each mutant was characterized using the general dose-response method against the opioid of interest and acetylcholine (if applicable). The mutant displaying the greatest improvement was taken forward for the next iteration of site saturation mutagenesis at another set of residues.

### Biophysical Characterization

#### *Isothermal titration calorimetry*

The Affinity ITC (TA Instruments) equipped with a 190  $\mu\text{L}$  cell was used for all isothermal titration calorimetry experiments. Biosensors were purified and buffer-exchanged into 3x PBS pH 7.0. Biosensor concentrations in the range of 20-50  $\mu\text{M}$  were sufficient to produce a large enough dynamic range between the first injection and final heats. The same batch of buffer was used to dilute the protein and prepare drug solutions used in the ITC experiment. The drug solution was prepared for a final concentration ten times that of the biosensor's final concentration in the ITC cell. All solutions were degassed before the experiment. The biosensor solution was added to the cell, and the drug solution to the syringe (titrant). 2-2.5  $\mu\text{L}$  injections of the titrant were injected at 300 s intervals 20 times, spanning 0 to

2.0-2.5 mol equivalents of the opioid to the biosensor. NanoAnalyze software (TA Instruments) was used to process and fit the data. The integrated heats were fit with the “independent” plus “constant” models to account for the drug-biosensor binding interaction and the drug solvation energy, respectively. The resulting fit from this model determined enthalpy, entropy, binding affinity, and stoichiometry for each biosensor-opioid pair.

#### *Stopped-flow kinetics experimentation and data analysis*

Stopped-flow kinetics were measured using a stopped-flow fluorimeter equipped with a 490 nm excitation LED and 510 nm long-pass filter (Applied Photophysics SX20) at room temperature (22 °C). Equal volumes of 0.2  $\mu$ M biosensor and varying drug concentrations were mixed (5 replicates). The first 3 ms were not included in the final analysis and fitting to isolate mixing artifacts and instrument dead time. Data were plotted, and time courses were fitted using Kaleidagraph (version 4.4).  $k_{\text{obs}}$  were plotted as a function of [ligand], and the linear regime was fitted; the slope reporting  $k_1$  and the y-intercept reporting  $k_{-1}$ . When the time course did not fit well to a single exponential component, it was fitted to the sum of two exponentials, and the faster phase ( $k_{\text{obs}1}$ ) was treated as above to determine  $k_1$  and  $k_{-1}$ .

#### Cell Line Imaging

##### *HeLa cell tissue culture and transfection*

HeLa cells were procured from ATCC and cultured according to their suggested protocol: cultured in 10% EMEM in FBS supplemented with penicillin/streptomycin media at 5% CO<sub>2</sub> and 37 °C. Medium changes were performed when flasks reached ~80% confluence (~48 h). The cells were thawed into a flask and passaged at least twice before any experiments. For imaging experiments, 100,000 HeLa cells were plated onto each 35 mm dish with a built-in 14 mm coverslip (MatTek) and incubated for 24 h. The cells were then transfected with Lipofectamine 3000 and either 100 ng of iFentanylSnFR1.0\_ER or 500 ng of iFentanylSnFR1.0\_PM in OptiMEM. The cells were incubated in the transfection medium for 18 h and then incubated in the standard growth medium for 24 h before the imaging experiment.

##### *Imaging under fentanyl bath perfusion*

The cells were then imaged under widefield epifluorescence (40x, 1.0 NA) on an inverted microscope (IX-81, Olympus) equipped with a camera (Andor) and a gravity-fed eight-channel perfusion system (Automate Scientific). Imaging was performed in widefield epifluorescence mode and recorded at 4 Hz using Andor's

iQ3 software. A programmable perfusion controller (Automate Scientific) was used to set the sequence and duration of perfusion. The chamber has inlet and outlet tubes spaced ~3 mm apart and are shaped to provide laminar flow across the cells in between. The solution change time is ~3 s. Generally, a 1 min HBSS control followed by a 1 min washout was applied to determine any artifacts from changes in pH due to bicarbonate exchange with the environment. Each drug dose was applied for 2 min and washed out for 2 min. The GFP response to the artifactual pH transient was subtracted to provide the true response to the drug perfusion as we have previously described (Shivange 2019).

### Virus Production and Titering

#### *Virus generation and purification*

We followed the protocol reported by Challis et al. (2019) to produce the virus used in this work. All the reagents listed in the protocol were used as stated, and only the vector and gene of interest were changed to pAAV-hSyn-iFentanylSnFR2.0-cyto-WPRE. HEK293T cells were transfected with the pAAV and two other plasmids, pHelper and AAV9 capsid, to assemble the viral particles. The media was changed at one and three days after transfection. The media from the second change was saved, and the cells and media were harvested after five days and combined with the saved media. The entire suspension was centrifuged to separate intact cells from the media. A polyethylene glycol (PEG) solution was added to the media, incubated for 2 h, and centrifuged to separate viral particles into the PEG pellet. The cell pellet was resuspended in a buffer with salt active nuclease (SAN) and incubated for 1 hour. The PEG pellet was resuspended and added to the cell suspension for further SAN digestion. An OptiSeal tube was prepared with an iodixanol gradient layered with 15%, 25%, 40%, and 60% weight/weight iodixanol in DPBS. The virus was loaded into the OptiSeal tube and purified by ultracentrifugation. The tube was removed from the rotor, and the layer bearing the virus was removed by a needle and syringe puncturing the tube. The virus was buffer exchanged to remove iodixanol and equilibrate into sterile DPBS with Pluronic F68 surfactant. The virus was stored in a sterile, low protein-binding screw cap vial at 4 °C. A typical yield from 10 x 15 cm culture dishes was a purified virus sample of ~0.6 mL at a concentration of ~1.0 x 10<sup>13</sup> vg/mL.

### *Titering by qPCR*

The titer was quantified before each batch of surgical injections. Briefly, a sample of the virus was treated with DNase followed by Proteinase K to isolate only the packaged DNA. A serial dilution of the packaged DNA was mixed with a SYBR green qPCR master mix (Roche). qPCR reaction was conducted on a thermocycler (C1000 Touch, BioRad) with a real-time detection system (CFX96, BioRad) using the protocol suggested by Challis et al.: Step 1: 95 °C, 10 min Step 2: 95 °C, 15 s Step 3: 60 °C, 20 s Step 4: 60 °C, 40 s Repeat steps 2–4 40×.

### Dissociated hippocampal neuronal culturing, transduction, and imaging

24 h prior to the dissociation, MatTek dishes with a 10 mm glass coverslip coated with poly-D-lysine were further coated with poly-L-ornithine and laminin. The next day, a pregnant mouse (C57BL/6NCrl, Charles River) was euthanized at embryonic day 16, and the uterine sac was removed. Each embryo was decapitated and then dissected. Hippocampi from several embryos were pooled and digested with 15 units of papain for 15 min at 37 °C and then treated with DNase. The dissociated cells were triturated in HBSS with 5% donor equine serum and centrifuged through a layer of 4% BSA in HBSS. The cells were plated on the treated dishes at a density of 90,000 cells/dish in 130  $\mu$ L of plating medium deposited on the coverslip. After 1 h, 3 mL of complete culture medium was added to fill the dish. Medium changes were performed twice a week. Four days after plating, the neurons were transduced with virus at a multiplicity of infection of 50,000. After 2 weeks, the neurons stably expressed the biosensor, and the dishes were imaged as in the HeLa cell experiments.

### Slice Experiments

#### *Surgical procedure*

Mice aged 8-12 weeks underwent anesthesia induction with 5% isoflurane in oxygen and were maintained under anesthesia at 1-2% isoflurane. Mice were kept on a heating pad during the surgery to maintain body temperature. The mice were mounted on a small animal stereotaxic apparatus (Stoelting) equipped with ear bars. The skull was leveled to place lambda and bregma on the same z-axis. The coordinates for the VTA used in this study were AP -3.30; ML +0.40; DV -4.30. A drill bit attached to the stereotactic rig was calibrated based on lambda and bregma and then used to drill a hole through the skull. Saline was used to flush the opening. A sub-microliter injection system with a 33 g needle (World Precision Instruments) attached to a micrometer controller (World Precision Instruments) was backfilled

with oil, loaded with the virus (AAV9-hSyn-iFentanylSnFR2.0-cyto-WPRE), and then lowered into position over the course of ~7 min. 250 nL of virus ( $2.5 \times 10^9$  vg) was injected at 100 nL/min, regulated by a MicroPump 4. We waited for 5 min to allow the virus to diffuse in the tissue before removing the needle. After the surgery, mice were placed in a new cage with a heating pad underneath half of the cage and observed until they recovered from the anesthesia. Thereafter, the mice were checked daily for a routine recovery. The mice were allowed > 2 weeks of recovery before the acute slice experiments.

#### *Acute brain slicing*

We followed the method of Ting et al. 2018 “Preparation of Acute Brain Slices Using an Optimized N-Methyl-D-glutamine Protective Recovery Method,” and the manufacturer’s protocols for operating the Compressstome (Precisionary Instruments). Solutions were prepared, their osmolarity adjusted according to Ting 2018, and temperature equilibrated prior to handling the animal. Animals were anesthetized, and once non-responsive, transcardiac perfusion was performed. The animal was decapitated and then the brain was removed into cold NMDG-HEPES aCSF (in mM: NMDG, 92; HCl, 92; KCl, 2.5;  $\text{NaH}_2\text{PO}_4$ , 1.2;  $\text{NaHCO}_3$ , 30; HEPES, 20; glucose, 25; sodium ascorbate, 5; thiourea, 2; sodium pyruvate, 3;  $\text{MgSO}_4$ , 10;  $\text{CaCl}_2$ , 0.5). The brain was sectioned and mounted on a block. Molten agar was poured to submerge the brain and then rapidly cooled over ~few seconds. The brain was cut into 200  $\mu\text{m}$  coronal slices while the block was bathed in cooled NMDG-HEPES aCSF solution. Beginning with the cutting step through the end of the experiment, all solutions were bubbled with Carbogen (5%  $\text{CO}_2$ , 95%  $\text{O}_2$ ). The VTA slices were recovered in a pre-warmed NMDG-HEPES aCSF solution at 34 °C and were subjected to a stepwise  $\text{Na}^+$  reintroduction. Recovered slices were then transferred to a HEPES aCSF holding solution (in mM: NaCl, 92; KCl, 2.5;  $\text{NaH}_2\text{PO}_4$ , 1.2;  $\text{NaHCO}_3$ , 30; HEPES, 20; glucose, 25; sodium ascorbate, 5; thiourea, 2; sodium pyruvate, 3;  $\text{MgSO}_4$ , 2;  $\text{CaCl}_2$ , 2) at room temperature for at least 1 h prior to imaging. Imaging experiments were performed in recording aCSF (in mM: NaCl, 124; KCl, 2.5;  $\text{NaH}_2\text{PO}_4$ , 1.2;  $\text{NaHCO}_3$ , 24; HEPES, 5; glucose, 12.5;  $\text{MgSO}_4$ , 2;  $\text{CaCl}_2$ , 2).

#### *Imaging acute slices under bath perfusion of fentanyl*

Slices were transferred to an imaging chamber (Warner Instruments) and held in place using a harp (Warner Instruments) during bath perfusion at ~2 mL/min of aCSF bubbled with Carbogen (5%  $\text{CO}_2$ , 95%  $\text{O}_2$ ) in gravity-fed syringes. The slices



were imaged on an upright fluorescence microscope (Olympus BX50WI) equipped with a blue LED, filters, a dichroic mirror for GFP excitation/emission, and a CMOS camera (Hamamatsu ORCA-03G). First, the slice was visualized through a 4x (NA 0.10) objective to locate the VTA. Then fluorescence imaging was performed using a 40x (NA 0.80) water immersion objective and excitation from a blue LED. During the imaging experiment, the slice was bathed in aCSF, the solution was changed to 1  $\mu$ M fentanyl, the drug was washed out, and then a pulse of aCSF from another syringe was applied as a pH control. No appreciable pH artifact was observed for the acute slice. Bath exchange time was  $\sim$ 10 s. No fluorescence was observed on the slice ipsilateral to the side of the injection site. Data were accepted from a slice that maintained its position throughout the imaging experiment, requiring no corrections.

#### *in vivo* iFentanylSnFR2.0 recordings

##### *Surgical procedures for fiber photometry*

Pre-prepared optical fibers (diameter = 400  $\mu$ m, NA 0.39) fixed in cannula were purchased from ThorLabs and cut to 4.9 mm using a ruby scribe. The fibers were inspected for their light transmittance and reflectance before use in surgery. Mice aged 8-12 weeks underwent anesthesia induction at 5% isoflurane mixed with oxygen and were maintained at 1-2% isoflurane during the surgery. Mice were kept on a heating pad during the surgery to maintain body temperature. The mice were mounted on a small animal stereotaxic apparatus (Stoelting) equipped with ear bars, and their skulls were leveled to place lambda and bregma on the same z-axis. A local anesthetic was applied, and the scalp was sterilized before beginning the surgery. The VTA was targeted for viral injection as described for the acute slice experiments using the same coordinates: AP -3.30; ML +0.40; DV -4.30. Viruses encoding functional and null versions of iFentanylSnFR2.0 were injected in different groups of animals. After the viral injection, the fiber optic cannula was mounted onto an adapter attached to the stereotaxic rig, and the position of the fiber tip was calibrated with respect to lambda and bregma. The fiber was lowered into position 100  $\mu$ m above the viral injection site over the course of  $\sim$ 5 min. The fiber was then secured to the skull with dental cement (Lang Dental). After the surgery, mice were placed in a new cage with a heating pad underneath half of the cage and observed until they regained movement. Thereafter, the mice were checked daily for a routine recovery. The mice were allowed 2 weeks of recovery before behavioral studies.

### *Fiber photometry*

Bulk fluorescence signals from the VTA were measured using a fiber photometry setup as previously described (Augustine 2018). Briefly, collimated light from 490 nm and 405 nm light-emitting diodes (ThorLabs, M490F1 and M405F1) was directed via a tether to the optical cannula. The excitation light power at the end of the patch cord was measured to be  $< 75 \mu\text{W}$  for all experiments. The fluorescence output was focused onto a silicon femtowatt photoreceiver (Newport, Model 2151). A real-time processor (Tucker-Davis Technologies) performed modulation and demodulation using a MATLAB script previously reported by Augustine et al. (2018). This method was applied to all animals, including the negative control experiment using the null mutant, iFentanylSnFR2.0-436L.

### *Videography rig*

A custom light and camera fixture was constructed for consistent videography and lighting during photometry experiments. A ceiling was constructed with two LED light bars (200 lumens, 4000K color, Defiant) fixed on each side of a 1080p camera (Logitech c920). The ceiling was fixed above an open arena (12" x 6" x 8"). A white paper towel was placed beneath the arena's mesh floor, and a flat white background was placed behind two of the three transparent walls (the fourth wall is solid metal, and the other transparent wall was left unobstructed for the side view camera). A duplicate 1080p camera was positioned to capture the side view of the animal.

### *Behavioral experiments involving photometry alongside videography*

Animals at 2-4 weeks post-surgery (10-12 weeks of age) were used for photometry plus videography experiments. All animals observed were opioid-naïve prior to the experiment. Animals were acclimated to the tether and the lit arena for 30 minutes before beginning the experiment. The photometry signal was verified, and the illumination power was set during this period. Each experiment consisted of a ~30 min baseline period, IP injection, and 3.5 h post-IP. Photometry and video recording were performed throughout the experiment uninterrupted, including the time spent handling and injecting the animal.

### *Machine vision applied to behavioral video*

The recorded mouse behavior video was processed and analyzed using DeepLabCut (DLC) (Mathis et al., 2018) to extract the positions of the body parts of the animal in each frame. A separate DLC model was trained for each of the top and side views. Frames were extracted from videos using k-means clustering. The experimenter

manually labeled the key points (annotated below). In the “top view,” the key points were the nose, head, fiber, ear\_left, ear\_right, neck, mid\_1, mid\_2, mid\_3, tail\_base, and tail\_mid. Only the fiber and mid\_1 key points were used for analyses from the top view. In the “side view,” the key points were the fiber, neck, body\_mid, tail\_base, tail\_1-5, and tail\_end. The tail\_2-5 were placed as a series of bisections (i.e., tail\_2 is halfway between tail\_base and tail\_end, tail\_3 is halfway between tail\_2 and tail\_end, tail\_4 is halfway between tail\_3 and tail\_end, and tail\_5 is halfway between tail\_4 and tail\_end). A convolutional neural network, ResNet-50, was trained on the labeled frames augmented with imgaug. DLC was also used to generate movies of the input videos with the labeled points in frames where confidence exceeded ‘pcutoff’ = 0.7.

### *Histology*

Mice were euthanized with an intraperitoneal injection of 100 mg/kg of euthasol. Transcardial perfusion was performed with 1x PBS followed by 4% paraformaldehyde in 1x PBS. The brain was removed from the skull and submerged in 4% PFA for 24 hours. The fixed brain was then rinsed three times with 1x PBS and sliced into 100  $\mu$ m sections on a vibratome (Leica VT1200).

Fixed brain sections were incubated with 0.2 % Triton X-100 and 10% donkey serum in 1x PBS pH 7.4 on an orbital shaker at room temperature for 1 h. The slices were then incubated with primary anti-tyrosine hydroxylase antibody (Sigma-Aldrich AB1542) (1:200) in 10% goat serum with 0.2% Triton X-100 overnight at 4 °C with gentle shaking. The slices were washed with three rinses with 1x PBS pH 7.4 for 5 min each and then incubated with donkey anti-sheep (IgG) secondary antibody conjugated to Alexa Fluor® 568 (Abcam, ab175712) (1:500) in 10% goat serum and 0.2% Triton X-100 with gentle shaking at room temperature 6 h. Slices were then rinsed three times in 1x PBS pH 7.4 for 5 min each. Primary anti-GFP antibody (Abcam ab13970) (1:200) and secondary Goat Anti-Chicken IgY H&L Alexa Fluor® 488 (Abcam ab150169) (1:500) antibody were subsequently applied sequentially to stain the slices using the same procedure using donkey serum in place of goat serum. The stained slices were mounted onto glass microscope slides with coverslips using a mounting medium containing DAPI (Vector Laboratories),

### *Fixed slice imaging*

The fixed slices were imaged using a Zeiss LSM980 confocal microscope to verify fiber placement above the VTA. A 2.5x objective was used to visualize entire slices

and determine the slice with the deepest fiber tract to determine the position of the fiber tip. The region adjacent to the end of the fiber tract was imaged using a 20x (0.8 NA) objective and three channels in separate tracks, optimized by Zeiss Zen software: AlexaFluor488, anti-GFP: 493 nm excitation, 508-578 nm emission, GaAsP-PMT detector AlexaFluor568 settings, anti-Th: 577 nm excitation, 587-693 nm emission, GaAsP-PMT detector DAPI: 353 nm excitation, 408-506 nm emission, Multialkali-PMT

Slice anatomy was checked against (Paxinos and Franklin) to verify the correct fiber position above the VTA. The Th-positive region provided a secondary validation of correct targeting. All reported animals showed a robust expression of the biosensor in the VTA and successful fiber positioning above the VTA.

### Maze Foraging Paradigm

#### *Maze construction, lighting, and videography*

A labyrinth maze and lighting setup previously constructed and reported by Rosenberg et al. (2021) was used without modification in this work. The details of the apparatus from Rosenberg et al. are summarized here: the maze has six levels of T-junctions (each a left/right decision point) within a 24" x 24" layout. The passageways were 1.5" wide, and the floor-to-ceiling distance was 2". The floor was constructed from IR-transparent acrylic. A water port (Sanworks) was installed at the peripheral end of one path and could be activated by nose-poking to break an IR beam. The port was calibrated to provide ~30  $\mu$ L of drinking water for each nose-poke. A Bpod behavior box (Sanworks) was used to record all nose poke activity at the port and enforce a 90-second timeout period where subsequent nose pokes would not administer water. The port was also connected to an indicator IR LED that would flash for 1 second if water was administered. A video camera (c920, Logitech) was fixed below the maze to capture the animal's movements within the maze and the indicator IR LED. Several IR illuminators (arrays of 12 IR LEDs) were placed throughout the room to provide an even lighting of the maze and contrast outlining the animal's body. Three of these illuminators were placed underneath the maze, pointed at a 45-degree angle, to produce contrast between the maze floor and the animals' footpads. The maze was slotted into a fixed frame, and the IR lights were fastened to arms on this frame so that the positions of all components were maintained across all experiments. A regular home cage was connected to the entry of the maze via a tube (3 cm in diameter, 1 meter long).

### *Foraging experiments using the maze*

Wildtype C57Bl/6 (Charles River) mice were used for foraging experiments and were naïve to any manipulation or. Experiments were conducted for 10 h within the regular dark cycle of the mice. Mice were divided into two cohorts: the “intrinsic” cohort received food and water ad libitum before and during the experiment and were allowed to enter the maze with no water port. The “water-deprived” cohort was housed in a cage with the water pack removed 21 h prior to the experiment. All animals were singly housed for two days prior to the experiment. The water-deprived animals received an IP injection of either saline, 0.1 mg/kg fentanyl, or 1.0 mg/kg fentanyl and were placed in the home cage connected to the maze. The intrinsic cohort received an IP of either saline or 1.0 mg/kg fentanyl. Video of the maze was recorded continuously for 10 h. After the experiment, mice were returned to their regular home cage with food and water provided ad lib. The maze was cleaned with 70% EtOH in between animals and, once a week, was washed with a detergent.

### Computational studies of proteins

#### *Docking*

All docking experiments were performed using AutoDock Vina (Eberhardt 2021 and Trott 2010) and repeated a method we previously used to dock an opioid into the crystal structure of iNicSnFR3a (PDB: 7S7T) (Muthusamy 2022). The protein structure and ligands were prepared in AutoDockTools by removing water, adding polar hydrogens, and assigning the Gasteiger charges. The ligands were allowed torsional freedom in the docking routine. The docking figures and measurements between atoms were generated with PyMol (version 2.5.0, Schrodinger).

#### *Structure generation in AlphaFold2 and alignment*

The structures of the periplasmic binding protein portion of iFentanylSnFR2.0 was generated using AlphaFold2 executed through ColabFold (Merdita 2022; Jumper 2021). The predicted structure of iFentanylSnFR2.0's PBP and the crystal structure of iNicSnFR3a's PBP (PDB: 7S7W) were aligned in ChimeraX using the Needleman-Wunsch sequence alignment algorithm, and the BLOSUM95 substitution matrix was used to determine the RMSD between the two structures.

## Quantification and Statistical Analysis

### *Dose response analysis for plate reader experiments*

The biosensor's response was expressed as  $\Delta F/F_0$  and was calculated for each application of [ligand] where  $\Delta F/F_0 = (F_{\text{drug+biosensor}} - F_{\text{biosensor}})/F_{\text{biosensor}}$  and each fluorescence readout (each 'F') was averaged across three replicates at a given [ligand]. The error is shown as the standard error of the mean where  $n = 3$ . The resulting  $\Delta F/F_0$  vs. [ligand] set was fit using the Hill equation in Origin 9.2 (OriginLabs). Where the biosensor demonstrated a linear dose-response (i.e., [ligand]  $\ll EC_{50}$ ), the data were fit with a linear regression with no y-axis restriction. This slope determined by the linear fit is termed the "S-Slope" and is expressed in the units of inverse concentration.

### *Principal component analyses (PCA)*

This work performed two distinct PCAs. In both cases, the vectors were normalized before the PCA step using the "StandardScaler" function from scikit-learn's "preprocessing" package, and the PCA function was called from scikit-learn's "decomposition" package. Figure 1H used RDKit to perform chemoinformatics and utilized PCA to display the groupings of chemical structures. The opioids used in this work were converted to their Morgan fingerprint vectors using RDKit's built-in functions. The groupings were drawn by the experimenter based on conventional opioid pharmacological classes, and the PCA results faithfully recapitulated the various classes shown in Figure 1H. In Figure 2A, PCA was performed on the S-Slope heatmap result from Figure 1G to identify outliers in their binding mode against the cholinergic biosensor library.

### *Dose responses live cell experiments*

This method applies to all live cell imaging time series data (culture and acute slice). Cells resolved in the focal plane along with a reference blank space were traced using the region of interest (ROI) tool in ImageJ. The "Time Series Analyzer" plugin determined the average pixel intensity in each ROI. These time series data were analyzed in Origin 9.1 (OriginLabs): the background ROI value was subtracted from each cell ROI to give F. A baseline was drawn from the initial and final periods, providing  $F_0$ . The difference in the response and the baseline gave  $\Delta F$  and  $\Delta F/F_0$  was plotted vs time. The steady-state response was determined by taking the average of final 40 frames (10 s) for each drug dose application. These steady-state responses were fit with either a linear regression or Hill fit.

### *Fiber photometry*

$\Delta F/F$  was calculated using a MATLAB code described by the Deisseroth lab (Lerner et al. 2015). The data for the 405 nm and 490 nm channels were processed by applying a 1.8 Hz low-pass filter and scaling the 405 nm signal to the 490 nm signal using a linear function.  $\Delta F/F$  was calculated as (raw 490 nm signal - fitted 405 nm signal) / (fitted 405 nm signal). The fluorescence data were subjected to a 1 min FFT filter for the plots.

### *Open arena machine vision outputs*

A custom Python script was written to analyze the outputs from the analysis of the open arena videos processed by DeepLabCut. The script largely uses the `scipy` and `statsmodels` libraries for signal processing and statistical analyses and `matplotlib` for plotting. Each animal has three data inputs in this notebook: “top view” DLC output .csv, “side view” DLC output .csv, and the processed photometry signal .csv. First, these files are read in for each animal. Two additional inputs are read: a master spreadsheet listing timings for LED on/off and IP events for each animal and an image of the top view video to set reference coordinates. The LED on and off times set a global time reference when plotting photometry against behavior video results. Only frames where the labels of interest had a confidence score of  $> 0.6$  were used for analysis. The “top view” outputs were used for all behavioral analyses except for the “Straub tail” angle measure, which is the only metric that uses the “side view” outputs. The velocity (Fig 5C) and total distance traveled (Fig 6.6 A) were calculated from the displacement of the “mid\_1” body part in the “top view.” The velocity was calculated for a rolling window of 100 frames (3.3 s). The resulting trace was Gaussian smoothed with  $\sigma = 1800$  frames (60 s) for the plot in Fig 5C.

The circling (Fig 6.6 B) and nose-in-corner (Fig 6.6 C) metrics used the cage corners and midpoints in between the corners as landmarks. A circling bout was defined as the mid\_1 body part passing within XXX cm from each reference point in sequence (i.e., tracing the cage’s perimeter) within 30 s. A nose-in-corner bout was defined as the fiber label held within a threshold of 3 cm from a cage corner point for greater than 3 sec. Fig 6C and 6B plot histograms of the fraction of time spent in circling bouts and nose-in-corner bouts, respectively, for each 5 min bin.

The “Straub tail” was operationalized as the angle between the tail and the body. The body vector was defined as the vector from the “tail\_base” label to the fiber label, and the tail vector was defined as the vector from the “tail\_base” to “tail\_4.”

The tail angle was set to NaN for frames where the tail was hidden, or labels did not have sufficient confidence. The resulting trace was Gaussian smoothed with  $\sigma = 1000$  frames (333.3 s) for the plot in Fig 5C.

### *Maze foraging behavior*

The analysis of the maze experiments replicated those previously reported by Rosenberg et al. 2021. Briefly, the raw video was analyzed in grayscale to determine the animal's trajectory (key points: nose, feet, tail base, and mid-body). This analysis provided the x-y coordinates vs. time used in the previously reported notebooks (<https://github.com/markusmeister/Rosenberg-2021-Repository>). This work had up to three experimental groups, so, where appropriate, the code for the plots were adapted to include a third group.

### Methods References:

Augustine, Vineet, Sertan Kutal Gokce, Sangjun Lee, Bo Wang, Thomas J. Davidson, Frank Reimann, Fiona Gribble, Karl Deisseroth, Carlos Lois, and Yuki Oka. "Hierarchical neural architecture underlying thirst regulation." *Nature* 555, no. 7695 (2018): 204-209.

Jumper, John, Richard Evans, Alexander Pritzel, Tim Green, Michael Figurnov, Olaf Ronneberger, Kathryn Tunyasuvunakool et al. "Highly accurate protein structure prediction with AlphaFold." *Nature* 596, no. 7873 (2021): 583-589.

Challis, Rosemary C., Sripriya Ravindra Kumar, Ken Y. Chan, Collin Challis, Keith Beadle, Min J. Jang, Hyun Min Kim et al. "Systemic AAV vectors for widespread and targeted gene delivery in rodents." *Nature protocols* 14, no. 2 (2019): 379-414.

Eberhardt, J., Santos-Martins, D., Tillack, A.F., Forli, S. (2021). AutoDock Vina 1.2.0: New Docking Methods, Expanded Force Field, and Python Bindings. *Journal of Chemical Information and Modeling*.

Paxinos, George, and Keith BJ Franklin. *Paxinos and Franklin's the mouse brain in stereotaxic coordinates*. Academic press, 2019.

Kille, Sabrina, Carlos G. Acevedo-Rocha, Loreto P. Parra, Zhi-Gang Zhang, Diederik J. Opperman, Manfred T. Reetz, and Juan Pablo Acevedo. "Reducing codon redundancy and screening effort of combinatorial protein libraries created by saturation mutagenesis." *ACS synthetic biology* 2, no. 2 (2013): 83-92.

Mirdita, Milot, Konstantin Schütze, Yoshitaka Moriwaki, Lim Heo, Sergey Ovchinnikov, and Martin Steinegger. "ColabFold: making protein folding accessible to



all." *Nature methods* 19, no. 6 (2022): 679-682.

Muthusamy, Anand K., Charlene H. Kim, Scott C. Virgil, Hailey J. Knox, Jonathan S. Marvin, Aaron L. Nichols, Bruce N. Cohen, Dennis A. Dougherty, Loren L. Looger, and Henry A. Lester. "Three mutations convert the selectivity of a protein sensor from nicotinic agonists to S-methadone for use in cells, organelles, and biofluids." *Journal of the American Chemical Society* 144, no. 19 (2022): 8480-8486.

Trott, O., & Olson, A. J. (2010). AutoDock Vina: improving the speed and accuracy of docking with a new scoring function, efficient optimization, and multithreading. *Journal of computational chemistry*, 31(2), 455-461.

Rosenberg, Matthew, Tony Zhang, Pietro Perona, and Markus Meister. "Mice in a labyrinth show rapid learning, sudden insight, and efficient exploration." *Elife* 10 (2021): e66175.

Schindelin, J., Arganda-Carreras, I., Frise, E., Kaynig, V., Longair, M., Pietzsch, T., . . . Cardona, A. (2012). Fiji: an open-source platform for biological-image analysis. *Nature Methods*, 9(7), 676–682. doi:10.1038/nmeth.2019

Ting, Jonathan T., Brian R. Lee, Peter Chong, Gilberto Soler-Llavina, Charles Cobbs, Christof Koch, Hongkui Zeng, and Ed Lein. "Preparation of acute brain slices using an optimized N-methyl-D-glucamine protective recovery method." *JoVE (Journal of Visualized Experiments)* 132 (2018): e53825.

## 6.9 References

Armenian, P., Vo, K. T., Barr-Walker, J., & Lynch, K. L. (2018). Fentanyl, fentanyl analogs and novel synthetic opioids: A comprehensive review. *Neuropharmacology*, 134, 121–132. <https://doi.org/10.1016/j.neuropharm.2017.10.016>

Arnold, F. H. (2018). Directed evolution: Bringing new chemistry to life. *Angewandte Chemie International Edition*, 57(16), 4143–4148. <https://doi.org/10.1002/anie.201708408>

Asinof, S. K., & Paine, T. A. (2014). The 5-choice serial reaction time task: A task of attention and impulse control for rodents. *Journal of Visualized Experiments*, (90), 51574. <https://doi.org/10.3791/51574>

Atlas, L. Y., Wielgosz, J., Whittington, R. A., & Wager, T. D. (2014). Specifying the non-specific factors underlying opioid analgesia: Expectancy, attention, and affect. *Psychopharmacology*, 231(5), 813–823. <https://doi.org/10.1007/s00213-013-3296-1>

- Beatty, Z., Muthusamy, A., Unger, E., Dougherty, D., Tian, L., Looger, L., Shivange, A., Bera, K., Lester, H., & Nichols, A. (2022). Fluorescence screens for identifying central nervous system-acting drug-biosensor pairs for subcellular and supracellular pharmacokinetics. *BIO-PROTOCOL*, *12*(22). <https://doi.org/10.21769/BioProtoc.4551>
- Beck, T. C., Hapstack, M. A., Beck, K. R., & Dix, T. A. (2019). Therapeutic potential of kappa opioid agonists. *Pharmaceuticals*, *12*(2), 95. <https://doi.org/10.3390/ph12020095>
- Belin, D., Belin-Rauscent, A., Everitt, B. J., & Dalley, J. W. (2016). In search of predictive endophenotypes in addiction: Insights from preclinical research: Vulnerability traits in addiction. *Genes, Brain and Behavior*, *15*(1), 74–88. <https://doi.org/10.1111/gbb.12265>
- Bick, M. J., Greisen, P. J., Morey, K. J., Antunes, M. S., La, D., Sankaran, B., Reymond, L., Johnsson, K., Medford, J. I., & Baker, D. (2017). Computational design of environmental sensors for the potent opioid fentanyl. *eLife*, *6*, e28909. <https://doi.org/10.7554/eLife.28909>
- Borden, P. M., Zhang, P., Shivange, A. V., Marvin, J. S., Cichon, J., Dan, C., Podgorski, K., Figueiredo, A., Novak, O., Tanimoto, M., Shigetomi, E., Lobas, M. A., Kim, H., Zhu, P. K., Zhang, Y., Zheng, W. S., Fan, C., Wang, G., Xiang, B., . . . Looger, L. L. (2020). A fast genetically encoded fluorescent sensor for faithful in vivo acetylcholine detection in mice, fish, worms and flies. *BioRxiv*. <https://doi.org/10.1101/2020.02.07.939504>
- Brownstein, M. J. (1993). A brief history of opiates, opioid peptides, and opioid receptors. *Proceedings of the National Academy of Sciences*, *90*(12), 5391–5393. <https://doi.org/10.1073/pnas.90.12.5391>
- Cahill, C. M. (2020). Opioid dose regimen shapes mesolimbic adaptations. *Neuropsychopharmacology*, *45*(11), 1777–1778. <https://doi.org/10.1038/s41386-020-0679-y>
- Campuzano, S., Pedrero, M., Gamella, M., Serafín, V., Yáñez-Sedeño, P., & Pingarón, J. M. (2020). Beyond sensitive and selective electrochemical biosensors: Towards continuous, real-time, antibiofouling, and calibration-free devices. *Sensors*, *20*(12), 3376. <https://doi.org/10.3390/s20123376>
- Chamoun, K., Chevillard, L., Hajj, A., Callebert, J., & Mégarbane, B. (2023). Mechanisms of neurorespiratory toxicity induced by fentanyl analogs—lessons from animal studies. *Pharmaceuticals*, *16*(3), 382. <https://doi.org/10.3390/ph16030382>
- Chang, H.-Y., Kharrazi, H., Bodycombe, D., Weiner, J. P., & Alexander, G. C. (2018). Healthcare costs and utilization associated with high-risk prescription opioid use: A retrospective cohort study. *BMC Medicine*, *16*(1), 69. <https://doi.org/10.1186/s12916-018-1058-y>

- Cicero, T. J., Ellis, M. S., Surratt, H. L., & Kurtz, S. P. (2014). The changing face of heroin use in the united states: A retrospective analysis of the past 50 years. *Journal of the American Medical Association Psychiatry*, *71*(7), 821. <https://doi.org/10.1001/jamapsychiatry.2014.366>
- Committee on Pain Management and Regulatory Strategies to Address Prescription Opioid Abuse, Board on Health Sciences Policy, Health and Medicine Division, & National Academies of Sciences, Engineering, and Medicine. (2017, September 28). *Pain management and the opioid epidemic: Balancing societal and individual benefits and risks of prescription opioid use* (R. J. Bonnie, M. A. Ford, & J. K. Phillips, Eds.) [Pages: 24781]. National Academies Press. <https://doi.org/10.17226/24781>
- Cooper, S., Robison, A. J., & Mazei-Robison, M. S. (2017). Reward circuitry in addiction. *Neurotherapeutics*, *14*(3), 687–697. <https://doi.org/10.1007/s13311-017-0525-z>
- Dong, C., Zheng, Y., Long-Iyer, K., Wright, E. C., Li, Y., & Tian, L. (2022). Fluorescence imaging of neural activity, neurochemical dynamics, and drug-specific receptor conformation with genetically encoded sensors. *Annual Review of Neuroscience*, *45*(1), 273–294. <https://doi.org/10.1146/annurev-neuro-110520-031137>
- Farida B. Ahmad, Lauren M. Rossen, & Paul Sutton. (2023, September 3). Provisional drug overdose death counts. Retrieved September 13, 2023, from <https://www.cdc.gov/nchs/nvss/vsrr/drug-overdose-data.htm>
- Friedman, A., & Nabong, L. (2020). Opioids. *Physical Medicine and Rehabilitation Clinics of North America*, *31*(2), 289–303. <https://doi.org/10.1016/j.pmr.2020.01.007>
- Glasheen, C., Batts, K., Karg, R., & Hunter, D. (n.d.). Impact of the DSM-IV to DSM-5 changes on the national survey on drug use and health.
- Haloi, N., Huang, S., Nichols, A. L., Fine, E. J., Friesenhahn, N. J., Marotta, C. B., Dougherty, D. A., Lindahl, E., Howard, R. J., Mayo, S. L., et al. (2024). Interactive computational and experimental approaches improve the sensitivity of periplasmic binding protein-based nicotine biosensors for measurements in biofluids. *Protein Engineering, Design and Selection*, *37*.
- Iversen, L. L., Iversen, S. D., & Snyder, S. H. (Eds.). (1977). *Handbook of psychopharmacology*. Springer US. <https://doi.org/10.1007/978-1-4613-4214-4>
- Joseph, J. I. (2021). Review of the long-term implantable senseonics continuous glucose monitoring system and other continuous glucose monitoring systems. *Journal of Diabetes Science and Technology*, *15*(1), 167–173. <https://doi.org/10.1177/1932296820911919>

- Jullié, D., Gondin, A. B., Von Zastrow, M., & Canals, M. (2020). Opioid pharmacology under the microscope. *Molecular Pharmacology*, *98*(4), 425–432. <https://doi.org/10.1124/mol.119.119321>
- Kalvass, J. C., Olson, E. R., Cassidy, M. P., Selley, D. E., & Pollack, G. M. (2007). Pharmacokinetics and pharmacodynamics of seven opioids in p-glycoprotein-competent mice: Assessment of unbound brain EC<sub>50,u</sub> and correlation of in vitro, preclinical, and clinical data. *Journal of Pharmacology and Experimental Therapeutics*, *323*(1), 346–355. <https://doi.org/10.1124/jpet.107.119560>
- Kimmey, B. A., McCall, N. M., Wooldridge, L. M., Satterthwaite, T. D., & Corder, G. (2022). Engaging endogenous opioid circuits in pain affective processes. *Journal of Neuroscience Research*, *100*(1), 66–98. <https://doi.org/10.1002/jnr.24762>
- Langford, R. M., Knaggs, R., Farquhar-Smith, P., & Dickenson, A. H. (2016). Is tapentadol different from classical opioids? a review of the evidence. *British Journal of Pain*, *10*(4), 217–221. <https://doi.org/10.1177/2049463716657363>
- Lankenau, S. E., Teti, M., Silva, K., Bloom, J. J., Harocopos, A., & Treese, M. (2012). Initiation into prescription opioid misuse amongst young injection drug users. *International Journal of Drug Policy*, *23*(1), 37–44. <https://doi.org/10.1016/j.drugpo.2011.05.014>
- Le Merrer, J., Becker, J. A. J., Befort, K., & Kieffer, B. L. (2009). Reward processing by the opioid system in the brain. *Physiological Reviews*, *89*(4), 1379–1412. <https://doi.org/10.1152/physrev.00005.2009>
- Lefevre, E. M., Pisansky, M. T., Toddes, C., Baruffaldi, F., Pravetoni, M., Tian, L., Kono, T. J. Y., & Rothwell, P. E. (2020). Interruption of continuous opioid exposure exacerbates drug-evoked adaptations in the mesolimbic dopamine system. *Neuropsychopharmacology*, *45*(11), 1781–1792. <https://doi.org/10.1038/s41386-020-0643-x>
- Liu, G. (2021). Grand challenges in biosensors and biomolecular electronics. *Frontiers in Bioengineering and Biotechnology*, *9*, 707615. <https://doi.org/10.3389/fbioe.2021.707615>
- Lobingier, B. T., & Von Zastrow, M. (2019). When trafficking and signaling mix: How subcellular location shapes g protein-coupled receptor activation of heterotrimeric g proteins. *Traffic*, *20*(2), 130–136. <https://doi.org/10.1111/tra.12634>
- Lutfy, K., & Cowan, A. (2004). Buprenorphine: A unique drug with complex pharmacology. *Current Neuropharmacology*, *2*(4), 395–402. <https://doi.org/10.2174/1570159043359477>

- Marvin, J. S., Borghuis, B. G., Tian, L., Cichon, J., Harnett, M. T., Akerboom, J., Gordus, A., Renninger, S. L., Chen, T.-W., Bargmann, C. I., Orger, M. B., Schreiter, E. R., Demb, J. B., Gan, W.-B., Hires, S. A., & Looger, L. L. (2013). An optimized fluorescent probe for visualizing glutamate neurotransmission. *Nature Methods*, *10*(2), 162–170. <https://doi.org/10.1038/nmeth.2333>
- Montandon, G., & Slutsky, A. S. (2019). Solving the opioid crisis. *Chest*, *156*(4), 653–658. <https://doi.org/10.1016/j.chest.2019.05.015>
- Moulin, D. E., Ling, G. S., & Pasternak, G. W. (1988). Unidirectional analgesic cross-tolerance between morphine and levorphanol in the rat. *Pain*, *33*(2), 233–239. [https://doi.org/10.1016/0304-3959\(88\)90095-4](https://doi.org/10.1016/0304-3959(88)90095-4)
- Muntean, B. S., Dao, M. T., & Martemyanov, K. A. (2019). Allostatic changes in the cAMP system drive opioid-induced adaptation in striatal dopamine signaling. *Cell Reports*, *29*(4), 946–960.e2. <https://doi.org/10.1016/j.celrep.2019.09.034>
- Muthusamy, A. K., Kim, C. H., Virgil, S. C., Knox, H. J., Marvin, J. S., Nichols, A. L., Cohen, B. N., Dougherty, D. A., Looger, L. L., & Lester, H. A. (2022). Three mutations convert the selectivity of a protein sensor from nicotinic agonists to S-methadone for use in cells, organelles, and biofluids. *Journal of the American Chemical Society*, *144*(19), 8480–8486. <https://doi.org/10.1021/jacs.2c02323>
- Nichols, A. L., Blumenfeld, Z., Fan, C., Luebbert, L., Blom, A. E. M., Cohen, B. N., Marvin, J. S., Borden, P. M., Kim, C. H., Muthusamy, A. K., Shivange, A. V., Knox, H. J., Campello, H. R., Wang, J. H., Dougherty, D. A., Looger, L. L., Gallagher, T., Rees, D. C., & Lester, H. A. (2021, October 4). *Fluorescence activation mechanism and imaging of drug permeation with new sensors for smoking-cessation ligands* (preprint). *Pharmacology and Toxicology*. <https://doi.org/10.1101/2021.10.04.463082>
- O'Donnell, J. K., Halpin, J., Mattson, C. L., Goldberger, B. A., & Gladden, R. M. (2017). Deaths involving fentanyl, fentanyl analogs, and u-47700 — 10 states, july–december 2016. *MMWR. Morbidity and Mortality Weekly Report*, *66*(43), 1197–1202. <https://doi.org/10.15585/mmwr.mm6643e1>
- Owens, R. L. (2020). Still just the tip of the iceberg. *Journal of Clinical Sleep Medicine*, *16*, 9–10. <https://doi.org/10.5664/jcsm.8876>
- Patriarchi, T., Cho, J. R., Merten, K., Howe, M. W., Marley, A., Xiong, W.-H., Folk, R. W., Broussard, G. J., Liang, R., Jang, M. J., Zhong, H., Dombeck, D., Von Zastrow, M., Nimmerjahn, A., Gradinaru, V., Williams, J. T., & Tian, L. (2018). Ultrafast neuronal imaging of dopamine dynamics with designed genetically encoded sensors. *Science*, *360*(6396), eaat4422. <https://doi.org/10.1126/science.aat4422>

- Pergolizzi, J. V., Webster, L. R., Vortsman, E., Ann LeQuang, J., & Raffa, R. B. (2021). Wooden chest syndrome: The atypical pharmacology of fentanyl overdose. *Journal of Clinical Pharmacy and Therapeutics*, 46(6), 1505–1508. <https://doi.org/10.1111/jcpt.13484>
- Pradip K. Muhuri, Joseph C. Gfroerer, & M. Christine Davies. (2013). Associations of nonmedical pain reliever use and initiation of heroin use in the united states. *CBHSQ Data Review*. <https://www.samhsa.gov/data/sites/default/files/DR006/DR006/nonmedical-pain-reliever-use-2013.htm>
- Prommer, E. (2007). Levorphanol: The forgotten opioid. *Supportive Care in Cancer*, 15(3), 259–264. <https://doi.org/10.1007/s00520-006-0146-2>
- Radoux-Mergault, A., Oberhauser, L., Aureli, S., Gervasio, F. L., & Stoeber, M. (2022, December 12). *Subcellular location defines GPCR signal transduction* (preprint). *Cell Biology*. <https://doi.org/10.1101/2022.12.12.520050>
- Rosalyn Chen, O.J. Michael Coppes, & Richard D. Urman. (2021). Receptor and molecular targets for the development of novel opioid and non-opioid analgesic therapies. *Pain Physician*, 153–163. <https://doi.org/10.36076/ppj.2021.24.153-163>
- Rosenberg, M., Zhang, T., Perona, P., & Meister, M. (2021). Mice in a labyrinth show rapid learning, sudden insight, and efficient exploration. *eLife*, 10, e66175. <https://doi.org/10.7554/eLife.66175>
- Saiz-Rodríguez, M., Ochoa, D., Herrador, C., Belmonte, C., Román, M., Alday, E., Koller, D., Zubiaur, P., Mejía, G., Hernández-Martínez, M., & Abad-Santos, F. (2019). Polymorphisms associated with fentanyl pharmacokinetics, pharmacodynamics and adverse effects. *Basic & Clinical Pharmacology & Toxicology*, 124(3), 321–329. <https://doi.org/10.1111/bcpt.13141>
- Saulo C. Riberio, Susan E. Kennedy, Yolanda R. Smith, Christian S. Stohler, & Jon-Kar Zubieta. (2005). Interface of physical and emotional stress regulation through the endogenous opioid system and  $\mu$ -opioid receptors. *Progress in Neuro-Psychopharmacology and Biological Psychiatry*, 29(8), 1264–1280.
- Schröder, W., Tzschentke, T. M., Terlinden, R., De Vry, J., Jahnel, U., Christoph, T., & Tallarida, R. J. (2011). Synergistic interaction between the two mechanisms of action of tapentadol in analgesia. *Journal of Pharmacology and Experimental Therapeutics*, 337(1), 312–320. <https://doi.org/10.1124/jpet.110.175042>
- Shivange, A. V., Borden, P. M., Muthusamy, A. K., Nichols, A. L., Bera, K., Bao, H., Bishara, I., Jeon, J., Mulcahy, M. J., Cohen, B., O’Riordan, S. L., Kim, C., Dougherty, D. A., Chapman, E. R., Marvin, J. S., Looger, L. L., & Lester, H. A. (2019). Determining the pharmacokinetics of nicotinic drugs in the endoplasmic reticulum using biosensors. *Journal of General Physiology*, 151(6), 738–757. <https://doi.org/10.1085/jgp.201812201>

- Singh, D., Nag, K., Shetti, A., & Krishnaveni, N. (2013). Tapentadol hydrochloride: A novel analgesic. *Saudi Journal of Anaesthesia*, 7(3), 322. <https://doi.org/10.4103/1658-354X.115319>
- Singh, S., Sarroza, D., English, A., McGrory, M., Dong, A., Zweifel, L., Land, B. B., Li, Y., Bruchas, M. R., & Stella, N. (2023, March 6). *Pharmacological characterization of the endocannabinoid sensor GRAB<sub>eCB2.0</sub>* (preprint). *Pharmacology and Toxicology*. <https://doi.org/10.1101/2023.03.03.531053>
- Srinivas, N., Maffuid, K., & Kashuba, A. D. M. (2018). Clinical pharmacokinetics and pharmacodynamics of drugs in the central nervous system. *Clinical Pharmacokinetics*, 57(9), 1059–1074. <https://doi.org/10.1007/s40262-018-0632-y>
- Steidl, S., Wasserman, D. I., Blaha, C. D., & Yeomans, J. S. (2017). Opioid-induced rewards, locomotion, and dopamine activation: A proposed model for control by mesopontine and rostromedial tegmental neurons. *Neuroscience & Biobehavioral Reviews*, 83, 72–82. <https://doi.org/10.1016/j.neubiorev.2017.09.022>
- Stoeber, M., Jullié, D., Lobingier, B. T., Laeremans, T., Steyaert, J., Schiller, P. W., Manglik, A., & von Zastrow, M. (2018). A genetically encoded biosensor reveals location bias of opioid drug action. *Neuron*, 98(5), 963–976.e5. <https://doi.org/10.1016/j.neuron.2018.04.021>
- Sun, F., Zhou, J., Dai, B., Qian, T., Zeng, J., Li, X., Zhuo, Y., Zhang, Y., Wang, Y., Qian, C., Tan, K., Feng, J., Dong, H., Lin, D., Cui, G., & Li, Y. (2020). Next-generation GRAB sensors for monitoring dopaminergic activity in vivo. *Nature Methods*, 17(11), 1156–1166. <https://doi.org/10.1038/s41592-020-00981-9>
- Tian, L., Dong, C., Gowrishankar, R., Jin, Y., He, X., Gupta, A., Wang, H., Atasoy, N., Flores-Garcia, R., Mahe, K., Liang, R., Or, G., Lo, D., Sun, Q., Whistler, J., Li, B., Gomes, I., Tejeda, H., Atasoy, D., . . . Banghart, M. (2023, May 30). *Unlocking opioid neuropeptide dynamics with genetically-encoded biosensors* (preprint). In Review. <https://doi.org/10.21203/rs.3.rs-2871083/v1>
- Tian, L., Hires, S. A., Mao, T., Huber, D., Chiappe, M. E., Chalasani, S. H., Petreanu, L., Akerboom, J., McKinney, S. A., Schreiter, E. R., Bargmann, C. I., Jayaraman, V., Svoboda, K., & Looger, L. L. (2009). Imaging neural activity in worms, flies and mice with improved GCaMP calcium indicators. *Nature Methods*, 6(12), 875–881. <https://doi.org/10.1038/nmeth.1398>
- Tzschentke, T. M. (1998). Measuring reward with the conditioned place preference paradigm: A comprehensive review of drug effects, recent progress and new issues. *Progress in Neurobiology*, 56(6), 613–672. [https://doi.org/10.1016/S0301-0082\(98\)00060-4](https://doi.org/10.1016/S0301-0082(98)00060-4)

- van Tilborg, D., Alenicheva, A., & Grisoni, F. (2022). Exposing the limitations of molecular machine learning with activity cliffs. *Journal of Chemical Information and Modeling*, *62*(23), 5938–5951. <https://doi.org/10.1021/acs.jcim.2c01073>
- Varshneya, N. B., Walentiny, D. M., Moisa, L. T., Walker, T. D., Akinfiresoye, L. R., & Beardsley, P. M. (2021). Fentanyl-related substances elicit antinociception and hyperlocomotion in mice via opioid receptors. *Pharmacology Biochemistry and Behavior*, *208*, 173242. <https://doi.org/10.1016/j.pbb.2021.173242>
- Wang, M., Yang, Y., Min, J., Song, Y., Tu, J., Mukasa, D., Ye, C., Xu, C., Heflin, N., McCune, J. S., Hsiai, T. K., Li, Z., & Gao, W. (2022). A wearable electrochemical biosensor for the monitoring of metabolites and nutrients. *Nature Biomedical Engineering*, *6*(11), 1225–1235. <https://doi.org/10.1038/s41551-022-00916-z>
- Williams, J. T., Ingram, S. L., Henderson, G., Chavkin, C., Von Zastrow, M., Schulz, S., Koch, T., Evans, C. J., & Christie, M. J. (2013). Regulation of  $\mu$ -opioid receptors: Desensitization, phosphorylation, internalization, and tolerance (A. C. Dolphin, Ed.). *Pharmacological Reviews*, *65*(1), 223–254. <https://doi.org/10.1124/pr.112.005942>
- Wu, Z., Cui, Y., Wang, H., Wu, H., Wan, Y., Li, B., Wang, L., Pan, S., Peng, W., Dong, A., Yuan, Z., Jing, M., Xu, M., Luo, M., & Li, Y. (2023). Neuronal activity-induced, equilibrative nucleoside transporter-dependent, somatodendritic adenosine release revealed by a GRAB sensor. *Proceedings of the National Academy of Sciences*, *120*(14), e2212387120. <https://doi.org/10.1073/pnas.2212387120>
- Zernia, S., Van Der Heide, N. J., Galenkamp, N. S., Gouridis, G., & Maglia, G. (2020). Current blockades of proteins inside nanopores for real-time metabolome analysis. *ACS Nano*, *14*(2), 2296–2307. <https://doi.org/10.1021/acsnano.9b09434>
- Zhang, Y., Rózsa, M., Liang, Y., Bushey, D., Wei, Z., Zheng, J., Reep, D., Broussard, G. J., Tsang, A., Tsegaye, G., Narayan, S., Obara, C. J., Lim, J.-X., Patel, R., Zhang, R., Ahrens, M. B., Turner, G. C., Wang, S. S.-H., Korff, W. L., . . . Looger, L. L. (2023). Fast and sensitive GCaMP calcium indicators for imaging neural populations. *Nature*, *615*(7954), 884–891. <https://doi.org/10.1038/s41586-023-05828-9>



*Appendix A*

## BIOSENSOR AMINO ACID SEQUENCES

Sequence ID 001: iFentanylSnFR1.0

10	20	30	40	50	60
ANDTVVVGSA	NFTEGIIVAN	MVAEMIEAHT	DLKVVRKLN	GGENVNFEAI	KRGGANNGID
70	80	90	100	110	120
IYVEYTGHL	VDILGFPEPN	VYITADKQKN	GIKANFKIRH	NVEDGSVQLA	DHYQQNTPIG
130	140	150	160	170	180
DGPVLLPDNH	YLSTQSVLSK	DPNEKRDHMV	LLEFVTAAGI	TLGMDELYKG	GTGGSMSKGE
190	200	210	220	230	240
ELFTGVVPIL	VELDGDVNGH	KFSVRGEGEG	DATNGKLT	FICTTGKLPV	PWPTLVTTLT
250	260	270	280	290	300
YGVQCFSRYP	DHMKQHDFFK	SAMPEGYVQE	RTISFKDDGT	YKTRAEVKFE	GDTLVNRIEL
310	320	330	340	350	360
KGIDFKEDGN	ILGHKLEYNF	PPPPSTDPEG	AYETVKKEYK	RKWNIVWLKP	LGFNNTGTLT
370	380	390	400	410	420
VKDELAKQYN	LKTFSDLAKI	SDKLILGATM	FFLEAPDGYP	GLQKLYNFKF	KHTKSMDMGI
430	440	450	460	470	480
RYTAIDNNEV	QVIDAWATDG	LLVSHKLIKIL	EDDKAFFPPY	YAAPIIRQDV	LDKHPELKDV
490	500	510	520		
LNKLANQISL	EEMQKLNKLV	DGEGQDPAKV	AKEFLKEKGL	I	

Sequence ID 002: iFentanylSnFR2.0

10	20	30	40	50	60
ANDTVVVGSA	NFTEGIIIVAN	MVAEMIEAHT	DLKVVRKLN	GGGNVNF EAI	KRGGANNGID
70	80	90	100	110	120
IYVEYTG HGL	VDILGFPEPN	VYITADKQKN	GIKANFKIRH	NVEDGSVQLA	DHYQQNTPIG
130	140	150	160	170	180
DGPVLLPDNH	YLSTQSVLSK	DPNEKRDH MV	LLEFVTAAGI	TLGMDELYKG	GTGGSMSKGE
190	200	210	220	230	240
ELFTGVVPIL	VELDGDVNGH	KFSVRGEGEG	DATNGKLT LK	FICTTGKLPV	PWPTLVTTLT
250	260	270	280	290	300
YGVQCFSRYP	DHMKQHDFFK	SAMPEGYVQE	RTISFKDDGT	YKTRAEVKFE	GDTLVNRIEL
310	320	330	340	350	360
KGIDFKEDGN	ILGHKLEYNF	PPPISTDPEG	AYETVKKEYK	RKWNIVWLKP	LGFNNTGTLT
370	380	390	400	410	420
VKDELAKQYN	LKTFSDLAKI	SDKLILGATM	FFLEAPDGY P	GLQKLYNFKF	KHTKSMDMGI
430	440	450	460	470	480
RYTAIDNNEV	QVIDAWATDG	LLVSHK LKIL	EDDKAFFPPY	YAAPIIRQDV	LDKHPELKD V
490	500	510	520		
LNKLANQISG	EEMQKLN YKV	DGEGQDPAKV	AKEFLKEKGL	I	

Sequence ID 003: iTapentadolSnFR1.0

```
      10      20      30      40      50      60
ANDTVVVGSI EFTEGIIIVAN MVAEMIEAHT DLKVVRKLNL GGENVNFEAI KRGGANNGID

      70      80      90     100     110     120
IYVEYTGHGL VDILGFPEPN VYITADKQKN GIKANFKIRH NVEDGSVQLA DHYQQNTPIG

     130     140     150     160     170     180
DGPVLLPDNH YLSTQSVLSK DPNEKRDHMV LLEFVTAAGI TLGMDELYKG GTGGSMSKGE

     190     200     210     220     230     240
ELFTGVVPIL VELDGDVNGH KFSVRGEGEG DATNGKLTLLK FICTTGKLPV PWPTLVTTLT

     250     260     270     280     290     300
YGVQCFSRYP DHMKQHDFFK SAMPEGYVQE RTISFKDDGT YKTRAEVKFE GDTLVNRIEL

     310     320     330     340     350     360
KGIDFKEDGN ILGHKLEYNF PPPSSTDPEG AYETVKKEYK RKWNIVWLKP LGFNNTYTLT

     370     380     390     400     410     420
VKDELAKQYN LKTFSDLAKI SDKLILGATM FFLEGPDGYP GLQKLYNFKF KHTKSMDMGI

     430     440     450     460     470     480
RYTAIDNNEV QVIDAAATDG LLVSHKLIKIL EDDKAFFPPY YAAPIIRQDV LDKHPELKDV

     490     500     510     520
LNKLANQISL EEMQKLNKYV DGEGQDPAKV AKEFLKEKGL I
```

Sequence ID 004: iS-methadoneSnFR1.0

```
      10      20      30      40      50      60
ANDTVVVGSI VFTEGIIVAN MVAEMIEAHT DLKVVRKLNL GGENVNFEAI KRGGANNGID

      70      80      90     100     110     120
IYVEYTGHL  VDILGFPEPN VYITADKQKN GIKANFKIRH NVEDGSVQLA DHYQQNTPIG

     130     140     150     160     170     180
DGPVLLPDNH YLSTQSVLSK DPNEKRDHMV LLEFVTAAGI TLGMDELYKG GTGGSMKGE

     190     200     210     220     230     240
ELFTGVVPIL VELDGDVNGH KFSVRGEGEG DATNGKLTLL FICTTGKLPV PWPTLVTTLT

     250     260     270     280     290     300
YGVQCFSRYP DHMKQHDFFK SAMPEGYVQE RTISFKDDGT YKTRAEVKFE GDTLVNRIEL

     310     320     330     340     350     360
KGIDFKEDGN ILGHKLEYNF PPPSSTDPEG AYETVKKEYK RKWNIVWLKP LGFNNTYTLT

     370     380     390     400     410     420
VKDELAKQYN LKTFSDLAKI SDKLILGATM FFLEGPDGYP GLQKLYNFKF KHTKSMDMGI

     430     440     450     460     470     480
RYTAIDNNEV QVIDAFATDG LLVSHKLLKIL EDDKAFFPPY YAAPIIRQDV LDKHPELKDV

     490     500     510     520
LNKLANQISA EEMQKLNKVV DGEGQDPAKV AKEFLKEKGL I
```

Sequence ID 005: iLevorphanolSnFR1.0

10	20	30	40	50	60
ANDTVVVGSI	IFTETIIIVAN	MVAEMIEAHT	DLKVVRKLN	GGVNVNFEAI	KRGGANNGID
70	80	90	100	110	120
IYVEYTGHL	VDILGFPEPN	VYITADKQKN	GIKANFKIRH	NVEDGSVQLA	DHYQQNTPIG
130	140	150	160	170	180
DGPVLLPDNH	YLSTQSVLSK	DPNEKRDHMV	LLEFVTAAGI	TLGMDELYKG	GTGGSMKGE
190	200	210	220	230	240
ELFTGVVPIL	VELDGDVNGH	KFSVRGEGEG	DATNGKLTLL	FICTTGKLPV	PWPTLVTTLT
250	260	270	280	290	300
YGVQCFSRYP	DHMKQHDFFK	SAMPEGYVQE	RTISFKDDGT	YKTRAEVKFE	GDTLVNRIEL
310	320	330	340	350	360
KGIDFKEDGN	ILGHKLEYNF	PPPATTDPEG	AYETVKKEYK	RKWNIVWLKP	LGFNNTYTLT
370	380	390	400	410	420
VKDELAKQYN	LKTFSDLAKI	SDKLILGATM	FFLEGPDGYP	GLQKLYNFKF	KHTKSMDMGI
430	440	450	460	470	480
RYTAIDNNEV	QVIDAWATDG	LLVSHKLLKIL	EDDKWFFPPY	YAAPIIRQDV	LDKHPELKDV
490	500	510	520		
LNKLANQISL	EEMQKLNKVV	DGEGQDPAKV	AKEFLKEKGL	I	

Sequence ID 006: iBRL52537SnFR lead 1

10	20	30	40	50	60
ANDTVVVGSI	EFTEGIIIVAN	MVAEMIEAHT	DLKVVRKLN	GGVNVNFEAI	KRGGANNGID
70	80	90	100	110	120
IYVEYTGTL	VDILGFPEPN	VYITADKQKN	GIKANFKIRH	NVEDGSVQLA	DHYQQNTPIG
130	140	150	160	170	180
DGPVLLPDNH	YLSTQSVLSK	DPNEKRDHMV	LLEFVTAAGI	TLGMDELYKG	GTGGSMSKGE
190	200	210	220	230	240
ELFTGVVPIL	VELDGDVNGH	KFSVRGEGEG	DATNGKLTLL	FICTTGKLPV	PWPTLVTTLT
250	260	270	280	290	300
YGVQCFSRYP	DHMKQHDFFK	SAMPEGYVQE	RTISFKDDGT	YKTRAEVKFE	GDTLVNRIEL
310	320	330	340	350	360
KGIDFKEDGN	ILGHKLEYNF	PPPPMTDPEG	AYETVKKEYK	RKWNIVWLKP	LGFNNTYTLT
370	380	390	400	410	420
VKDELAKQYN	LKTFSDLAKI	SDKLILGATM	FFLEGPDGYP	GLQKLYNFKF	KHTKSMDMGI
430	440	450	460	470	480
RYTAIDNNEV	QVIDAWATDG	LLVSHKLLKIL	EDDKAFFPPY	YAAPIIRQDV	LDKHPELKDV
490	500	510	520		
LNKLANQISL	EEMQKLNKVV	DGEGQDPAKV	AKEFLKEKGL	I	

Sequence ID 007: iBRL52537SnFR lead 2

10	20	30	40	50	60
ANDTVVVGSI	EFTEGIIIVAN	MVAEMIEAHT	DLKVVRKLN	GGVNVNFEAI	KRGGANNGID
70	80	90	100	110	120
IYVEYTGTL	VDILGFPEPN	VYITADKQKN	GIKANFKIRH	NVEDGSVQLA	DHYQQNTPIG
130	140	150	160	170	180
DGPVLLPDNH	YLSTQSVLSK	DPNEKRDHMV	LLEFVTAAGI	TLGMDELYKG	GTGGSMKGE
190	200	210	220	230	240
ELFTGVVPIL	VELDGDVNGH	KFSVRGEGEG	DATNGKLTLL	FICTTGKLPV	PWPTLVTTLT
250	260	270	280	290	300
YGVQCFSRYP	DHMKQHDFFK	SAMPEGYVQE	RTISFKDDGT	YKTRAEVKFE	GDTLVNRIEL
310	320	330	340	350	360
KGIDFKEDGN	ILGHKLEYNF	PPPPVTDPEG	AYETVKKEYK	RKWNIVWLKP	LGFNNTYTLT
370	380	390	400	410	420
VKDELAKQYN	LKTFSDLAKI	SDKLILGATM	FFLEGPDGYP	GLQKLYNFKF	KHTKSMDMGI
430	440	450	460	470	480
RYTAIDNNEV	QVIDAWATDG	LLVSHKLIKIL	EDDKAFFPPY	YAAPIIRQDV	LDKHPELKDV
490	500	510	520		
LNKLANQISL	EEMQKLNKVV	DGEGQDPAKV	AKEFLKEKGL	I	

Sequence ID 008: iBRL52537SnFR lead 3

10	20	30	40	50	60
ANDTVVVGSI	EFTEGIIIVAN	MVAEMIEAHT	DLKVVRKLN	GGVNVNFEAI	KRGGANNGID
70	80	90	100	110	120
IYVEYTGTL	VDILGFPEPN	VYITADKQKN	GIKANFKIRH	NVEDGSVQLA	DHYQQNTPIG
130	140	150	160	170	180
DGPVLLPDNH	YLSTQSVLSK	DPNEKRDHMV	LLEFVTAAGI	TLGMDELYKG	GTGGSMKGE
190	200	210	220	230	240
ELFTGVVPIL	VELDGDVNGH	KFSVRGEGEG	DATNGKLTLL	FICTTGKLPV	PWPTLVTTLT
250	260	270	280	290	300
YGVQCFSRYP	DHMKQHDFFK	SAMPEGYVQE	RTISFKDDGT	YKTRAEVKFE	GDTLVNRIEL
310	320	330	340	350	360
KGIDFKEDGN	ILGHKLEYNF	PPPPRTDPEG	AYETVKKEYK	RKWNIVWLKP	LGFNNTYTLT
370	380	390	400	410	420
VKDELAKQYN	LKTFSDLAKI	SDKLILGATM	FFLEGPDPYP	GLQKLYNFKF	KHTKSMDMGI
430	440	450	460	470	480
RYTAIDNNEV	QVIDAWATDG	LLVSHKLLKIL	EDDKAFFPPY	YAAPIIRQDV	LDKHPELKDV
490	500	510	520		
LNKLANQISL	EEMQKLNKVV	DGEGQDPAKV	AKEFLKEKGL	I	



Sequence ID 009: iTramadolSnFR lead 1

```
      10      20      30      40      50      60
ANDTVVVGSI EFTEGIIIVAN MVAEMIEAHT DLKVVRKLNL GGENVNFEAI KRGGANNGID

      70      80      90     100     110     120
IYVEYTGHL  VDILGFPEPN VYITADKQKN GIKANFKIRH NVEDGSVQLA DHYQQNTPIG

     130     140     150     160     170     180
DGPVLLPDNH YLSTQSVLSK DPNEKRDHMV LLEFVTAAGI TLGMDELYKG GTGGSMKGE

     190     200     210     220     230     240
ELFTGVVPIL VELDGDVNGH KFSVRGEGEG DATNGKLTLLK FICTTGKLPV PWPTLVTTLT

     250     260     270     280     290     300
YGVQCFSRYP DHMKQHDFFK SAMPEGYVQE RTISFKDDGT YKTRAEVKFE GDTLVNRIEL

     310     320     330     340     350     360
KGIDFKEDGN ILGHKLEYNF PPPSSTDPEG AYETVKKEYK RKWNIVWLKP LGFNNTYTLT

     370     380     390     400     410     420
VKDELAKQYN LKTFSDLAKI SDKLILGATM FFLEGPDPGYP GLQKLYNFKF KHTKSMDMGI

     430     440     450     460     470     480
RYTAIDNNEV QVIDATATDG LLVSHKLIKIL EDDKAFFPPY YAAPIIRQDV LDKHPELKDV

     490     500     510     520
LNKLANQISL EEMQKLNKYV DGEGQDPAKV AKEFLKEKGL I
```

Sequence ID 010: iTramadolSnFR lead 2

```
      10      20      30      40      50      60
ANDTVVVGSI EFTEGIIIVAN MVAEMIEAHT DLKVVRKLNL GGENVNFEAI KRGGANNGID

      70      80      90     100     110     120
IYVEYTGHGL VDILGFPEPN VYITADKQKN GIKANFKIRH NVEDGSVQLA DHYQQNTPIG

     130     140     150     160     170     180
DGPVLLPDNH YLSTQSVLSK DPNEKRDHMV LLEFVTAAGI TLGMDELYKG GTGGSMSKGE

     190     200     210     220     230     240
ELFTGVVPIL VELDGDVNGH KFSVRGEGEG DATNGKLTLLK FICTTGKLPV PWPTLVTTLT

     250     260     270     280     290     300
YGVQCFSRYP DHMKQHDFFK SAMPEGYVQE RTISFKDDGT YKTRAEVKFE GDTLVNRIEL

     310     320     330     340     350     360
KGIDFKEDGN ILGHKLEYNF PPPSSTDPEG AYETVKKEYK RKWNIVWLKP LGFNNTYTLT

     370     380     390     400     410     420
VKDELAKQYN LKTFSDLAKI SDKLILGATM FFLEGPDGYP GLQKLYNFKF KHTKSMDMGI

     430     440     450     460     470     480
RYTAIDNNEV QVIDACATDG LLVSHKLIKIL EDDKAFFPPY YAAPIIRQDV LDKHPELKDV

     490     500     510     520
LNKLANQISL EEMQKLNKYV DGEGQDPAKV AKEFLKEKGL I
```

## Sequence ID 011: iButorphanolSnFR lead 1

```
      10      20      30      40      50      60
ANDTVVVGSI EFTEGIIIVAN MVAEMIEAHT DLKVVRKLNL GGVNVNFEAI KRGGANNGID

      70      80      90     100     110     120
IYVEYTGTLG VDILGFPEPN VYITADKQKN GIKANFKIRH NVEDGSVQLA DHYQQNTPIG

     130     140     150     160     170     180
DGPVLLPDNH YLSTQSVLSK DPNEKRDHMV LLEFVTAAGI TLGMDELYKG GTGGSMSKGE

     190     200     210     220     230     240
ELFTGVVPIL VELDGDVNGH KFSVRGEGEG DATNGKLTLLK FICTTGKLPV PWPTLVTTLT

     250     260     270     280     290     300
YGVQCFSRYP DHMKQHDFFK SAMPEGYVQE RTISFKDDGT YKTRAEVKFE GDTLVNRIEL

     310     320     330     340     350     360
KGIDFKEDGN ILGHKLEYNF PPPSSTDPEG AYETVKKEYK RKWNIVWLKP LGFNNTYTLT

     370     380     390     400     410     420
VKDELAKQYN LKTFSDLAKI SDKLILGATM FFLEGPDGYP GLQKLYNFKF KHTKSMDMGI

     430     440     450     460     470     480
RYTAIDNNEV QVIDAWATDG LLVSHKLLKIL EDDKAFFPPY YAAPIIRQDV LDKHPELKDV

     490     500     510     520
LNKLANQISL EEMQKLNKYV DGEGQDPAKV AKEFLKEKGL I
```

## Sequence ID 012: iNorfentanylSnFR lead 1

```
      10      20      30      40      50      60
ANDTVVVGSI EFTEGIIIVAN MVAEMIEAHT DLKVVRKLNL GGVNVNFEAI KRGGANNGID

      70      80      90     100     110     120
IYVEYTG TGL VDILGFPEPN VYITADKQKN GIKANFKIRH NVEDGSVQLA DHYQQNTPIG

     130     140     150     160     170     180
DGPVLLPDNH YLSTQSVLSK DPNEKRDHMV LLEFVTAAGI TLGMDELYKG GTGGSMSKGE

     190     200     210     220     230     240
ELFTGVVPIL VELDGDVNGH KFSVRGEGEG DATNGKLT LK FICTTGKLPV PWPTLVTTLT

     250     260     270     280     290     300
YGVQCFSRYP DHMKQHDFFK SAMPEGYVQE RTISFKDDGT YKTRAEVKFE GDTLVNRIEL

     310     320     330     340     350     360
KGIDFKEDGN ILGHKLEYNF PPPSSTDPEG AYETVKKEYK RKWNIVWLKP LGFNNTYTLT

     370     380     390     400     410     420
VKDELAKQYN LKTFSDLAKI SDKLILGATM FFLERPDGYP GLQKLYNFKF KHTKSMDMGI

     430     440     450     460     470     480
RYTAIDNNEV QVIDAWATDG LLVSHK LKIL EDDKAFFPPY YAAPIIRQDV LDKHPELKDV

     490     500     510     520
LNKLANQISL EEMQKLN YKV DGEGQDPAKV AKEFLKEKGL I
```

## Sequence ID 013: iSufentanilSnFR lead 1

```
      10      20      30      40      50      60
ANDTVVVGSI NFTEGIIVAN MVAEMIEAHT DLKVVRKLNL GGENVNFEAI KRGGANNGID

      70      80      90     100     110     120
IYVEYTGHL  VDILGFPEPN VYITADKQKN GIKANFKIRH NVEDGSVQLA DHYQQNTPIG

     130     140     150     160     170     180
DGPVLLPDNH YLSTQSVLSK DPNEKRDHMV LLEFVTAAGI TLGMDELYKG GTGGSMKGE

     190     200     210     220     230     240
ELFTGVVPIL VELDGDVNGH KFSVRGEGEG DATNGKLTLL FICTTGKLPV PWPTLVTTLT

     250     260     270     280     290     300
YGVQCFSRYP DHMKQHDFFK SAMPEGYVQE RTISFKDDGT YKTRAEVKFE GDTLVNRIEL

     310     320     330     340     350     360
KGIDFKEDGN ILGHKLEYNF PPPPSTDPEG AYETVKKEYK RKWNIVWLKP LGFNNTGTLT

     370     380     390     400     410     420
VKDELAKQYN LKTFSDLAKI SDKLILGATM FFLEAPDGYG GLQKLYNFKF KHTKSMDMGI

     430     440     450     460     470     480
RYTAIDNNEV QVIDAWATDG LLVSHKLIKIL EDDKAFFPPY YAAPIIRQDV LDKHPELKDV

     490     500     510     520
LNKLANQISL EEMQKLNKYV DGEGQDPAKV AKEFLKEKGL I
```

## Sequence ID 014: iMorphineSnFR lead 1

10	20	30	40	50	60
ANDTVVVGSI	PFTEGIIVAN	MVAEMIEAHT	DLKVVRKLN	GGINVNFEAI	KRGGANNGID
70	80	90	100	110	120
IYVEYTGHL	VDILGFPEPN	VYITADKQKN	GIKANFKIRH	NVEDGSVQLA	DHYQQNTPIG
130	140	150	160	170	180
DGPVLLPDNH	YLSTQSVLSK	DPNEKRDHMV	LLEFVTAAGI	TLGMDELYKG	GTGGSMSKGE
190	200	210	220	230	240
ELFTGVVPIL	VELDGDVNGH	KFSVRGEGEG	DATNGKLTLL	FICTTGKLPV	PWPTLVTTLT
250	260	270	280	290	300
YGVQCFSRYP	DHMKQHDFFK	SAMPEGYVQE	RTISFKDDGT	YKTRAEVKFE	GDTLVNRIEL
310	320	330	340	350	360
KGIDFKEDGN	ILGHKLEYNF	PPPATTDPEG	AYETVKKEYK	RKWNIVWLKP	LGFNNTYTLT
370	380	390	400	410	420
VKDELAKQYN	LKTFSDLAKI	SDKLILGATM	FFLEGPDGYP	GLQKLYNFKF	KHTKSMDMGI
430	440	450	460	470	480
RYTAIDNNEV	QVIDAWATDG	LLVSHKLLKIL	EDDKGFFPPY	YAAPIIRQDV	LDKHPELKDV
490	500	510	520		
LNKLANQISL	EEMQKLNKVV	DGEGQDPAKV	AKEFLKEKGL	I	

## Sequence ID 015: iMorphineSnFR lead 2

```
      10      20      30      40      50      60
ANDTVVVGSI PFTEGIIIVAN MVAEMIEAHT DLKVVRKLNL GGINVNF EAI KRGGANNGID

      70      80      90     100     110     120
IYVEYTG HGL VDILGFPEPN VYITADKQKN GIKANFKIRH NVEDGSVQLA DHYQQNTPIG

     130     140     150     160     170     180
DGPVLLPDNH YLSTQSVLSK DPNEKRDHMV LLEFVTAAGI TLGMDELYKG GTGGSMSKGE

     190     200     210     220     230     240
ELFTGVVPIL VELDGDVNGH KFSVRGEGEG DATNGKLT LK FICTTGKLPV PWPTLVTTLT

     250     260     270     280     290     300
YGVQCFSRYP DHMKQHDFFK SAMPEGYVQE RTISFKDDGT YKTRAEVKFE GDTLVNRIEL

     310     320     330     340     350     360
KGIDFKEDGN ILGHKLEYNF PPPATTDPEG AYETVKKEYK RKWNIVWLKP LGFNNTYTTLT

     370     380     390     400     410     420
VKDELAKQYN LKTFSDLAKI SDKLILGATM FFLEGPDGYP GLQKLYNFKF KHTKSMDMGI

     430     440     450     460     470     480
RYTAIDNNEV QVIDAWATDG LLVSHK LKIL EDDKQFFPPY YAAPIIRQDV LDKHPELKDV

     490     500     510     520
LNKLANQISL EEMQKLN YKV DGEGQDPAKV AKEFLKEKGL I
```

## Sequence ID 016: iCodeineSnFR lead 1

```
      10      20      30      40      50      60
ANDTVVVGSI FFTEGIIIVAN MVAEMIEAHT DLKVVRKLNL GGVNVNFEAI KRGGANNGID

      70      80      90     100     110     120
IYVEYTGHGL VDILGFPEPN VYITADKQKN GIKANFKIRH NVEDGSVQLA DHYQQNTPIG

     130     140     150     160     170     180
DGPVLLPDNH YLSTQSVLSK DPNEKRDHMV LLEFVTAAGI TLGMDELYKG GTGGSMSKGE

     190     200     210     220     230     240
ELFTGVVPIL VELDGDVNGH KFSVRGEGEG DATNGKLTLLK FICTTGKLPV PWPTLVTTLT

     250     260     270     280     290     300
YGVQCFSRYP DHMKQHDFFK SAMPEGYVQE RTISFKDDGT YKTRAEVKFE GDTLVNRIEL

     310     320     330     340     350     360
KGIDFKEDGN ILGHKLEYNF PPPATTDPEG AYETVKKEYK RKWNIVWLKP LGFNNTYTLT

     370     380     390     400     410     420
VKDELAKQYN LKTFSDLAKI SDKLILGATM FFLEGPDGYP GLQKLYNFKF KHTKSMDMGI

     430     440     450     460     470     480
RYTAIDNNEV QVIDAWATDG LLVSHKLLKIL EDDKAFFPPY YAAPIIRQDV LDKHPELKDV

     490     500     510     520
LNKLANQISL EEMQKLNKYV DGEGQDPAKV AKEFLKEKGL I
```



## Sequence ID 017: iCodeineSnFR lead 2

10	20	30	40	50	60
ANDTVVVGSI	LFTEGIIIVAN	MVAEMIEAHT	DLKVVRKLN	GGVNVNFEAI	KRGGANNGID
70	80	90	100	110	120
IYVEYTGHL	VDILGFPEPN	VYITADKQKN	GIKANFKIRH	NVEDGSVQLA	DHYQQNTPIG
130	140	150	160	170	180
DGPVLLPDNH	YLSTQSVLSK	DPNEKRDHMV	LLEFVTAAGI	TLGMDELYKG	GTGGSMSKGE
190	200	210	220	230	240
ELFTGVVPIL	VELDGDVNGH	KFSVRGEGEG	DATNGKLTLL	FICTTGKLPV	PWPTLVTTLT
250	260	270	280	290	300
YGVQCFSRYP	DHMKQHDFFK	SAMPEGYVQE	RTISFKDDGT	YKTRAEVKFE	GDTLVNRIEL
310	320	330	340	350	360
KGIDFKEDGN	ILGHKLEYNF	PPPATTDPEG	AYETVKKEYK	RKWNIVWLKP	LGFNNTYTLT
370	380	390	400	410	420
VKDELAKQYN	LKTFSDLAKI	SDKLILGATM	FFLEGPDPYP	GLQKLYNFKF	KHTKSMDMGI
430	440	450	460	470	480
RYTAIDNNEV	QVIDAWATDG	LLVSHKLLKIL	EDDKAFFPPY	YAAPIIRQDV	LDKHPELKDV
490	500	510	520		
LNKLANQISL	EEMQKLNKVV	DGEGQDPAKV	AKEFLKEKGL	I	

## Sequence ID 018: iCodeineSnFR lead 3

```
      10      20      30      40      50      60
ANDTVVVGSI PFTEGIIVAN MVAEMIEAHT DLKVVRKLNL GGVNVNFEAI KRGGANNGID

      70      80      90     100     110     120
IYVEYTGHL  VDILGFPEPN VYITADKQKN GIKANFKIRH NVEDGSVQLA DHYQQNTPIG

     130     140     150     160     170     180
DGPVLLPDNH YLSTQSVLSK DPNEKRDHMV LLEFVTAAGI TLGMDELYKG GTGGSMSKGE

     190     200     210     220     230     240
ELFTGVVPIL VELDGDVNGH KFSVRGEGEG DATNGKLTLLK FICTTGKLPV PWPTLVTTLT

     250     260     270     280     290     300
YGVQCFSRYP DHMKQHDFFK SAMPEGYVQE RTISFKDDGT YKTRAEVKFE GDTLVNRIEL

     310     320     330     340     350     360
KGIDFKEDGN ILGHKLEYNF PPPATTDPEG AYETVKKEYK RKWNIVWLKP LGFNNTYTLT

     370     380     390     400     410     420
VKDELAKQYN LKTFSDLAKI SDKLILGATM FFLEGPDGYP GLQKLYNFKF KHTKSMDMGI

     430     440     450     460     470     480
RYTAIDNNEV QVIDAWATDG LLVSHKLLKIL EDDKAFFPPY YAAPIIRQDV LDKHPELKDV

     490     500     510     520
LNKLANQISL EEMQKLNKYV DGEGQDPAKV AKEFLKEKGL I
```

Sequence ID 019: iHydromorphoneSnFR lead 1/iHydrocodoneSnFR lead 1

```
      10      20      30      40      50      60
ANDTVVVGSI DFTEGIIIVAN MVAEMIEAHT DLKVVRKLNL GGVNVNFEAI KRGGANNGID

      70      80      90     100     110     120
IYVEYTGHL  VDILGFPEPN VYITADKQKN GIKANFKIRH NVEDGSVQLA DHYQQNTPIG

     130     140     150     160     170     180
DGPVLLPDNH YLSTQSVLSK DPNEKRDHMV LLEFVTAAGI TLGMDELYKG GTGGSMSKGE

     190     200     210     220     230     240
ELFTGVVPIL VELDGDVNGH KFSVRGEGEG DATNGKLTLLK FICTTGKLPV PWPTLVTTLT

     250     260     270     280     290     300
YGVQCFSRYP DHMKQHDFFK SAMPEGYVQE RTISFKDDGT YKTRAEVKFE GDTLVNRIEL

     310     320     330     340     350     360
KGIDFKEDGN ILGHKLEYNF PPPATTDPEG AYETVKKEYK RKWNIVWLKP LGFNNTYTLT

     370     380     390     400     410     420
VKDELAKQYN LKTFSDLAKI SDKLILGATM FFLEGPDGYP GLQKLYNFKF KHTKSMDMGI

     430     440     450     460     470     480
RYTAIDNNEV QVIDAWATDG LLVSHKLIKIL EDDKAFFPPY YAAPIIRQDV LDKHPELKDV

     490     500     510     520
LNKLANQISL EEMQKLNKVV DGEGQDPAKV AKEFLKEKGL I
```

Sequence ID 020: iNaltrexoneSnFR lead 1

```
      10      20      30      40      50      60
ANDTVVVGSV EFTEGIIIVAN MVAEMIEAHT DLKVVRKLNL GGVNVNFEAI KRGGANNGID

      70      80      90     100     110     120
IYVEYTG TGL VDILGFPEPN VYITADKQKN GIKANFKIRH NVEDGSVQLA DHYQQNTPIG

     130     140     150     160     170     180
DGPVLLPDNH YLSTQSVLSK DPNEKRDHMV LLEFVTAAGI TLGMDELYKG GTGGSMSKGE

     190     200     210     220     230     240
ELFTGVVPIL VELDGDVNGH KFSVRGEGEG DATNGKLT LK FICTTGKLPV PWPTLVTTLT

     250     260     270     280     290     300
YGVQCFSRYP DHMKQHDFFK SAMPEGYVQE RTISFKDDGT YKTRAEVKFE GDTLVNRIEL

     310     320     330     340     350     360
KGIDFKEDGN ILGHKLEYNF PPPSSTDPEG AYETVKKEYK RKWNIVWLKP LGFNNTYTLT

     370     380     390     400     410     420
VKDELAKQYN LKTFSDLAKI SDKLILGATM FFLEGPDGYP GLQKLYNFKF KHTKSMDMGI

     430     440     450     460     470     480
RYTAIDNNEV QVIDAWATDG LLVSHK LKIL EDDKAFFPPY YAAPIIRQDV LDKHPELKDV

     490     500     510     520
LNKLANQISL EEMQKLN YKV DGEGQDPAKV AKEFLKEKGL I
```

## Sequence ID 021: iNaltrexoneSnFR lead 2

```
      10      20      30      40      50      60
ANDTVVVGSA EFTEGIIIVAN MVAEMIEAHT DLKVVRKLNL GGVNVNFEAI KRGGANNGID

      70      80      90     100     110     120
IYVEYTGTLG VDILGFPEPN VYITADKQKN GIKANFKIRH NVEDGSVQLA DHYQQNTPIG

     130     140     150     160     170     180
DGPVLLPDNH YLSTQSVLSK DPNEKRDHMV LLEFVTAAGI TLGMDELYKG GTGGSMSKGE

     190     200     210     220     230     240
ELFTGVVPIL VELDGDVNGH KFSVRGEGEG DATNGKLTLLK FICTTGKLPV PWPTLVTTLT

     250     260     270     280     290     300
YGVQCFSRYP DHMKQHDFFK SAMPEGYVQE RTISFKDDGT YKTRAEVKFE GDTLVNRIEL

     310     320     330     340     350     360
KGIDFKEDGN ILGHKLEYNF PPPSSTDPEG AYETVKKEYK RKWNIVWLKP LGFNNTYTLT

     370     380     390     400     410     420
VKDELAKQYN LKTFSDLAKI SDKLILGATM FFLEGPDGYP GLQKLYNFKF KHTKSMDMGI

     430     440     450     460     470     480
RYTAIDNNEV QVIDAWATDG LLVSHKLLKIL EDDKAFFPPY YAAPIIRQDV LDKHPELKDV

     490     500     510     520
LNKLANQISL EEMQKLNKYV DGEGQDPAKV AKEFLKEKGL I
```

Sequence ID 022: iNaltrexoneSnFR lead 3

10	20	30	40	50	60
ANDTVVVGSM	EFTEGIIIVAN	MVAEMIEAHT	DLKVVRKLN	GGVNVNFEAI	KRGGANNGID
70	80	90	100	110	120
IYVEYTGTL	VDILGFPEPN	VYITADKQKN	GIKANFKIRH	NVEDGSVQLA	DHYQQNTPIG
130	140	150	160	170	180
DGPVLLPDNH	YLSTQSVLSK	DPNEKRDHMV	LLEFVTAAGI	TLGMDELYKG	GTGGSMSKGE
190	200	210	220	230	240
ELFTGVVPIL	VELDGDVNGH	KFSVRGEGEG	DATNGKLTLL	FICTTGKLPV	PWPTLVTTLT
250	260	270	280	290	300
YGVQCFSRYP	DHMKQHDFFK	SAMPEGYVQE	RTISFKDDGT	YKTRAEVKFE	GDTLVNRIEL
310	320	330	340	350	360
KGIDFKEDGN	ILGHKLEYNF	PPPSSTDPEG	AYETVKKEYK	RKWNIVWLKP	LGFNNTYTLT
370	380	390	400	410	420
VKDELAKQYN	LKTFSDLAKI	SDKLILGATM	FFLEGPDPYP	GLQKLYNFKF	KHTKSMDMGI
430	440	450	460	470	480
RYTAIDNNEV	QVIDAWATDG	LLVSHKLIKIL	EDDKAFFPPY	YAAPIIRQDV	LDKHPELKDV
490	500	510	520		
LNKLANQISL	EEMQKLNKVV	DGEGQDPAKV	AKEFLKEKGL	I	

## Sequence ID 022: iR-MethadoneSnFR lead 1

```
      10      20      30      40      50      60
ANDTVVVGSI EFTEGIIIVAN MVAEMIEAHT DLKVVRKLNL GGENVNF EAI KRGGANNGID

      70      80      90     100     110     120
IYVEYTG HGL VDILGFPEPN VYITADKQKN GIKANFKIRH NVEDGSVQLA DHYQQNTPIG

     130     140     150     160     170     180
DGPVLLPDNH YLSTQSVLSK DPNEKRDH MV LLEFVTAAGI TLGMDELYKG GTGGSMSKGE

     190     200     210     220     230     240
ELFTGVVPIL VELDGDVNGH KFSVRGEGEG DATNGKLT LK FICTTGKLPV PWPTLVTTLT

     250     260     270     280     290     300
YGVQCFSRYP DHMKQHDFFK SAMPEGYVQE RTISFKDDGT YKTRAEVKFE GDTLVNRIEL

     310     320     330     340     350     360
KGIDFKEDGN ILGHKLEYNF PPPSSTDPEG AYETVKKEYK RKWNIVWLKP LGFNNTYTLT

     370     380     390     400     410     420
VKDELAKQYN LKTFSDLAKI SDKLILGATM FFLEGPDGYP GLQKLYNFKF KHTKSMDMGI

     430     440     450     460     470     480
RYTAIDNNEV QVIDAFATDG LLVSHK LKIL EDDKAFFPPY YAAPIIRQDV LDKHPELKDV

     490     500     510     520
LNKLANQISL EEMQKLN YKV DGEGQDPAKV AKEFLKEKGL I
```

## Sequence ID 023: iFentanylSnFR-mTurquoise0.1

```
      10      20      30      40      50      60
ANDTVVVGSA NFTEGIIIVAN MVAEMIEAHT DLKVVRKLNL GGENVNFEAI KRGGANNGID

      70      80      90     100     110     120
IYVEYTGHGL VDILGFPEPN VYITADKQKN GIKANFKIRH NVEDGSVQLA DHYQQNTPIG

     130     140     150     160     170     180
DGPVLLPDNH YLSTQSVLSK DPNEKRDHMV LLEFVTAAGI TLGMDELYKG GTGGSMSKGE

     190     200     210     220     230     240
ELFTGVVPIL VELDGDVNGH KFSVRGEGEG DATNGKLTLLK FICTTGKLPV PWPTLVTTLS

     250     260     270     280     290     300
WGVQCFARYP DHMKQHDFFK SAMPEGYVQE RTISFKDDGT YKTRAEVKFE GDTLVNRIEL

     310     320     330     340     350     360
KGIDFKEDGN ILGHKLEYNF APPPSTDPEG AYETVKKEYK RKWNIVWLKP LGFNNTGTLT

     370     380     390     400     410     420
VKDELAKQYN LKTFSDLAKI SDKLILGATM FFLEAPDGYP GLQKLYNFKF KHTKSMDMGI

     430     440     450     460     470     480
RYTAIDNNEV QVIDAWATDG LLVSHKLIKIL EDDKAFFPPY YAAPIIRQDV LDKHPELKDV

     490     500     510     520
LNKLANQISL EEMQKLNKYV DGEGQDPAKV AKEFLKEKGL I
```



## Sequence ID 024: iTapentadolSnFR-mTurquoise0.1

```

      10      20      30      40      50      60
ANDTVVVGSI EFTEGIIIVAN MVAEMIEAHT DLKVVRKLNL GGENVNFEAI KRGGANNGID

      70      80      90     100     110     120
IYVEYTGHL  VDILGFPEPN VYITADKQKN GIKANFKIRH NVEDGSVQLA DHYQQNTPIG

     130     140     150     160     170     180
DGPVLLPDNH YLSTQSVLSK DPNEKRDHMV LLEFVTAAGI TLGMDELYKG GTGGSMSKGE

     190     200     210     220     230     240
ELFTGVVPIL VELDGDVNGH KFSVRGEGEG DATNGKLTLL FICTTGKLPV PWPTLVTTLS

     250     260     270     280     290     300
WGVQCFARYP DHMKQHDFFK SAMPEGYVQE RTISFKDDGT YKTRAEVKFE GDTLVNRIEL

     310     320     330     340     350     360
KGIDFKEDGN ILGHKLEYNF EPPSSTDPEG AYETVKKEYK RKWNIVWLKP LGFNNTYTLT

     370     380     390     400     410     420
VKDELAKQYN LKTFSDLAKI SDKLILGATM FFLEGPDGYP GLQKLYNFKF KHTKSMDMGI

     430     440     450     460     470     480
RYTAIDNNEV QVIDAAATDG LLVSHKLIKIL EDDKAFFPPY YAAPIIRQDV LDKHPELKDV

     490     500     510     520
LNKLANQISL EEMQKLNKYV DGEGQDPAKV AKEFLKEKGL I
```

Sequence ID 025: iS-methadoneSnFR1.0-mTurquoise0.0

10	20	30	40	50	60
ANDTVVVGSI	VFTEGIIIVAN	MVAEMIEAHT	DLKVVRKLN	GGENVNFEAI	KRGGANNGID
70	80	90	100	110	120
IYVEYTGHL	VDILGFPEPN	VYITADKQKN	GIKANFKIRH	NVEDGSVQLA	DHYQQNTPIG
130	140	150	160	170	180
DGPVLLPDNH	YLSTQSVLSK	DPNEKRDHMV	LLEFVTAAGI	TLGMDELYKG	GTGGSMKGE
190	200	210	220	230	240
ELFTGVVPIL	VELDGDVNGH	KFSVRGEGEG	DATNGKLTLL	FICTTGKLPV	PWPTLVTTLS
250	260	270	280	290	300
WGVQCFARYP	DHMKQHDFFK	SAMPEGYVQE	RTISFKDDGT	YKTRAEVKFE	GDTLVNRIEL
310	320	330	340	350	360
KGIDFKEDGN	ILGHKLEYNF	PPPSSTDPEG	AYETVKKEYK	RKWNIVWLKP	LGFNNTYTLT
370	380	390	400	410	420
VKDELAKQYN	LKTFSDLAKI	SDKLILGATM	FFLEGPDPYP	GLQKLYNFKF	KHTKSMDMGI
430	440	450	460	470	480
RYTAIDNNEV	QVIDAFATDG	LLVSHKLLKIL	EDDKAFFPPY	YAAPIIRQDV	LDKHPELKDV
490	500	510	520		
LNKLANQISA	EEMQKLNKVV	DGEGQDPAKV	AKEFLKEKGL	I	